SEMI-ACTIVE VIBRATION CONTROL OF A PARALLEL PLATFORM MECHANISM USING MAGNETORHEOLOGICAL DAMPING

By

MEMET UNSAL

A DISSERTATION PRESENTED TO THE GRADUATE SCHOOL
OF THE UNIVERSITY OF FLORIDA IN PARTIAL FULFILLMENT
OF THE REQUIREMENTS FOR THE DEGREE OF
DOCTOR OF PHILOSOPHY

UNIVERSITY OF FLORIDA

2006

Copyright 2006

by

Memet Unsal

To my family, whose love and support always found a way to reach me from thousands of miles away, and to those who never ceased to offer their love and friendship.

ACKNOWLEDGMENTS

Since I was old enough to get on a plane by myself, I've always been leaving home: Leaving my home town to go to secondary school, to high school, and to college; and finally, leaving my country to go to graduate school. Those I left behind, I've never really left behind. The country that I left behind is waiting for me to return.

All these years, I felt the support and love of my family with me. I thank my parents Belkıs and Ercan Ünsal for their part in making me who I am; and my brothers Bulut and Doruk who have become my friends along the way.

Wherever I went, I met people who left their mark. I owe thanks to them for long hours of discussion, and for their insight and inspiration. The greatest inspiration appeared out of nowhere, smiling, and held my hand. I thank Emel for appearing.

Finally, I would like to thank my advisors Carl Crane and Christopher Niezrecki for their help, advice, and support. I would also like to thank John Schueller, Gloria Wiens, and Antonio Arroyo for serving on my supervisory committee.

TABLE OF CONTENTS

page

ACKNOWLEDGMENTS iv

LIST OF FIGURES viii

ABSTRACT xvi

CHAPTER

1 INTRODUCTION 1

1.1 Problem Statement 1
1.2 Hexapod Review 3
1.2.1 Hard Platforms 3
1.2.2 Soft Platforms 5
1.3 Need for Vibration Control of Hexapods 8
1.4 Vibrations in Space Applications 9
1.4.1 Launch Operation 9
1.4.2 On Orbit Operation 10

2 VIBRATION ISOLATION 12

2.1 Vibration Control Strategies 12
2.2 Single-Axis Passive Isolator 15
2.3 Single-Axis Active Isolator 17
2.4 Single-Axis Semi-Active Isolator 19

3 SMART MATERIALS AND MAGNETORHEOLOGICAL TECHNOLOGY 22

3.1 Smart Materials Used in Semi-Active Vibration Control 22
3.1.1 Piezoelectric Materials 22
3.1.2 Shape Memory Alloys 24
3.1.3 Ionic Gels 24
3.1.4 Electroactive Polymers 25
3.1.5 Smart Fluids 25
3.2 Magnetorheological (MR) Technology 26
3.2.1 Magnetorheological Fluids 26
3.2.2 Magnetorheological Devices and Fluid Dampers 27
3.3 Magnetorheological Fluid Models 30

3.3.1 Equivalent Viscous Damping 30
3.3.2 Bingham Model 31
3.3.3 Bouc-Wen Model 32
3.3.4 Herschel-Bulkley Model 32

4 MAGNETORHEOLOGICAL DAMPER DESIGN 35

4.1 Damper Design Criteria 35
4.2 Magnetorheological Damper Prototypes 36
4.2.1 Double-Shafted Damper with Aluminum Housing 37
4.2.2 Double-Shafted Damper with Steel Housing 39
4.2.3 Syringe Type Damper with Parallel Rod 40
4.2.4 Syringe Type Damper with Cylindrical Outer Housing 42
4.3 Experimental Setup 44
4.3.1 Shaker 44
4.3.2 Vibration Isolator Setup 44
4.4 Results 45
4.4.1 Shaker Tests 45
4.4.2 Tension Tests 45

5 PARALLEL PLATFORM MECHANISMS 47

5.1 Statics of a Rigid Body 47
5.2 Forward and Reverse Static Analysis of Parallel Platform Mechanisms 49
5.3 Stiffness Mapping of Parallel Platform Mechanisms 51
5.4 Geometry of Parallel Platform Mechanisms 53

6 MODELING OF THE PARALLEL PLATFORM MECHANISM 60

6.1 Single Leg Connector Models 60
6.1.1 Basic Connector Model 60
6.1.2 Two-Stage Connector Model 63
6.1.3 Connector Model with Decoupling Stage 68
6.1.4 Semi-Active Connector Model with Decoupling Stage 71
6.2 Magnetorheological Damper Model 76
6.3 6 DOF Parallel Platform Model 82
6.3.1 6 DOF Parallel Platform Model with the Basic Connector Leg 83
6.3.2 6 DOF Parallel Platform Model with the Two-Stage Connector Leg 85

7 SIMULATION RESULTS 87

7.1 Basic Connector Leg Simulation Results 88
7.1.1 Passive Basic Connector Leg 89
7.1.2 Active Basic Connector Leg 91
7.1.3 Semi-Active Basic Connector Leg 92
7.1.4 6 DOF Parallel Platform Mechanism with the Basic Connector Leg 94

7.2 Two-Stage Connector Leg Simulation Results 97
7.2.1 Passive Two-Stage Connector Leg 97
7.2.2 Active Two-Stage Connector Leg 99
7.2.3 Semi-Active Two-Stage Connector Leg 101
7.2.4 6 DOF Parallel Platform Mechanism with the Two-stage Connector Leg 103
7.3 6 DOF Vibration Isolation of the Semi-active PKM 106
7.3.1 Linear Disturbance in the X-axis 107
7.3.2 Linear Disturbance in the Y-axis 108
7.3.3 Angular Disturbance around the Z-axis 108
7.3.4 Angular Disturbance around the X-axis 109
7.3.5 Angular Disturbance around the Y-axis 109
7.4 6 DOF Positioning 111
7.4.1 Positioning with Linear Disturbance in the Z-axis 114
7.4.2 Positioning with Linear Disturbance in the Y-axis 117
7.4.3 Positioning with Angular Disturbance around the Z-axis 119
7.4.4 Positioning with Angular Disturbance around the Y-axis 121

8 CONCLUSIONS 123

8.1 Summary and Conclusions 123
8.2 Future Work 131

A MATLAB CODE 133

A.1 Basic Connector Leg Model 133
A.2 Two-stage Connector Leg Model 138
A.3 Connector Leg Model with Decoupling Stage 144
A.4 Two-Stage Connector Leg Natural Frequencies 148

B SIMULINK MODELS OF CONNECTOR LEGS 149

B.1 Basic Connector Leg Model 149
B.2 Two-Stage Connector Leg Model 154
B.3 Connector Leg Model with Decoupling Stage 159

C PROTOTYPE DRAWINGS 165

C.1 Prototype 1: Double-Shafted Damper with Aluminum Housing 165
C.2 Prototype 2: Double-Shafted Damper with Steel Housing 167
C.3 Prototype 3: Syringe-Type Damper with Parallel Rod 168
C.4 Prototype 4: Syringe Type Damper with Cylindrical Outer Housing 169

D 6 DOF VIBRATION ISOLATION ADDITIONAL RESULTS 171

LIST OF REFERENCES 174

BIOGRAPHICAL SKETCH 180

LIST OF FIGURES

Figure page

1-1 Hexapod Active Vibration Isolation (HAVI) system from Intelligent Automation Inc 4

1-2 Hexapod assembly (SUITE) from CSA Engineering 5

1-3 Bipod configuration showing the Honeywell hybrid D-struts 6

1-4 Hexapod with no internal springs from JPL 7

1-5 University of Wyoming/JPL hexapod with internal springs 7

1-6 Soft hexapod from HT/UW 7

1-7 Soft hexapod from ULB 7

1-8 Two possible cases of vibration isolation 8

1-9 Launch of Minatour 10

2-1 Sensitive equipment mounted on a vibrating structure via passive isolator 15

2-2 Transmissibility FRF of a passive damper for various values of damping ratio 17

2-3 Skyhook damper configuration 18

2-4 Transmissibility of the skyhook damper system compared to that of the passive system for various values of damping ratio 19

2-5 Active implementation of the skyhook damper 19

2-6 Semi-active implementation of the skyhook damper 20

2-7 Clipping strategy of the semi-active controller 21

3-1 Piezoelectric actuator (FPA-1700-LV) from Dynamic Structures and Materials, LLC 23

3-2 Magnetorheological fluid: a) no magnetic field, b) with magnetic field 26

3-3 Flow modes of MR devices: a) Valve Mode b) Direct Shear Mode c) Squeeze Film Model 27

3-4 By-pass Type Damper 29

3-5 Schematic of the by-pass type MR damper 29

3-6 Schematic of RD-1500 MR fluid damper by the Lord Corporation 30

3-7 Double-shafted 20-ton large-scale MR fluid damper 30

3-8 Schematics of the models reviewed. 33

3-9 Controllable fluid damper models a) Bingham model b) Bouc-Wen model 34

4-1 Force decomposition of MR dampers 36

4-2 Magnetorheological fluid damper (SD-1000) from Lord Corporation 38

4-3 Inside view of damper showing Teflon seal 38

4-4 Schematic of the double-shafted damper with steel housing 39

4-5 Schematic of the damper showing the path of the flux lines 40

4-6 Low-carbon steel housing of the double-shafted MR damper 40

4-7 Magnetorheological fluid demonstration device from Lord Corporation 41

4-8 Syringe dampers with varying housing and valve dimensions 41

4-9 Syringe type damper with parallel rod 42

4-10 Syringe type damper with cylindrical outer housing with a) exploded view showing the inner housing and the coil; b) view of the fully assembled damper 43

4-11 Syringe type damper on the experimental setup 43

4-12 SigLab (20-42) signal analyzer 44

4-13 Increase in force for the syringe type damper when the input current is increased from 0 to 0.5 A at 4.5 seconds 45

4-14 Force-displacement curves for varying current at 5 in/min 46

4-15 Force-velocity curves for varying current 46

5-1 Representation of a force and a moment 47

5-2 Representation of a moment as a line at infinity multiplied by a force magnitude..48

5-3 Geometry of the a) top platform b) base platform.....54

5-4 The schematic of the parallel platform mechanism showing the orientation of the top platform to the base platform 55

5-5 The value of $\left|\det J\right|_{\max}$ for $0 \le \alpha \le 1$ 59

5-6 The optimal geometry of the parallel platform mechanism 59

6-1 Basic connector model 61

6-2 Basic connector Simulink model.....63

6-3 Frequency response of the basic connector for varying damping 63

6-4 Two-stage connector model 64

6-5 Two-stage connector Simulink model.....67

6-6 Frequency response of the two-stage connector for varying damping, b_2 67

6-7 Connector model with decoupling stage 68

6-8 Connector with decoupling stage Simulink model 72

6-9 Connector model with variable damping elements 73

6-10 Connector model with decoupling stage damper deactivated 73

6-11 Frequency response of the connector model with decoupling stage damping coefficient, b_3 = 100 Ns/m and varying b_2 74

6-12 Connector model with coupling stage damper blocked 74

6-13 Frequency response of the connector model with coupling stage damping coefficient, b_2 = 800 Ns/m and varying b_3 75

6-14 Comparison of the frequency response of the basic connector, the two-stage connector, and four modes of the connector model with the decoupling stage 76

6-15 Curve-fitting applied on the experimental force-velocity curves of the prototype ..77

6-16 Force vs. velocity curves for varying input for the prototype MR damper model 78

6-17 Force vs. velocity curves for varying input current for MR damper model.....79

6-18 SimMechanics model of MR damper control 79

6-19 Semi-active implementation of the skyhook damper control policy.....80

6-20 Semi-active implementation of the skyhook damper control policy.....80

6-21 Semi-active implementation of the skyhook damper control policy.....80

6-22 Two-stage connector system with the semi-active implementation of the skyhook damper control policy 81

6-23 SimMechanics model of the 6 DOF PKM model 82

6-24 SimMechanics model of the basic connector leg 83

6-25 Basic connector leg model 84

6-26 6 DOF parallel platform mechanism with basic connector leg model 84

6-27 SimMechanics model of the two-stage connector leg.....85

6-28 Two-stage connector leg model 86

6-29 6 DOF parallel platform mechanism with the two-stage connector leg models 86

7-1 Representative plots for comparison of displacement and acceleration transmissibility noise showing a) displacement transmissibility of active 6 DOF platform b) displacement transmissibility of semi-active 2 DOF connector leg and c) acceleration transmissibility of the same semi-active 2 DOF connector leg 88

7-2 SimMechanics model of the passive basic connector leg model 89

7-3 Acceleration transmissibility between the top and bottom masses of the passive basic connector leg modeled in a) Simulink and b) SimMechanics.....90

7-4 Natural frequency and corner frequency of the basic connector leg shown on the acceleration transmissibility plot of the passive leg.....90

7-5 SimMechanics model of the active basic connector leg model 91

7-6 Acceleration transmissibility between the top and bottom masses of the active basic connector leg modeled in a) Simulink and b) SimMechanics.....92

7-7 SimMechanics model of the semi-active basic connector leg model.....93

7-8 Acceleration transmissibility between the top and bottom masses of the semi-active basic connector leg modeled in a) Simulink and b) SimMechanics 93

7-9 Comparison of the acceleration transmissibility between the passive, active, and semi-active basic connector legs 94

7-10 Parallel platform mechanism with the basic connector leg 95

7-11 Passive – acceleration transmissibility between the top and bottom platforms of 6 DOF PKM with the passive basic connector legs 95

7-12 Active – acceleration transmissibility between the top and bottom platforms of 6 DOF PKM with the active basic connector legs 96

7-13 Semi-active – acceleration transmissibility between the top and bottom platforms of 6 DOF PKM with the semi-active basic connector legs 96

7-14 SimMechanics model of the passive two-stage connector leg model 98

7-15 Acceleration transmissibility between the top and bottom masses of the passive two-stage connector leg modeled in a) Simulink and b) SimMechanics 98

7-16 Natural frequency and corner frequency of the two-stage connector leg shown on the acceleration transmissibility plot of the passive leg 99

7-17 SimMechanics model of the active two-stage connector leg model 100

7-18 Acceleration transmissibility between the top and bottom masses of the active two-stage connector leg modeled in a) Simulink and b) SimMechanics 100

7-19 SimMechanics model of the semi-active two-stage connector leg model 101

7-20 Acceleration transmissibility between the top and bottom masses of the semi-active two-stage connector leg modeled in a) Simulink and b) SimMechanics 102

7-21 Comparison of the acceleration transmissibility between the passive, active, and semi-active two-stage connector legs 102

7-22 Parallel platform with the two-stage connector leg 103

7-23 Passive – acceleration transmissibility between the top and bottom platforms of 6 DOF PKM with the passive two-stage connector legs 104

7-24 Active – acceleration transmissibility between the top and bottom platforms of 6 DOF PKM with the active two-stage connector legs 104

7-25 Semi-active – acceleration transmissibility between the top and bottom platforms of 6 DOF PKM with the semi-active two-stage connector legs 105

7-26 Comparison of the acceleration transmissibility between the top and bottom platforms of the passive, active, and semi-active two-stage connector legs 106

7-27 X-axis RMS acceleration transmissibility between the top and bottom platforms for an input sinusoidal force in the x-axis 107

7-28 Y-axis RMS acceleration transmissibility between the top and bottom platforms for an input sinusoidal force in the y-axis 108

7-29 Z-axis RMS angular acceleration transmissibility between the top and bottom platforms for an input sinusoidal torque around the z-axis 109

7-30 X-axis RMS angular acceleration transmissibility between the top and bottom platforms for an input sinusoidal torque around the x-axis.....110

7-31 Y-axis RMS angular acceleration transmissibility between the top and bottom platforms for an input sinusoidal torque around the y-axis.....110

7-32 SimMechanics block diagram for positioning control of the semi-active parallel platform mechanism 111

7-33 Semi-active parallel platform mechanism used in positioning control 112

7-34 Position of the top platform center of mass.....113

7-35 Position errors in all three axes 113

7-36 Force applied by the actuators.....114

7-37 Position of the top platform center of mass in the z-axis with and without vibration control for a sinusoidal disturbance in the z-axis and with no disturbance 115

7-38 Position error of the top platform center of mass in the z-axis with and without vibration control for a sinusoidal disturbance in the z-axis and with no disturbance 116

7-39 Force applied by a single actuator with and without vibration control for a sinusoidal disturbance in the z-axis and with no disturbance 116

7-40 Position of the top platform center of mass in the y-axis with and without vibration control for a sinusoidal disturbance in the y-axis and with no disturbance 117

7-41 Position error of the top platform center of mass in the y-axis with and without vibration control for a sinusoidal disturbance in the y-axis and with no disturbance 118

7-42 Force applied by a single actuator with and without vibration control for a sinusoidal disturbance in the y-axis and with no disturbance 118

7-43 Position of the top platform center of mass around the z-axis with and without vibration control for a sinusoidal disturbance around the z-axis and with no disturbance 119

7-44 Position error of the top platform center of mass around the z-axis with and without vibration control for a sinusoidal disturbance around the z-axis and with no disturbance 120

7-45 Force applied by a single actuator with and without vibration control for a sinusoidal disturbance around the z-axis and with no disturbance 120

7-46 Position of the top platform center of mass around the y-axis with and without vibration control for a sinusoidal disturbance around the y-axis and with no disturbance 121

7-47 Position error of the top platform center of mass around the y-axis with and without vibration control for a sinusoidal disturbance around the y-axis and with no disturbance 122

7-48 Force applied by a single actuator with and without vibration control for a sinusoidal disturbance around the y-axis and with no disturbance 122

A-1 Magnitude and phase frequency response plots of passive basic connector leg with varying damping....137

A-2 Magnitude of the frequency response for the passive basic connector leg with varying damping....137

A-3 Magnitude and phase frequency response plots for the passive two-stage connector leg with varying damping....143

A-4 Magnitude of the frequency response for the passive two-stage connector leg with varying damping....143

A-5 Magnitude and phase frequency response plots for the passive two-stage connector leg with varying damping....147

A-6 Magnitude of the frequency response for the passive two-stage connector leg with varying damping....147

B-1 Simulink block diagram of the passive basic connector leg 149

B-2 Magnitude and phase frequency response plots of the passive basic connector leg 153

B-4 Magnitude and phase frequency response plots of the passive two-stage connector leg 158

B-5 Simulink block diagram of the passive connector leg with decoupling stage 159

B-6 Magnitude and phase frequency response plots of the passive connector leg with decoupling stage 164

C-1 Technical drawing of double-shafted damper with aluminum housing 165

C-2 Inside view of damper showing Teflon seal.....166

C-3 Outside view of double-shafted damper with aluminum housing.....166

C-4 Magnetic body around which the magnet wire is wrapped.....166

C-5 Schematic of the double-shafted damper with steel housing 167

C-6 Schematic of the damper showing the path of the flux lines 167

C-7 Low-carbon steel housing of the double-shafted damper 167

C-8 Double-shafted MR damper with steel housing.....168

C-9 Syringe type damper with parallel rod 168

C-10 Technical drawing of syringe type damper with parallel rod.....168

C-11 Syringe type damper with cylindrical outer housing with a) exploded view showing the inner housing and the coil; b) view of the fully assembled damper ..169

D-1 RMS transmissibility between the top platform angular acceleration around the y-axis and the bottom platform linear acceleration around the x-axis for an input sinusoidal force in the x-axis.....171

D-2 RMS transmissibility between the top platform angular acceleration around the x-axis and the bottom platform linear acceleration in the y-axis for an input sinusoidal force in the y-axis.....172

D-3 RMS transmissibility between the top platform linear acceleration in the y-axis and the bottom platform angular acceleration around the x-axis for an input sinusoidal torque around the x-axis.....173

D-4 RMS transmissibility between the top platform linear acceleration in the x-axis and the bottom platform angular acceleration around the y-axis for an input sinusoidal torque around the y-axis.....173

Abstract of Dissertation Presented to the Graduate School
of the University of Florida in Partial Fulfillment of the
Requirements for the Degree of Doctor of Philosophy

SEMI-ACTIVE VIBRATION CONTROL OF A PARALLEL PLATFORM MECHANISM USING MAGNETORHEOLOGICAL DAMPING

By

Memet Unsal

August 2006

Chair: Carl D. Crane, III
Cochair: Christopher Niezrecki
Major Department: Mechanical and Aerospace Engineering

Parallel platform mechanisms with 6 degrees-of-freedom (DOF) are ideal candidates for precision positioning applications. Compared to serial kinematic mechanisms, their 6 kinematic chains give them greater load carrying capacity, higher stiffness, the ability to remain stable in the unpowered configuration, and redundancy in motion. Many of the precision positioning applications are located in environments where certain degrees of disturbances exist. These disturbances in the form of vibrations degrade the performance of the sensitive instruments needed for precision positioning. Therefore, it is important to create a vibration-free environment to enable precision positioning. From a design perspective, it would be logical to have a parallel platform mechanism which is inherently an ideal mechanism for precise positioning to provide vibration isolation at the same time.

Within this work, a model of a 6 DOF vibration isolation system with semi-active control, using magnetorheological (MR) technology, is investigated. While passive vibration control and active vibration control have been extensively used in parallel platforms, a 6 DOF parallel platform which uses semi-active vibration control has not received as much attention. Advantages of semi-active control include reduced cost (by using a simpler actuator intended for only positioning), reduced power requirements, and improved stability. Within this work, a 6 DOF parallel platform model is created. Each leg of the platform is modeled as a 2 DOF system with an MR damper for adjustable damping in parallel with a stiffness element and in series with an actuator used for positioning. The vibration isolation performance of the parallel platform mechanism and its positioning capability are quantified through simulations. Simulation results show that MR dampers are effective in 6 DOF vibration isolation applications when they are incorporated into parallel platform mechanisms.

CHAPTER 1
INTRODUCTION

This dissertation addresses the issue of how semi-active variable-damping coupled with passive damping can improve vibration isolation. The multi-axis vibration control problem is further investigated. Semi-active control is based on smart material dampers: specifically, magnetorheological (MR) dampers. The multi-axis structure is a parallel kinematic mechanism with 6 degrees-of-freedom (hexapod).

1.1 Problem Statement

Disturbances in the form of vibrations can degrade the performance of sensitive equipment. As technology advances, more and more precision is expected from instruments used in a broad range of applications (such as machining, precision pointing, and space applications). Completely removing the source of vibration is impossible as external disturbances or vibration generating equipment will always be present. Therefore, the goal should be to isolate the vibrations at the interfaces between the vibration source and the sensitive equipment. This work is motivated by the need for a mechanism that can isolate vibrations while providing accurate 6 degree-of-freedom (DOF) positioning requirements. This is where parallel kinematic mechanisms emerge as an ideal candidate. Due to their six kinematic chains they have greater load carrying capacity, higher stiffness, the ability to remain stable in the unpowered configuration, and redundancy in motion (which makes them more tolerant to positioning errors) compared to serial kinematic mechanisms (Anderson *et al*., 2004; Hall *et al.,* 2003). They also have the minimum number of actuators to generate 6 DOF motion. These advantages make

them ideal for precision positioning applications. If precision positioning and the ability to isolate vibrations in all 6 DOF are combined in the same mechanism, this would result in significant savings in system complexity and weight (Geng and Haynes, 1994). Geng and Haynes (1994) also point out that compared with a truss mechanism where the forces at the connection modes include components in all 6 DOF; all forces transmitted between the top and bottom plates of a parallel mechanism are purely axial forces of the actuators, assuming the gravity and the inertial load of the connectors are neglected. If these axial forces can be successfully decoupled, they can be calculated and the vibrations caused by these forces can be eliminated (Geng and Haynes, 1994).

The literature offers a few examples of parallel platforms that aim to combine precision positioning and vibration isolation in the same mechanism. All of these use either passive or active control, or a combination of both. Active control (piezoceramic, electromagnetic, magnetostrictive, and voice-coil actuators are possible candidates) is used for positioning and also reduces vibration transmissions at low frequencies. Passive control (elastomer, fluid damping, and eddy currents are commonly used) attenuates high frequency inputs. The literature survey showed no examples of semi-active vibration control in a parallel platform mechanism which also performs positioning. However, two recent examples of parallel platform mechanisms which are solely built for vibration control through the use of semi-active magnetorheological (MR) dampers were found (Red Team Too, 2005; Jean *et al*., 2006).

The advantage of semi-active control is that it requires low external power, provides passive energy dissipation if the semi-active part fails, and has inherent stability. A variable damping device using semi-active control would approach the performance of

an active actuator in reducing low frequency vibrations while offering several advantages. These advantages include reduced cost by using a simpler actuator intended for only positioning, reduced power requirement, and improved stability. Therefore, this research will be focused on implementing semi-active vibration control on a parallel platform mechanism with an actuator for positioning and a passive isolation element for attenuating high frequency inputs.

1.2 Hexapod Review

Several different hexapod platforms were developed by various research groups to provide 6-axis vibration isolation in precision systems. Some of these platforms have larger actuation strokes than others that also give them 6-axis positioning capability. Two groups of these hexapods (Thayer *et al.*, 2002) (Table 1-1) are as follows:

- **Hard platforms:** These platforms use a stiff actuator, alone or in series with a soft spring. They typically have a very small actuation stroke (~50 μm).
- **Soft platforms:** These platforms use a soft actuator, typically a voice coil actuator. The voice coil actuator is used in parallel with a soft spring and provides far more actuation stroke (1000 μm or more).

1.2.1 Hard Platforms

The first hard hexapod was made by Intelligent Automation, Inc (Rockville, MD) (Figure 1-1). This hexapod uses a stiff actuator that uses the magnetostrictive alloy Terfenol-D. Terfenol-D provides accurate linear and oscillatory motion under a magnetic field generated by a low voltage electric current. The actuation stroke is ±127 microns. The struts have no passive isolation capability and use a spring to compensate for the mass of the payload. A load cell measures the axial force of the actuator, and

accelerometers are placed on both the bottom and top of each actuator (Geng *et al.*, 1995).

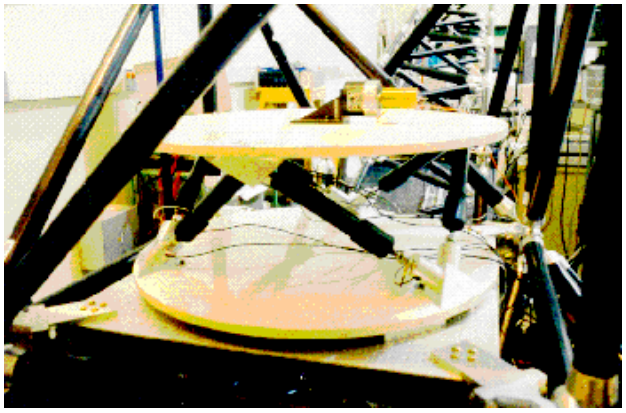

Figure 1-1. Hexapod Active Vibration Isolation (HAVI) system from Intelligent Automation Inc

Table 1-1. Summary of Hexapods[a]

Hexapod	**Actuator**	**Stroke (mm)**	**Sensor**	**Passive Damping**
Intelligent Automation	Magnetostrictive	±0.127	Load Cell, accelerometer	—
Draper	Piezoceramic	±0.025	Load Cell	—
Harris	Piezoceramic	±0.025	Accelerometers	—
CSA (UQP)	Electromagnetic	±0.020	Geophone	Elastomer
CSA (SUITE)	Piezoceramic	±0.030	Geophone	Elastomer
Honeywell	Voice Coil	±0.2	Accelerometer	Fluid
JPL	Voice Coil	±0.5	Load Cell	Eddy Current
JPL / Univ. of Wyoming	Voice Coil	±0.5	Load Cell	Eddy Current
Hood / UW	Voice Coil	±5	Load Cell, Geophone, LVDT	Elastomer
ULB	Voice Coil	±1.5	Load Cell	—

[a](Thayer *et al.*, 2002)

The hexapod designed by Draper Labs (Cambridge, MA) uses piezoceramic actuators. Load cells are used for feedback sensors. This hexapod has no passive isolation capability (Thayer *et al.*, 2002). Harris Corporation (Melbourne, FL) also built a hexapod with piezoceramic actuators. Base and payload accelerometers are used for

control. There is no passive isolation and the actuation stroke is ±25 microns (Thayer *et al.*, 2002).

CSA Engineering (Mountainview, CA) built two hard hexapods. The first is the UltraQuiet Platform (UQP). Stiff electromagnetic actuators provide the force, and six geophones are implemented in each strut to provide a single measurement of motion (Anderson *et al*., 1996). The second hard hexapod by CSA Engineering is the Satellite Ultraquiet Isolation Technology Experiment (SUITE) hexapod assembly (HXA) (Figure 1-2). The SUITE hexapod uses piezoceramic actuators. In series with the actuators are also passive isolation flexures (Anderson *et al*., 2000).

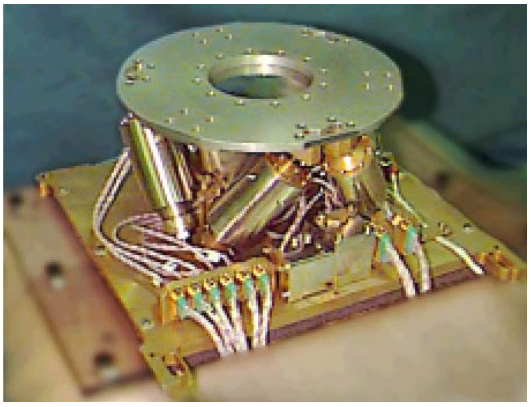

Figure 1-2. Hexapod assembly (SUITE) from CSA Engineering (Flint and Anderson, 2001)

1.2.2 Soft Platforms

The first soft platform to be reviewed is the Vibration Isolation and Suppression System (VISS) hexapod by Honeywell. The Hybrid D-Strut (Figure 1-3) is the key component of VISS. The hybrid D-strut consists of a voice coil actuator and bellows filled with damping fluid flowing through the orifice between the bellows. Accelerometers are used for feedback and the actuation stroke is ±2 mm (which is an

order of magnitude greater than the displacement of any hard hexapod systems). This gives the VISS (as with most soft hexapod systems) low frequency positioning capability.

The second soft hexapod (Figure 1-4) was built by the Jet Propulsion Laboratory (JPL) (Pasadena, CA). It uses voice coil actuators and load cells; and relies on external suspension to off-load the mass of the payload from the actuators. It has an actuation stroke of ±0.5 mm. A similar hexapod at the University of Wyoming (Figure 1-5) was also built by JPL. The only difference is that this hexapod has internal springs. This system also has an actuation stroke of ±0.5 mm (Thayer *et al.*, 2002).

Figure 1-3. Bipod configuration showing the Honeywell hybrid D-struts

The hexapod by Hood Technology (Hood River, OR) and University of Washington (Figure 1-6) also uses voice coil actuators which have an actuation stroke of ±5 mm. A load cell, an LVDT, and geophones are integrated into the struts as sensors. Elastomer flexures are used for passive damping.

The final hexapod (Figure 1-7) was manufactured by Université Libre de Bruxelles (ULB). Voice coil actuators and load cells are used. Passive damping is not included and external suspension is used to compensate for the mass of the payload. The stroke of the voice coil actuators is ±1.5 mm (Abu Hanieh, 2003).

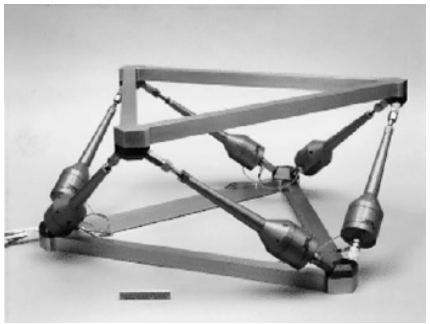

Figure 1-4. Hexapod with no internal springs from JPL

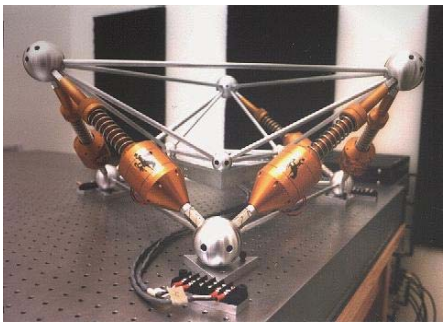

Figure 1-5. University of Wyoming/JPL hexapod with internal springs

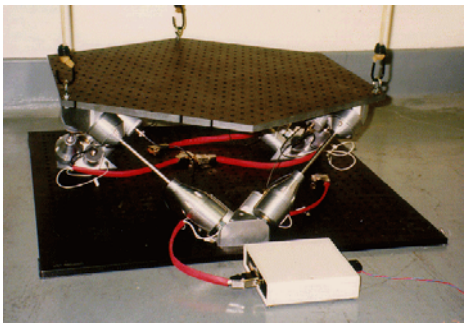

Figure 1-6. Soft hexapod from HT/UW (Thayer *et al.*, 2002)

Figure 1-7. Soft hexapod from ULB (Abu Hanieh, 2003)

1.3 Need for Vibration Control of Hexapods

Parallel kinematic manipulators have received much attention because they have distinct advantages over their serial counterparts. They have six serial kinematic chains (connectors) giving them greater load carrying capacity, higher stiffness, and redundancy in motion which makes them more tolerant to individual actuator positioning errors (Anderson *et al*., 2004; Hall *et al.,* 2003). These advantages make them ideal for precision positioning applications. However, many of these applications are located in environments where certain degrees of disturbances exist. These disturbances in the form of vibrations degrade the performance of the sensitive instruments which are essential for precision positioning. Therefore, it is a priority to create a vibration-free environment to enable precision positioning. To design a whole system free of vibrations is not a viable solution, as this would be extremely costly and is usually not feasible. Therefore, the disturbances need to be eliminated at the interfaces between either the vibration source and the main structure or the main structure and the sensitive equipment used for precision applications (Figure 1-8). From a design perspective, it would be logical to have a hexapod that is inherently an ideal mechanism for precise positioning, to provide vibration isolation at the same time.

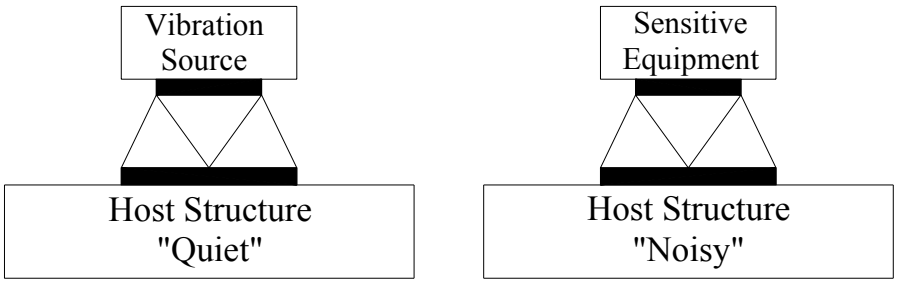

Figure 1-8. Two possible cases of vibration isolation

Hexapods have been used in machining processes, simulators, and space applications. The most promising area of research involving the use of hexapods for vibration isolation is space applications, where the need for vibration isolation of precision equipment is especially felt.

1.4 Vibrations in Space Applications

The vibration problem with space applications can be divided into launch operation and on orbit operation.

1.4.1 Launch Operation

Launch dynamics are a major factor affecting design of the spacecraft structure. Ensuring launch survival may often be a more difficult design problem than establishing the desired performance in orbit. The major concern during the launch operation is to make sure structural and acoustical vibrations do not cause damage to the payload. The main purposes of launch isolation are to enable more sensitive equipment to be launched, reduce the risk of equipment failures (Johnson *et al*., 2001), and reduce the cost and the mass of the spacecraft, which in turn increases the mass margin of additional payload that can be launched (Denoyer and Johnson, 2001). Passive isolation has been successfully used during several launch events such as the Hubble Space Telescope servicing missions (Winthrop and Cobb, 2003). A multi-axis isolation system, which greatly reduced the dynamic launch loads, has been developed for Minotaur (Figure 1-9) (Johnson *et al*., 2001). Active, passive, and hybrid isolators have been extensively studied and several designs in the literature show improved performance of active and hybrid isolation over purely passive isolation (Lee-Glauser *et al.,*1996; Winthrop and Cobb, 2003).

Figure 1-9. Launch of Minatour (Johnson *et al*., 2001)

1.4.2 On Orbit Operation

Spacecraft deal with numerous disturbances that can significantly reduce the effectiveness of the sensitive equipment on board. Therefore, it is of primary interest to reduce the vibrations that spacecraft are subject to during their life times. External disturbances include solar radiation pressure, thermal effects, micro-meteorite impacts, atmospheric drag, and gravity gradients. There are various internal disturbances including reaction wheels that control attitude, control moment gyros, cryogenic coolers (needed for removing heat from certain equipment), and solar array drives that direct the light gathering surfaces towards the sun. The satellite may also contain instruments that use gimbals or scanning articulating components to make their measurements (Denoyer and Johnson, 2001; Winthrop and Cobb, 2003). Also, when the spacecraft is manned, pumps, compressors, electric motors, fans, impacts, and astronaut motions create additional disturbances (Winthrop and Cobb, 2003).

Current and future satellite systems require increasing precision from the spacecraft bus whereas one of the major design considerations is to reduce the cost by moving

toward lighter and cheaper spacecraft buses (Cobb *et al*., 1999). These two trends seem to be incompatible as the lighter and cheaper bus will be unable to provide the quiet environment required for precision pointing. The solution is therefore to provide the isolation and suppression either between the noise generating equipment and the bus or between the sensitive equipment and the bus. In the first case, the vibrations generated by machinery are propagating into the host structure. In the second case, the host structure may have disturbances affecting sensitive equipment.

CHAPTER 2
VIBRATION ISOLATION

The proposed theoretical 6 DOF hexapod model uses a combination of passive and semi-active control for vibration isolation. In this chapter, a review of different vibration isolation strategies is provided. Then the single-axis passive isolator is described, followed by the active isolator using skyhook damper control, and finally the semi-active isolator.

2.1 Vibration Control Strategies

Structures and mechanical systems should be designed to enable better performance under different types of loading: particularly dynamic and transient loads. There are three fundamental control strategies to regulate or control the response of a system: passive control, active control, and semi-active control.

Traditionally, vibration isolation has focused on passive control. For passive control, mechanical devices such as energy dissipation devices or isolators are added to a mechanical system to increase energy dissipation and improve the performance of the system (Taniwangsa and Kelly, 1997). Several applications of this method have been reported and implemented (Tarics, 1984). For example, rubber isolators have been used in structures to decrease ground motion from earthquakes. An external power source for operation is not required for passive control systems. Instead the relative motion of the structure is used to develop the control forces to induce strain within the damping material (Symans and Constantinou, 1997). The primary advantage of passive damping systems is that they have will not induce instability under any degree of model

uncertainty (Lane and Ferri, 1995). However, the performance of such a system is limited because system parameters, especially damping cannot be varied. This causes passive systems to behave differently under changing conditions; therefore, they cannot always meet the design requirements. Guntur and Sankar (1981) show that if the parameters of an isolation system can be adjusted in response to varying external conditions, the performance of the system can be significantly improved.

Unlike passive systems, active systems can constantly supply and vary the flow of energy into the system. Based on the change in the instantaneous operating conditions as measured by sensors, the properties of the system can be adjusted (Hac and Youn, 1992). The heart of the control system is the actuator, which behaves as an artificial muscle and can potentially affect the system in an intelligent manner. This enables the active system to command arbitrary control forces (Lee and Clark, 1999). The actuators that are typically used in active control are pneumatic, hydraulic, electromagnetic, or intelligent material actuators. The practical disadvantages to these types of control approaches are the large power requirements needed for these actuators to do work on relatively stiff and massive structures and the limitations of the actuators. Hydraulic actuators offer a significant amount of force and displacement; however, they lack the frequency response to mitigate the forces induced by a shock. They cannot respond quickly enough to actively control shock or vibration (except at very low frequencies). Typically, intelligent material actuators are capable of generating sufficient force and have the required bandwidth. Unfortunately, they lack the required displacement capabilities for large stroke applications. Traditional piezoelectric stacks can only generate a few micrometers of displacement when they are not being loaded. When they are loaded, the displacement

is severely impaired. The current designs implementing intelligent material actuators can only control microvibrations (Bamford *et al.*, 1995; Fujita *et al.*, 1993; Vaillon *et al.*, 1999). It is possible that in the near future, these actuators will have better authority, as new materials are developed. One such material is the new relaxor ferroelectric single crystals (PZN-PT and PMN-PT), that can develop strains in excess of 1% and have ~5 times the strain energy density of conventional piezoceramics (Park and Shrout, 1997). Electromechanical actuators have the necessary force and displacement capabilities for many applications. However, their implementation is often not practical because of their large weight, electrical demands, and limited bandwidth. An electromechanical actuator which is required to generate the necessary force and displacement would be extremely heavy and demand a significant electrical current. This makes electromagnetic actuators poorly suited to directly controlling vibrations of large amplitude and high bandwidth. Besides requiring a significant external power supply for actuators, active control has the inherent danger of becoming unstable through the injection of mechanical energy into the system.

Semi-active control has been developed as a compromise between passive and active control. Karnopp and co-workers first proposed varying the properties of a passive element by using active control, which was termed semi-active control. They suggested controlling the orifice area of a viscous damper to vary the force it provided. A semi-active control system is incapable of injecting energy into a system comprising the structure and actuator, but can achieve favorable results through selective energy dissipation (Scruggs and Lindner, 1999). Instead of directly opposing a primary disturbance, semi-active vibration control is used to apply a secondary force, which

counteracts the effects of the disturbance by altering the properties of the system, such as stiffness and damping (Brennan *et al.*, 1998). The adjustment of mechanical properties, which is based on feedback from the excitation and/or from the measured response, is what differentiates semi-active control from passive control. A controller monitors the feedback measurements and an appropriate command signal is generated for the semi-active devices. Unlike an active system, the control forces developed are related to the motion of the structure. Furthermore, the stability of the semi-active system is guaranteed as the control forces typically oppose the motion of the structure and can only remove energy from the system (Symans and Constantinou, 1997). In principle, a semi-active damper can emulate an active system as long as the required control force input of the active system is used to dissipate energy and the supply of energy into the system is not required.

2.2 Single-Axis Passive Isolator

Consider the single-axis isolator (Figure 2-1), where M is the mass of sensitive equipment, *k* and *c* are the stiffness and damping of the isolator, respectively.

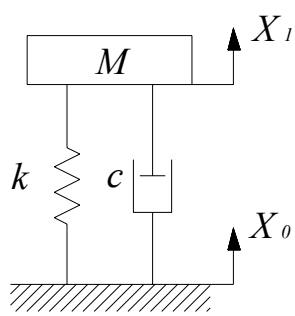

Figure 2-1. Sensitive equipment mounted on a vibrating structure via passive isolator

The isolation mount consists of a linear spring in parallel with a passive damper. The natural frequency of the system is $\omega_n = \sqrt{k/M}$ and the amount of damping in the

isolator is defined by the damping ratio ξ, where $b/M = 2\xi\omega_n$. The transfer function written in the Laplace domain, between the base disturbance displacement x_0 and the payload displacement x_1 is given by

$$\frac{X_1(s)}{X_0(s)} = \frac{1 + 2\xi s/\omega_n}{1 + 2\xi s/\omega_n + s^2/\omega_n^{\ 2}}. \tag{2-1}$$

Substituting $s = j\omega$, the transmissibility between the two masses is found:

$$\left|\frac{X_1(s)}{X_0(s)}\right| = \left[\frac{1 + \left(2\xi\dfrac{\omega}{\omega_n}\right)^2}{\left(1 - \dfrac{\omega^2}{\omega_n^{\ 2}}\right)^2 + \left(2\xi\dfrac{\omega}{\omega_n}\right)^2}\right]^{1/2}. \tag{2-2}$$

Figure 2-2 shows a general plot for the transmissibility frequency response function (FRF) of Eq. (2-1) where the abscissa is the ratio between the disturbing frequency ω and the natural frequency ω_n. From Figure 2-2, it seen that the critical frequency where the curve crosses over the 0 dB line is equal to $\omega = \sqrt{2}\omega_n$ (Thomson, 1988). This corner frequency separates amplification from isolation. At the natural frequency of the system, a resonance appears which is controlled by the value of the damping ratio. In the low frequency range well below the resonance, the displacement of the payload essentially follows the displacement of the disturbance source. After the corner frequency where isolation begins, the curve rolls-off and the displacement of the payload decreases gradually at the high frequency range (Abu Hanieh, 2003). Increasing the damping ratio ξ reduces the resonance at the natural frequency, but it also compromises the high frequency isolation. As a result, the design of a passive damper involves a trade-off between the resonant peak reduction and the high frequency attenuation.

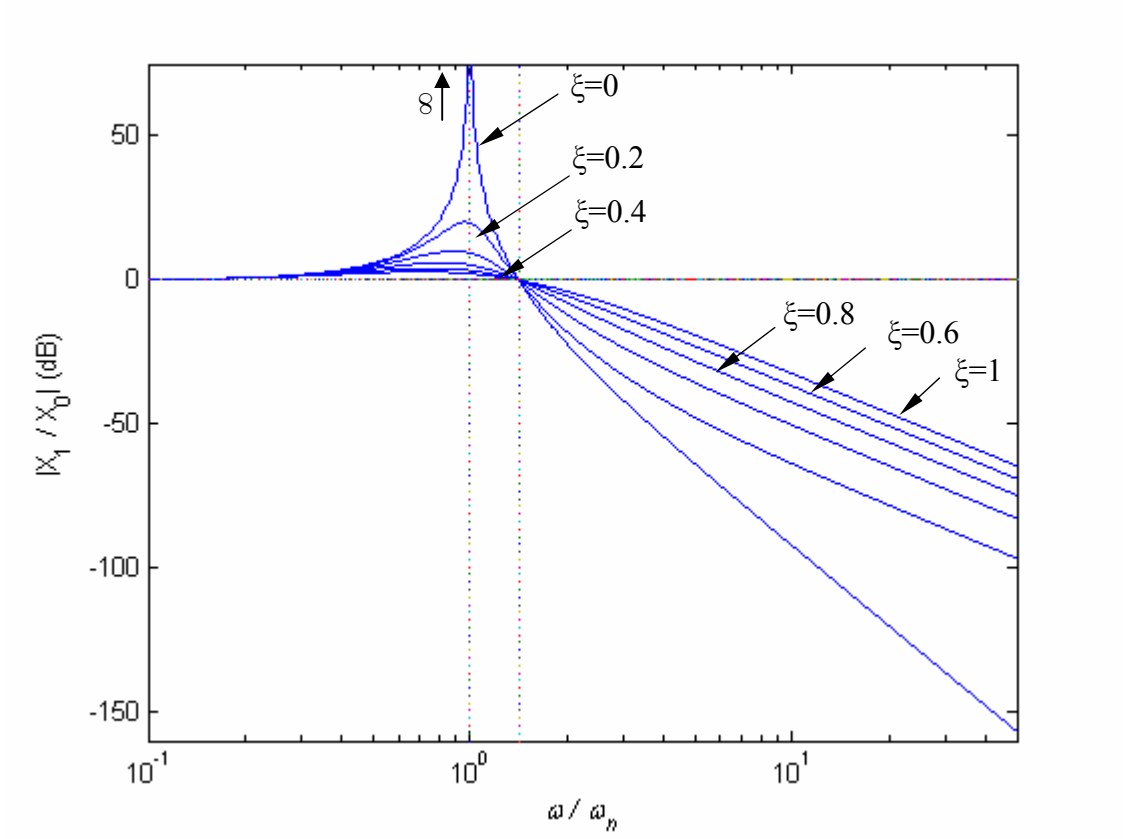

Figure 2-2. Transmissibility FRF of a passive damper for various values of damping ratio

2.3 Single-Axis Active Isolator

The resonance at the natural frequency may be avoided without the penalty of reduced high frequency isolation by using the "skyhook damper" control which was introduced by Crosby and Karnopp (Crosby and Karnopp, 1973). It is called the skyhook damper control because the system is arranged in such a way that the damper is connected to an inertial frame in the sky as shown in Figure 2-3.

Such a configuration cannot exist, but the goal is to implement a controller which would make the system respond in the same way the fictitious configuration would. In this configuration, the damper force is proportional to the absolute velocity of the clean body, so the equation of motion of this system becomes

$$M\ddot{x}_1 + c_{sky}\dot{x}_1 + k\left(x_1 - x_0\right) = 0\,. \tag{2-3}$$

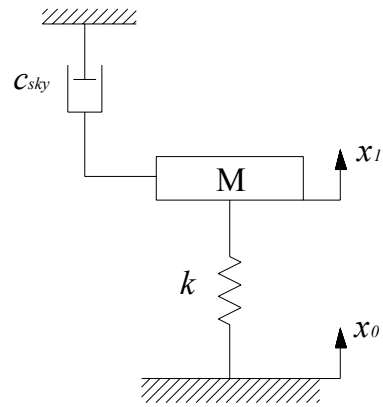

Figure 2-3. Skyhook damper configuration

The transfer function written in the Laplace domain, between the base disturbance displacement, x_0, and the payload displacement, x_1, is therefore given by

$$\frac{X_1(s)}{X_0(s)} = \frac{1}{1 + 2\xi s/\omega_n + s^2/\omega_n^{\,2}} \tag{2-4}$$

which in turn gives the transmissibility of the system with the skyhook damper:

$$\left|\frac{X_1(s)}{X_0(s)}\right| = \frac{1}{\left[\left(1 - \frac{\omega^2}{\omega_n^{\,2}}\right)^2 + \left(2\xi\frac{\omega}{\omega_n}\right)^2\right]^{1/2}}\,. \tag{2-5}$$

The transmissibility of the skyhook damper system is compared to that of the passive isolator in Figure 2-4. The skyhook damper control provides a reduction of resonance at the natural frequency as damping is increased without the trade-off of reduced performance of isolation at higher frequencies. One method of realizing the equivalent damping force of the skyhook damper control without physically implementing this configuration is to replace the passive damper with an active force

element as shown in Figure 2-5. In this active isolator, the force actuator applies a force proportional to the absolute velocity of the clean body (Preumont, 2002).

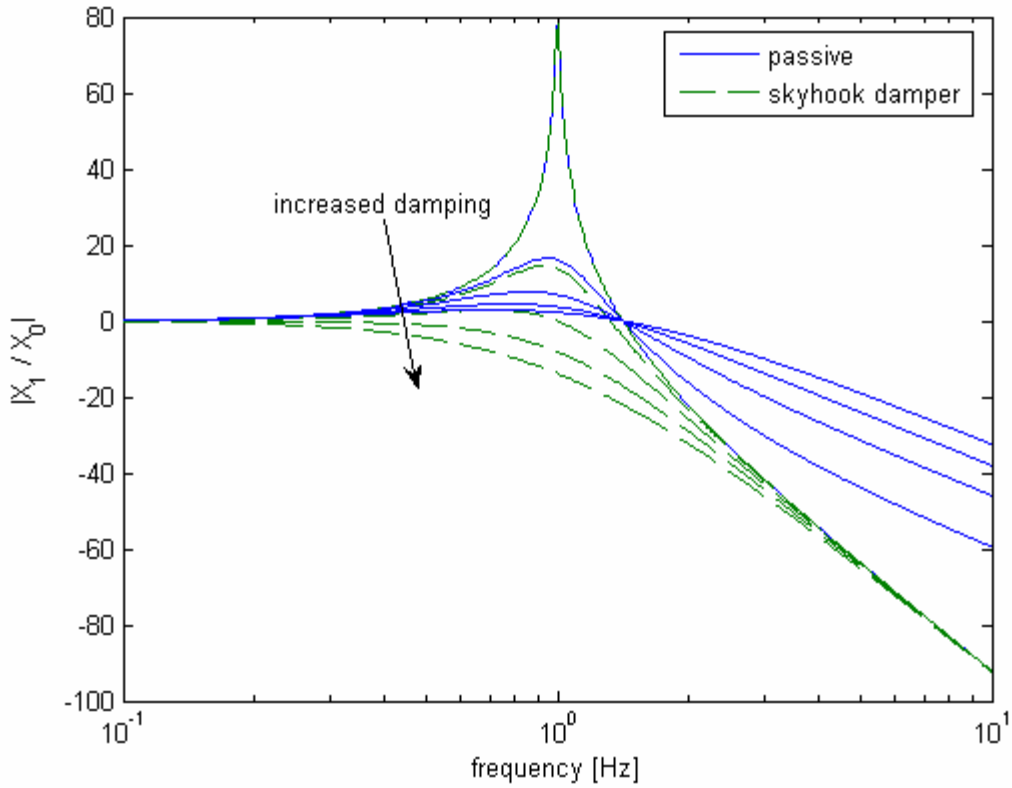

Figure 2-4. Transmissibility of the skyhook damper system compared to that of the passive system for various values of damping ratio

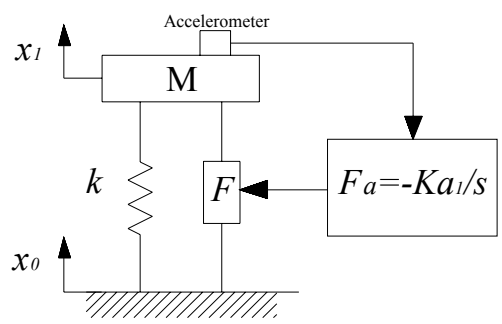

Figure 2-5. Active implementation of the skyhook damper

2.4 Single-Axis Semi-Active Isolator

Another method of implementing the skyhook damper control is through the use of semi-active dampers. The semi-active damper has to be modulated so that it applies the

desired control force which is proportional to the absolute velocity of the clean body as shown in Figure 2-6.

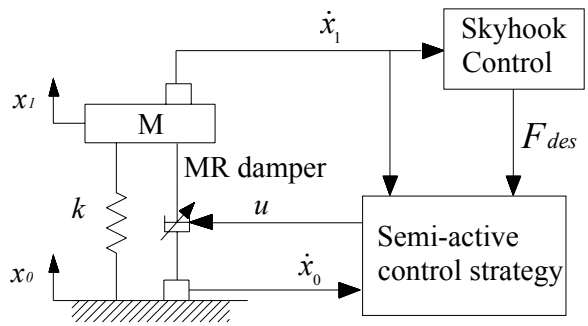

Figure 2-6. Semi-active implementation of the skyhook damper

The semi-active damper can only generate this force if the sign of the relative velocity of the clean body with respect to the base velocity, $(\dot{x}_1 - \dot{x}_0)$ is the same as that of its absolute velocity, $\dot{x}_1$ to ensure that the damping force is dissipative. If this is not the case, the best that the damper can do is to apply its minimum damping force. The desired force also has to lie within the operating range of the damper (Preumont, 2002). The semi-active control is therefore

$$F = \begin{Bmatrix} F_{\max} & \text{when} & (\dot{x}_2 - \dot{x}_1)\dot{x}_2 > 0 \\ F_{\min} & \text{when} & (\dot{x}_2 - \dot{x}_1)\dot{x}_2 \le 0 \end{Bmatrix} \tag{2-6}$$

This is an on/off type controller which applies the maximum damping force of the damper if the desired force is greater than the actual damper force or the minimum force if the desired force is smaller than the actual damping force. The clipping strategy is shown in Figure 2-7.

Finally, Figure 2-8 shows the connector leg of the parallel platform mechanism which has an MR damper implemented with skyhook damper control. The skyhook damper control calculates the desired control force while the semi-active control

compares the relative velocity of mass m_2 with respect to that of mass m_1 with the absolute velocity of mass m_2 and determines the value of control input signal, u.

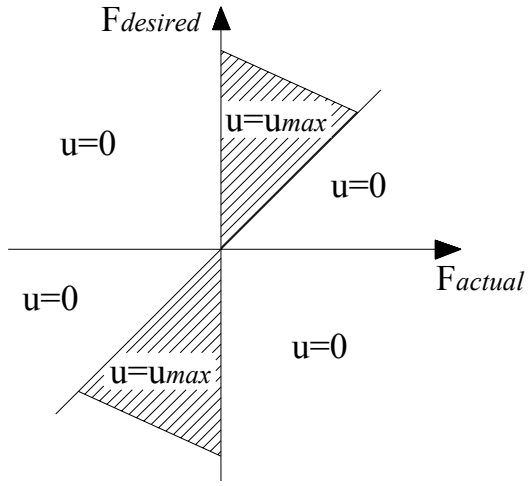

Figure 2-7. Clipping strategy of the semi-active controller (Dyke *et al.,* 1996)

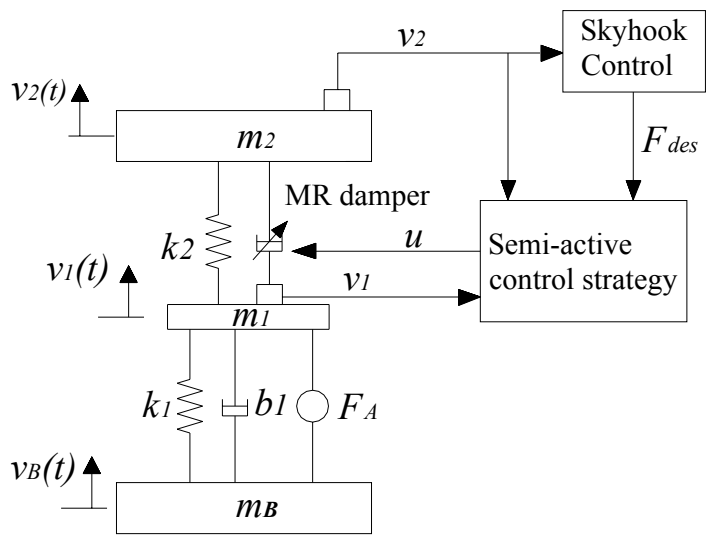

Figure 2-8. Magnetorheological damper with skyhook damper control implemented in the connector leg

CHAPTER 3
SMART MATERIALS AND MAGNETORHEOLOGICAL TECHNOLOGY

In this chapter, smart materials and their use in semi-active vibration control are reviewed. These smart materials are considered as possible candidates for use in vibration isolation of a 6 DOF parallel mechanism. In choosing which technology to use for the vibration damper, important considerations are the cost of the damper, size, weight, repeatability, and power requirements. Magnetorheology stands out from the rest of the smart material options, as a more practical and feasible answer to the vibration isolation problem. It represents a novel technology which promises new design solutions. This technology is discussed in detail in this chapter.

3.1 Smart Materials Used in Semi-Active Vibration Control

3.1.1 Piezoelectric Materials

Direct piezoelectricity is the ability of certain crystalline materials to develop an electric charge proportional to a mechanical stress. Piezoelectric materials also display the converse piezoelectric effect where a significant amount of stress/strain is generated when an electric field is applied to the crystal. This property has been extensively used to suppress excessive vibration of mechanical and aerospace systems (Garrett *et al.*, 2001). While traditional piezoelectric actuators have high force and bandwidth capability, their maximum (freely loaded) mechanical strain is around 0.1%. This means that an actuator 1 inch long could only deflect 0.001 inch (significantly less under load). The recently developed relaxor ferroelectric single crystals (PZN-PT and PMN-PT) can develop strains in excess of 1% (~10 times larger than traditional piezoelectric actuators) and have

~5 times the strain energy density of conventional piezoceramics (Park and Shrout, 1997). Piezoelectric stacks using the new single crystals are currently commercially available (TRS Ceramics). It is possible to use a flextensional mechanical amplifier to increase the displacement of the actuator. A flextensional piezoelectric amplifier (using an ordinary piezoelectric material) developed by Dynamic Structures and Materials, LLC is shown in Figure 3-1. This actuator can generate a 1.5 mm displacement under a load of 10 lbs. This specific actuator was implemented in a friction damper where it provides the normal force required for the friction force (Unsal *et al.*, 2003). The disadvantage of this kind of a piezoelectric actuator is its high cost and current consumption at high frequencies.

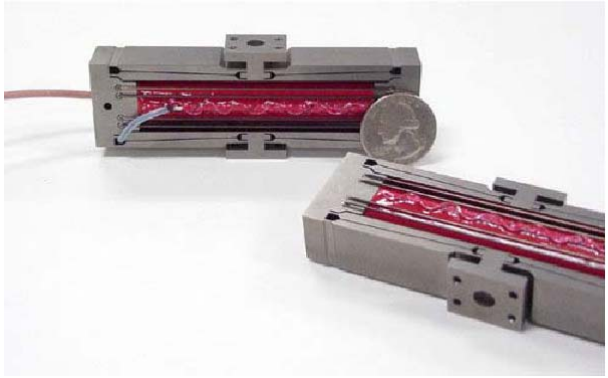

Figure 3-1. Piezoelectric actuator (FPA-1700-LV) from Dynamic Structures and Materials, LLC

Piezoelectrics have been extensively used in vibration damping. The piezoelectric material can be used in combination with a resistor where the piezoelectric acts like a capacitor. This creates a resistor-capacitor (RC) shunt network that can be used for damping (Hagood and Von Flotow, 1991). The stiffness of piezoelectric materials can also be varied by connecting them to a capacitive shunt circuit. Varying stiffness has been used to adjust vibration absorbers when the resonant frequency is not fixed (Winthrop and Cobb, 2003).

3.1.2 Shape Memory Alloys

Shape Memory Alloys (SMAs) are a unique class of metal alloys that can recover apparent permanent strains when they are heated above a certain temperature. The SMAs have two stable phases - the high-temperature phase, called austenite and the low-temperature phase, called martensite. A phase transformation which occurs between these two phases upon heating and cooling is the basis for the unique properties of the SMAs. The key effects of SMAs associated with the phase transformation are pseudoelasticity (PE) and shape memory effect (SME) that are exploited for use in vibration control. PE occurs when a load applied to a SMA forces it to change its form from austenitic to martensitic. Removing the load transforms the SMA back to its austenitic form and causes it to recover its original shape. SME occurs when a SMA in martensitic form is deformed under a load. Its original shape is recovered when it is heated to austenitic form. There are a couple semi-active isolators that take advantage of the SME. In one of them, the stiffness of the system is changed by heating the SMA wires that are placed in parallel (Williams *et al.*, 2002). In another, a novel actuator which consists of a weave of SMA wires surrounding disks with passive springs in between, uses mechanical advantage to increase stroke length and has very fast response rates (Grant and Hayward, 1995). The disadvantages of these SMA applications are that it takes a long time to dissipate the heat, they are relatively expensive to manufacture and machine, and they have poor fatigue properties (SMA/MEMS Research Group and University of Alberta, 2001).

3.1.3 Ionic Gels

Gels are materials with an elastomeric matrix filled with fluid. The stiffness of these gels can be adjusted by controlling the diffusion of water and also chemicals into

and out of the matrix. The less fluid the gel has, the stiffer it is going to be. This process which is controlled by the concentration of ions in the gel is relatively slow and temperature dependent. Also, the stability of these gels has not been proven (Kornbluh *et al.*, 2004)

3.1.4 Electroactive Polymers

Electroactive polymers (EAPs) are polymers which respond to external electric charge by changing their shape and size. They can be deformed repetitively and regain their original shape when the polarity of the external charge is reversed. There are different groups of EAPs which exhibit piezoelectric, pyroelectric, or electrostrictive properties in response to electric or mechanical fields. Potential applications of these polymers are acoustic, impact, and strain sensors, microphones, hydrophones, optical and mechanical switching devices, tunable-membrane structures, electromechanical transducers, MEMS devices, and artificial muscles. Low actuation forces, mechanical energy density, and lack of robustness are the limiting factors of these polymers (NASA, 2004).

3.1.5 Smart Fluids

By applying a low-power control signal, smart fluids can be used to continuously vary the force developed in a suitable damping device (Sims *et al.*, 1999). These smart fluids exploit the rheological effect, which causes the solid particles in the fluid to align when the appropriate energy field is applied. This alignment creates a reduction in the ability of the fluid to flow, or shear. Each of the two main types of rheological fluids that have been researched is based on different applied energy fields. Electrorheological (ER) fluids are responsive to a voltage field and magnetorheological (MR) fluids are responsive to a magnetic field. ER fluids have been extensively investigated. Some of

the disadvantages of these fluids are that they require thousands of volts for operation, and yield low shear stresses. The fact that these fluids are sensitive to contaminants and the high voltage needed for operation clearly make safety and packaging significant design problems. On the other hand, MR fluids operate with minimal voltage and generate high fluid shear stress (Sims *et al.*, 1999). Commercially produced ER fluids are now available, but despite the design, construction, and testing of numerous prototype devices, the mass-production of an ER device is still awaited. However, the more recent MR devices are commercially available. This is because of the performance characteristics of MR fluids. They generate much higher dynamic yield stress, they have a wider temperature range, and they are insensitive to temperature variations and contaminants. The low power requirement is also a clear advantage.

3.2 Magnetorheological (MR) Technology

3.2.1 Magnetorheological Fluids

MR fluids were first discovered and developed by Jacob Rabinow at the US National Bureau of Standards in 1948 (Rabinow, 1948). MR fluids are suspensions of small iron particles in a base fluid. They are able to reversibly change from free-flowing, linear viscous liquids to semi-solids having controllable yield strength under a magnetic field. When the fluid is exposed to a magnetic field, the particles form linear chains parallel to the applied field as shown in Figure 3-2.

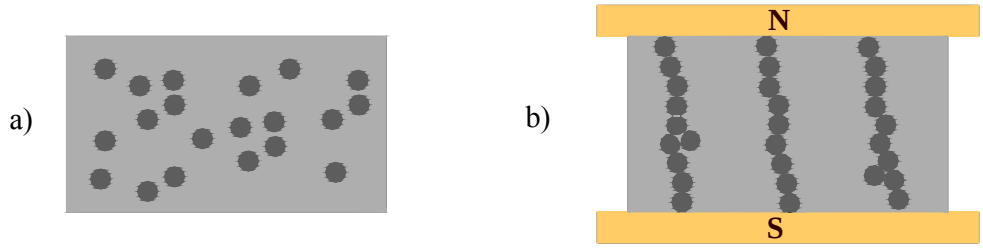

Figure 3-2. Magnetorheological fluid: a) no magnetic field, b) with magnetic field

These chains impede the flow and solidify the fluid in a matter of milliseconds. This phenomenon develops a yield stress which increases as the magnitude of the applied magnetic field increases (Jolly *et al.*, 1998). Typically, 20-40% of the MR fluid consists of soft iron particles by volume (e.g., carbonyl iron). Mineral oil, synthetic oil, water or glycol is used as a suspension. In order to prevent gravitational settling, promote particle suspension, enhance lubricity, change viscosity, and inhibit wear, a variety of additives are used. The strength of a MR fluid is directly proportional to the amount of saturation magnetization. Alloys of iron and cobalt have large saturation magnetization and are therefore ideal, but they are very expensive. Therefore, simple iron particles which have a moderately high saturation magnetization are commonly used (Carlson and Spencer Jr., 1996).

3.2.2 Magnetorheological Devices and Fluid Dampers

MR devices can be divided into three groups of operational modes or a combination of the three based on the design of the device components. These modes are shown in Figure 3-3.

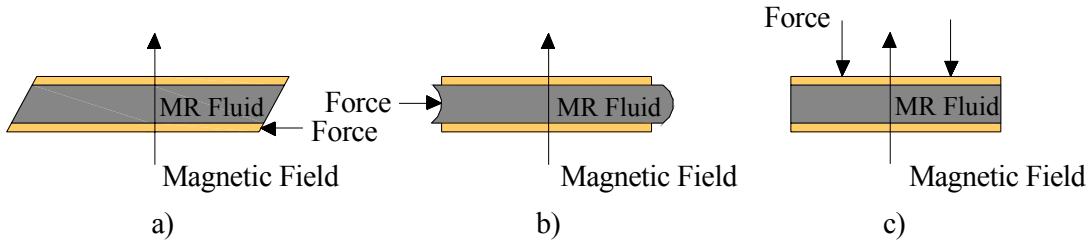

Figure 3-3. Flow modes of MR devices: a) Valve Mode b) Direct Shear Mode c) Squeeze Film Model

In the valve mode, of the two surfaces that are in contact with the MR fluid, one surface moves relative to the fluid. This relative motion creates a shear stress in the fluid. The shear strength of the fluid may be varied by applying different levels of magnetic

field. In the direct shear mode, the fluid is pressurized to flow between two surfaces which are stationary. The flow rate and the pressure of the fluid may be adjusted by varying the magnetic field. In the squeeze film mode, two parallel surfaces squeeze the fluid in between and the motion of the fluid is perpendicular to that of the surfaces. The applied magnetic field determines the force needed to squeeze the fluid and also the speed of the parallel surfaces during the squeezing motion (Yalcintas, 1999).

A magnetic circuit is necessary to induce the changes in the viscosity of the MR fluid. The magnetic circuit typically uses low carbon steel, which has a high magnetic permeability and saturation. This steel effectively directs magnetic flux into the fluid gap. In an optimal design, magnetic field energy in the fluid gap is kept at a maximum while the energy lost in steel flux conduit and regions of non-working areas is minimized. This requires the total amount of steel in the magnetic circuit to be minimized. However, sufficient cross-section of steel must be maintained such that the magnetic field intensity in the steel is very low.

Several different designs of MR dampers have been built and tested in the past. The first of these designs which is shown in Figure 3-4 is the bypass damper where the bypass flow occurs outside the cylinder and an electromagnet applies a magnetic field to the bypass duct (Sodeyama *et al.*, 2003; Sunakoda *et al.*, 2000). A simple schematic of this damper is displayed in Figure 3-5. While this design has a clear advantage that the MR fluid is not directly affected by the heat build-up in the electromagnet, the presence of the bypass duct makes it a less compact design. Figure 3-6 shows a design by the Lord Corporation, where the electromagnet is inside the cylinder and the MR fluid passes through an annular gap between the electromagnet and the inner cylinder. This design

uses an accumulator to make up for the volume of fluid displaced by the piston rod which is going into the damper (Snyder *et al.*, 2000; Snyder and Wereley, 1999). A way to get rid of the accumulator and simplify the design is to build a double-shafted damper as shown in Figure 3-7 (Guangqiang, 2001).

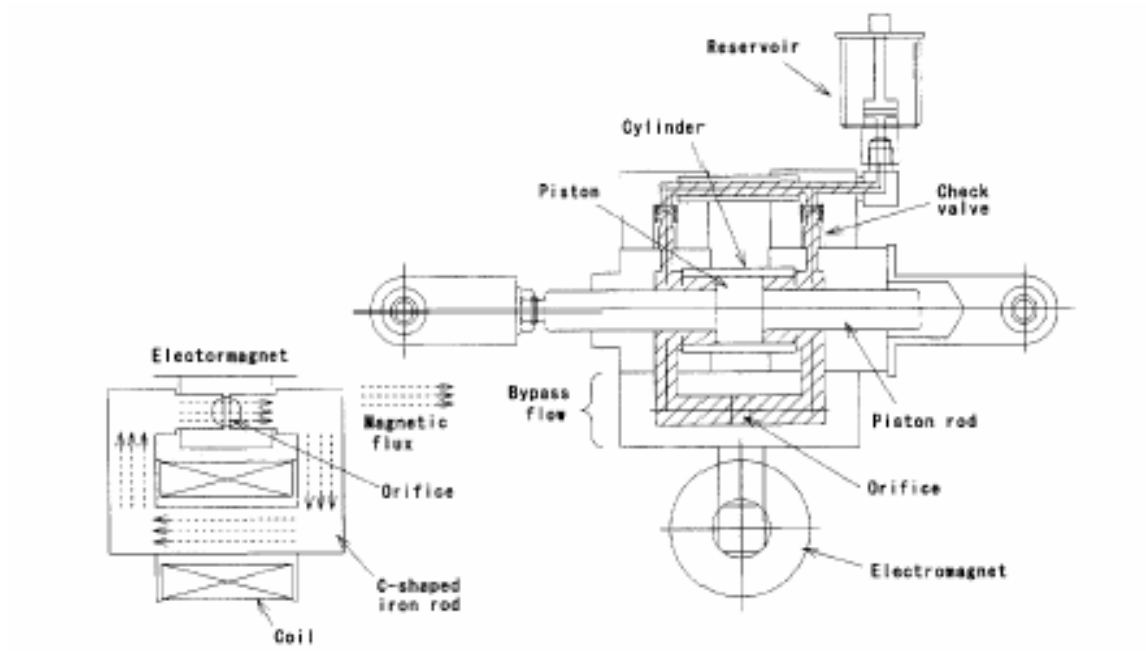

Figure 3-4. By-pass Type Damper (Sodeyama *et al.*, 2003; Sunakoda *et al.*, 2000)

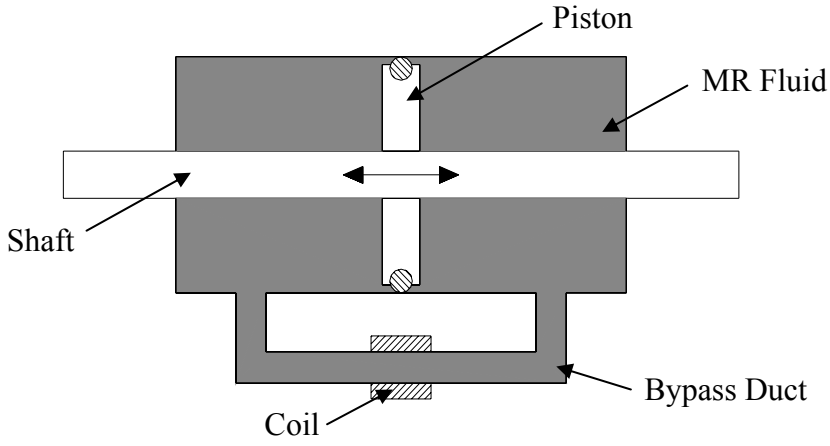

Figure 3-5. Schematic of the by-pass type MR damper

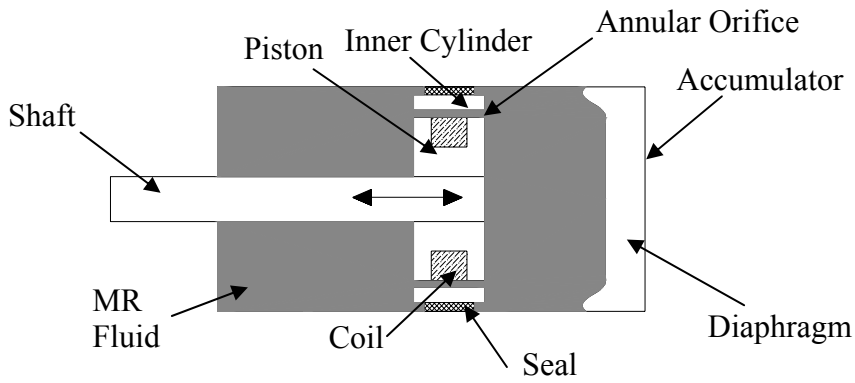

Figure 3-6. Schematic of RD-1500 MR fluid damper by the Lord Corporation

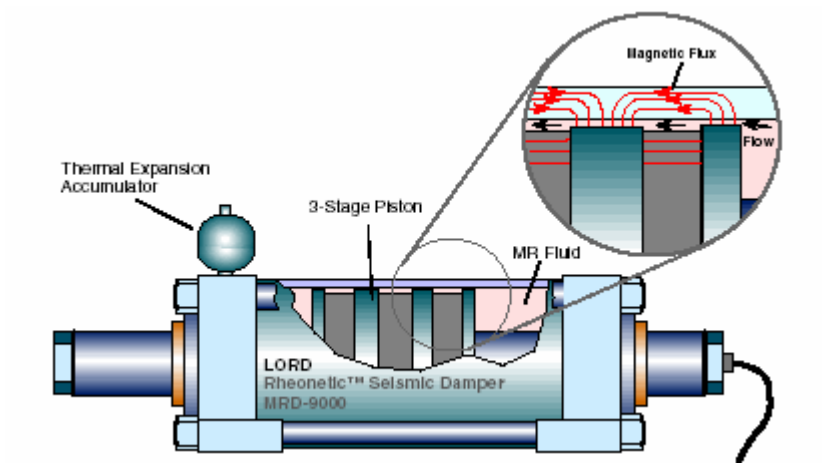

Figure 3-7. Double-shafted 20-ton large-scale MR fluid damper (Guangqiang, 2001)

3.3 Magnetorheological Fluid Models

Four different models to describe the behavior of MR fluids are now reviewed: (1) Equivalent viscous damping, (2) Bingham plastic model, (3) Bouc-Wen model, and (4) Hershel-Bulkley model.

3.3.1 Equivalent Viscous Damping

Among the four models to be reviewed, equivalent viscous damping is the only linearized approach. The other three are all nonlinear models. In this model, an equivalent viscous damping, C_{eq} is obtained by equating the dissipated energy of the

nonlinear device to that of an equivalent viscous damper (Wereley *et al.*, 1999). The dissipated energy, E is found over a cycle of frequency, Ω,

$$E = \oint F(t)dx = \int_0^{2\pi/\Omega} F(t)v(t)dt \tag{3.1}$$

where $F(t)$ is the measured force, $x(t)$ is the measured shaft displacement, and v(t) is the measured shaft velocity of the damper. In the schematic of this model shown in Figure 3-8 a), the slope of the force-velocity curve is equal to the equivalent viscous damping, C_{eq}. Equating the dissipated energy to that of an equivalent viscous damper, we get

$$C_{eq} = \frac{E}{\pi\Omega X_0^{\ 2}} \tag{3.2}$$

where X_0 is the sinusoidal displacement input amplitude.

3.3.2 Bingham Model

This model is an extension of the Newtonian flow and it is obtained by also taking into account the yield stress of the fluid. It assumes that flow will occur when the dynamic yield stress is reached. The total stress is given by

$$\tau = \tau_y \operatorname{sgn}(\dot{\gamma}) + \eta\dot{\gamma} \tag{3.3}$$

where τ_y is the yield stress induced by the magnetic field, $\dot{\gamma}$ is the shear rate and η is the viscosity of the fluid. Stanway *et al*. came up with an idealized mechanical model based on this model which has a Coulomb friction element in parallel with a viscous damper, as shown in Figure 3-9 a) (Stanway *et al.*, 1987). In this model, for nonzero piston velocities, the force generated is given by

$$F = f_c \operatorname{sgn}(\dot{x}) + c_o\dot{x} \tag{3.4}$$

where c_o is the damping coefficient and f_c is the frictional force, which is related to the fluid yield stress. In the post-yield part, the slope of the force-velocity curve is equal to the damping coefficient which is essentially the viscosity of the fluid, η, as shown in Figure 3-8 b).

3.3.3 Bouc-Wen Model

Another model that has been used extensively to model hysteretic systems is the Bouc-Wen model. The schematic of this model is shown in Figure 3-9 b). The force in this system is given by

$$F = c_o \dot{x} + k_0 (x - x_0) + \alpha z \tag{3.5}$$

where the variable z is governed by

$$\dot{z} = -\gamma |\dot{x}| z |z|^{n-1} - \beta \dot{x} |z|^n + A |\dot{x}| \tag{3.6}$$

The parameters of the model, γ, β and A can be adjusted to control the linearity in the unloading and the smoothness of the transition from the pre-yield to the post-yield region (Stanway *et al.*, 1987). The force-velocity relationship of this model is shown in Figure 3-8 c).

3.3.4 Herschel-Bulkley Model

The shear flow relationship for the Herschel-Bulkley model is

$$\tau = \tau_y \operatorname{sgn}(\dot{\gamma}) + \eta (\dot{\gamma})^n \tag{3.7}$$

where n is called the flow behavior index. Note that the pre-yield behavior is identical to that of the Bingham plastic model and for the case when n=1, the model simplifies to the Bingham model. The Herschel-Bulkley is a more general approach which accounts for post-yield shear thinning or thickening behavior as follows: (a) n>1:shear thickening behavior, (b) n=1: Bingham behavior, (c) n<1:shear thinning behavior, as shown in

Figure 3-8 d)-e). Comparing this model with a Newtonian fluid, we can define the apparent viscosity, μ_a, as

$$\tau = \tau_y \operatorname{sgn}(\dot{\gamma}) + \mu_a \dot{\gamma} \tag{3.8}$$

where the apparent viscosity is given by,

$$\mu_a = \eta(\dot{\gamma})^{n-1} \tag{3.9}$$

The apparent viscosity decreases with increasing shear rate for shear thinning fluids (n<1) and it increases with shear rate for shear thickening fluids (n>1) (Wereley *et al.*, 1999).

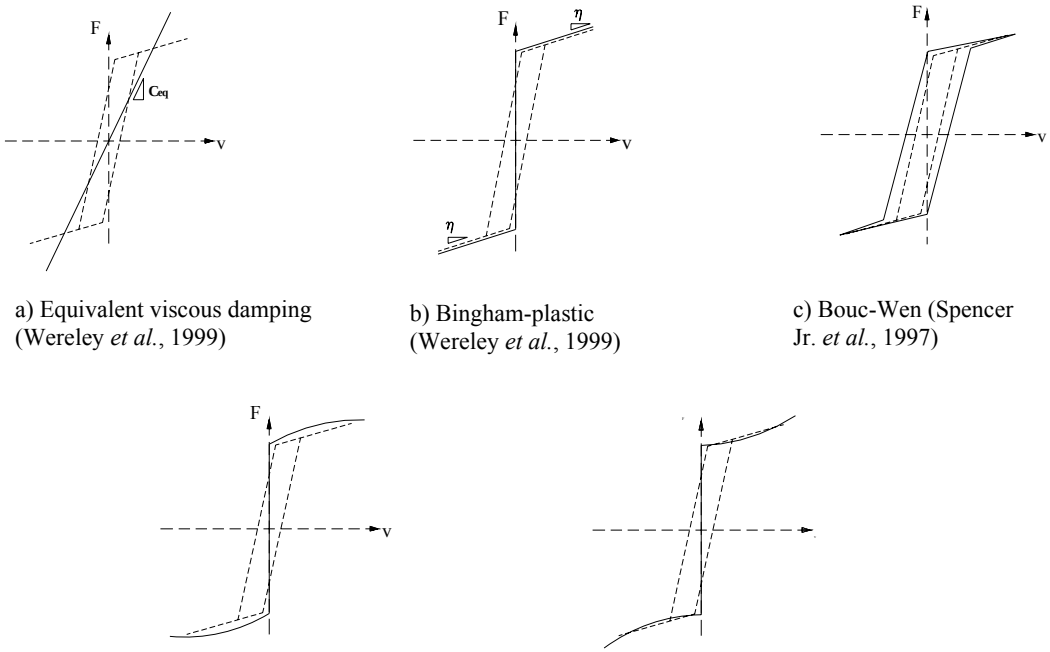

a) Equivalent viscous damping (Wereley *et al.*, 1999)

b) Bingham-plastic (Wereley *et al.*, 1999)

c) Bouc-Wen (Spencer Jr. *et al.*, 1997)

d) Shear Thinning (Wereley *et al.*, 1999)

e) Shear Thickening (Wereley *et al.*, 1999)

Figure 3-8. Schematics of the models reviewed (The idealized model is represented by a solid line, while the actual damper behavior is represented by a dashed line).

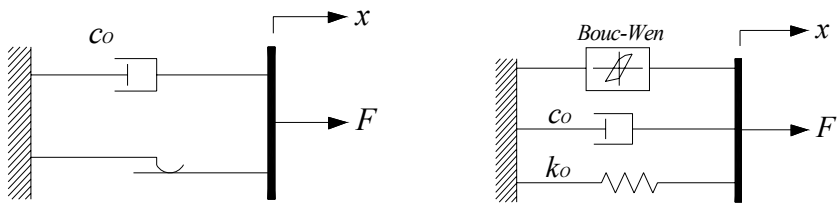

a) b)

Figure 3-9. Controllable fluid damper models a) Bingham model b) Bouc-Wen model (Stanway *et al.*, 1987)

CHAPTER 4
MAGNETORHEOLOGICAL DAMPER DESIGN

In this chapter, the criteria for designing MR dampers are investigated. Several MR damper prototypes based on different designs which were built during the course of this research are reviewed. Test results on two prototypes are given.

4.1 Damper Design Criteria

Certain geometry parameters need to be carefully chosen to get optimal performance, controllable force, and dynamic range from the damper. The two most important parameters in quantifying the performance of the damper are the controllable force and the dynamic ratio. The total damper force consists of the controllable force, F_τ and the uncontrollable force, F_u as shown in Figure 4-1. The controllable force is controlled by varying the yield stress, τ_0 of the fluid. The uncontrollable force is the sum of a friction force, F_f and a plastic viscous force, F_η. The ratio of the controllable force to the uncontrollable force is defined as the dynamic ratio:

$$D = \frac{F_\tau}{F_u} = \frac{F_\tau}{F_f + F_\eta} \tag{4.1}$$

In order to increase the dynamic range, the controllable force needs to be increased while the F_u is kept at a minimum. The controllable force depends on several parameters including the dynamic yield stress of the fluid, the valve gap geometry, and the effective magnetic field acting on the fluid. The friction force and the plastic viscous force need to be reduced to decrease the amount of uncontrollable force. The plastic viscous force increases steadily with the flow rate, so the dynamic range is relatively lower at higher

flow rates. The viscous force also increases as the gap size is reduced. However, the controllable force is also inversely related to the gap size. As both the controllable force and the viscous force increase with decreasing gap size, an optimal dynamic range based on gap size exists (Yang *et al.*, 2002).

In this chapter, important parameters affecting the performance of the MR damper are examined. In the design process of the damper, these parameters will be taken into consideration.

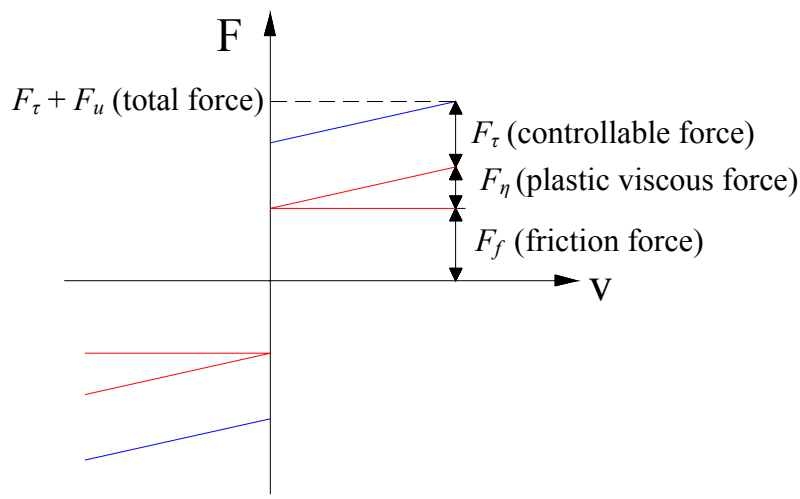

Figure 4-1. Force decomposition of MR dampers (Yang *et al.*, 2002)

4.2 Magnetorheological Damper Prototypes

In this section, the three MR damper prototypes that were designed, built, and tested are described and the preliminary experiment results are presented. The designs of various MR dampers commercially available and in the literature were carefully studied as a starting point for the designs within this work. Changes and modifications were made in order to come up with a better design. The following parameters were considered during the process:

- **Ease of manufacturing and simplicity in design:** Keeping the individual parts of the prototype simple makes the troubleshooting easier.
- **Friction:** The major cause of friction in an MR damper is the contact between the seals and the housing or the shaft depending on the design. Also, in the case when the moving shaft is not properly aligned, there may be contact between the shaft and other metal surfaces.
- **Size and weight:** Since the damper is intended for the legs of the hexapod, a smaller damper minimizes the size and weight of the overall hexapod design.
- **The placement of the coil and the wiring:** Depending on the design, the coil may either be placed inside the housing where the only barrier separating it from the MR fluid is its coating or it may be outside the housing or the bypass duct if there exists one.

4.2.1 Double-Shafted Damper with Aluminum Housing

This design is based on a commercial damper, SD-1000 MR damper by the Lord Corporation shown in Figure 4-2. The damper operates in a combination of valve and direct shear modes. The fluid passes through an annular orifice between the coil bobbin and an inner cylinder. A magnetic field is created along this gap through the use of the coil. When the magnetic field is applied, the viscosity of the magnetorheological fluid increases in a matter of milliseconds. The field causes a resistance to the flow of fluid between the two reservoirs. This way, the damping coefficient of the damper is adjusted. Therefore, the damping coefficient of the damper can be adjusted by feeding back a conditioned sensor signal to the coil.

A Teflon seal around the inner cylinder as shown in Figure 4-3 prevents the flow of the fluid between the housing and the inner cylinder. A hollow shaft enables the wires to deliver current to the electromagnet. Since the flux lines do not pass through the outer housing, the housing may be built out of aluminum which makes a reduction in the overall weight of the damper possible. The original design was modified to have two shafts and therefore the accumulator which compensated for the volume of fluid

displaced by the shaft going into the damper was no longer necessary. More photographs and drawings of this prototype are shown in Appendix C.

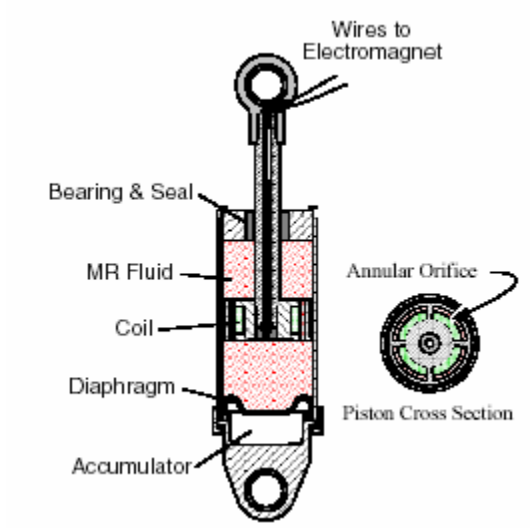

Figure 4-2. Magnetorheological fluid damper (SD-1000) from Lord Corporation

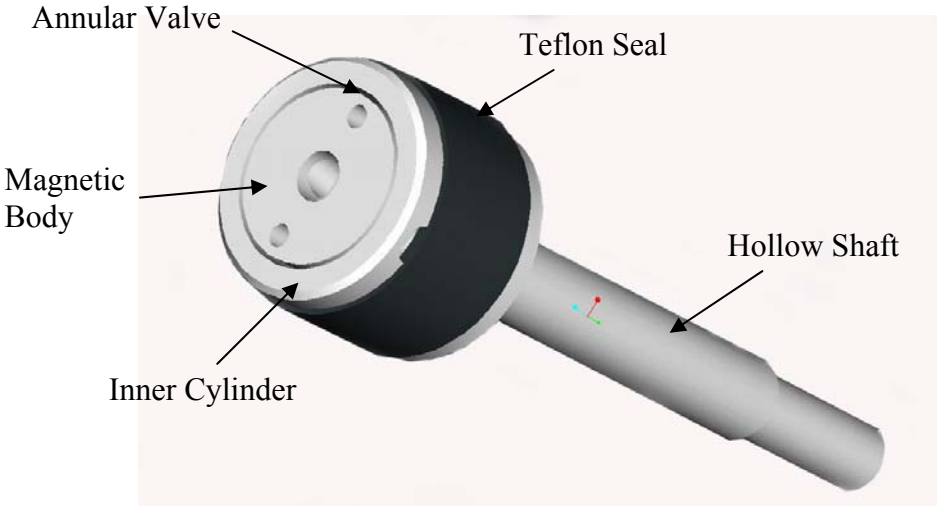

Figure 4-3. Inside view of damper showing Teflon seal

This design had several disadvantages. First of all, the Teflon seal created a significant amount of additional friction. Secondly, it was observed that the magnetic body did not remain centered during operation which caused sealing malfunction and leaking, scratching of the insulation of the coil, and asymmetry in the annular gap which

may result in non-uniform temperature increases. Finally, since the coil was inside the fluid, the fluid was directly affected by the heat build-up in the coil. An increase in the temperature of the MR fluid causes its viscosity to drop and reduces the force capacity of the damper (Dogrouz *et al.*, 2003).

4.2.2 Double-Shafted Damper with Steel Housing

This damper is also double-shafted. However, in this design, unlike the previous one, there is no additional inner cylinder between the magnetic body and the outer housing as shown in Figure 4-4. The outer housing is made up of low carbon steel. Therefore the flux lines pass through the housing in their return path while the magnetorheological fluid flows through the annular gap between the housing and the magnetic body around which the coil is wound as seen in Figure 4-4.

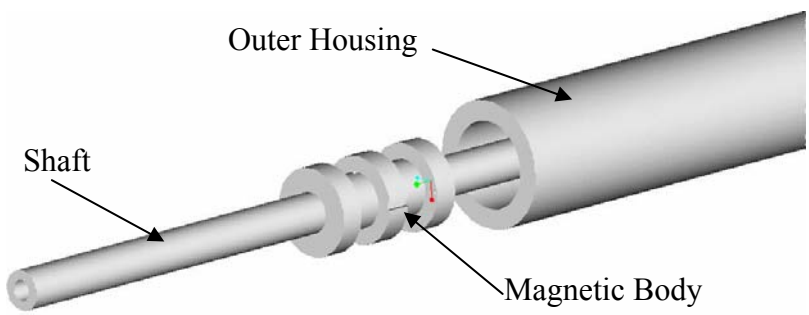

Figure 4-4. Schematic of the double-shafted damper with steel housing

The magnetic body was designed to divide the coil into two parts which creates three effective magnetic surfaces. The two coils were wound in directions opposite to each other so that the flux lines would add up in the middle, as shown in Figure 4-5. All the parts of this damper were manufactured from low-carbon steel which has a high magnetic permeability which is shown in Figure 4-6. This damper was heavier than the previous one since it was made out of steel and not aluminum. However, it has a simpler design as the inner cylinder and the Teflon seal is not used. Instead of the inner cylinder,

the outer housing itself serves as the return path of the flux lines. More photographs and drawings of this prototype are shown in Appendix C.

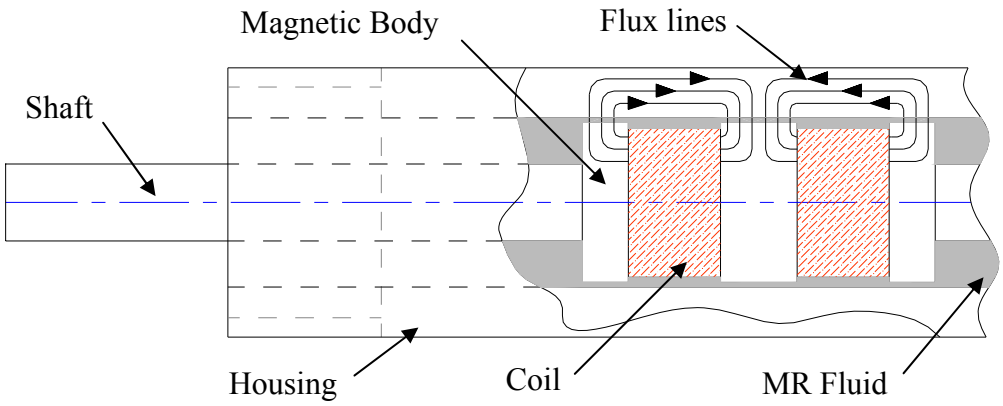

Figure 4-5. Schematic of the damper showing the path of the flux lines

It was observed that the overall friction in the damper was lower due to the fact that the Teflon seal was not used. The performance of this damper also suffered from heat build-up in the coil and the fact that the magnetic body did not remain centered during the operation.

Figure 4-6. Low-carbon steel housing of the double-shafted MR damper

4.2.3 Syringe Type Damper with Parallel Rod

The idea of this design was born from a demonstration device by the Lord Corporation displayed in Figure 4-7. This device is simply made of two syringes connected together by a plastic hollow cylinder through which the fluid flows from one

syringe to the other. When a permanent magnet is attached onto the hollow cylinder, it causes the fluid in the cylinder to turn to semi-solid and therefore stops the flow which in turn blocks the motion of the syringes.

Figure 4-7. Magnetorheological fluid demonstration device from Lord Corporation

Several similar syringe devices were built, using two syringes and a hollow aluminum rod for the valve as displayed in Figure 4-8. Magnet wire was wrapped around the aluminum rod and differing valve and housing dimensions were tested.

Figure 4-8. Syringe dampers with varying housing and valve dimensions

An aluminum housing was built to resemble the two syringes connected with a hollow rod as shown in Figure 4-9. In this design, a parallel rod is connected to both of the shafts so that a vacuum will not be created when either one of the shafts is pulled back. The main advantage of this design is that the coil is not inside the housing which makes the wiring much simpler where as in the previous two designs, the wiring needed

to be sealed against contact with the fluid. The MR fluid is also not affected as much from the heat build-up in the coil. More photographs and drawings of this prototype are shown in Appendix C.

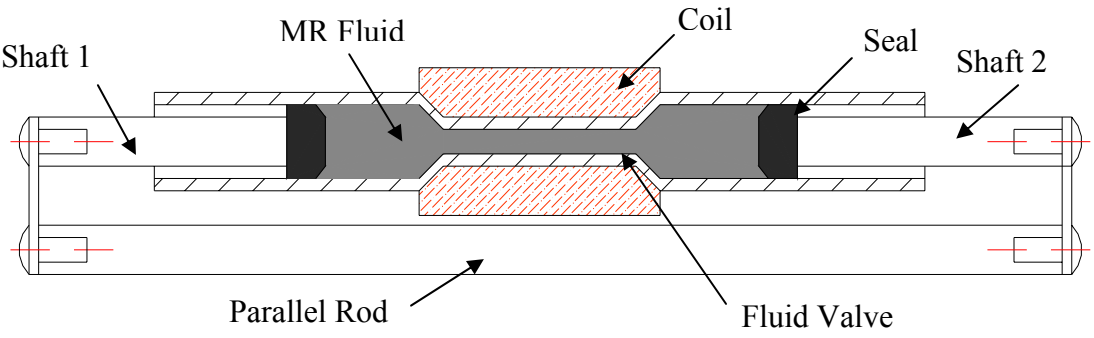

Figure 4-9. Syringe type damper with parallel rod

It is clear that the asymmetrical design of this prototype will induce bending moments on the shafts. Therefore, in the next design, the parallel rod was replaced by a hollow cylinder that encloses the entire damper.

4.2.4 Syringe Type Damper with Cylindrical Outer Housing

The difference between this design and the previous one is the addition of an aluminum hollow cylinder which serves the same purpose of the parallel rod in the previous design and connects the two shafts as shown in Figure 4-10.

On one side, the two base rods are connected to the extension rod. On the other side, shaft 1 is attached to the force transducer (PCB 208C02) which is connected to the shaker through the stinger as shown in Figure 4-11. When the shaker is excited, shaft 1 moves. Shaft 2 moves with shaft 1 since they are connected together through the outer housing. Meanwhile, the inner housing is motionless as it is connected to the extension rod which is fixed. An accelerometer (PCB 333B4) is attached to the housing using wax. More photographs and drawings of this prototype are shown in Appendix C.

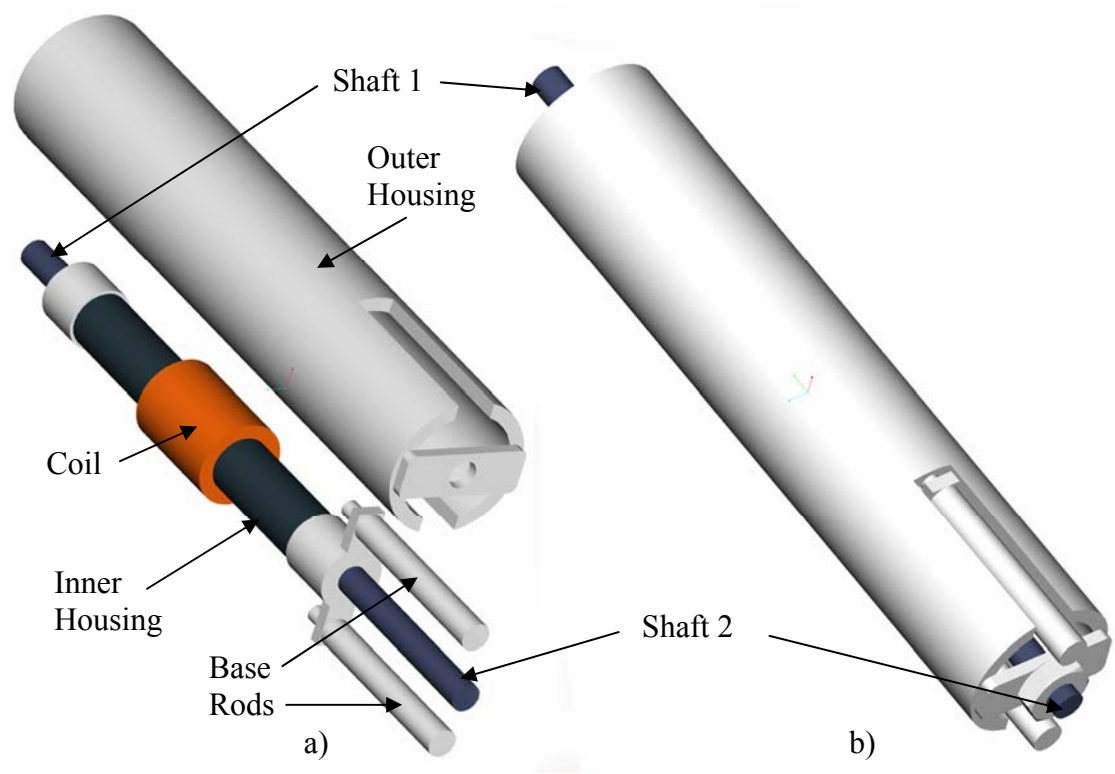

Figure 4-10. Syringe type damper with cylindrical outer housing with a) exploded view showing the inner housing and the coil; b) view of the fully assembled damper

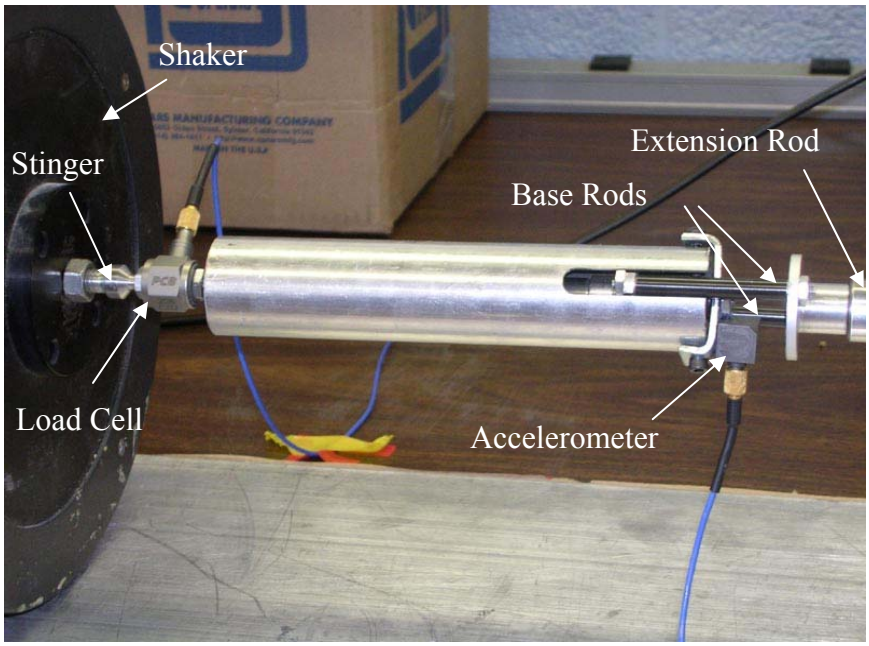

Figure 4-11. Syringe type damper on the experimental setup

4.3 Experimental Setup

4.3.1 Shaker

The shaker that is used to excite the vibration isolator is the PM Vibration Exciter Type 4808 from B&K. It has a force rating of 112 N and a frequency range of 5 Hz to 10 kHz. Its maximum displacement is 12.7 mm. The amplifier that is used to drive this shaker is the Power Amplifier Type 2712 from B&K. A custom made aluminum stinger is used to transfer the force from the fixing hole at the center of the vibration table on the shaker. The stinger is threaded on one side to this fixing hole and to the force transducer on the other side.

4.3.2 Vibration Isolator Setup

The vibration isolator has been designed so that the MR damper is fixed horizontally. The two base rods of the MR damper are screwed onto a fixed shaft and the moving outer housing is connected to the shaker through the force transducer and the stinger. The shaker is bolted onto two steel plates. It is positioned so that the MR damper's line of symmetry is in line with the central fixing hole of the shaker. The accelerometer is fixed to the outer housing using wax. The signals from the force transducer and the accelerometer are fed to the DSPT SigLab (20-42) analyzer (Figure 4-12) through two signal conditioners, model 480E09 from PCB Piezoelectronics. The shaker input signal is generated with the SigLab analyzer.

Figure 4-12. SigLab (20-42) signal analyzer

4.4 Results

4.4.1 Shaker Tests

Preliminary tests were conducted on the vibration isolator setup described above. The syringe type damper was tested under varying shaker excitation amplitudes, frequencies and input current. The results show that there is only a slight increase in the damping force when a magnetic field is applied. In Figure 4-13, the increase in the damping force is shown when the input current is increased from 0 to 0.5A.

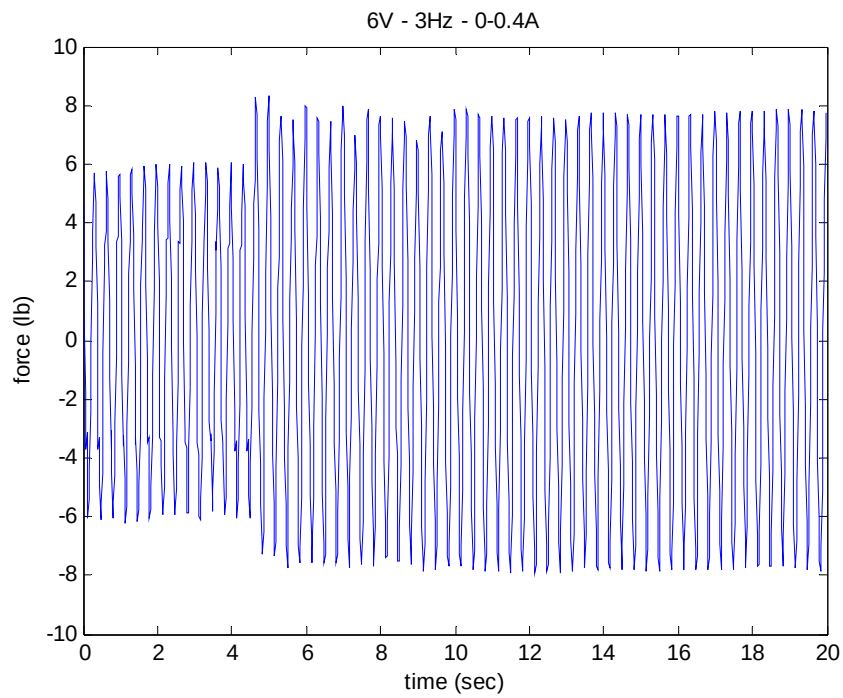

Figure 4-13. Increase in force for the syringe type damper when the input current is increased from 0 to 0.5 A at 4.5 seconds

4.4.2 Tension Tests

Preliminary tests were conducted on an Instron universal tester to determine the force characteristics of the double-shafted damper with steel housing. Figures 4.14 and 4.15 show the results of tension tests carried out. The force versus displacement plot shown in Figure 4-14 was obtained from data at velocity 5 in/min for a 1.5 in.

displacement of the stroke. For velocities 1, 2, 3, 4, and 5 in/min, the damping force generated by the damper was measured for varying magnitudes of the applied current and the results are displayed in Figure 4-15. It was noted that a significant increase in the damping force did not occur for currents above 0.4A due to saturation of the coil. Therefore, the maximum damping force that can be generated by this damper is approximately 40 lb.

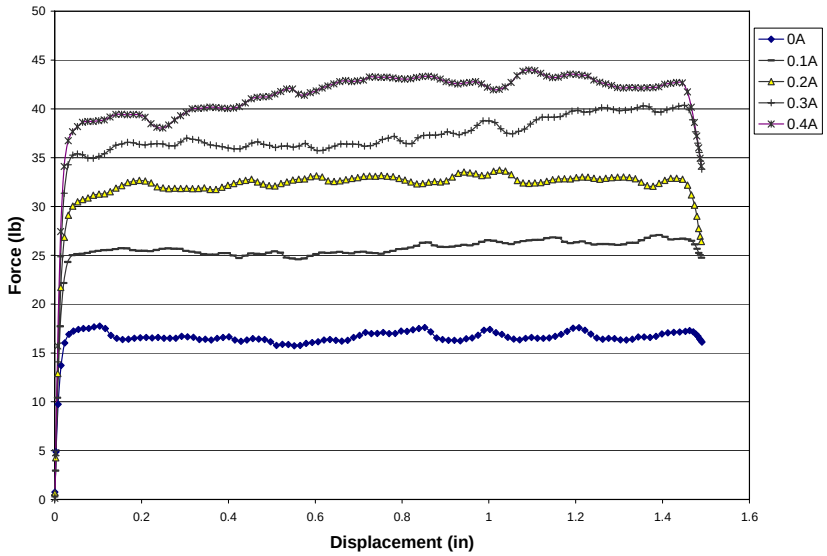

Figure 4-14. Force-displacement curves for varying current at 5 in/min

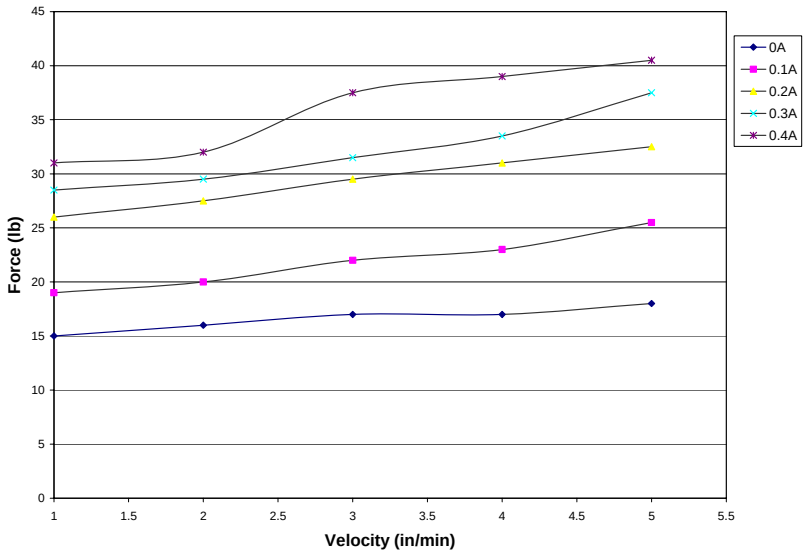

Figure 4-15. Force-velocity curves for varying current

CHAPTER 5
PARALLEL PLATFORM MECHANISMS

In this chapter, after a summary of the statics of a rigid body, the forward and reverse static analyses of parallel platform mechanisms are given. The stiffness mapping of a platform at its unloaded central configuration is presented and finally the dimensions of the parallel platform mechanism used in this work are determined based on calculating the quality index of the mechanism.

5.1 Statics of a Rigid Body

The direction of a force f acting on a rigid body can be expressed as a scalar multiple fS of the magnitude f and the unit vector S. The force is acting on a line **$** with ray coordinates $\hat{\boldsymbol{s}} = \{\boldsymbol{S}; \boldsymbol{S}_{0L}\}$ where $|\boldsymbol{S}| = 1$ and $\boldsymbol{S}_{0L}$ is the moment vector of the line **$**, i.e. $\boldsymbol{S}_{0L} = \boldsymbol{r} \times \boldsymbol{S}$. The moment of the force about the reference point, O is written as $\boldsymbol{m_0} = \boldsymbol{r} \times \boldsymbol{f}$ where r is a vector to any point on the line **$** as shown in Figure 5-1.

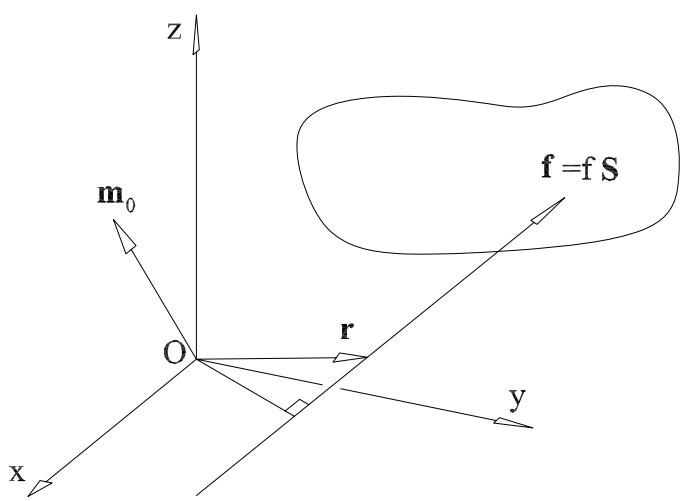

Figure 5-1. Representation of a force and a moment (Crane *et al.*, 2006)

The coordinates of the force are given in Eq. 5-1, where $\boldsymbol{S}\cdot\boldsymbol{S}=1$ and $\boldsymbol{S}\cdot\boldsymbol{S}_{0L}=0$.

$$\hat{\boldsymbol{\omega}} = f\hat{\boldsymbol{s}} = f\left\{\boldsymbol{S};\boldsymbol{S}_{0L}\right\} \tag{5-1}$$

Eq. 5-1 can be expressed in the form

$$\hat{\boldsymbol{\omega}} = f\hat{\boldsymbol{s}} = f\left\{\boldsymbol{f};\boldsymbol{m}_0\right\}. \tag{5-2}$$

The moment, or couple exerted by a couple of forces can be considered as equivalent to $\boldsymbol{m} = f\boldsymbol{S}_m$ where f is a force magnitude and $\boldsymbol{S}_m$ is a line at infinity with coordinates $\left\{0;\boldsymbol{S}_{0L}\right\}$ with $\left|\boldsymbol{S}_m\right|=1$ and the coordinates of $\boldsymbol{S}_m$ having units of length. The moment $\left\{0;\boldsymbol{m}\right\} = f\left\{0;\boldsymbol{S}_m\right\}$ is shown in Figure 5-2. In other words, a pure couple can be expressed as a scalar multiple of a line at infinity.

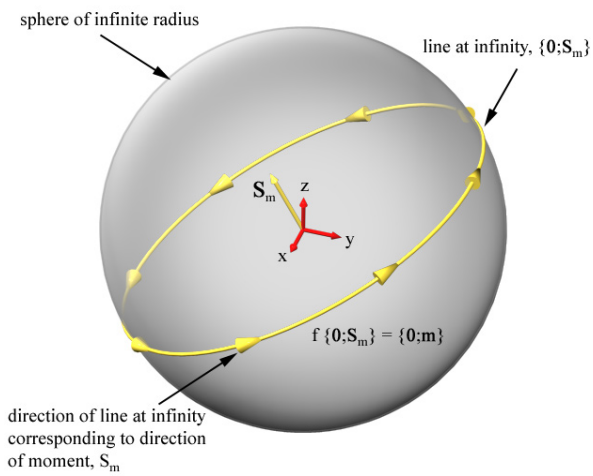

Figure 5-2. Representation of a moment as a line at infinity multiplied by a force magnitude (Crane *et al*., 2006)

A system of forces and couples acting on a rigid body can be reduced to a resultant force, $\boldsymbol{f} = \sum_{i=1}^{n}\boldsymbol{f}_i$ whose coordinates can be written as $\left\{\boldsymbol{f};0\right\}$ and a moment, $\boldsymbol{m} = \sum_{i=1}^{n}\boldsymbol{m}_{0i}$ whose coordinates can be written as $\left\{0;\boldsymbol{m}_0\right\}$ about a reference point, O. The sum of these two coordinates may be written as

$$\hat{\boldsymbol{\omega}} = \{\boldsymbol{f}; \boldsymbol{m}_0\}. \tag{5-3}$$

which was defined as a dyname by Plücker. The moment, $\boldsymbol{m}_0$, may be written as the sum of two components:

$$\boldsymbol{m}_0 = \boldsymbol{m}_a + \boldsymbol{m}_t \tag{5-4}$$

where $\boldsymbol{m}_a$ is parallel to $\boldsymbol{f}$ and $\boldsymbol{m}_t$ is perpendicular to $\boldsymbol{f}$. The dyname may now be written as

$$\hat{\boldsymbol{\omega}} = \{\boldsymbol{f}; \boldsymbol{m}_0\} = \{\boldsymbol{f}; \boldsymbol{m}_t\} + \{\boldsymbol{0}; \boldsymbol{m}_a\}. \tag{5-5}$$

This representation is called a wrench (Ball, 1900). Since $\boldsymbol{m}_a$ is parallel to $\boldsymbol{f}$ we may write

$$\boldsymbol{m}_a = h\boldsymbol{f} \tag{5-6}$$

where h is a non-zero scalar named the pitch of the wrench. A wrench acting on a body can be expressed as a scalar multiple of a unit screw $f\hat{\boldsymbol{s}}$ where

$$\hat{\boldsymbol{s}} = \{\boldsymbol{S}; \boldsymbol{S}_0\}. \tag{5-7}$$

The pitch of the screw is given by

$$h = \boldsymbol{S} \cdot \boldsymbol{S}_0 \tag{5-8}$$

where, as stated before, S is a unit vector. Eq. 5-7 can be written as

$$\hat{\boldsymbol{s}} = \{\boldsymbol{S}; \boldsymbol{S}_0\} = \{\boldsymbol{S}; \boldsymbol{S}_0 - h\boldsymbol{S}\} + \{0; h\boldsymbol{S}\}. \tag{5-9}$$

where $\{\boldsymbol{S}; \boldsymbol{S}_{0L}\} = \{\boldsymbol{S}; \boldsymbol{S}_0 - h\boldsymbol{S}\}$ is the Plücker coordinates for the screw axis (Crane, et al., 2006).

5.2 Forward and Reverse Static Analysis of Parallel Platform Mechanisms

A unit wrench, $\hat{\boldsymbol{s}}$, is defined with respect to a reference frame by

$$\hat{\boldsymbol{s}} = \begin{bmatrix} \boldsymbol{S} \\ \boldsymbol{r} \times \boldsymbol{S} + h\boldsymbol{S} \end{bmatrix}. \tag{5-10}$$

For a pure force, h=0, and the unit wrench reduces to

$$\hat{\boldsymbol{s}} = \begin{bmatrix} \boldsymbol{S} \\ \boldsymbol{r} \times \boldsymbol{S} \end{bmatrix} = \begin{bmatrix} \boldsymbol{S} \\ \boldsymbol{S}_{0L} \end{bmatrix}. \tag{5-11}$$

The forward static analysis computes the wrench $\hat{\boldsymbol{\omega}} = \{\boldsymbol{f}; \boldsymbol{m}_0\}$ acting on the top platform given the six leg forces. The wrench, $\hat{\boldsymbol{\omega}}$, may be expressed in the form

$$\hat{\boldsymbol{\omega}} = \{\boldsymbol{f}_1; \boldsymbol{m}_{01}\} + \{\boldsymbol{f}_2; \boldsymbol{m}_{02}\} + \cdots + \{\boldsymbol{f}_6; \boldsymbol{m}_{06}\}. \tag{5-12}$$

or

$$\hat{\boldsymbol{\omega}} = f_1 \begin{bmatrix} \boldsymbol{S}_1 \\ \boldsymbol{S}_{0L1} \end{bmatrix} + f_2 \begin{bmatrix} \boldsymbol{S}_2 \\ \boldsymbol{S}_{0L2} \end{bmatrix} + \cdots + f_6 \begin{bmatrix} \boldsymbol{S}_6 \\ \boldsymbol{S}_{0L6} \end{bmatrix} \tag{5-13}$$

which may be written as

$$\hat{\boldsymbol{\omega}} = \boldsymbol{JF} \tag{5-14}$$

where J which is called the Jacobian matrix is a 6×6 matrix given as

$$\boldsymbol{J} = \begin{bmatrix} \boldsymbol{S}_1 & \boldsymbol{S}_2 & \boldsymbol{S}_3 & \boldsymbol{S}_4 & \boldsymbol{S}_5 & \boldsymbol{S}_6 \\ \boldsymbol{S}_{0L1} & \boldsymbol{S}_{0L2} & \boldsymbol{S}_{0L3} & \boldsymbol{S}_{0L4} & \boldsymbol{S}_{0L5} & \boldsymbol{S}_{0L6} \end{bmatrix} \tag{5-15}$$

and $\boldsymbol{F}$ is a column vector given as

$$\boldsymbol{F} = \begin{bmatrix} \boldsymbol{f}_1 \\ \boldsymbol{f}_2 \\ \boldsymbol{f}_3 \\ \boldsymbol{f}_4 \\ \boldsymbol{f}_5 \\ \boldsymbol{f}_6 \end{bmatrix}. \tag{5-16}$$

The position and the orientation of the top platform relative to the base are known which means the six columns of the matrix, J is known. Also, the magnitude $f_i,\ i = 1...6$ of each of the leg forces is known. The coordinates of the wrench can be computed from (5.14) which may be written as

$$\hat{\boldsymbol{\omega}} = \begin{bmatrix} \boldsymbol{f} \\ \boldsymbol{m}_0 \end{bmatrix} = \begin{bmatrix} L \\ M \\ N \\ P \\ Q \\ R \end{bmatrix}. \tag{5-17}$$

The magnitude of the resultant wrench and the pitch h are

$$f = |\boldsymbol{f}| = \sqrt{L^2 + M^2 + N^2}\ , \tag{5-18}$$

$$h = \frac{\boldsymbol{f} \cdot \boldsymbol{m}_0}{\boldsymbol{f} \cdot \boldsymbol{f}} = \frac{LP + MQ + NR}{L^2 + M^2 + N^2} \tag{5-19}$$

and the coordinates of the line of action of the resultant wrench are

$$S = \left[\frac{L}{|\boldsymbol{f}|}, \frac{M}{|\boldsymbol{f}|}, \frac{N}{|\boldsymbol{f}|} \right]^T, \tag{5-20}$$

$$\boldsymbol{S}_{0L} = \left[\frac{P - hL}{|\boldsymbol{f}|}, \frac{Q - hM}{|\boldsymbol{f}|}, \frac{R - hN}{|\boldsymbol{f}|} \right]^T. \tag{5-21}$$

The reverse static analysis computes the magnitudes of the leg forces given the position and orientation of the top platform relative to the base and the wrench applied to the top platform. This is accomplished by solving for $\boldsymbol{F}$ as

$$\boldsymbol{F} = \boldsymbol{J}^{-1}\hat{\boldsymbol{\omega}} \tag{5-22}$$

where $\boldsymbol{J}^{-1}$ is the called the inverse Jacobian matrix (Crane, *et al*., 2006).

5.3 Stiffness Mapping of Parallel Platform Mechanisms

Let $\delta \boldsymbol{l} = [\delta l_1, \delta l_2, ..., \delta l_6]^T$ be the vector of prismatic joint deflections from the initial free length of each connector. Assuming there is no initial load applied to the top platform, one can relate $\delta \boldsymbol{l}$ to $\boldsymbol{F}$ by a 6×6 diagonal matrix, $\chi = diag[k_1, k_2, ..., k_6]$:

$$\boldsymbol{F} = \chi \delta \boldsymbol{l} \,. \tag{5-23}$$

The infinitesimal displacement in each leg $\delta \boldsymbol{l}_i$ is related to the infinitesimal displacement twist of the top platform by the transpose of the Jacobian matrix:

$$\delta \boldsymbol{l} = \boldsymbol{J}^T \delta \hat{\boldsymbol{D}} \tag{5-24}$$

where $\delta \hat{\boldsymbol{D}} = \left[\delta x, \delta y, \delta z, \delta\theta_x, \delta\theta_y, \delta\theta_z \right]^T$. Substituting (5.24) into (5.23), we get

$$\boldsymbol{F} = \chi \boldsymbol{J}^T \delta \hat{\boldsymbol{D}} \tag{5-25}$$

Substituting Eq. 5-25 into Eq. 5-14 gives

$$\hat{\boldsymbol{\omega}} = \boldsymbol{J} \chi \boldsymbol{J}^T \delta \hat{\boldsymbol{D}} \tag{5-26}$$

Equation 5-26 can be written as $\hat{\boldsymbol{\omega}} = K \delta \hat{\boldsymbol{D}}$ where $K = \boldsymbol{J} \chi \boldsymbol{J}^T$ is called the stiffness matrix of a parallel platform, evaluated for the specific instance where each leg connector is at its unloaded free length. Eq. 5-26 implies that the top platform output force is related to its deflection by the stiffness matrix, K. K, in this case is symmetrical, positive semi-definite, and manipulator configuration dependent.

If all spring constants are equal ($k_1 = k_2 = \ldots\ k_6 = k$), the stiffness matrix reduces to the form (Tsai, 1999, Zhang, 2000):

$$\begin{aligned} K &= k\boldsymbol{J}\boldsymbol{J}^T \\ &= k \begin{bmatrix} \begin{bmatrix} \text{translational} \\ \text{stiffness} \end{bmatrix}_{3x3} & \begin{bmatrix} \text{cross-coupling} \\ \text{between rotations} \\ \text{and translations} \end{bmatrix}_{3x3} \\ \begin{bmatrix} \text{cross-coupling} \\ \text{between rotations} \\ \text{and translations} \end{bmatrix}_{3x3} & \begin{bmatrix} \text{torsional} \\ \text{stiffness} \end{bmatrix}_{3x3} \end{bmatrix}. \end{aligned} \tag{5-27}$$

5.4 Geometry of Parallel Platform Mechanisms

It is a difficult task for a designer to determine the geometry of a parallel platform mechanism due to the complexity of its kinematics. Its behavior is not as intuitive as a serial manipulator and the geometric properties which will cause singularities are difficult to identify (Fichter, 1986, Merlet, 1996). The quality index was proposed to facilitate the design process of the parallel platform mechanism. It was initially defined for a planar 3-3 parallel mechanism (Lee *et al*, 2000) and later extended to the 6-6 parallel mechanism (Lee and Duffy, 2000) which is the geometry examined within this work. It is defined by the dimensionless ratio

$$\lambda = \frac{\left|\det \boldsymbol{J}\right|}{\left|\det \boldsymbol{J}\right|_{\max}} \tag{5-28}$$

where $\boldsymbol{J}$ is the six-by-six matrix of the normalized coordinates of the six leg lines and $\left|\det \boldsymbol{J}\right|_{\max}$ is the greatest absolute value of the determinant of this Jacobian matrix. The quality index takes a maximum value of 1 at the central configuration. When the top platform departs from the central configuration, the determinant of the Jacobian matrix always diminishes and it is zero when a singularity is encountered where the platform gains one or more uncontrollable freedoms. Therefore, $0 \le \lambda \le 1$ at every reachable configuration. The quality index is dependent neither on the choice of units of the leg lengths nor on the coordinate frame in which the line coordinates are determined. It is dependent solely on the configuration (Lee, 2000).

Within this work, the quality index is used to determine the relative sizes of the base and the top platform and the initial height of the top platform. Not only were designs which would lead to low or zero quality indexes avoided, but also the geometry

of the 6-6 parallel platform was determined by setting dimensions which gave the highest quality index possible at the nominal home position and orientation.

The geometry of the top platform is displayed in Figure 5-3 a). It is an equilateral triangle with the tips of the triangle removed where the joints are located. The top platform joints are separated symmetrically by an angle of 2.5 degrees on each side of the internal angle bisector which passes through the orthocenter of the triangle. This corresponds to a distance of αa between each two top platform joint where $\alpha = 0.047$.

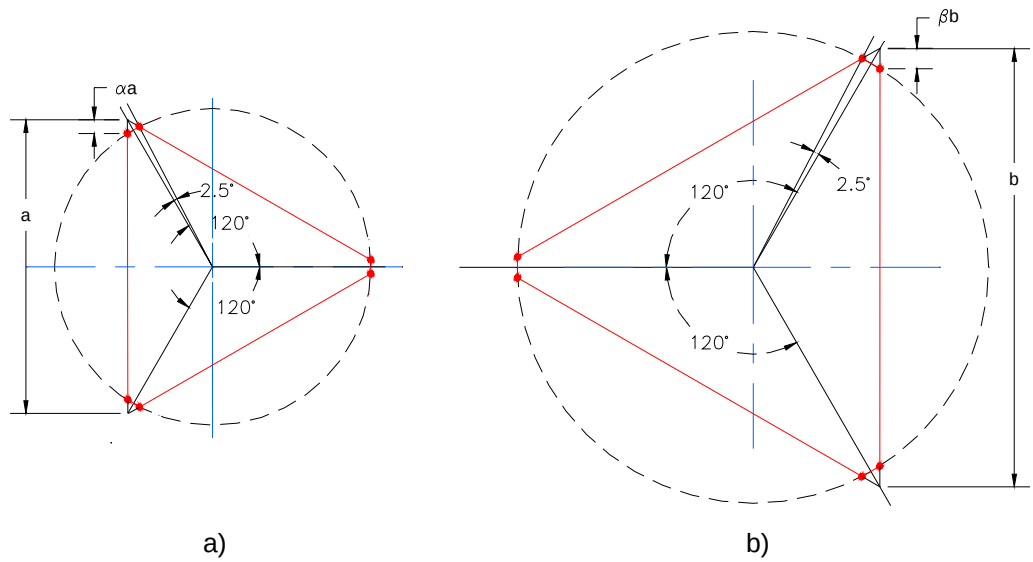

Figure 5-3. Geometry of the a) top platform b) base platform

The geometry of the base platform is displayed in Figure 5-3 b). It is also an equilateral triangle with the tips of the triangle removed where the joints are located. The base platform joints are separated symmetrically by an angle of 2.5 degrees on each side of the internal angle bisector which passes through the orthocenter of the triangle. This corresponds to a distance of βb between each two base platform joint where $\beta = 0.047$.

Figure 5-4 shows the orientation of the top platform to the bottom platform where the top is rotated 60 degrees from the bottom. The top platform is raised to a distance of

h and the top is connected to the bottom through the six legs A_1B_1, A_2B_2, A_3B_3, A_4B_4, A_5B_5, and A_6B_6.

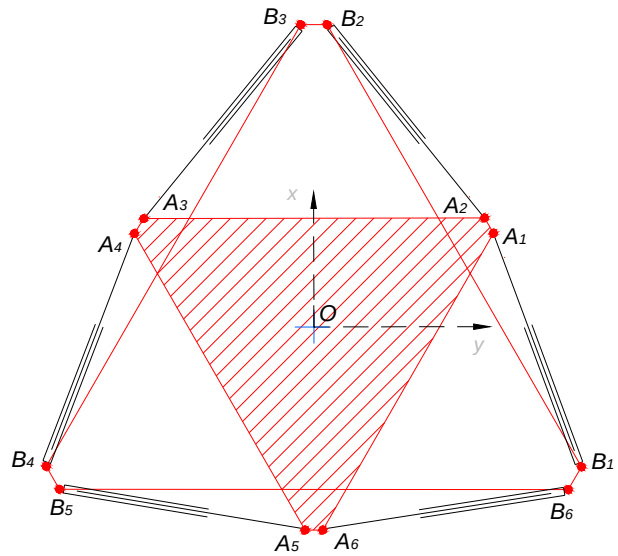

Figure 5-4. The schematic of the parallel platform mechanism showing the orientation of the top platform to the base platform

The coordinates of the joints are determined with respect to the coordinate frame placed at the center of the base platform, O.

$$
\begin{aligned}
&A_1\left(\frac{a(1-\alpha)}{2} \quad \frac{a(1-3\alpha)}{2\sqrt{3}} \quad h\right) && A_2\left(\frac{a(1-2\alpha)}{2} \quad \frac{a}{2\sqrt{3}} \quad h\right)\\
&A_3\left(\frac{a(2\alpha-1)}{2} \quad \frac{a}{2\sqrt{3}} \quad h\right) && A_4\left(\frac{a(\alpha-1)}{2} \quad \frac{a(1-3\alpha)}{2\sqrt{3}} \quad h\right)\\
&A_5\left(-\frac{\alpha a}{2} \quad \frac{a(3\alpha-2)}{2\sqrt{3}} \quad h\right) && A_6\left(\frac{\alpha a}{2} \quad \frac{a(3\alpha-2)}{2\sqrt{3}} \quad h\right)\\
&B_1\left(\frac{b(1-\beta)}{2} \quad \frac{b(3\beta-1)}{2\sqrt{3}} \quad 0\right) && B_2\left(\frac{\beta b}{2} \quad \frac{b(2-3\beta)}{2\sqrt{3}} \quad 0\right)\\
&B_3\left(-\frac{\beta b}{2} \quad \frac{b(2-3\beta)}{2\sqrt{3}} \quad 0\right) && B_4\left(\frac{b(\beta-1)}{2} \quad \frac{b(3\beta-1)}{2\sqrt{3}} \quad 0\right)\\
&B_5\left(\frac{b(2\beta-1)}{2} \quad -\frac{b}{2\sqrt{3}} \quad 0\right) && B_6\left(\frac{b(1-2\beta)}{2} \quad -\frac{b}{2\sqrt{3}} \quad 0\right)
\end{aligned}
\tag{5-29}
$$

The coordinates of a line joining two finite points with coordinates (x_1, y_1, z_1) and (x_2, y_2, z_2) are given by the second-order determinants of the array

$$\begin{vmatrix} 1 & x_1 & y_1 & z_1 \\ 1 & x_2 & y_2 & z_2 \end{vmatrix} \tag{5-30}$$

The Plücker coordinates of the six legs are similarly found:

$$\boldsymbol{S}_1 \equiv \begin{pmatrix} \frac{a(1-\alpha)}{2} - \frac{b(1-\beta)}{2} & \frac{a(1-3\alpha)-b(3\beta-1)}{2\sqrt{3}} & h; \\ \frac{bh(3\beta-1)}{2\sqrt{3}} & \frac{bh(\beta-1)}{2} & \frac{ab\left[(1-3\alpha)(1-\beta)-(1-\alpha)(3\beta-1)\right]}{4\sqrt{3}} \end{pmatrix} \tag{5-31}$$

$$\boldsymbol{S}_2 \equiv \begin{pmatrix} \frac{a(1-2\alpha)-\beta b}{2} & \frac{a-b(2-3\beta)}{2\sqrt{3}} & h; \\ \frac{bh(2-3\beta)}{2\sqrt{3}} & -\frac{\beta bh}{2} & \frac{\beta ab - ab(2-3\beta)(1-2\alpha)}{4\sqrt{3}} \end{pmatrix} \tag{5-32}$$

$$\boldsymbol{S}_3 \equiv \begin{pmatrix} \frac{a(2\alpha-1)+\beta b}{2} & \frac{a-b(2-3\beta)}{2\sqrt{3}} & h; \\ \frac{bh(2-3\beta)}{2\sqrt{3}} & \frac{\beta bh}{2} & -\frac{a\beta b + ab(2\alpha-1)(2-3\beta)}{4\sqrt{3}} \end{pmatrix} \tag{5-33}$$

$$\boldsymbol{S}_4 \equiv \begin{pmatrix} \frac{a(\alpha-1)-b(\beta-1)}{2} & \frac{a(1-3\alpha)-b(3\beta-1)}{2\sqrt{3}} & h; \\ \frac{bh(3\beta-1)}{2\sqrt{3}} & \frac{bh(1-\beta)}{2} & \frac{ab\left[(3\beta-1)(1-\alpha)-(1-\beta)(1-3\alpha)\right]}{4\sqrt{3}} \end{pmatrix} \tag{5-34}$$

$$\boldsymbol{S}_5 \equiv \begin{pmatrix} -\frac{\alpha a - b(2\beta-1)}{2} & \frac{a(3\alpha-2)+b}{2\sqrt{3}} & h; \\ -\frac{bh}{2\sqrt{3}} & \frac{bh(1-2\beta)}{2} & \frac{ab(2\beta-1)(3\alpha-2)-\alpha ab}{4\sqrt{3}} \end{pmatrix} \tag{5-35}$$

$$\boldsymbol{S}_6 \equiv \begin{pmatrix} \frac{\alpha a - b(1-2\beta)}{2} & \frac{a(3\alpha-2)+b}{2\sqrt{3}} & h; & & & \\ & & & -\frac{bh}{2\sqrt{3}} & \frac{bh(2\beta-1)}{2} & \frac{ab(1-2\beta)(3\alpha-2)+\alpha ab}{4\sqrt{3}} \end{pmatrix} \tag{5-36}$$

The normalized determinant of the six lines from Eq. 5-31 to 5.36 is

$$\det \boldsymbol{J} = \frac{1}{l^6}\left|\boldsymbol{S}^{\mathrm{T}}{}_1 \quad \boldsymbol{S}^{\mathrm{T}}{}_2 \quad \boldsymbol{S}^{\mathrm{T}}{}_3 \quad \boldsymbol{S}^{\mathrm{T}}{}_4 \quad \boldsymbol{S}^{\mathrm{T}}{}_5 \quad \boldsymbol{S}^{\mathrm{T}}{}_6\right| \tag{5-37}$$

where $l = B_1A_1 = B_2A_2 = B_3A_3 = B_4A_4 = B_5A_5 = B_6A_6$ is the same length for each leg and is equal to

$$l = \sqrt{\frac{1}{3}\left(a^2(3\alpha^2-3\alpha+1)+ab(3\alpha\beta-1)+b^2(3\beta^2-3\beta+1)+3h^2\right)} \tag{5-38}$$

Expanding (5.40) yields

$$\det \boldsymbol{J} = \frac{81\sqrt{3}a^3b^3h^3(3\alpha\beta-2\alpha-2\beta+1)^3}{4\left(a^2(3\alpha^2-3\alpha+1)+ab(3\alpha\beta-1)+b^2(3\beta^2-3\beta+1)+3h^2\right)^3} \tag{5-39}$$

The derivative of (5.42) is taken to find the maximum value of $\det J$ and $\left|\det J\right|_{\max}$ occurs when

$$h = \sqrt{\frac{1}{3}\left(a^2(3\alpha^2-3\alpha+1)+ab(3\alpha\beta-1)+b^2(3\beta^2-3\beta+1)\right)} \tag{5-40}$$

Substituting (5.43) into (5.42) yields

$$\left|\det \boldsymbol{J}\right|_{\max} = \frac{27a^3b^3(3\alpha\beta-2\alpha-2\beta+1)^3}{32\left(a^2(3\alpha^2-3\alpha+1)+ab(3\alpha\beta-1)+b^2(3\beta^2-3\beta+1)\right)^{3/2}} \tag{5-41}$$

Substituting $b = \gamma a$ into (5.44) where γ is a measure of the relative sizes of the top and base platforms and multiplying the numerator and the denominator by γ gives

$$\left|\det \boldsymbol{J}\right|_{\max} = \frac{27a^3(3\alpha\beta-2\alpha-2\beta+1)^3}{32\left(\frac{1}{\gamma^2}(3\alpha^2-3\alpha+1)+\frac{1}{\gamma}(3\alpha\beta-1)+(3\beta^2-3\beta+1)\right)^{3/2}} \tag{5-42}$$

The derivative of $\left|\det \boldsymbol{J}\right|_{\max}$ is taken with respect to γ in order to find its absolute maximum value which yields

$$-\frac{1}{\gamma^2}\left(\frac{2}{\gamma}(3\alpha^2-3\alpha+1)+3\alpha\beta-1)\right)=0 \tag{5-43}$$

and therefore

$$\gamma=\frac{b}{a}=\frac{-6\alpha^2+6\alpha-2}{3\alpha\beta-1} \tag{5-44}$$

Substituting (5.47) into (5.45) yields

$$\left|\det \boldsymbol{J}\right|_{\max}=\frac{3\sqrt{3}}{4}a^3\left(3\alpha^2-3\alpha+1\right)^{3/2} \tag{5-45}$$

One significant thing to note from (5.45) is that $\left|\det \boldsymbol{J}\right|_{\max}$ is dependent only on α and it is independent of β. When $\alpha=1$ or 0, $\left|\det \boldsymbol{J}\right|_{\max}$ has a maximum value of $\frac{3\sqrt{3}}{4}a^3$, and its minimum value of $\frac{3\sqrt{3}}{32}a^3$ occurs when $\alpha=\frac{1}{2}$ as shown in Figure 5-5.

The 6-6 platform investigated within this work has $\alpha=0.047$ and $\beta=0.047$. From (5.40), the height of the top platform in the optimal configuration is calculated and it is found to be $h=0.77a$. From (5.44), $\gamma=1.74$ which further gives $b=1.74a$. The optimal configuration taking into account these geometrical constraints is shown in Figure 5-6.

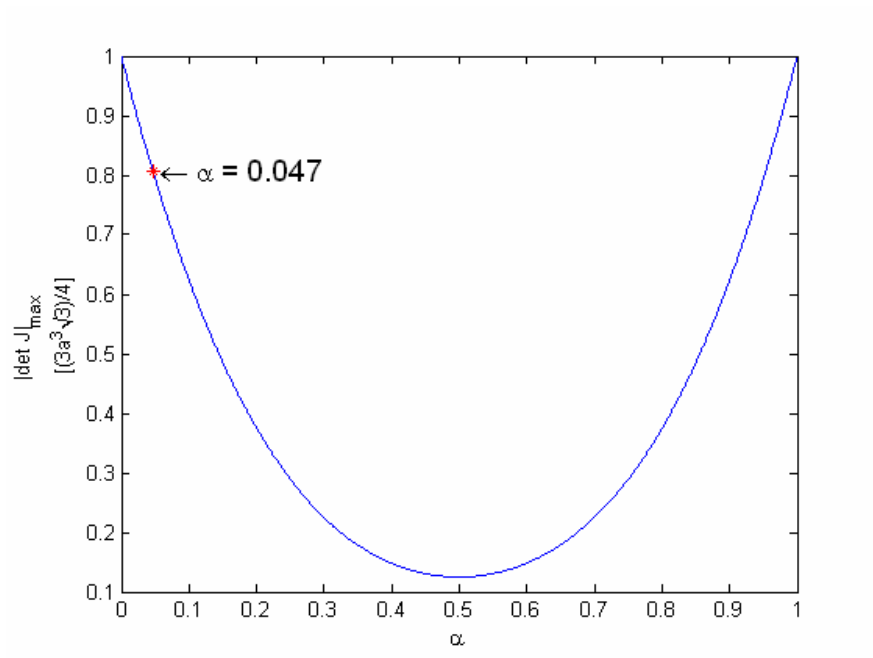

Figure 5-5. The value of $\left|\det J\right|_{\max}$ for $0 \le \alpha \le 1$

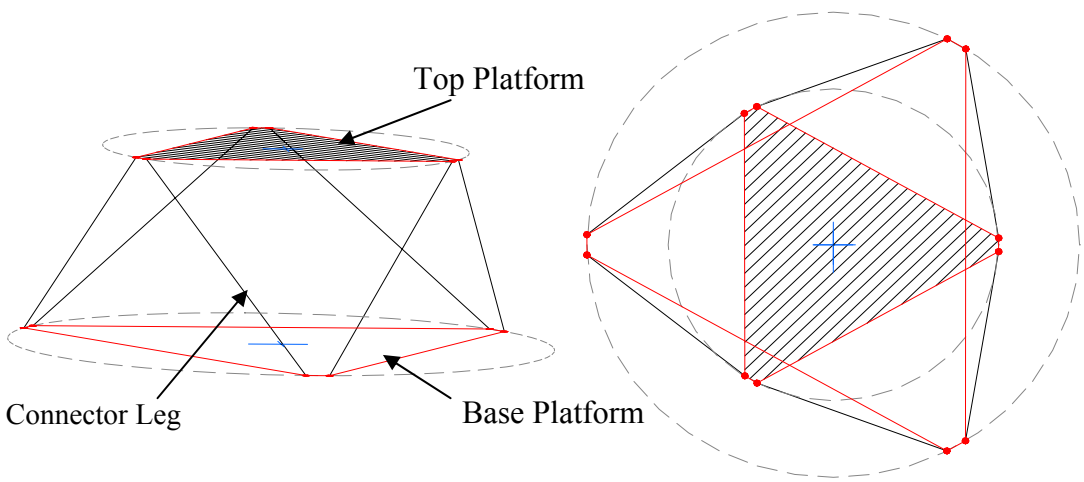

Figure 5-6. The optimal geometry of the parallel platform mechanism

CHAPTER 6
MODELING OF THE PARALLEL PLATFORM MECHANISM

In this chapter, the modeling of the parallel platform mechanism is explained in detail. The parallel platform model consists of six identical legs which may be modeled in different ways. Several models including the state-space formulations are given, starting with the basic connector model, to which first a coupling stage, then a decoupling stage and lastly semi-active MR dampers are incorporated. For verification purposes, the leg models are first created in MATLAB® and their response is compared to the response of those modeled in Simulink®. Next, the transmissibility results of the Simulink and SimMechanics leg models are compared to verify the correctness of the SimMechanics models which are implemented in the final 6 DOF models. The modeling of the legs is followed by the section explaining the modeling of the MR damper which is used in the simulations. Finally, the model of the 6 DOF parallel platform mechanism is presented.

6.1 Single Leg Connector Models

6.1.1 Basic Connector Model

In this simple model of the connector shown in Figure 6-1, the parameters and variables used are

x_1, the displacement of mass, m_1;

x_0, the displacement of mass, m_0;

k_1, the equivalent stiffness of the connector;

b_1, the actuator friction and damping, modeled as a viscous damper, and

F_A, the force generated by the actuator.

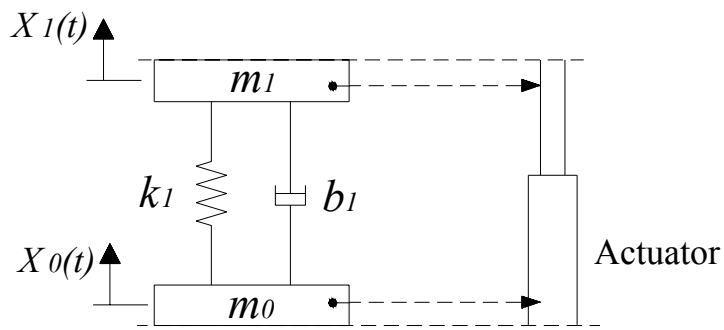

Figure 6-1. Basic connector model

In this model, if the damping required for vibration control is provided by the active control of the actuator, then the dynamic behavior of the system is determined by the dynamic response of the actuator and the controller. The main disadvantage of this is that the dynamic response of the actuator may not match the desired dynamic performance of the system. Also, all the energy will be dissipated by the actuator. This can overheat the actuator. Furthermore, the power efficiency of the system is reduced when active devices (actuator) are used to simulate passive ones (spring, damper) (Baiges-Valentin, 1996). If passive control is preferred, the active actuator may be replaced by a spring- damper pair.

The equations of motion for the basic connector are given in Eq. 6-1 and then put into matrix form in Eq. 6-2.

$$\begin{aligned} m_0\ddot{x}_0 + b_1(\dot{x}_0 - \dot{x}_1) + k_1(x_0 - x_1) &= F_D - F_A \\ m_1\ddot{x}_1 + b_1(\dot{x}_1 - \dot{x}_0) + k_1(x_1 - x_0) &= F_A \end{aligned} \tag{6-1}$$

$$\begin{bmatrix} m_0 & 0 \\ 0 & m_1 \end{bmatrix}\begin{bmatrix} \ddot{x}_0 \\ \ddot{x}_1 \end{bmatrix} + \begin{bmatrix} b_1 & -b_1 \\ -b_1 & b_1 \end{bmatrix}\begin{bmatrix} \dot{x}_0 \\ \dot{x}_1 \end{bmatrix} + \begin{bmatrix} k_1 & -k_1 \\ -k_1 & k_1 \end{bmatrix}\begin{bmatrix} x_0 \\ x_1 \end{bmatrix} = \begin{bmatrix} F_D - F_A \\ F_A \end{bmatrix} \tag{6-2}$$

The state-space formulation is given in Eq. 6-3 and then put into matrix form in Eq. 6-4.

$$\begin{aligned} x_1 &= x_0 & \dot{x}_1 &= x_3 \\ x_2 &= x_1 & \dot{x}_2 &= x_4 \\ x_3 &= \dot{x}_0 & \dot{x}_3 &= \ddot{x}_0 = 1/m_0\left[F_D - F_A - b_1(x_3 - x_4) - k_1(x_1 - x_2)\right] \\ x_4 &= \dot{x}_1 & \dot{x}_4 &= \ddot{x}_1 = 1/m_1\left[F_A - b_1(x_4 - x_3) - k_1(x_2 - x_1)\right] \end{aligned} \tag{6-3}$$

$$\underline{\dot{x} = Ax + Bu}$$

$$\begin{bmatrix} \dot{x}_1 \\ \dot{x}_2 \\ \dot{x}_3 \\ \dot{x}_4 \end{bmatrix} = \begin{bmatrix} 0 & 0 & 1 & 0 \\ 0 & 0 & 0 & 1 \\ -k_1/m_0 & k_1/m_0 & -b_1/m_0 & b_1/m_0 \\ k_1/m_1 & -k_1/m_1 & b_1/m_1 & -b_1/m_1 \end{bmatrix} \begin{bmatrix} x_1 \\ x_2 \\ x_3 \\ x_4 \end{bmatrix} + \begin{bmatrix} \begin{bmatrix} 0 & 0 \\ 0 & 0 \end{bmatrix} \\ \begin{bmatrix} 1/m_0 & -1/m_0 \\ 0 & 1/m_1 \end{bmatrix} \end{bmatrix} \begin{bmatrix} F_D \\ F_A \end{bmatrix} \tag{6-4}$$

$$\underline{y = Cx}$$

$$y = \begin{bmatrix} 1 & 0 & 0 & 0 \\ 0 & 1 & 0 & 0 \end{bmatrix} \begin{bmatrix} x_1 \\ x_2 \\ x_3 \\ x_4 \end{bmatrix}$$

Next, the frequency response of the system between the displacement of m_1 and F_D which is the input disturbance force applied to the bottom mass, m_0, is found. $F_A = 0$ for the case where vibration isolation is carried out by the passive spring-damper pair incorporated into the system. The bottom mass, m_0 is 38 kg, the top mass, m_1, is 16 kg, and the stiffness, k_1, is 5,000 N/m. The state-space formulation is carried out in MATLAB as shown in A.1 in the appendix. The damping is varied to see how the response of the system changes with varying damping. The same system is modeled in Simulink as shown in Figure 6-2.

The frequency response obtained by the MATLAB and the Simulink models is the same and is shown in Figure 6-3.

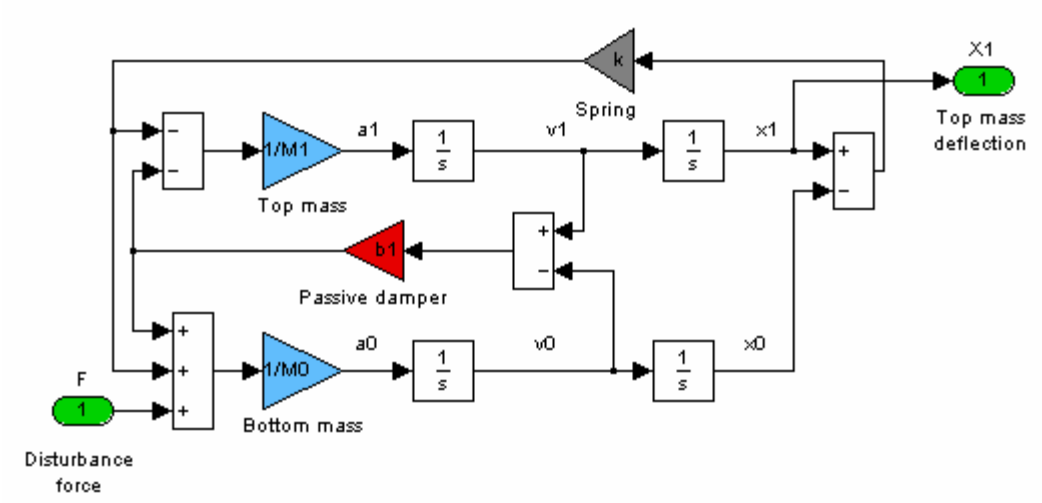

Figure 6-2. Basic connector Simulink model

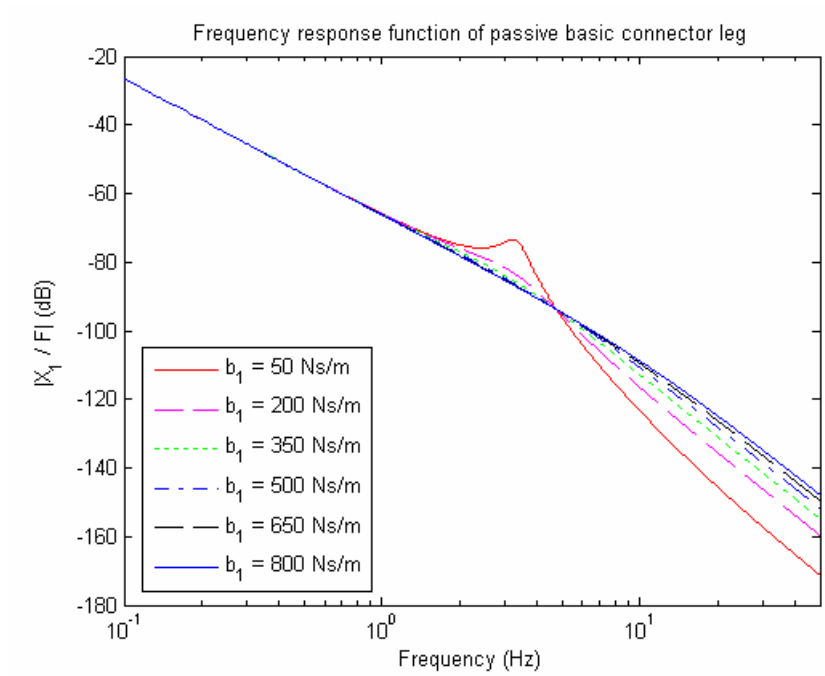

Figure 6-3. Frequency response of the basic connector for varying damping

6.1.2 Two-Stage Connector Model

A coupling stage may be introduced to improve the vibration isolation performance of the first model as shown in Figure 6-4. The additional components are

k_2, the stiffness of the coupling stage

b_2, the damping in the coupling stage, and

m_2, the mass of the coupling stage.

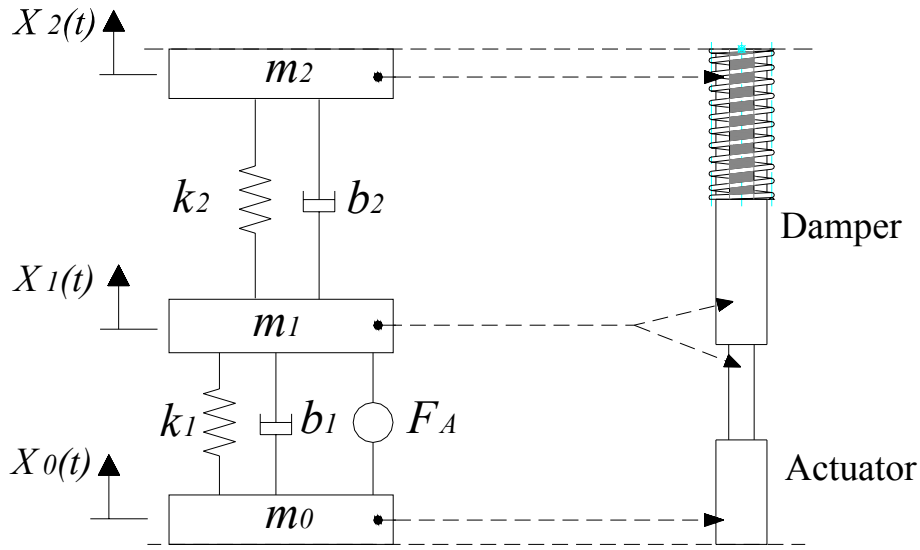

Figure 6-4. Two-stage connector model

The displacement of the spring in the coupling stage can be controlled to generate a force. The force applied by the connector to the payload is a function of the coupling stage displacement and velocity, and also the coupling stage stiffness and damping coefficients:

$$F = k_2(x_2 - x_1) + b_2(\dot{x}_2 - \dot{x}_1) \tag{6-5}$$

The coupling spring stiffness is much lower than the actuator stiffness. Therefore, most of the deflection occurs in the coupling stage. The main disadvantage of this model is that when the actuator applies a force, the coupling stage has to deform before this force can be transferred to the payload and this introduces a delay and degrades the dynamic performance. The damping element attenuates some of the high-frequency vibrations, but it also increases the reaction time of the system. Also, some of the energy

provided by the actuator is dissipated in the damper instead of being transmitted to the payload (Baiges-Valentin, 1996).

The equations of motion for the connector model with the coupling stage are given in Eq. 6-6 and then put into matrix form in Eq. 6-7.

$$\begin{aligned} &m_0\ddot{x}_0 + b_1(\dot{x}_0 - \dot{x}_1) + k_1(x_0 - x_1) = F_D - F_A \\ &m_1\ddot{x}_1 + b_1(\dot{x}_1 - \dot{x}_0) + k_1(x_1 - x_0) + b_2(\dot{x}_1 - \dot{x}_2) + k_2(x_1 - x_2) = F_A \\ &m_2\ddot{x}_2 + b_2(\dot{x}_2 - \dot{x}_1) + k_2(x_2 - x_1) = 0 \end{aligned} \tag{6-6}$$

$$\begin{bmatrix} m_0 & 0 & 0 \\ 0 & m_1 & 0 \\ 0 & 0 & m_2 \end{bmatrix}\begin{bmatrix} \ddot{x}_0 \\ \ddot{x}_1 \\ \ddot{x}_2 \end{bmatrix} + \begin{bmatrix} b_1 & -b_1 & 0 \\ -b_1 & b_1 + b_2 & -b_2 \\ 0 & -b_2 & b_2 \end{bmatrix}\begin{bmatrix} \dot{x}_0 \\ \dot{x}_1 \\ \dot{x}_2 \end{bmatrix} + \begin{bmatrix} k_1 & -k_1 & 0 \\ -k_1 & k_1 + k_2 & -k_2 \\ 0 & -k_2 & k_2 \end{bmatrix}\begin{bmatrix} x_0 \\ x_1 \\ x_2 \end{bmatrix} = \begin{bmatrix} F_D - F_A \\ F_A \\ 0 \end{bmatrix} \tag{6-7}$$

The state-space formulation is given in Eq. 6-8 and then put into matrix form in Eq. 6-9.

$$\begin{aligned} &x_1 = x_0 && \dot{x}_1 = x_4 \\ &x_2 = x_1 && \dot{x}_2 = x_5 \\ &x_3 = x_2 && \dot{x}_3 = x_6 \\ &x_4 = \dot{x}_0 && \dot{x}_4 = \ddot{x}_0 = 1/m_0\left[F_D - F_A - b_1x_4 + b_1x_5 - k_1x_1 + k_1x_2\right] \\ &x_5 = \dot{x}_1 && \dot{x}_5 = \ddot{x}_1 = 1/m_1\left[F_A + b_1x_4 - (b_1 + b_2)x_5 + b_2x_6 + k_1x_1 - (k_1 + k_2)x_2 + k_2x_3\right] \\ &x_6 = \dot{x}_2 && \dot{x}_6 = \ddot{x}_2 = 1/m_2\left[b_2x_5 - b_2x_6 + k_2x_2 - k_2x_3\right] \end{aligned} \tag{6-8}$$

$$\underline{\dot{x} = Ax + Bu}$$

$$\begin{bmatrix} \dot{x}_1 \\ \dot{x}_2 \\ \dot{x}_3 \\ \dot{x}_4 \\ \dot{x}_5 \\ \dot{x}_6 \end{bmatrix} = \begin{bmatrix} \begin{bmatrix} 0 & 0 & 0 \\ 0 & 0 & 0 \\ 0 & 0 & 0 \end{bmatrix} & \begin{bmatrix} 1 & 0 & 0 \\ 0 & 1 & 0 \\ 0 & 0 & 1 \end{bmatrix} \\ \begin{bmatrix} -k_1/m_0 & k_1/m_0 & 0 \\ -k_1/m_1 & -(k_1+k_2)/m_1 & k_2/m_1 \\ 0 & k_2/m_2 & -k_2/m_2 \end{bmatrix} & \begin{bmatrix} -b_1/m_0 & b_1/m_0 & 0 \\ -b_1/m_1 & -(b_1+b_2)/m_1 & b_2/m_1 \\ 0 & b_2/m_2 & -b_2/m_2 \end{bmatrix} \end{bmatrix} \begin{bmatrix} x_1 \\ x_2 \\ x_3 \\ x_4 \\ x_5 \\ x_6 \end{bmatrix}$$

$$+ \begin{bmatrix} \begin{bmatrix} 0 & 0 \\ 0 & 0 \\ 0 & 0 \end{bmatrix} \\ \begin{bmatrix} 1/m_0 & -1/m_0 \\ 0 & 1/m_1 \\ 0 & 0 \end{bmatrix} \end{bmatrix} \begin{bmatrix} F_D \\ F_A \end{bmatrix}$$

$$\underline{y = Cx}$$

$$y = \begin{bmatrix} 1 & 0 & 0 & 0 & 0 & 0 \\ 0 & 1 & 0 & 0 & 0 & 0 \\ 0 & 0 & 1 & 0 & 0 & 0 \end{bmatrix} \begin{bmatrix} x_1 \\ x_2 \\ x_3 \\ x_4 \\ x_5 \\ x_6 \end{bmatrix} \tag{6-9}$$

Next, the frequency response of the system between the displacement of m_2 and F_D which is the input disturbance force applied to the bottom mass, m_0, is found. $F_A = 0$ for the case where the force actuator is used only for positioning and the vibration isolation is carried out by the passive damping and stiffness in the system. The bottom mass, m_0, is 23 kg, the intermediate mass, m_1, is 15 kg, and the top mass, m_2, is 16 kg. The stiffness constants, k_1 and k_2 are 10,000 and 5,000 N/m, respectively, and the damping coefficient, b_1, is 100 Ns/m. The state-space formulation is done in MATLAB as shown in A.2 in the appendix. The damping coefficient, b_2, is varied to see how the response of the system changes with varying damping. The same system is modeled in Simulink as shown in

Figure 6-5. The frequency response obtained by the MATLAB and the Simulink models is the same and is shown in Figure 6-6.

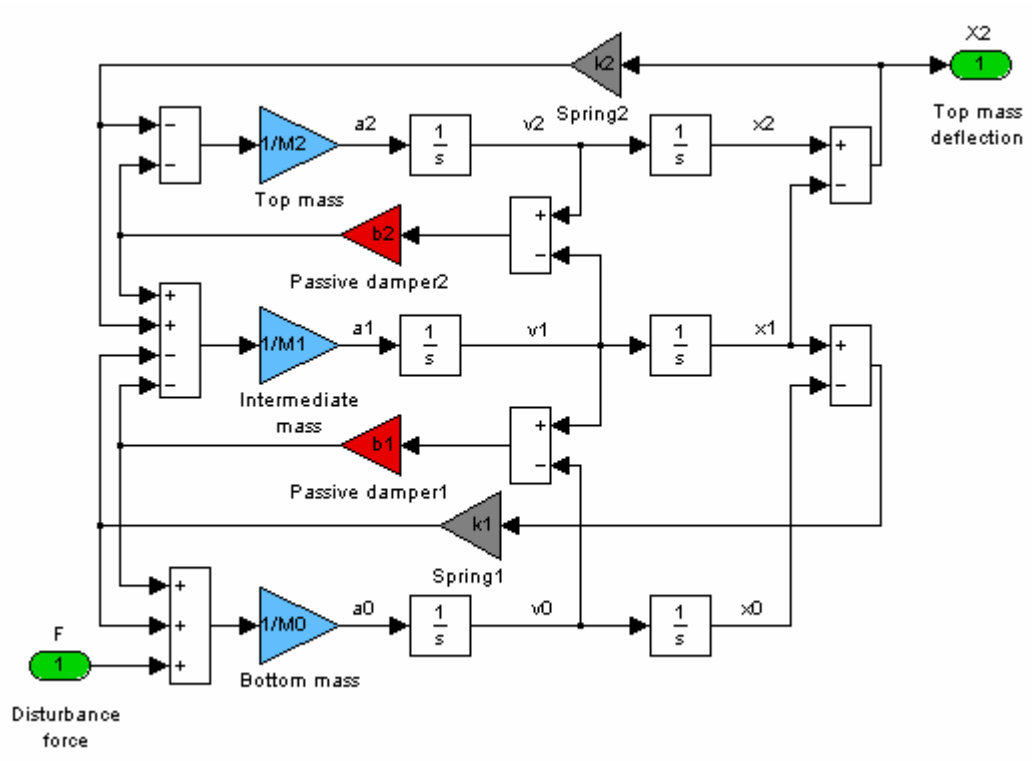

Figure 6-5. Two-stage connector Simulink model

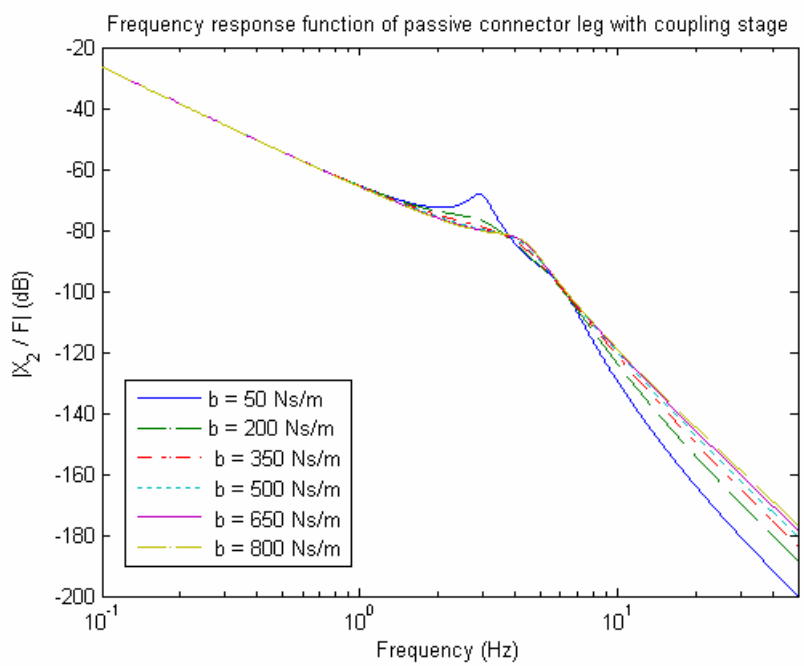

Figure 6-6. Frequency response of the two-stage connector for varying damping, b_2

6.1.3 Connector Model with Decoupling Stage

In order to eliminate high-frequency vibrations which are transmitted to the actuator through the connector stiffness element, a decoupling stage is introduced to the model as shown in Figure 6-7. Additional components are

k_3, the stiffness element in the decoupling stage,

b_3, the viscous damping element in the decoupling stage, and

m_3, the mass of the decoupling stage.

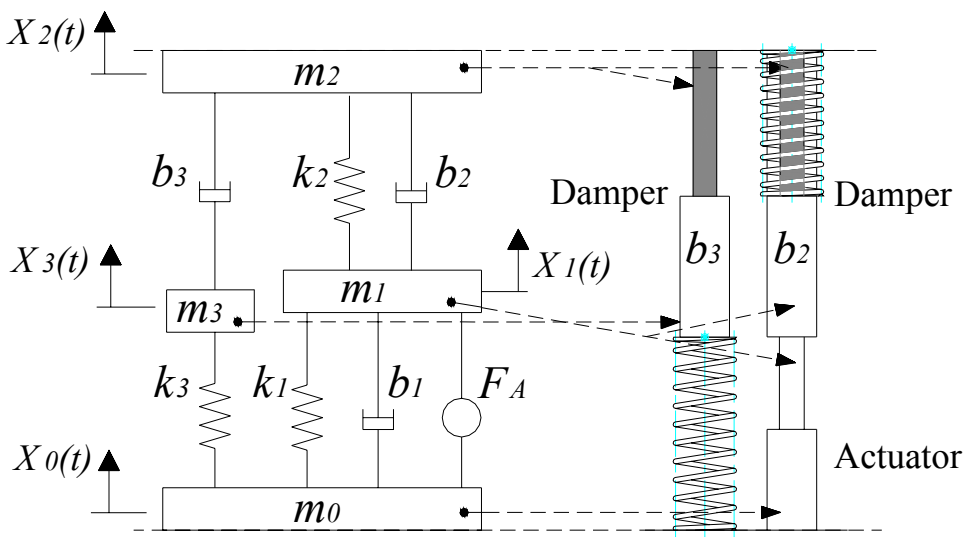

Figure 6-7. Connector model with decoupling stage

Unlike the coupling stage damper, the decoupling stage damper will not transmit the disturbances to the actuator and it will be used to attenuate high-frequency vibrations. The decoupling stage stiffness needs to be very high as it will be supporting the decoupling stage damper. If it is not stiff enough, the decoupling stage will deform the spring instead of the damper dissipating energy. The force applied by the connector to the payload is a combination of the force generated in the coupling and decoupling

stages. This force is a function the displacement and velocity of the coupling stage and the velocity of decoupling stage:

$$F = k_2(x_2 - x_1) + b_2(\dot{x}_2 - \dot{x}_1) + b_3(\dot{x}_2 - \dot{x}_3) \tag{6-10}$$

The problem with this model is that the decoupling stage damper will always be dissipating energy, both from the disturbance and from the actuator. In the latter case, some of the energy of the actuator which would normally be used to move the payload will be dissipated in the damper. The decoupling stage will also increase the overall mass and inertia of the connector (Baiges-Valentin, 1996; Hauge and Campbell, 2004).

The equations of motion for the connector model with the decoupling stage are given in Eq. 6-11 and then put into matrix form in Eq. 6-12.

$$\begin{aligned}
&m_0\ddot{x}_0 + b_1(\dot{x}_0 - \dot{x}_1) + k_1(x_0 - x_1) + k_3(x_0 - x_3) = F_D - F_A \\
&m_1\ddot{x}_1 + b_1(\dot{x}_1 - \dot{x}_0) + k_1(x_1 - x_0) + b_2(\dot{x}_1 - \dot{x}_2) + k_2(x_1 - x_2) = F_A \\
&m_2\ddot{x}_2 + b_2(\dot{x}_2 - \dot{x}_1) + k_2(x_2 - x_1) + b_3(\dot{x}_2 - \dot{x}_3) = 0 \\
&m_3\ddot{x}_3 + b_3(\dot{x}_3 - \dot{x}_2) + k_3(x_3 - x_0) = F_D
\end{aligned} \tag{6-11}$$

$$\begin{bmatrix} m_0 & 0 & 0 & 0 \\ 0 & m_1 & 0 & 0 \\ 0 & 0 & m_2 & 0 \\ 0 & 0 & 0 & m_3 \end{bmatrix} \begin{bmatrix} \ddot{x}_0 \\ \ddot{x}_1 \\ \ddot{x}_2 \\ \ddot{x}_3 \end{bmatrix} + \begin{bmatrix} b_1 & -b_1 & 0 & 0 \\ -b_1 & b_1 + b_2 & -b_2 & 0 \\ 0 & -b_2 & b_2 + b_3 & -b_3 \\ 0 & 0 & -b_3 & b_3 \end{bmatrix} \begin{bmatrix} \dot{x}_0 \\ \dot{x}_1 \\ \dot{x}_2 \\ \dot{x}_3 \end{bmatrix} + \begin{bmatrix} k_1 + k_3 & -k_1 & 0 & -k_3 \\ -k_1 & k_1 + k_2 & -k_2 & 0 \\ 0 & -k_2 & k_2 & 0 \\ -k_3 & 0 & 0 & k_3 \end{bmatrix} \begin{bmatrix} x_0 \\ x_1 \\ x_2 \\ x_3 \end{bmatrix} = \begin{bmatrix} F_D - F_A \\ F_A \\ 0 \\ F_D \end{bmatrix} \tag{6-12}$$

The state-space formulation is given in Eq. 6-13 and then put into matrix form in Eq. 6-14.

$$
\begin{aligned}
x_1 &= x_0 & \dot{x}_1 &= x_5 \\
x_2 &= x_1 & \dot{x}_2 &= x_6 \\
x_3 &= x_2 & \dot{x}_3 &= x_7 \\
x_4 &= x_3 & \dot{x}_4 &= x_8 \\
x_5 &= \dot{x}_0 & \dot{x}_5 &= \ddot{x}_0 = 1/m_0\left[F_D - F_A - b_1x_5 + b_1x_6 - (k_1+k_3)x_1 + k_1x_2 + k_3x_2\right] \\
x_6 &= \dot{x}_1 & \dot{x}_6 &= \ddot{x}_1 = 1/m_1\left[F_A + b_1x_5 - (b_1+b_2)x_6 + b_2x_7 + k_1x_1 - (k_1+k_2)x_2 + k_2x_3\right] \\
x_7 &= \dot{x}_2 & \dot{x}_7 &= \ddot{x}_2 = 1/m_2\left[b_2x_6 - (b_2+b_3)x_7 + b_3x_8 + k_2x_2 - k_2x_3\right] \\
x_8 &= \dot{x}_3 & \dot{x}_8 &= \ddot{x}_3 = 1/m_2\left[b_3x_7 - b_3x_8 + k_3x_1 - k_2x_3\right]
\end{aligned}
\tag{6-13}
$$

$\underline{\dot{x} = Ax + Bu}$

$$
\begin{bmatrix} \dot{x}_1 \\ \dot{x}_2 \\ \dot{x}_3 \\ \dot{x}_4 \\ \dot{x}_5 \\ \dot{x}_6 \\ \dot{x}_7 \\ \dot{x}_8 \end{bmatrix}
=
\begin{bmatrix}
\begin{bmatrix} 0 & 0 & 0 & 0 \\ 0 & 0 & 0 & 0 \\ 0 & 0 & 0 & 0 \\ 0 & 0 & 0 & 0 \end{bmatrix} & \begin{bmatrix} 1 & 0 & 0 & 0 \\ 0 & 1 & 0 & 0 \\ 0 & 0 & 1 & 0 \\ 0 & 0 & 0 & 1 \end{bmatrix} \\
\begin{bmatrix} \frac{-(k_1+k_3)}{m_0} & \frac{k_1}{m_0} & \frac{k_3}{m_0} & 0 \\ \frac{k_1}{m_1} & \frac{-(k_1+k_2)}{m_1} & \frac{k_2}{m_1} & 0 \\ 0 & \frac{k_2}{m_2} & \frac{-k_2}{m_2} & 0 \\ \frac{k_3}{m_3} & 0 & \frac{-k_3}{m_3} & 0 \end{bmatrix} & \begin{bmatrix} \frac{-b_1}{m_0} & \frac{b_1}{m_0} & 0 & 0 \\ \frac{b_1}{m_1} & \frac{-(b_1+b_2)}{m_1} & \frac{b_2}{m_1} & 0 \\ 0 & \frac{b_2}{m_2} & \frac{-(b_2+b_3)}{m_2} & \frac{b_3}{m_2} \\ 0 & 0 & \frac{b_3}{m_3} & \frac{-b_3}{m_3} \end{bmatrix}
\end{bmatrix}
\begin{bmatrix} x_1 \\ x_2 \\ x_3 \\ x_4 \\ x_5 \\ x_6 \\ x_7 \\ x_8 \end{bmatrix}
$$

$$
+
\begin{bmatrix}
\begin{bmatrix} 0 & 0 \\ 0 & 0 \\ 0 & 0 \\ 0 & 0 \end{bmatrix} \\
\begin{bmatrix} 1/m_0 & -1/m_0 \\ 0 & 1/m_1 \\ 0 & 0 \\ 1/m_3 & 0 \end{bmatrix}
\end{bmatrix}
\begin{bmatrix} F_D \\ F_A \end{bmatrix}
$$

$$\underline{y = Cx}$$

$$y = \begin{bmatrix} \begin{bmatrix} 1 & 0 & 0 & 0 \\ 0 & 1 & 0 & 0 \\ 0 & 0 & 1 & 0 \\ 0 & 0 & 0 & 1 \end{bmatrix} & \begin{bmatrix} 0 & 0 & 0 & 0 \\ 0 & 0 & 0 & 0 \\ 0 & 0 & 0 & 0 \\ 0 & 0 & 0 & 0 \end{bmatrix} \end{bmatrix} \begin{bmatrix} x_1 \\ x_2 \\ x_3 \\ x_4 \\ x_5 \\ x_6 \\ x_7 \\ x_8 \end{bmatrix} \tag{6-14}$$

Next, the frequency response of the system between the displacement of m_2 and F_D which is the input disturbance force applied to the bottom mass, m_0, is found. $F_A = 0$ for the case where the force actuator is used only for positioning and the vibration isolation is carried out by the passive damping and stiffness in the system. The bottom mass, m_0, is 23 kg, the intermediate mass, m_1, is 15 kg, the top mass, m_2, is 16 kg, and the decoupling stage mass, m_3, is 10 kg. The stiffness constants, k_1, k_2, and k_3 are 10,000, 5,000, and 10,000 N/m, respectively; and the damping coefficient, b_1, is 100 Ns/m. The state-space formulation is done in MATLAB as shown in A.3 in the appendix. The coupling stage damping coefficient, b_2, and the decoupling stage damping coefficient, b_3, are varied in the next section to see how the response of the system changes with varying damping. The same system is modeled in Simulink (Figure 6-8).

6.1.4 Semi-Active Connector Model with Decoupling Stage

It would be desirable to combine the advantages of the models above in one model. At low frequencies, the model with no decoupling stage provides minimum energy loss. However, at high frequencies, it does not provide enough energy dissipation and the decoupling stage is necessary. A connector with optimal performance at both low-frequencies and high-frequencies can be achieved by varying the amount of damping in

both the coupling and decoupling stage dampers as shown in Figure 6-9. An MR damper is an ideal candidate for this purpose. When maximum current is applied, the damping will be very high. The damper will be blocked and will behave essentially as a rigid element. When there is no magnetic field, the damper will act as a low energy dissipating device.

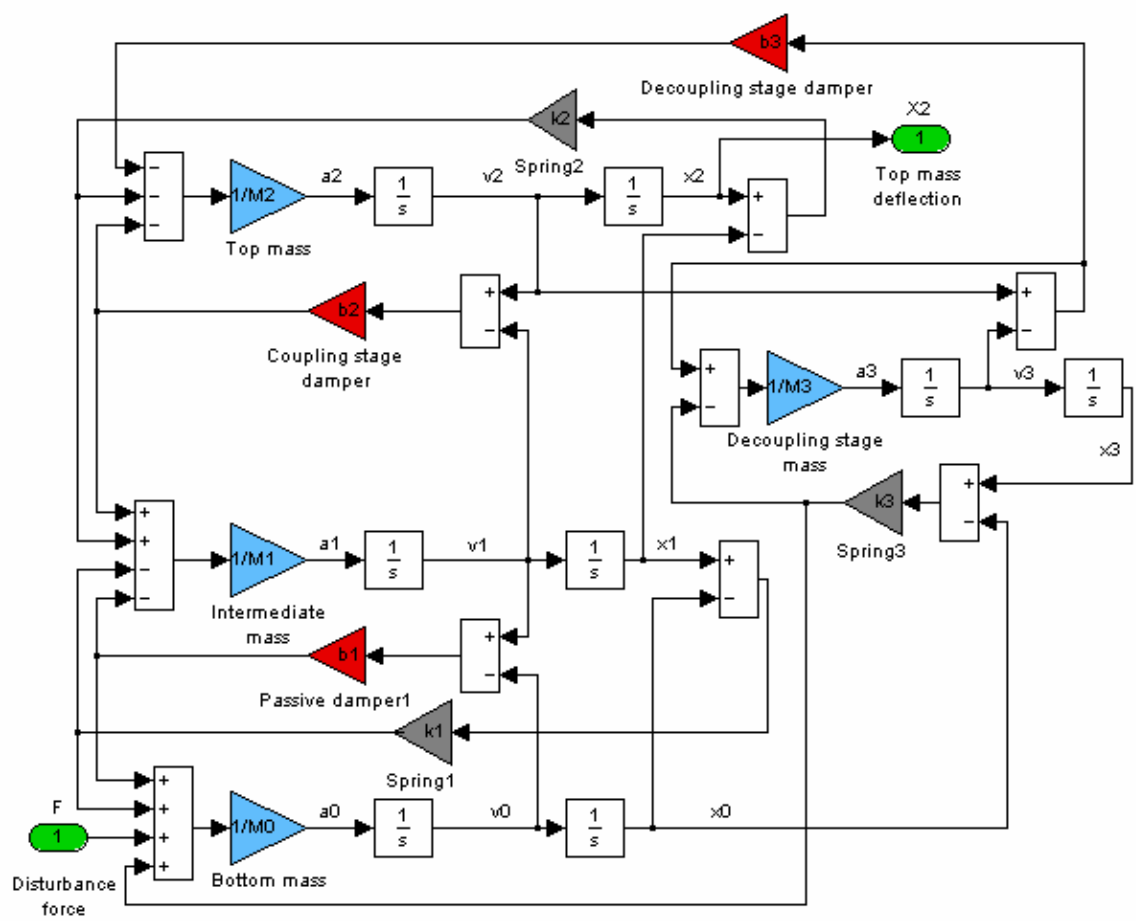

Figure 6-8. Connector with decoupling stage Simulink model

For the low-frequency mode, the decoupling stage must be deactivated. Therefore, there will be no current being applied to the decoupling stage damper. Only a small amount of energy will be dissipated here. Ideally, the decoupling stage damping would be equal to zero and the model would look like as in Figure 6-10. The current being

applied to the coupling stage may be adjusted depending on the amount of damping desired here. The frequency response of this model calculated by the MATLAB code in A.3 and the Simulink model in Figure 6-8 is the same and is shown in Figure 6-11. The decoupling stage damping coefficient is minimal (100 Ns/m) and the coupling stage damping is varied.

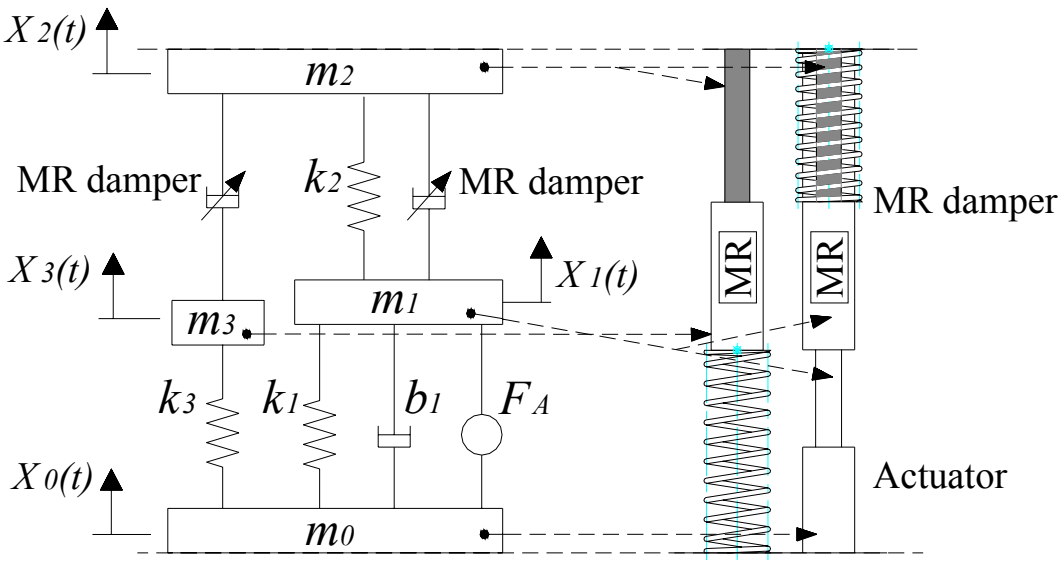

Figure 6-9. Connector model with variable damping elements

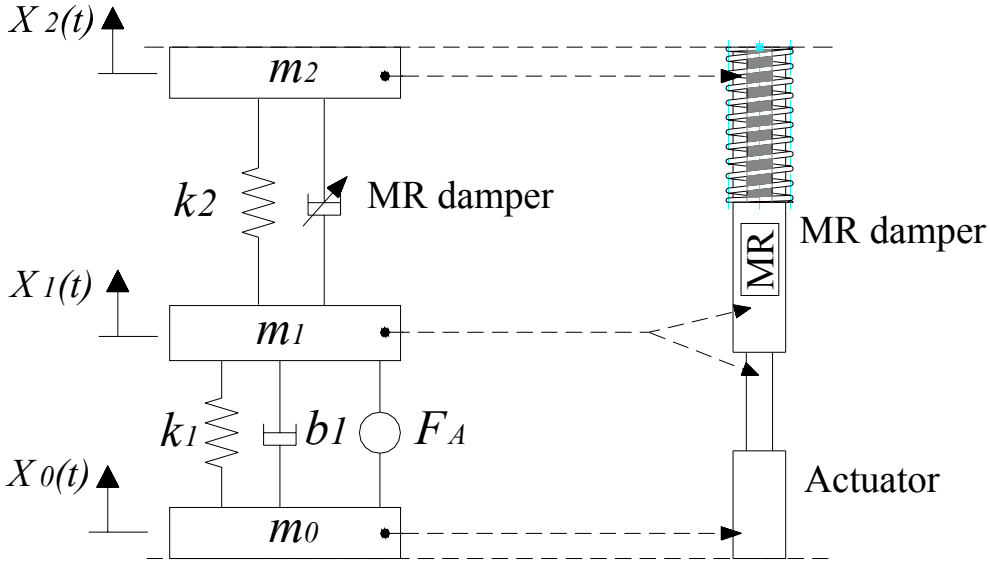

Figure 6-10. Connector model with decoupling stage damper deactivated

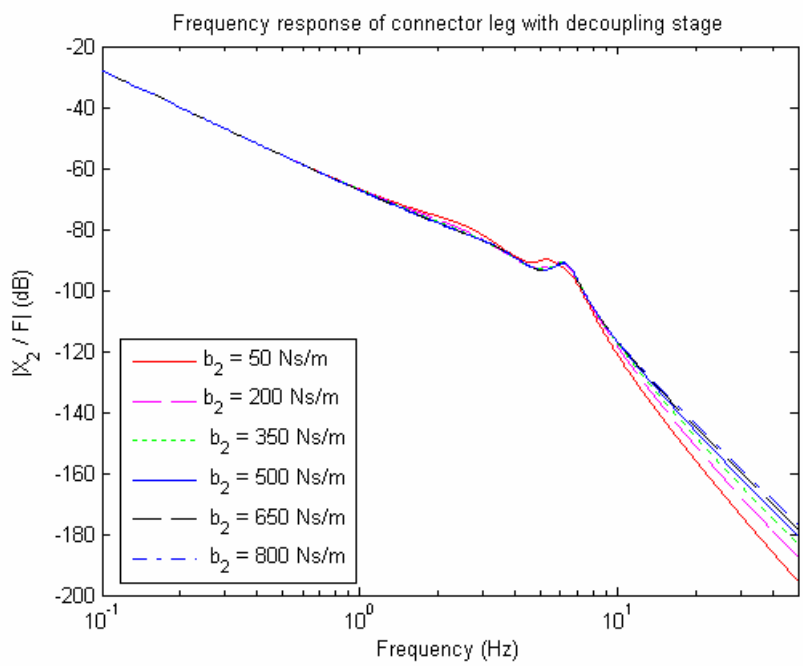

Figure 6-11. Frequency response of the connector model with decoupling stage damping coefficient, b_3 = 100 Ns/m and varying b_2

For the high-frequency mode, the coupling stage needs to be deactivated. The coupling stage damper will be blocked in this case and the coupling stage will behave essentially as a rigid element as shown in Figure 6-12.

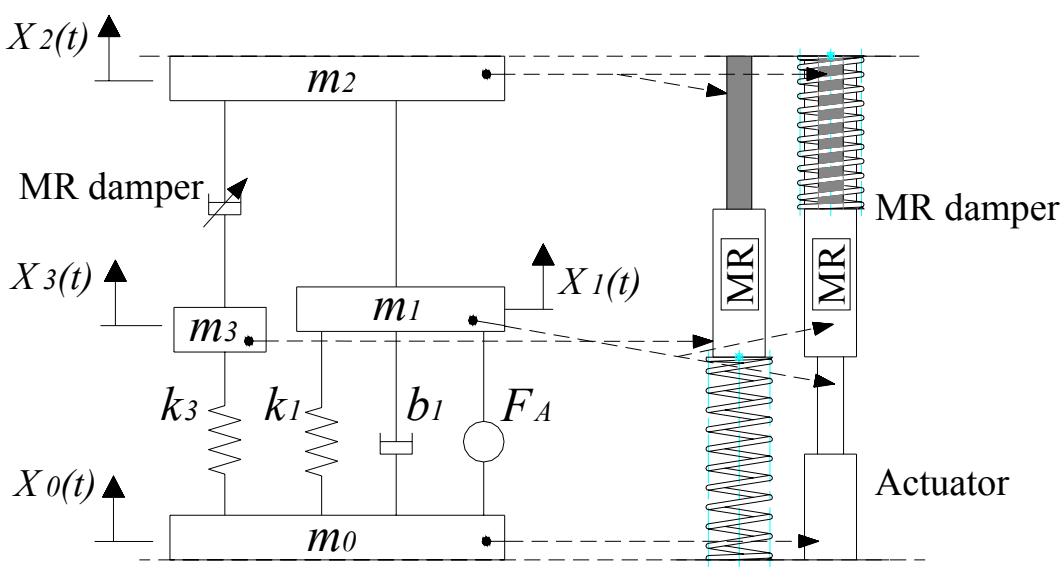

Figure 6-12. Connector model with coupling stage damper blocked

The damping coefficient of the decoupling stage would be set to a desirable value. The frequency response of this model (Figure 6-13) calculated by the MATLAB code in A.3 and the Simulink model is the same and is shown in Figure 6-8. The decoupling stage damping coefficient is varied and the decoupling stage damping coefficient is set to its maximum value (800 Ns/m).

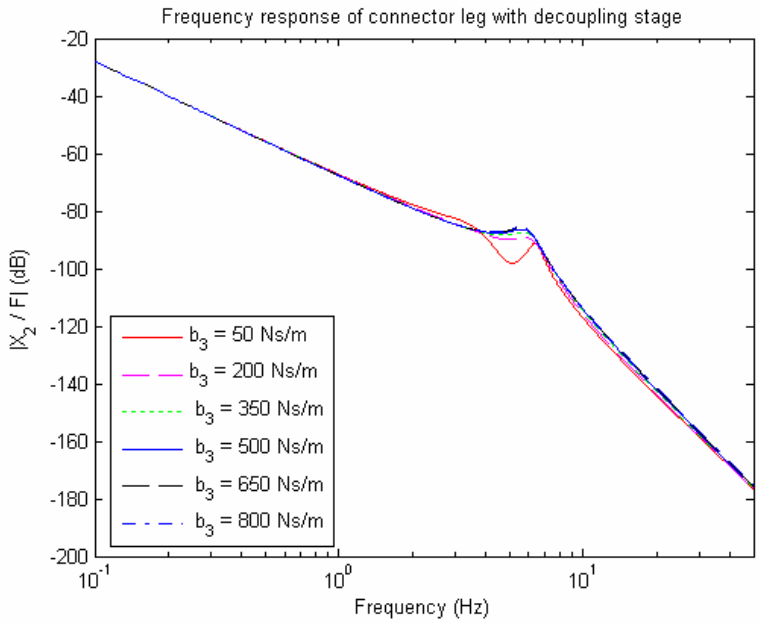

Figure 6-13. Frequency response of the connector model with coupling stage damping coefficient, b_2 = 800 Ns/m and varying b_3

Next, the performances of the basic connector, the two-stage connector, and the connector with the decoupling stage are compared in Figure 6-14. For the model with the decoupling stage, in addition to the high frequency and the low frequency modes, two other modes are included in the comparison. The first of these two modes is when the decoupling stage damping is set to its maximum value as the coupling stage damping is varied. The second mode is when the coupling stage damping is set to its minimum value as the decoupling stage damping is varied. It is seen from Figure 6-14 that none of the four modes of the connector model with the decoupling stage has a superior performance

over the two-stage connector model which would make it worthwhile to incorporate the decoupling stage to the connector leg model. Therefore, the two-stage connector model is chosen as the model to be incorporated into the 6 DOF model due to its simplicity in design and its performance which is superior and comparable to the performance of the basic connector model and the connector model with the decoupling stage, respectively.

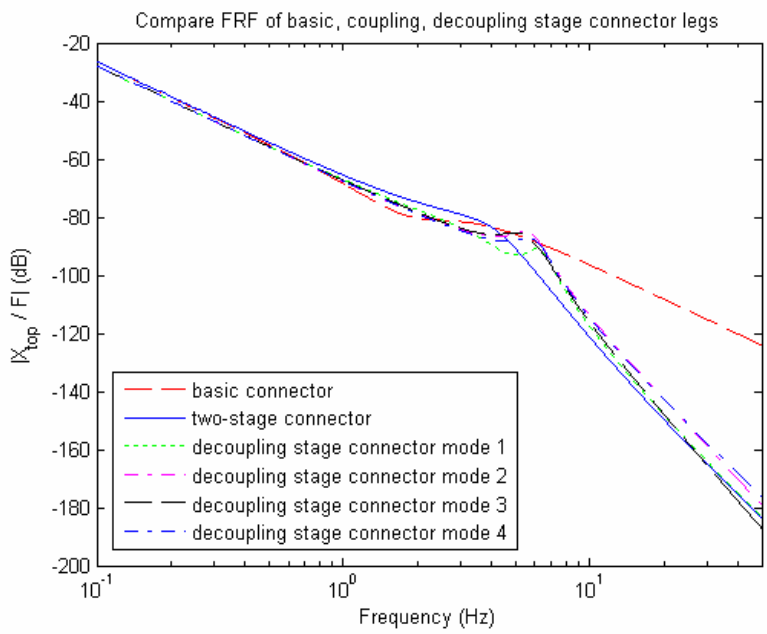

Figure 6-14. Comparison of the frequency response of the basic connector, the two-stage connector, and four modes of the connector model with the decoupling stage

6.2 Magnetorheological Damper Model

The model used in this work to model the MR damper is the Bingham plastic model. This model is an extension of the Newtonian flow and it is obtained by also taking into account the yield stress of the fluid. It assumes that flow will occur when the dynamic yield stress is reached. The total stress is given by

$$\tau = \tau_y \operatorname{sgn}(\dot{\gamma}) + \eta\dot{\gamma} \tag{6-15}$$

where τ_y is the yield stress induced by the magnetic field, $\dot{\gamma}$ is the shear rate and η is the viscosity of the fluid. In this model, the relationship between the damper force and the shear velocity may also be given as

$$F = \begin{cases} F_y \operatorname{sgn}(\dot{x}) + C_o \dot{x} & \dot{x} \neq 0 \\ -F_y < F < F_y & \dot{x} = 0 \end{cases} \tag{6-16}$$

where C_o is the post-yield damping coefficient and F_y is the yield force. In the post-yield part, the slope of the force-velocity curve is equal to the damping coefficient which is essentially the viscosity of the fluid, η.

Using curve-fitting, the first model is formed based on the experimental data obtained from the double-shafted damper prototype in Figure 4.6 as shown in Figure 6-15. The force-velocity lines are extrapolated to higher values of velocity and are shown in Figure 6-16.

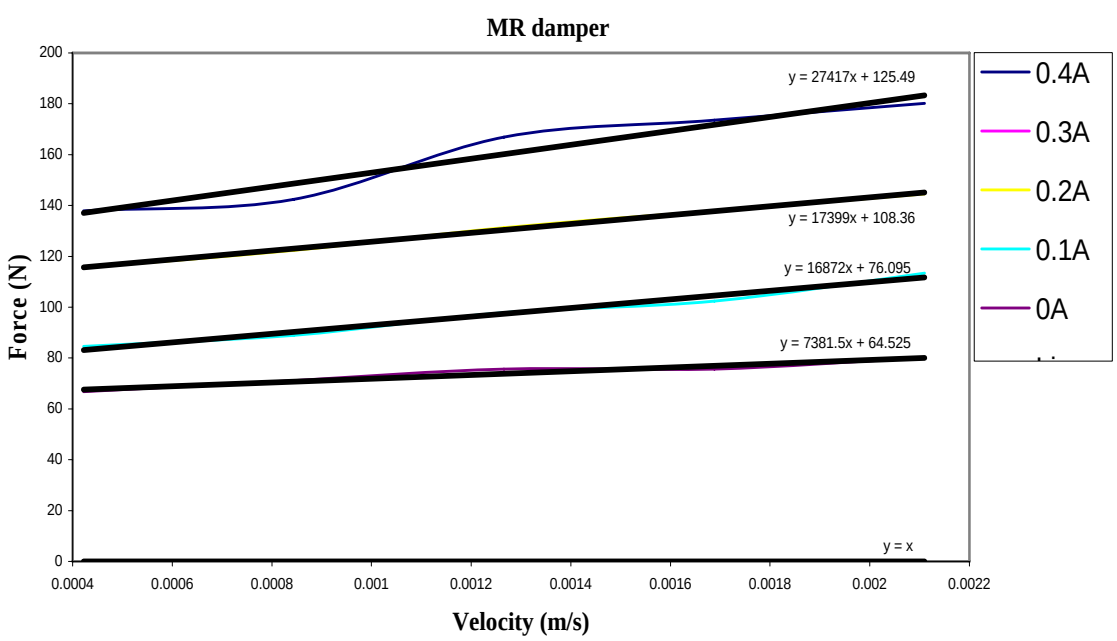

Figure 6-15. Curve-fitting applied on the experimental force-velocity curves of the prototype

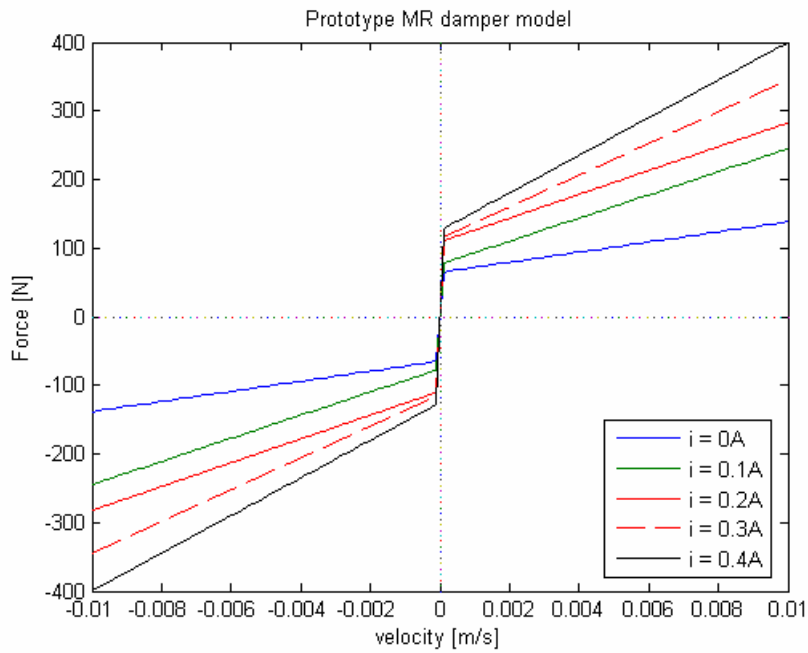

Figure 6-16. Force vs. velocity curves for varying input for the prototype MR damper model

The damping force exerted by the prototype MR damper was determined to be too high for the size of the parallel platform mechanism considered. Therefore, another MR damper model was used for the simulations. In this model, C_o and F_y which are functions of the control current input, *i*, can be modeled as second order polynomial functions (Ni *et al.,* 2002):

$$\begin{aligned} F_y(i) &= F_{yc} i^2 + F_{yb} i + F_{ya} \\ C_o(i) &= C_c i^2 + C_b i + C_a \end{aligned} \tag{6-17}$$

The force-velocity curves for this MR damper model are shown in Figure 6-17 for varying input current.

The MR damper control is modeled in SimMechanics as shown in Figure 6-18. In the first block, the desired damping force which would have been applied by an active skyhook damper control system is calculated. Since the semi-active damper can only

dissipate energy, in the semi-active implementation of the skyhook damper control, the desired skyhook damper force is only positive when the relative velocity between the two bodies and the absolute velocity of the clean body are in the same direction. Otherwise, the desired skyhook damper force is set to zero as shown in Figure 6-18. The control policy is therefore

$$F_{\text{des}} = \begin{cases} F_{\text{sky}} & \text{when} \quad (\dot{x}_2 - \dot{x}_1)\dot{x}_2 > 0 \\ 0 & \text{when} \quad (\dot{x}_2 - \dot{x}_1)\dot{x}_2 \le 0 \end{cases} \tag{6-18}$$

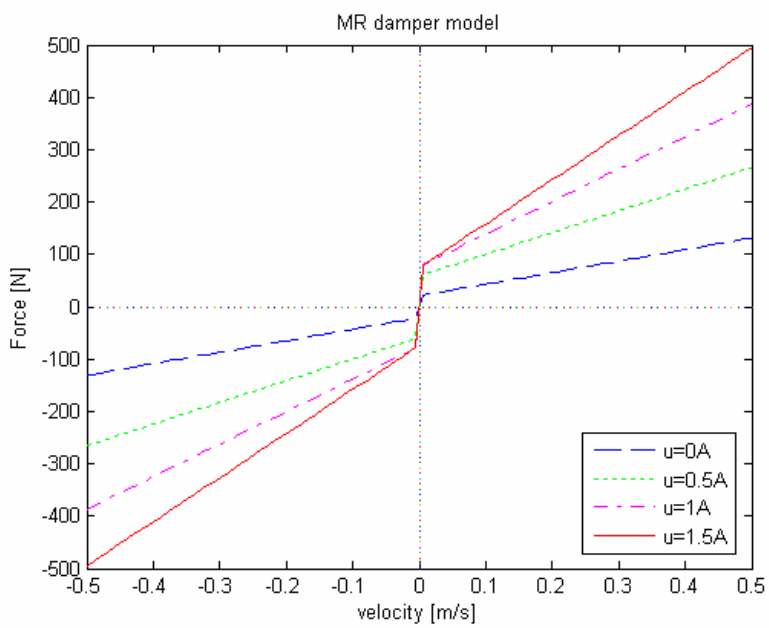

Figure 6-17. Force vs. velocity curves for varying input current for MR damper model

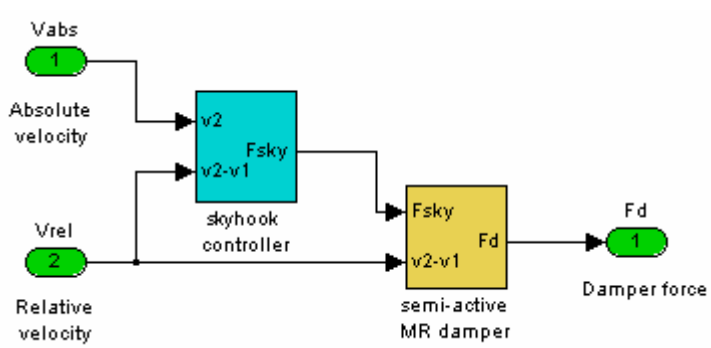

Figure 6-18. SimMechanics model of MR damper control

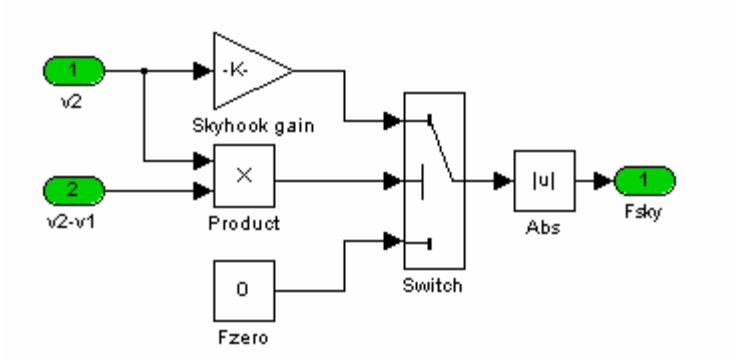

Figure 6-19. Calculating the desired skyhook damper force

The second block in Figure 6-18 compares the desired force to the dynamic force range of the MR damper and applies a damping force which is within this range as shown in Figure 6-20 and Figure 6-21.

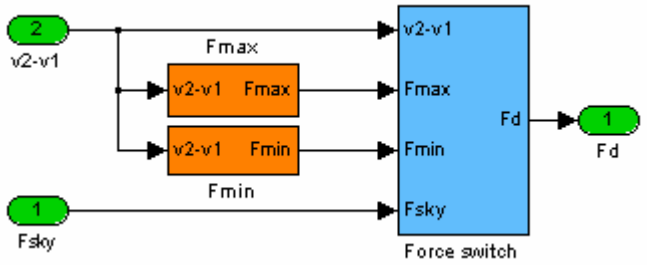

Figure 6-20. Semi-active implementation of the skyhook damper control policy

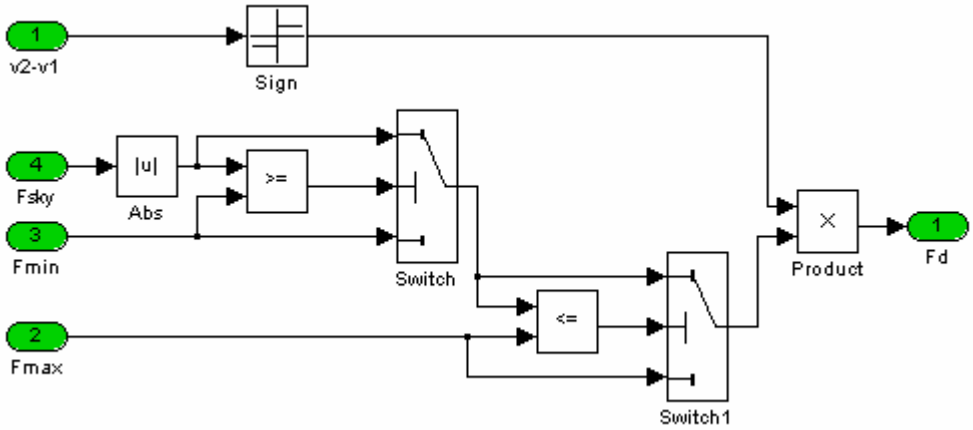

Figure 6-21. Force switch sub block

The controller first compares the desired force to the minimum force which the damper can apply. If the desired force is smaller, then the damper applies the minimum force because it cannot apply a force smaller than its minimum force. If the desired force is greater than the minimum damper force, then the controller compares the desired force this time to the maximum damper force. If the desired force is greater than the maximum damper force, then the damper applies the maximum damping force because it cannot apply a force greater than its maximum damping force. If the desired force is within the force capability of the MR damper, then the damper applies the desired force calculated by the skyhook damper control in the previous block. In this model, the mechanical delay of the MR damper is ignored. The schematic of the two-stage connector system which has this semi-active control policy implemented is shown in Figure 6-22.

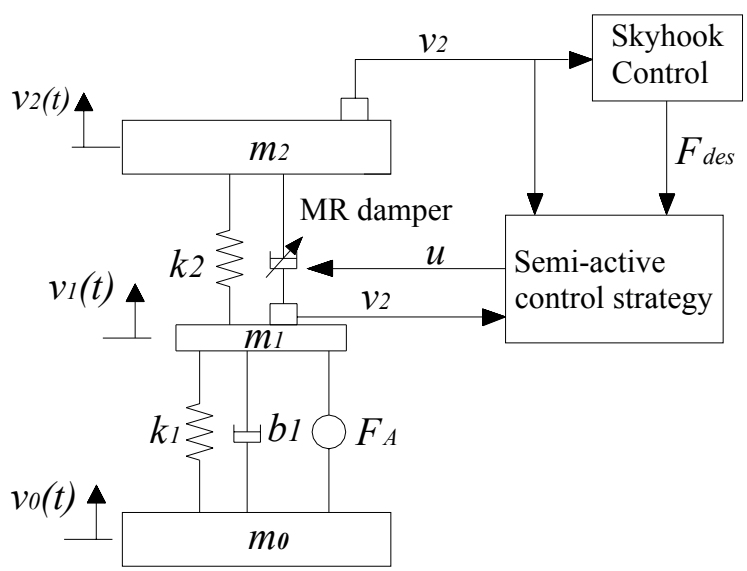

Figure 6-22. Two-stage connector system with the semi-active implementation of the skyhook damper control policy

6.3 6 DOF Parallel Platform Model

In this section, the 6 DOF parallel platform is first modeled with the basic connector model forming the basis of the legs. This simpler model is investigated as a preamble to the more complex 6 DOF parallel platform model with the two-stage connectors which is also presented in this section. The 6 DOF parallel platform is modeled in SimMechanics which works under Simulink and is a block diagram modeling environment where rigid bodies and their motions can be designed and simulated using the standard Newtonian dynamics of forces and torques. The 6 DOF parallel platform mechanism model is shown in Figure 6-23.

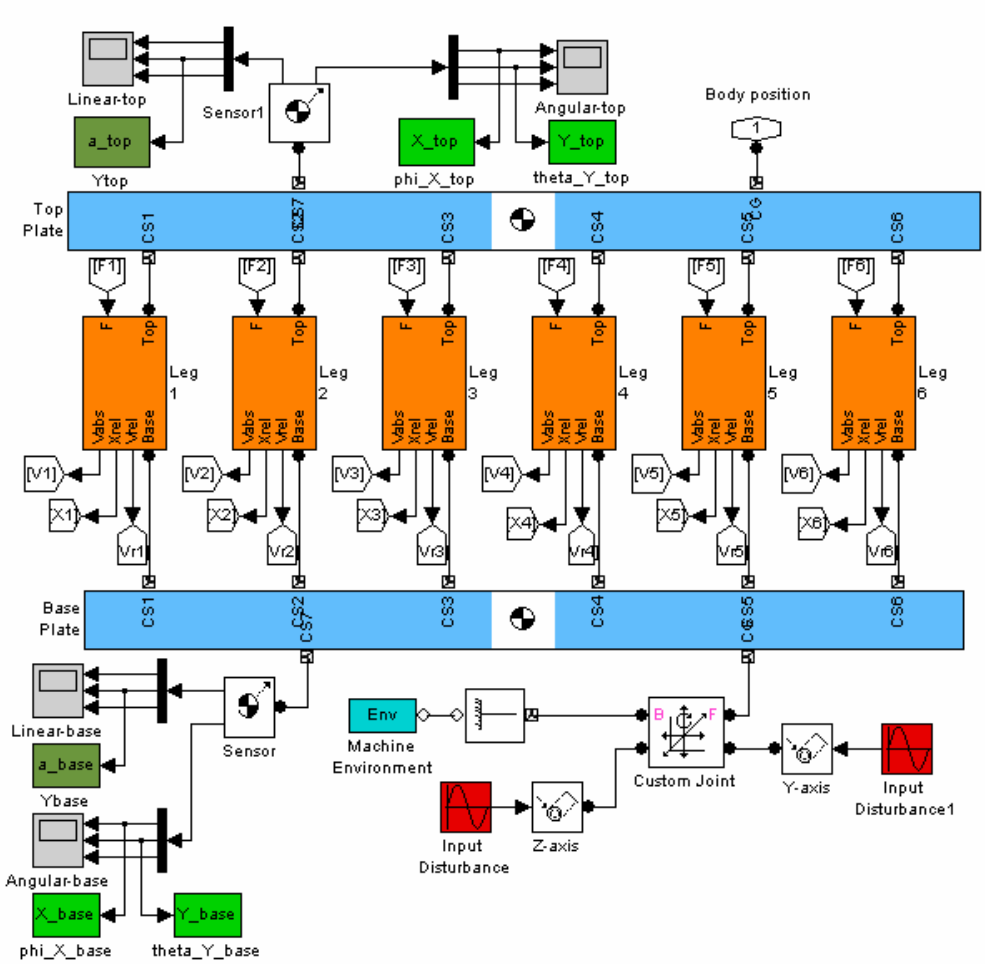

Figure 6-23. SimMechanics model of the 6 DOF PKM model

The base platform is excited by a sinusoidal input disturbance. This disturbance can either be a force with its direction in the x, y, or z-axis or a torque with its axis of rotation being x, y, or z-axis. The linear and angular accelerations of both the top and the base platforms are measured by sensors and sent to the MATLAB workspace to measure the transmissibility between the two platforms.

6.3.1 6 DOF Parallel Platform Model with the Basic Connector Leg

The SimMechanics model of the basic connector is shown in Figure 6-24. The top and the bottom masses are connected together by a prismatic joint through which the spring and the MR damper forces are applied.

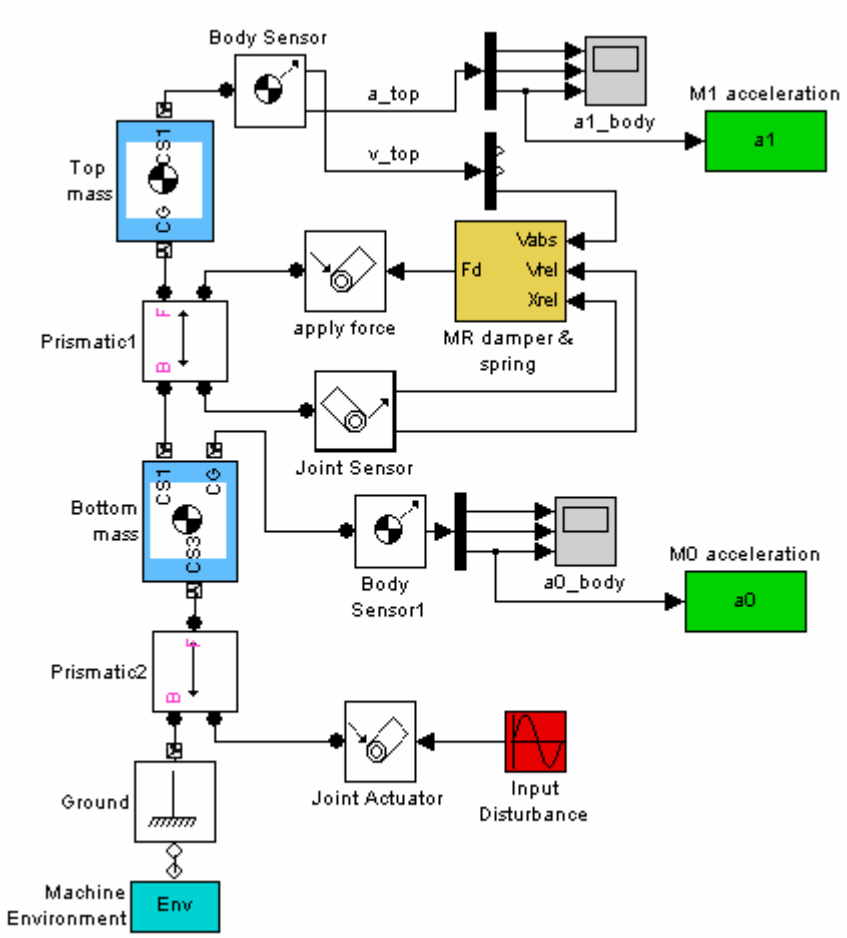

Figure 6-24. SimMechanics model of the basic connector leg

The bottom mass is subjected to a sinusoidal disturbance. The absolute velocity of the top mass besides the relative displacement and the relative velocity between the two masses are measured by sensors and input to the MR damper & spring subsystem where the MR damper and spring forces are calculated. The acceleration of both masses are measured and sent to the MATLAB workspace where the transmissibility between the two is calculated. This model is incorporated into each of leg subsystems of the parallel platform model shown in Figure 6-23. The schematic of the basic connector model is shown in Figure 6-25. The 6 DOF parallel platform mechanism with the basic connector legs is shown in Figure 6-26 as it is simulated using MATLAB graphics.

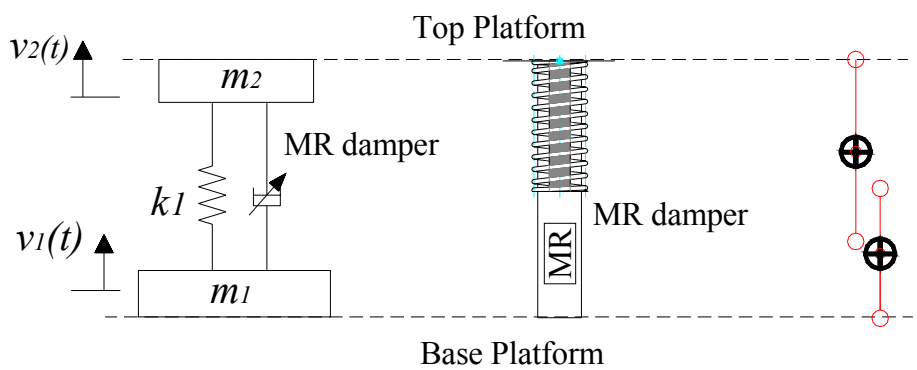

Figure 6-25. Basic connector leg model

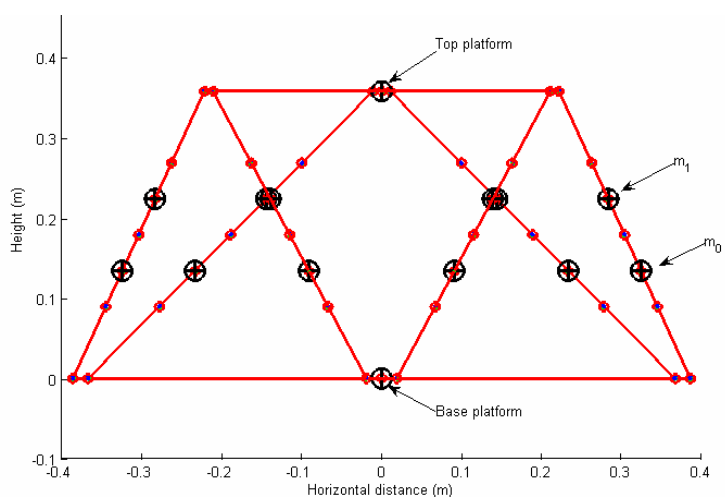

Figure 6-26. 6 DOF parallel platform mechanism with basic connector leg model

6.3.2 6 DOF Parallel Platform Model with the Two-Stage Connector Leg

The SimMechanics model of the two-stage connector leg model is shown in Figure 6-27. The bottom mass is subjected to a sinusoidal disturbance. The bottom mass and the intermediate mass are connected by a prismatic joint through which the passive spring and damper forces are applied using the SimMechanics Joint Spring & Damper block.

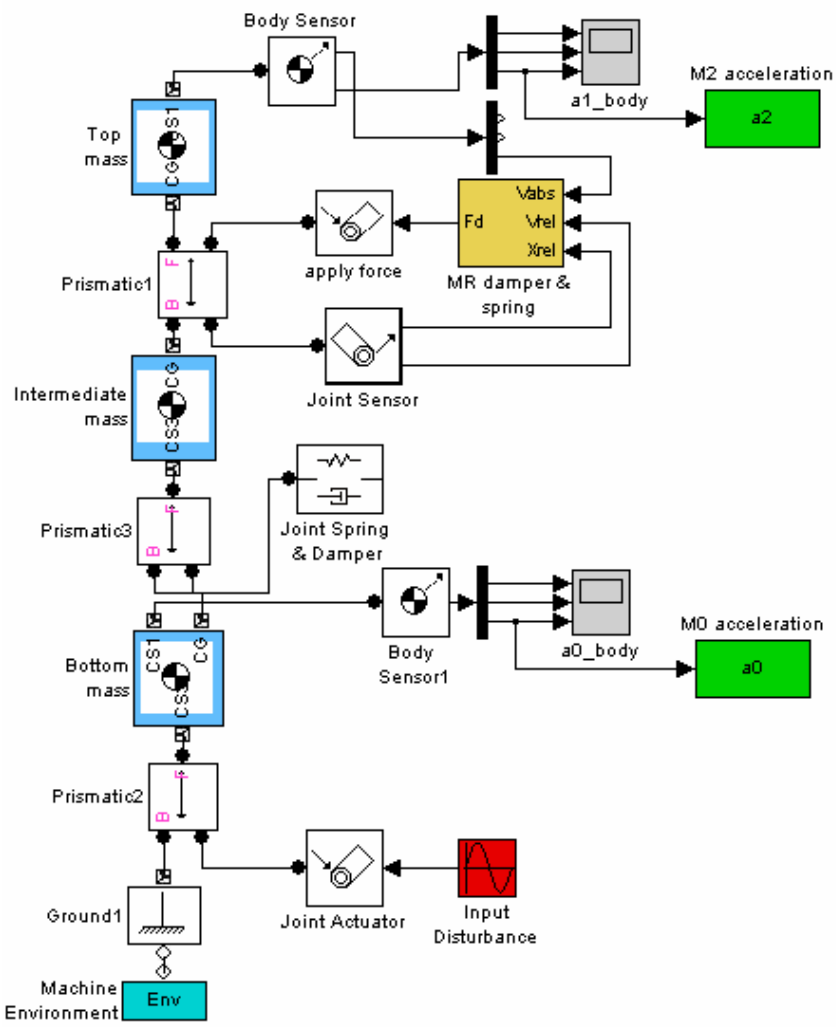

Figure 6-27. SimMechanics model of the two-stage connector leg

The intermediate mass and the top mass are similarly connected by a prismatic joint through which the MR damper and the spring forces are applied. The displacement, velocity and acceleration of the bodies are measured by sensors. The absolute

acceleration of the top mass and the bottom mass are also measured and sent to the workspace where the transmissibility between the two is calculated. This model is incorporated into each of leg subsystems of the parallel platform model shown in Figure 6-23. The schematic of the two-stage connector model is shown in Figure 6-28. The 6 DOF parallel platform mechanism with the two-stage connector legs is shown in Figure 6-29 as it is simulated using MATLAB graphics.

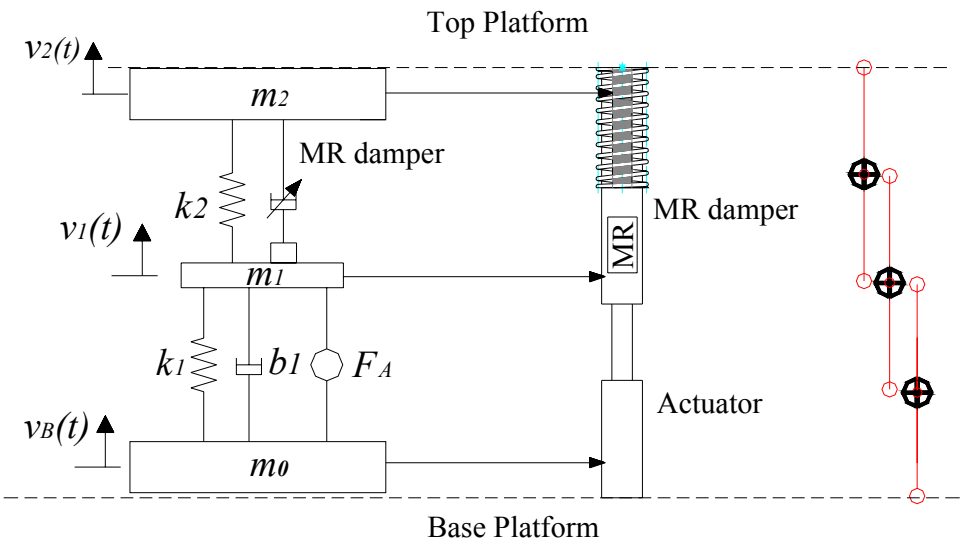

Figure 6-28. Two-stage connector leg model

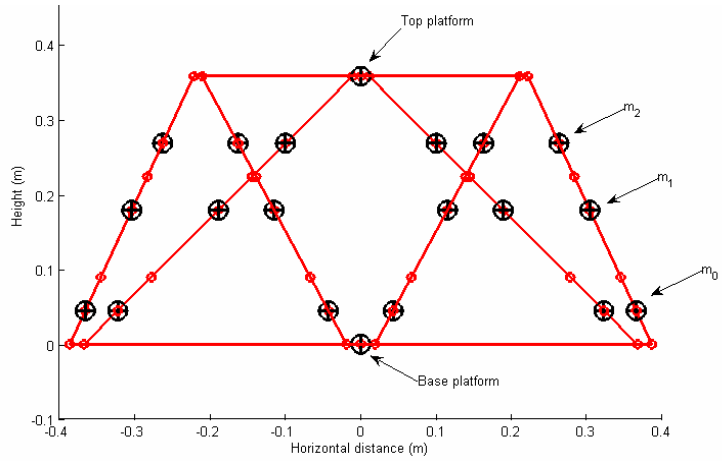

Figure 6-29. 6 DOF parallel platform mechanism with the two-stage connector leg models

CHAPTER 7
SIMULATION RESULTS

In this chapter, the vibration isolation performance of the models presented in the previous chapter is quantified through simulations. For verification purposes, each model is modeled both in Simulink and in SimMechanics and the results for both are compared. First, the results for the passive, active, and the semi-active basic connector leg models are presented followed by the results of the 6 DOF parallel platform mechanism based on the basic connector leg model. Secondly, the results for the passive, active, and the semi-active two-stage connector leg models are given followed by results of the 6 DOF parallel platform mechanism based on the two-stage connector leg model. Next, acceleration transmissibilities in multiple degrees-of-freedom are given for the semi-active platform with the two-stage connector leg while it is being exposed to linear or angular disturbances. Finally, positioning capability of the semi-active parallel platform with the two-stage connector legs is examined under various disturbances.

The simulations are conducted in MATLAB® using the Simulink® dynamic simulation environment. SimMechanics works under Simulink and is a block diagram modeling environment where rigid bodies and their motions can be designed and simulated using the standard Newtonian dynamics of forces and torques. Unlike Simulink blocks which operate on signals or which represent mathematical operations, the blocks in SimMechanics represent physical components and relationships directly. 3D visualization of rigid bodies is realized using MATLAB Graphics systems (The Mathworks, Inc., 2006).

While both Simulink and SimMechanics models are used for the connector leg simulations, for the more complex 6 DOF simulations, only SimMechanics is used. MATLAB code is used to calculate the acceleration transmissibility for each model. Acceleration transmissibility between the clean and the noisy side is used to compare the performance of each model and each control strategy instead of displacement transmissibility because there is too much noise in the latter due to small displacements at higher frequencies. Figure 7-1 shows the displacement transmissibility of the active 6 DOF platform and the displacement and acceleration transmissibilities of the semi-active two DOF connector legs for comparison of the noise in the data.

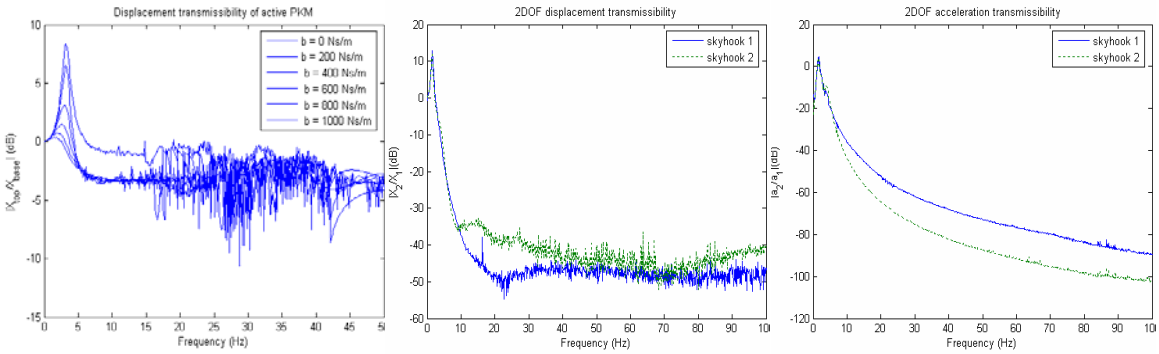

a) b) c)

Figure 7-1. Representative plots for comparison of displacement and acceleration transmissibility noise showing a) displacement transmissibility of active 6 DOF platform b) displacement transmissibility of semi-active 2 DOF connector leg and c) acceleration transmissibility of the same semi-active 2 DOF connector leg

7.1 Basic Connector Leg Simulation Results

The basic connector leg modeled in the previous chapter is simulated in this section using passive, active, and semi-active control and the acceleration transmissibility is calculated between the top and the bottom mass for each. Next, the 6 DOF parallel platform mechanism with the basic connector legs is simulated and the acceleration

transmissibility between the top and the base platforms is found for passive, active, and semi-active control.

7.1.1 Passive Basic Connector Leg

This model has a viscous damper between the two masses. The bottom mass is excited by a sinusoidal disturbance in the z-axis with a frequency from 0.1 to 50 Hz. For each 0.1 Hz frequency increment, the root-mean-square (RMS) value of the acceleration transmissibility between the top and the bottom mass is calculated. For verification purposes, both the Simulink model and the SimMechanics model shown in Figure 7-2 are used in the simulations.

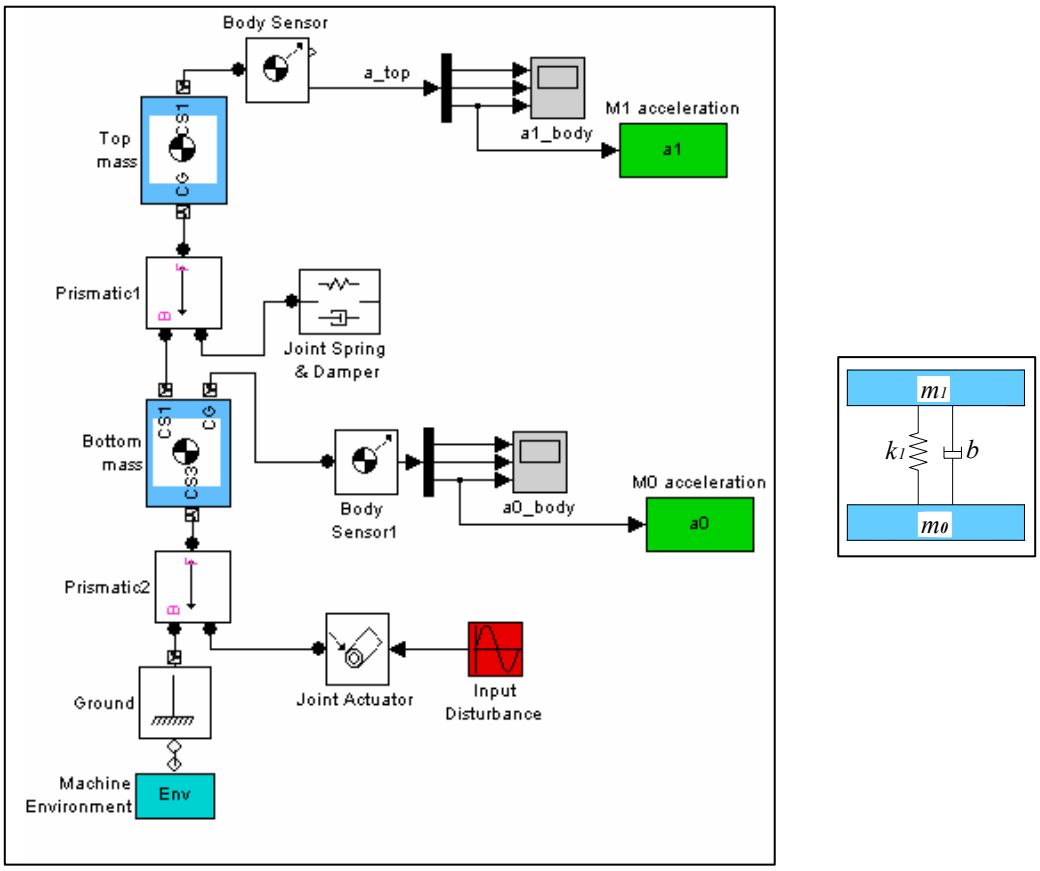

Figure 7-2. SimMechanics model of the passive basic connector leg model

The bottom mass is 38 kg, the top mass is 16 kg, and the stiffness of the spring, k_1 is 5,000 N/m. The results for the Simulink and SimMechanics models are shown in Figure 7-3 a) and b), respectively for varying damping coefficients.

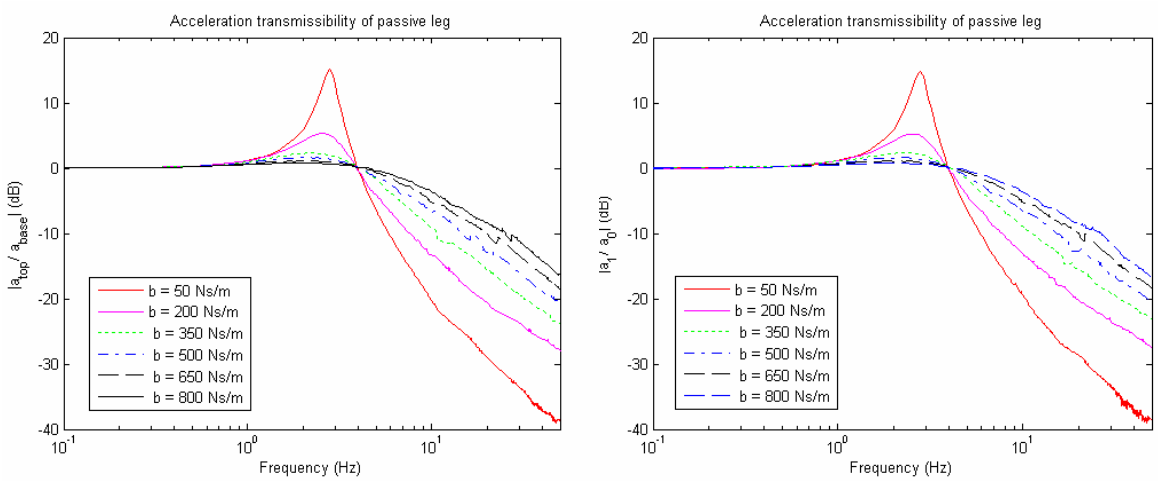

a) b)

Figure 7-3. Acceleration transmissibility between the top and bottom masses of the passive basic connector leg modeled in a) Simulink and b) SimMechanics

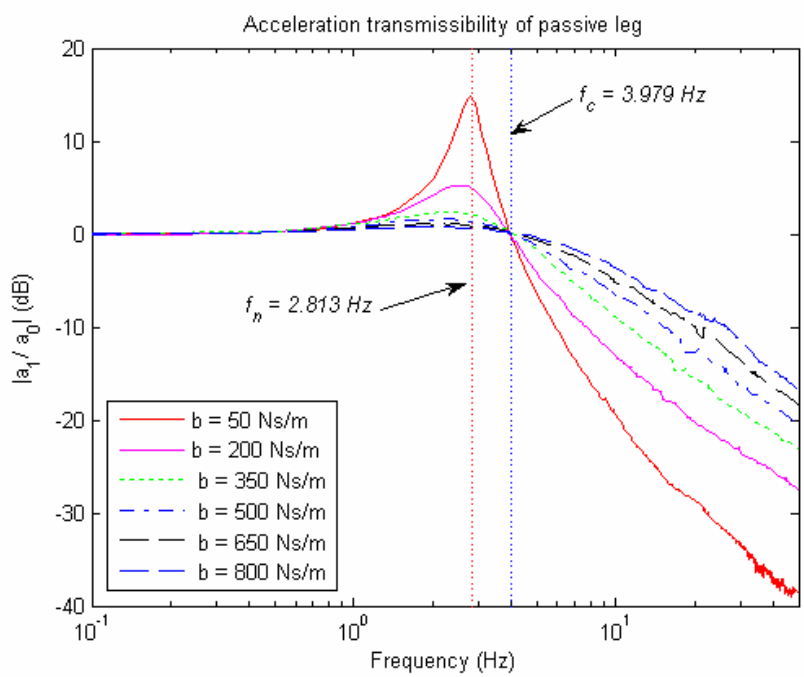

Figure 7-4. Natural frequency and corner frequency of the basic connector leg shown on the acceleration transmissibility plot of the passive leg

The natural frequency of the single DOF system is

$$\begin{aligned} \omega_n &= \sqrt{k_1/m_1} = \sqrt{5000/16} = 17.678 \ \text{ rad/s} \\ f_n &= \omega_n / 2\pi = 2.813 \text{ Hz} \end{aligned} \tag{7-1}$$

and the corner frequency is $f_c = \sqrt{2} \cdot f_n = 3.979$ Hz as can also be seen in Figure 7-4.

7.1.2 Active Basic Connector Leg

This model incorporates an active force actuator between the two masses. The bottom mass is excited by a sinusoidal disturbance in the z-axis with a frequency from 0.1 to 50 Hz. For each 0.1 Hz frequency increment, RMS value of the acceleration transmissibility between the top and the bottom mass is calculated. For verification purposes, both the Simulink model and the SimMechanics model shown in Figure 7-5 are used in the simulations.

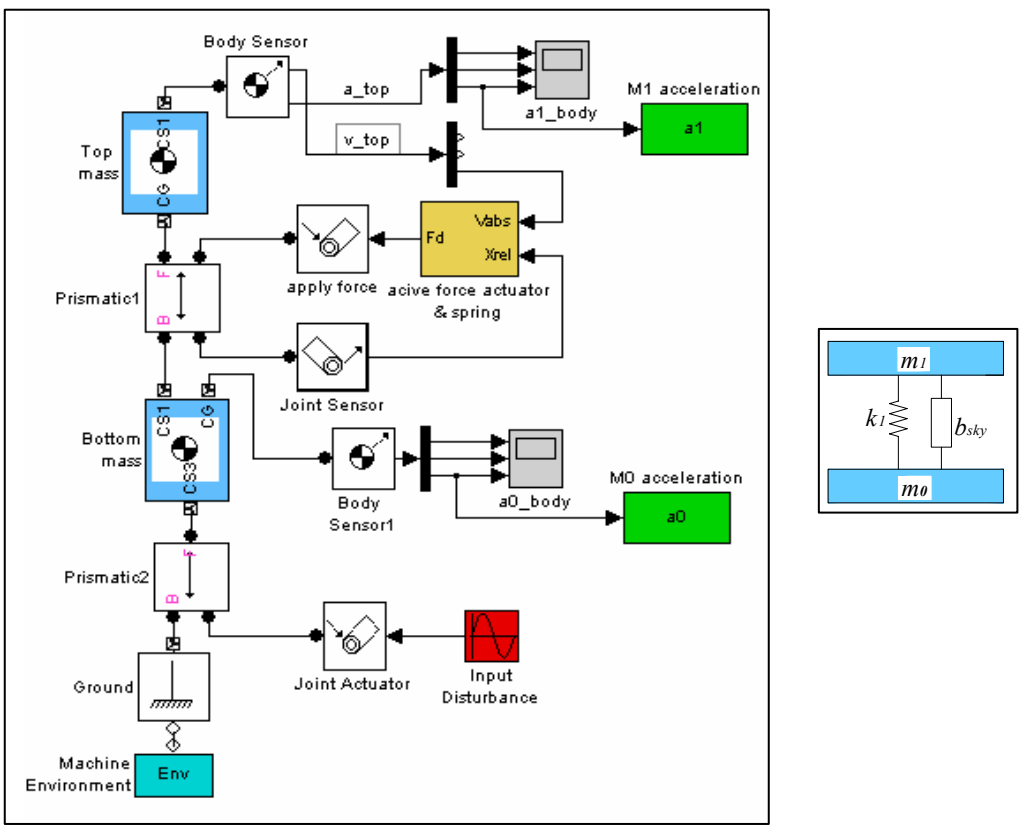

Figure 7-5. SimMechanics model of the active basic connector leg model

The bottom mass is 38 kg, the top mass is 16 kg, and the stiffness of the spring, k_1 is 5,000 N/m. The results for the Simulink and SimMechanics models are shown in Figure 7-6 a) and b), respectively for varying actuator gains.

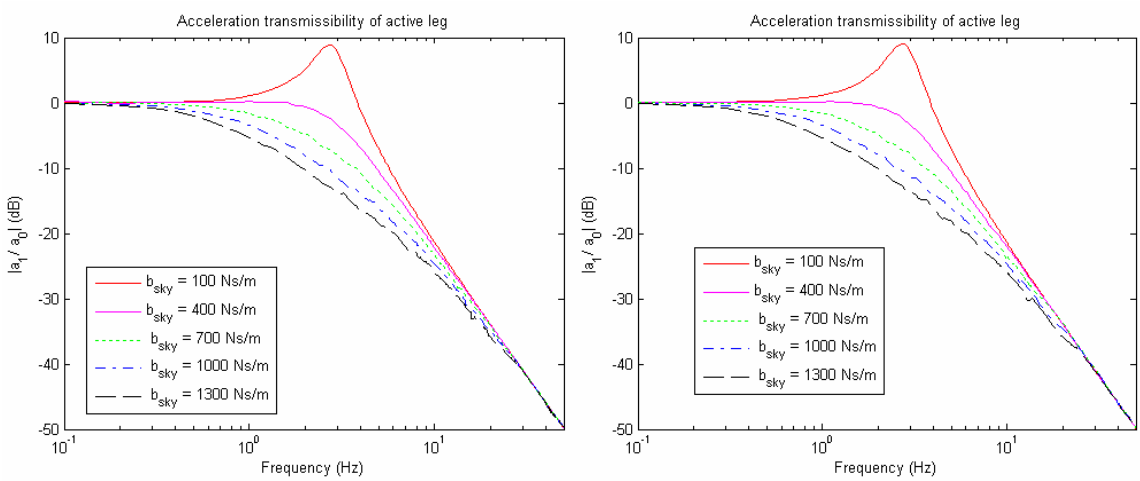

a) b)

Figure 7-6. Acceleration transmissibility between the top and bottom masses of the active basic connector leg modeled in a) Simulink and b) SimMechanics

7.1.3 Semi-Active Basic Connector Leg

This model incorporates a semi-active MR damper between the two masses. The bottom mass is excited by a sinusoidal disturbance in the z-axis with a frequency from 0.1 to 50 Hz. For each 0.1 Hz frequency increment, RMS value of the acceleration transmissibility between the top and the bottom mass is calculated. For verification purposes, both the Simulink model and the SimMechanics model shown in Figure 7-7 are used in the simulations. The bottom mass is 38 kg, the top mass is 16 kg, and the stiffness of the spring, k_1 is 5,000 N/m. The results for the Simulink and SimMechanics models are shown in Figure 7-8 a) and b), respectively for varying maximum input currents which essentially vary the upper limit of the damping force applied by the MR damper.

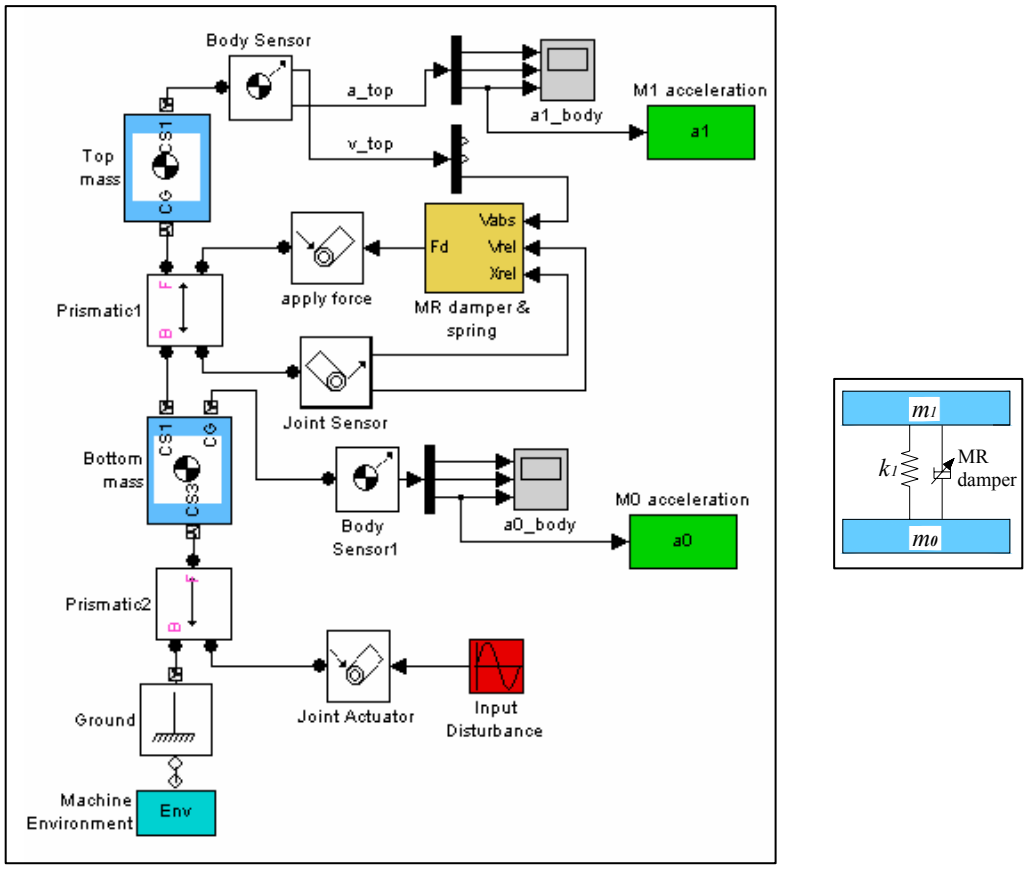

Figure 7-7. SimMechanics model of the semi-active basic connector leg model

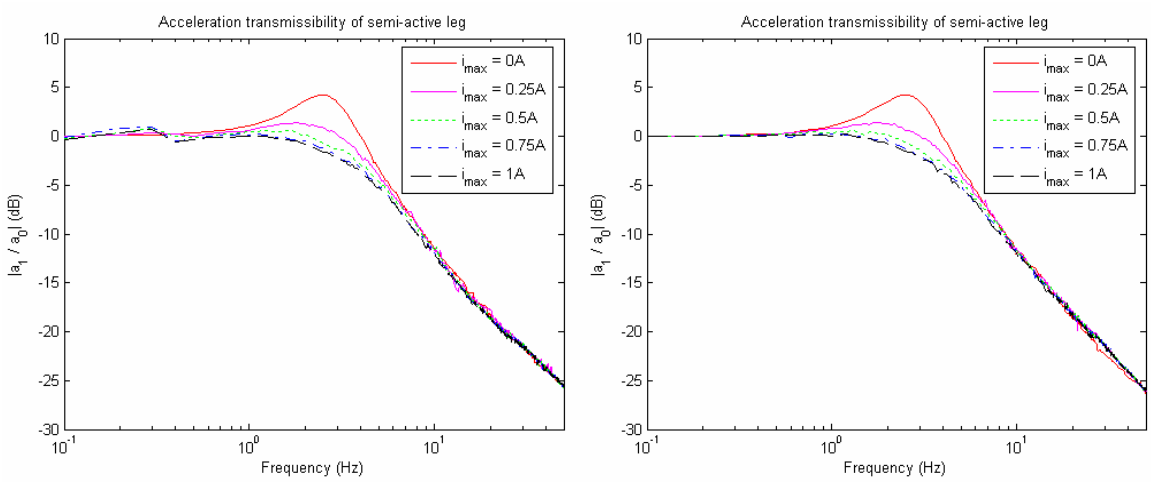

a) b)

Figure 7-8. Acceleration transmissibility between the top and bottom masses of the semi-active basic connector leg modeled in a) Simulink and b) SimMechanics

The performances of the passive, active and semi-active basic connector legs are compared in Figure 7-9. The semi-active connector performs better than the passive

connector with 25 dB reduction at 50 Hz. The active connector has the best performance overall with 50 dB reduction at 50 Hz.

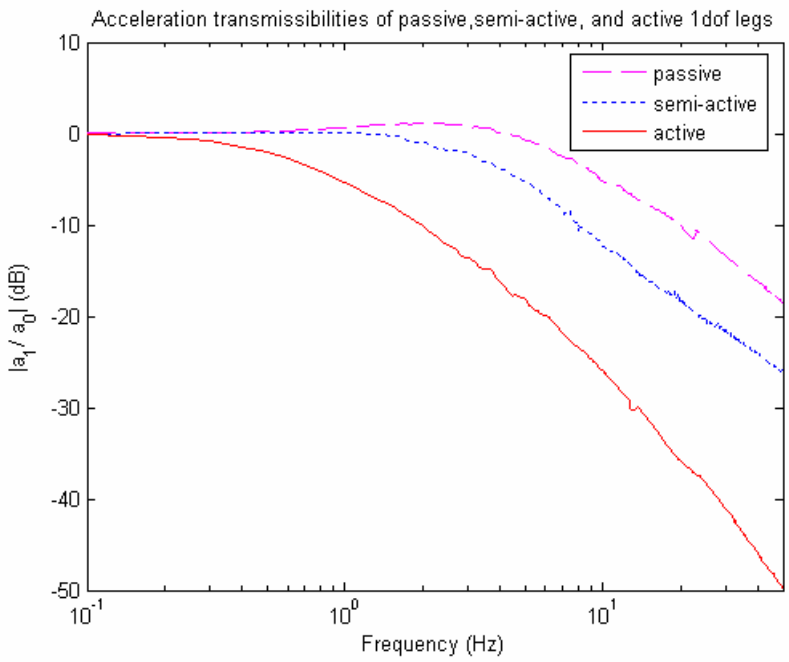

Figure 7-9. Comparison of the acceleration transmissibility between the passive, active, and semi-active basic connector legs

7.1.4 6 DOF Parallel Platform Mechanism with the Basic Connector Leg

After the single DOF simulations, 6 DOF simulations are carried out with the parallel platform mechanism which incorporates the basic connecter leg model in its legs. The platform and its coordinate axes are displayed in Figure 7-10. The bottom platform is excited by a sinusoidal disturbance at its center of mass in the z-axis with a frequency bandwidth from 0.1 to 50 Hz in 0.1 Hz increments. The accelerations of the top and bottom platform centers of gravity in the z-axis are measured and the RMS transmissibility between the two accelerations is calculated for each 0.1 Hz.

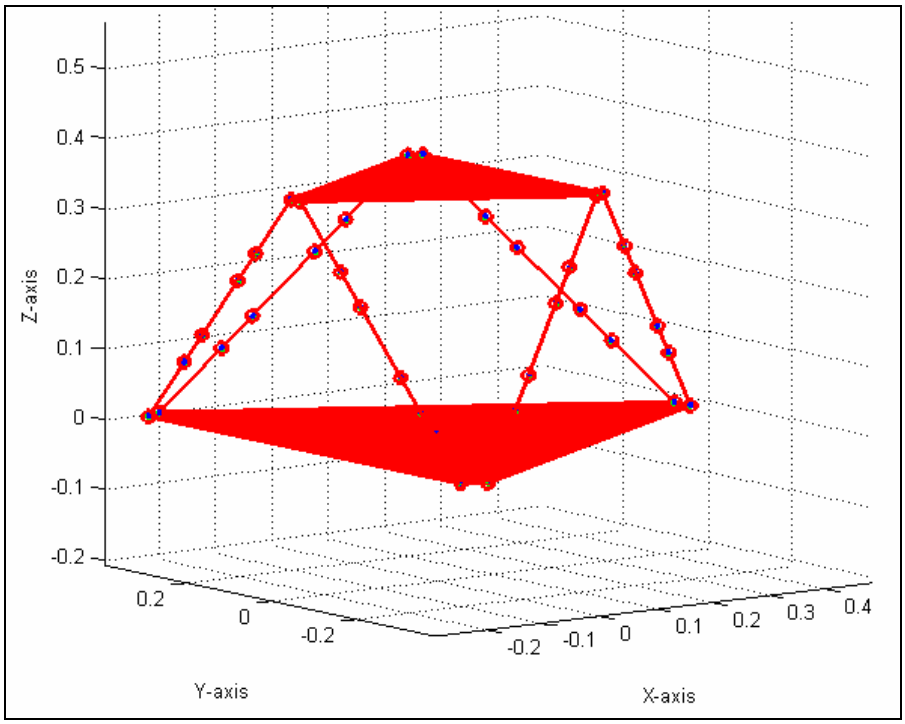

Figure 7-10. Parallel platform mechanism with the basic connector leg

The results for the passive, active, and semi-active parallel platform mechanisms are presented in Figure 7-11, Figure 7-12, and Figure 7-13, respectively.

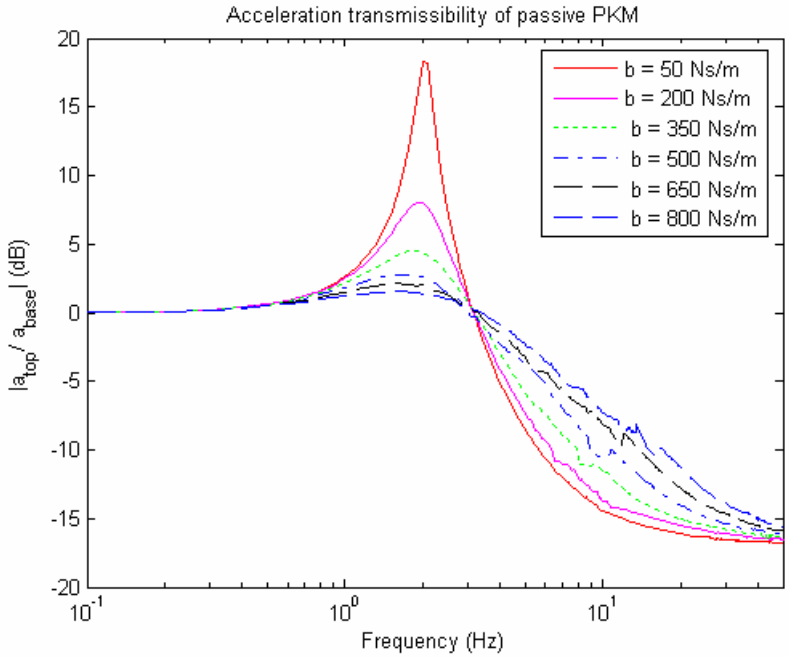

Figure 7-11. Passive – acceleration transmissibility between the top and bottom platforms of 6 DOF PKM with the passive basic connector legs

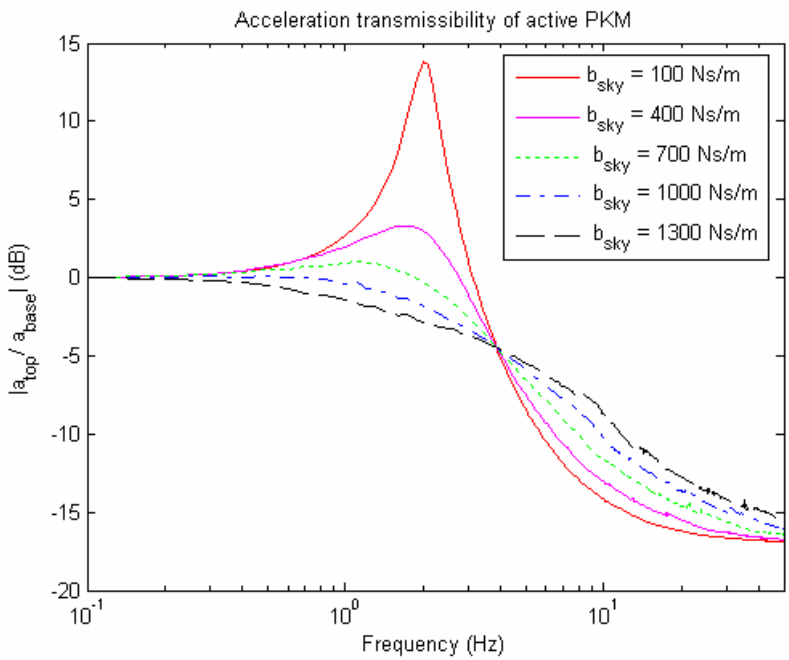

Figure 7-12. Active – acceleration transmissibility between the top and bottom platforms of 6 DOF PKM with the active basic connector legs

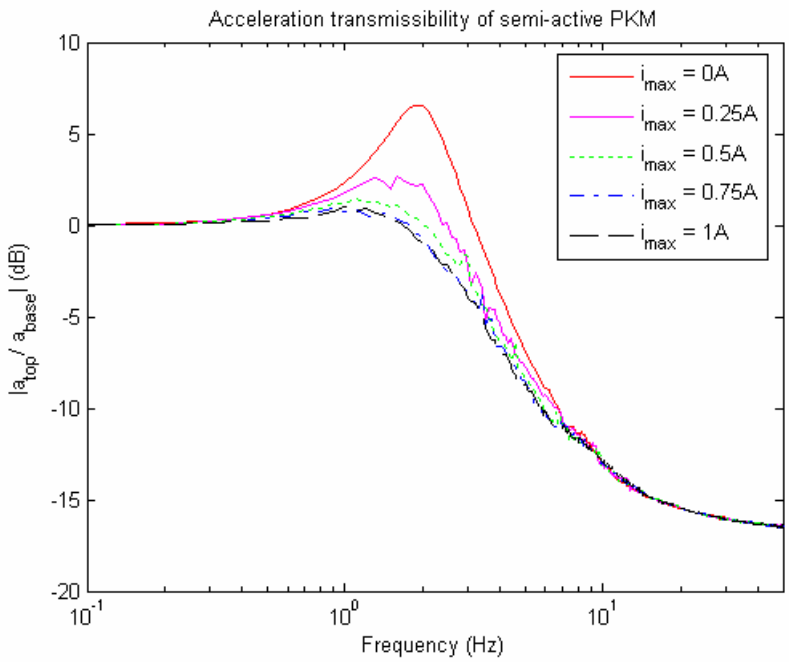

Figure 7-13. Semi-active – acceleration transmissibility between the top and bottom platforms of 6 DOF PKM with the semi-active basic connector legs

7.2 Two-Stage Connector Leg Simulation Results

The two-stage connector leg modeled in the previous chapter is simulated in this section using passive, active, and semi-active control and the acceleration transmissibility is found between the top mass and the bottom mass for each control system. Next, the 6 DOF parallel platform mechanism with the two-stage connector legs is simulated and the acceleration transmissibility between the top and the base platform is found for passive, active, and semi-active control.

7.2.1 Passive Two-Stage Connector Leg

For the passive connector leg, the bottom mass is excited by a sinusoidal disturbance with a frequency from 0.1 to 50 Hz. For each 0.1 Hz frequency increment, the RMS value of the acceleration transmissibility between the top and the bottom mass is calculated. For verification purposes, both the Simulink model and the SimMechanics model (Figure 7-14) are used in the simulations.

The results for the Simulink and SimMechanics models are shown in Figure 7-15 a) and 7.15 b), respectively for varying damping coefficients in the coupling stage.

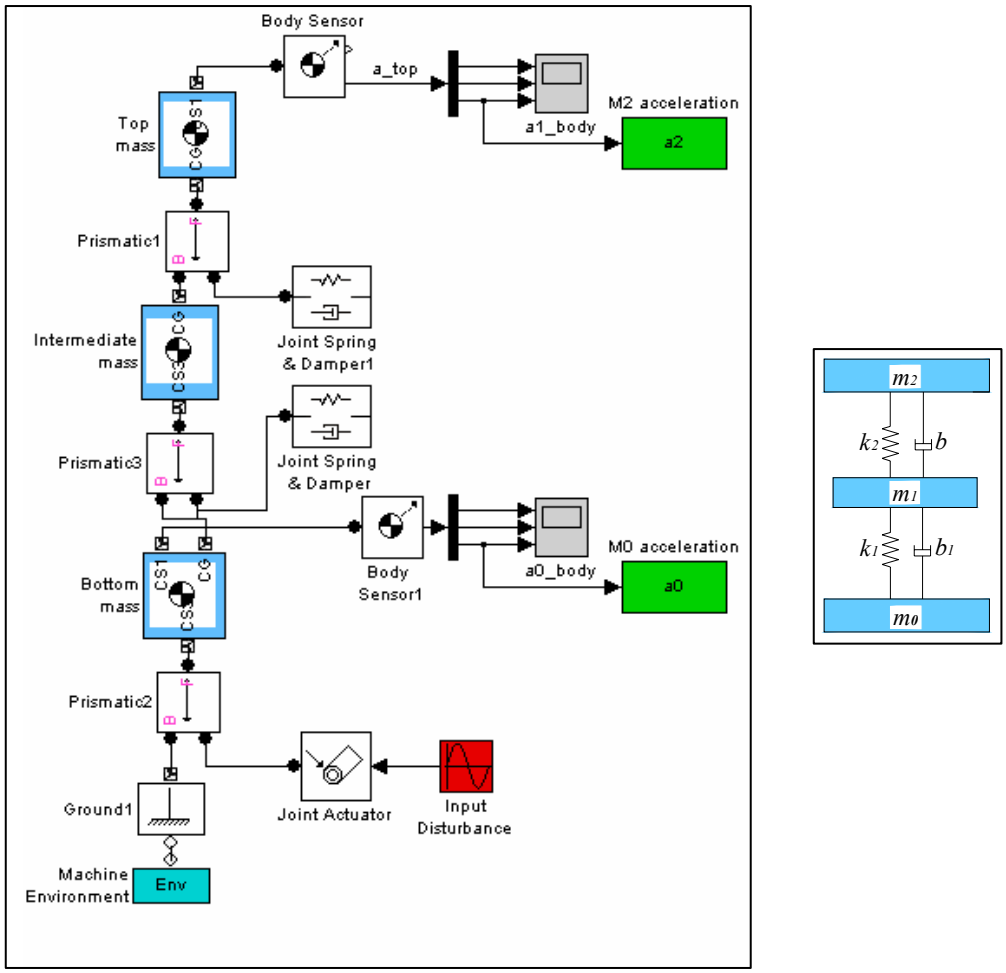

Figure 7-14. SimMechanics model of the passive two-stage connector leg model

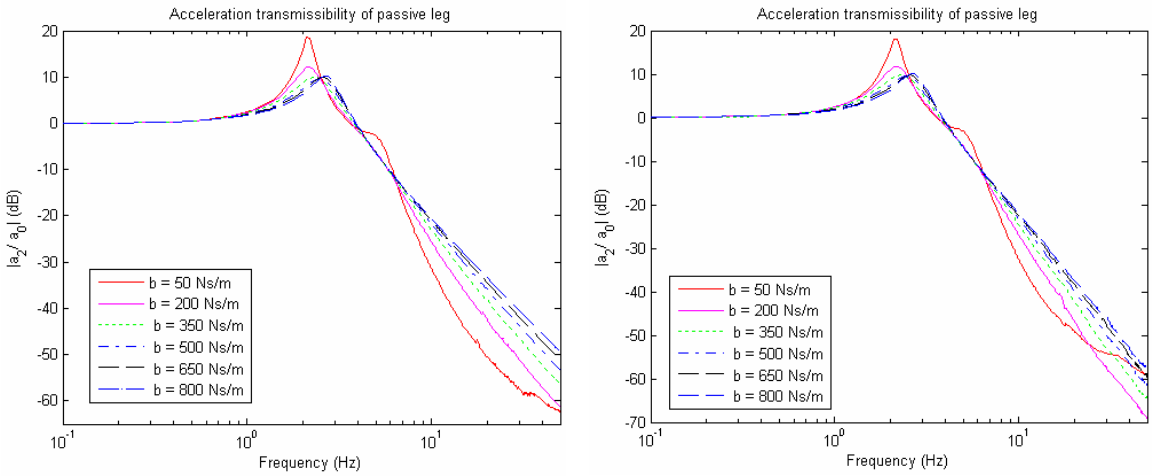

a) b)

Figure 7-15. Acceleration transmissibility between the top and bottom masses of the passive two-stage connector leg modeled in a) Simulink and b) SimMechanics

The natural frequencies of the two DOF system are calculated in Appendix A.4 and the results are

$$\begin{aligned} \omega_{n_1} &= 13.592 \text{ rad/s} & \omega_{n_2} &= 33.582 \text{ rad/s} \\ f_{n_1} &= \omega_{n_1}/2\pi = 2.163 \text{ Hz} & f_{n_2} &= \omega_{n_2}/2\pi = 5.345 \text{ Hz} \end{aligned} \tag{7-2}$$

These frequencies are shown in Figure 7-16 on the acceleration transmissibility plot of the two-stage connector leg with b = 50 Ns/m where low damping allows both peaks to be visible.

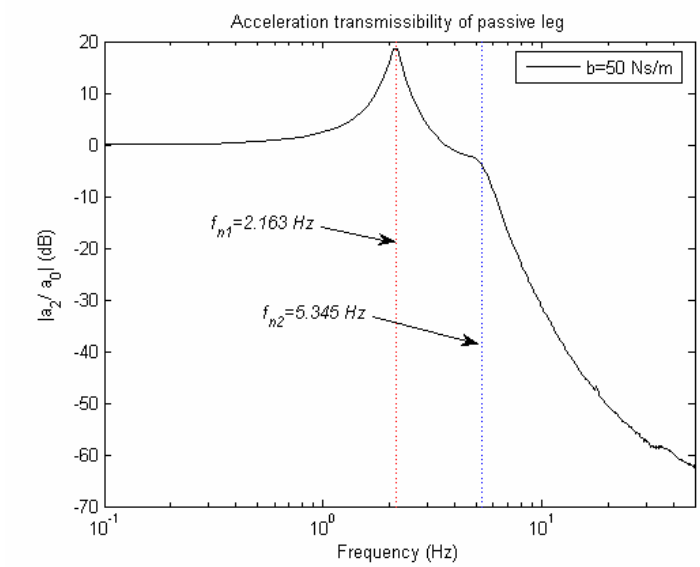

Figure 7-16. Natural frequency and corner frequency of the two-stage connector leg shown on the acceleration transmissibility plot of the passive leg

7.2.2 Active Two-Stage Connector Leg

For the active connector leg, the bottom mass is also excited by a sinusoidal disturbance with a frequency from 0.1 to 50 Hz. For each 0.1 Hz frequency increment, the RMS value of the acceleration transmissibility between the top and the bottom mass is calculated. For verification purposes, both the Simulink model and the SimMechanics model (Figure 7-17) are used in the simulations. The results for the Simulink (Figure 7-18 a)) and SimMechanics (Figure 7-18 b)) models are similar.

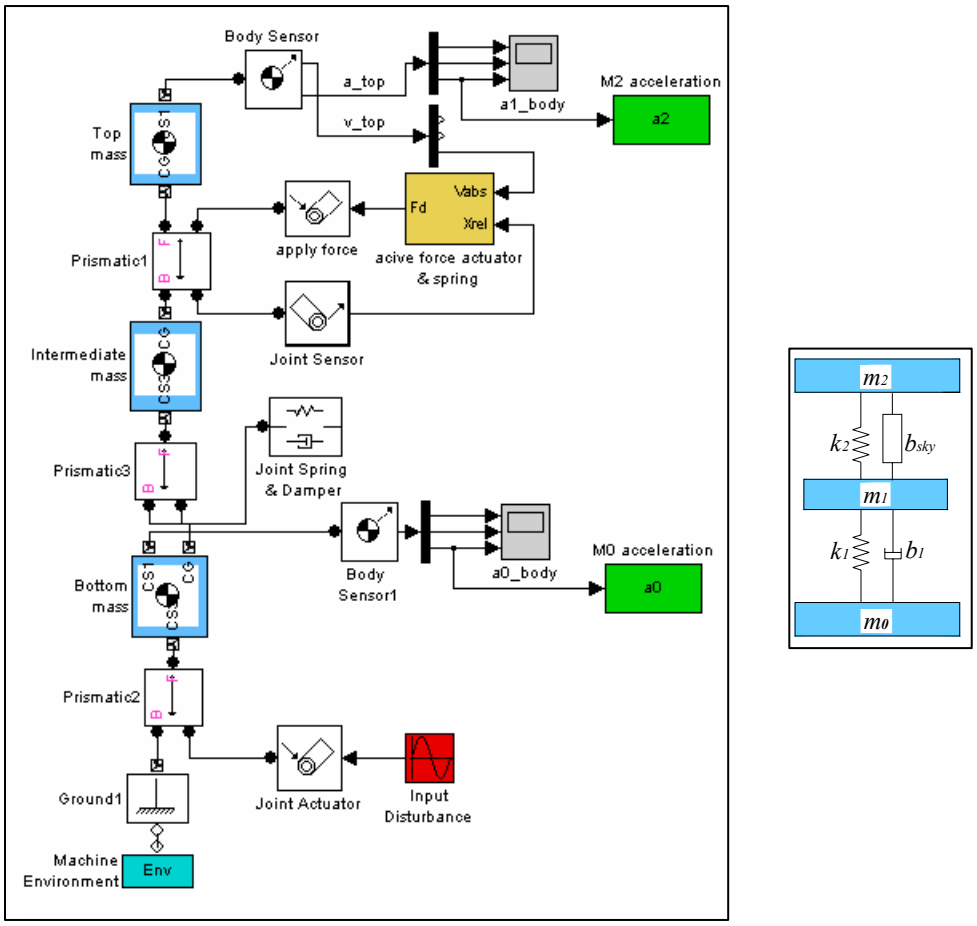

Figure 7-17. SimMechanics model of the active two-stage connector leg model

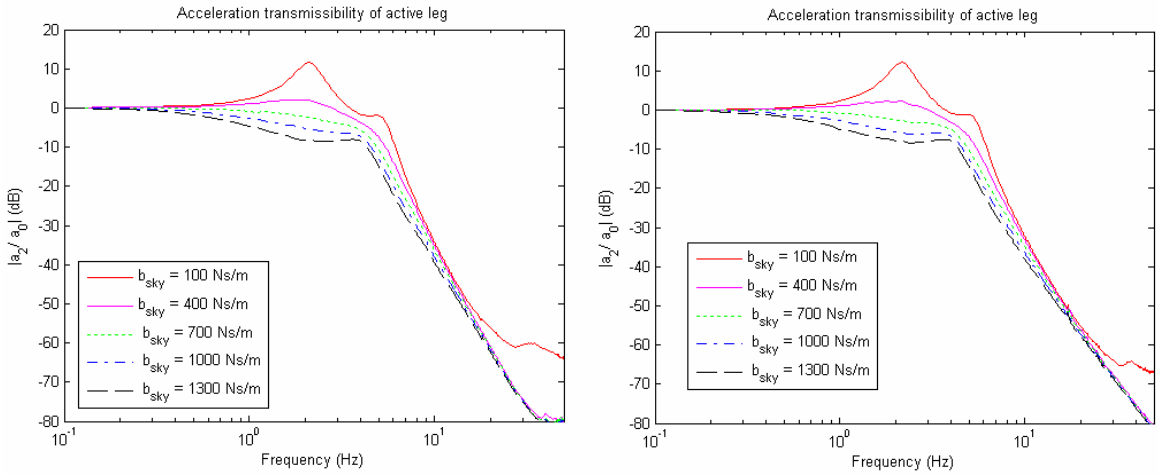

a) b)

Figure 7-18. Acceleration transmissibility between the top and bottom masses of the active two-stage connector leg modeled in a) Simulink and b) SimMechanics

7.2.3 Semi-Active Two-Stage Connector Leg

For the semi-active connector leg, the bottom mass is also excited by a sinusoidal disturbance with a frequency from 0.1 to 50 Hz. For each 0.1 Hz frequency increment, the RMS value of the acceleration transmissibility between the top and the bottom mass is calculated. For verification purposes, both the Simulink model and the SimMechanics model shown in Figure 7-19 are used in the simulations. The results for the Simulink and SimMechanics models are shown in Figure 7-20 a) and b), respectively for varying maximum input currents applied to the MR damper.

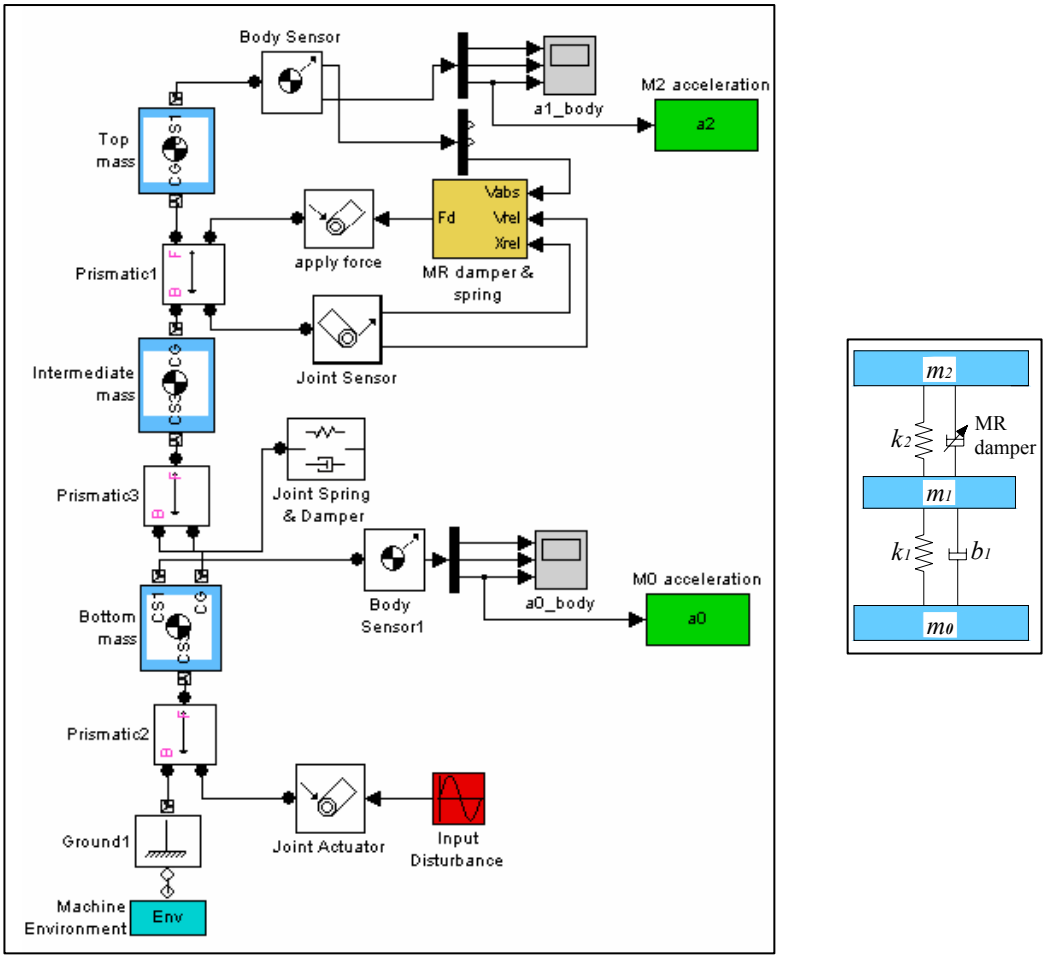

Figure 7-19. SimMechanics model of the semi-active two-stage connector leg model

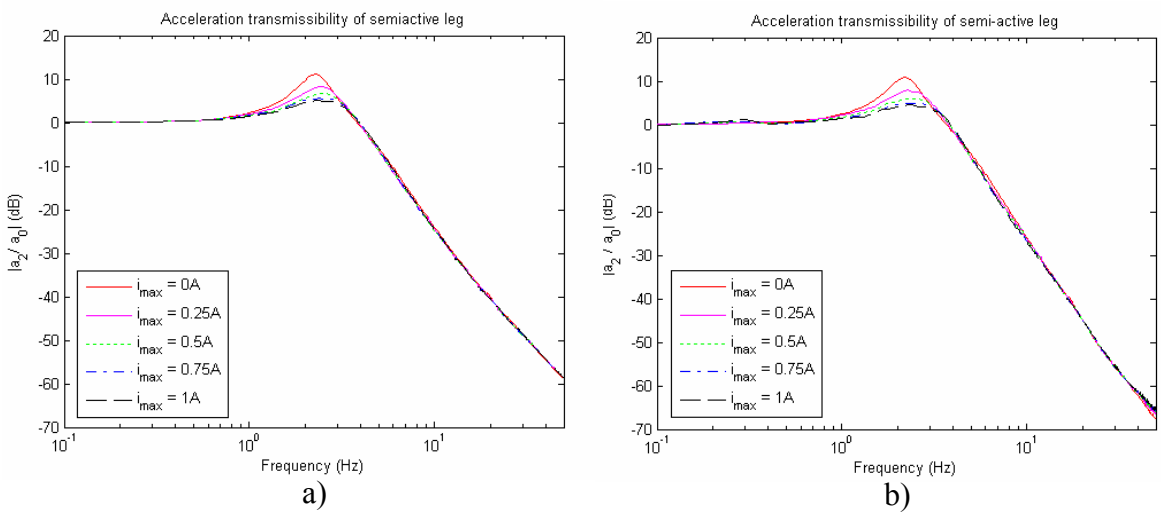

Figure 7-20. Acceleration transmissibility between the top and bottom masses of the semi-active two-stage connector leg modeled in a) Simulink and b) SimMechanics

The results for the passive, active and semi-active basic connecter legs are compared in Figure 7-21. The semi-active connector performs better than the passive connector both at low frequencies by reducing the resonant peak and at high frequencies. The active connector has the best performance overall.

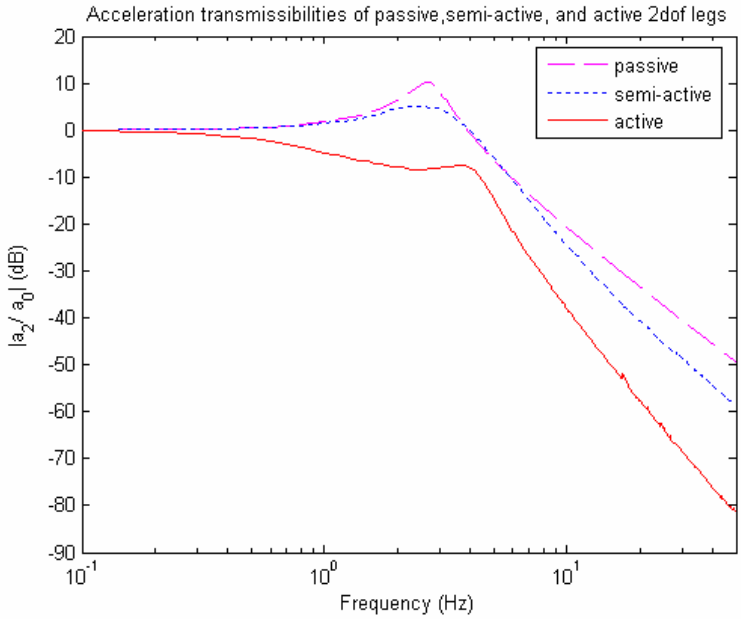

Figure 7-21. Comparison of the acceleration transmissibility between the passive, active, and semi-active two-stage connector legs

7.2.4 6 DOF Parallel Platform Mechanism with the Two-stage Connector Leg

After the single DOF simulations, 6 DOF simulations are carried out with the parallel platform mechanism which incorporates the two-stage connecter leg model in its legs. The platform and its coordinate axes are shown in Figure 7-22.

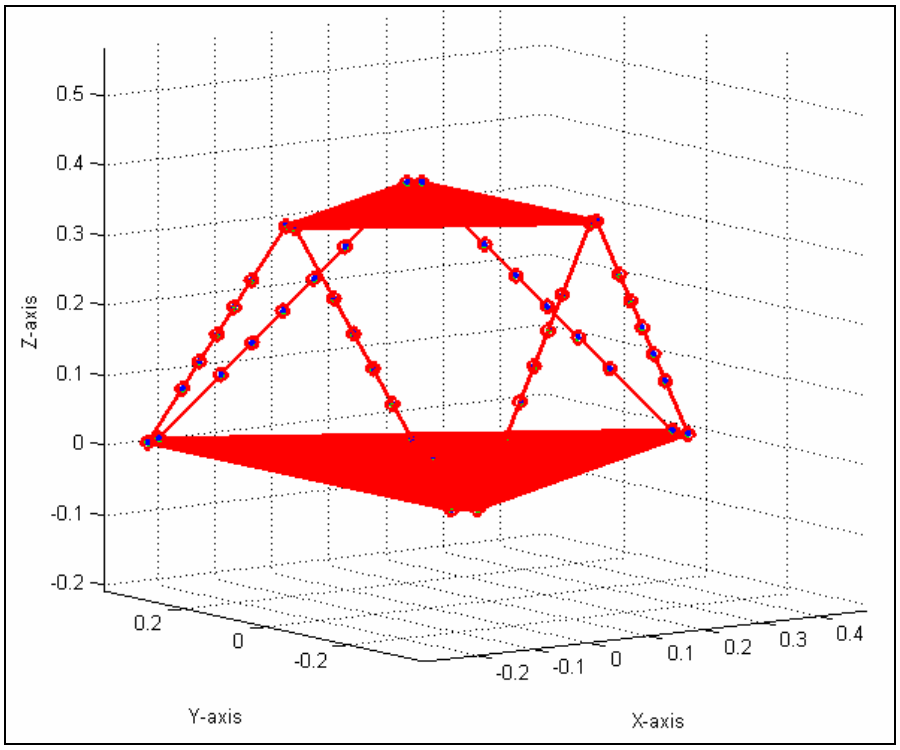

Figure 7-22. Parallel platform with the two-stage connector leg

The bottom platform is excited by a sinusoidal disturbance at its center of mass in the z-axis with a frequency bandwidth from 0.1 to 50 Hz in 0.1 Hz increments. The accelerations of the top and bottom platform centers of gravity in the z-axis are measured and the RMS transmissibility between the two accelerations is calculated for each 0.1 Hz.

The results for the passive, active, and semi-active parallel platform mechanisms are presented in Figures 7.23, 7.24, and 7.25, respectively.

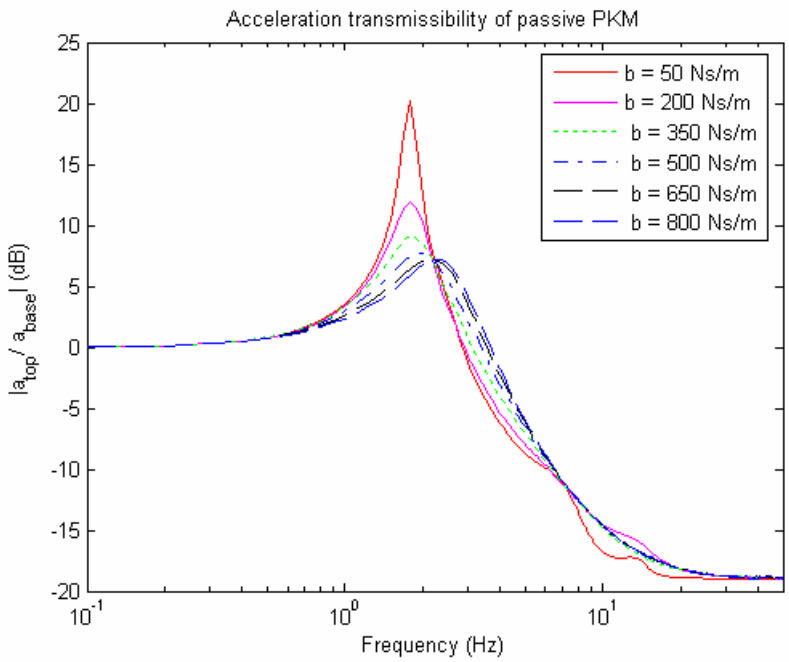

Figure 7-23. Passive – acceleration transmissibility between the top and bottom platforms of 6 DOF PKM with the passive two-stage connector legs

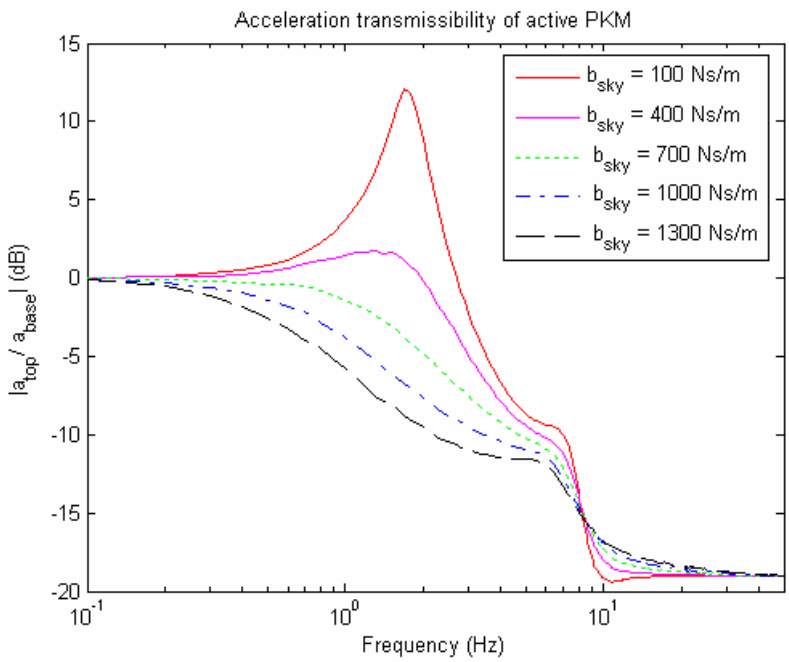

Figure 7-24. Active – acceleration transmissibility between the top and bottom platforms of 6 DOF PKM with the active two-stage connector legs

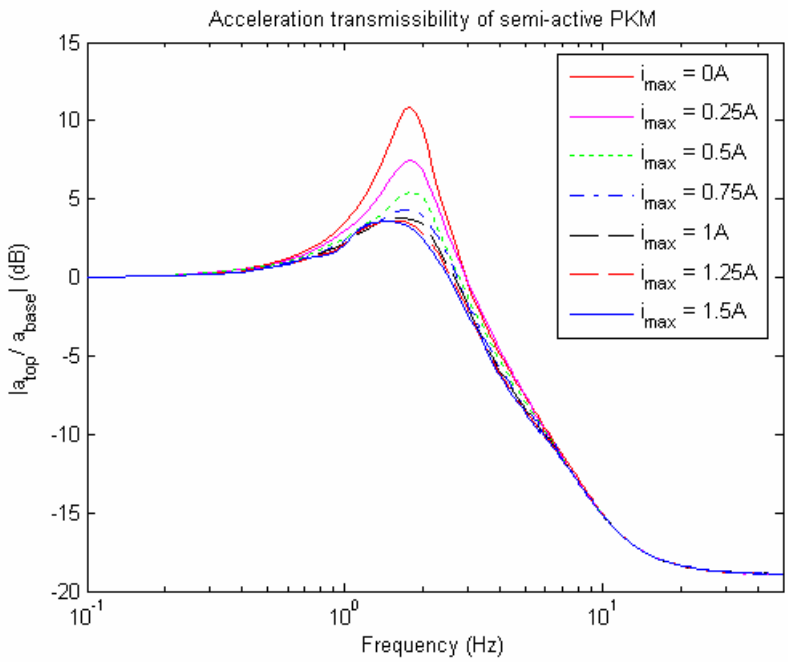

Figure 7-25. Semi-active – acceleration transmissibility between the top and bottom platforms of 6 DOF PKM with the semi-active two-stage connector legs

The performances of the passive, active and semi-active parallel platform mechanisms are compared in Figure 7-26. The performances of all three systems are comparable at high frequencies while semi-active system offers more reduction at lower frequencies compared to the passive system. Even though the active system performs better than the semi-active system at lower frequencies, it comes with a trade-off. The MR dampers are relatively inexpensive compared to the active force actuators and they behave essentially as passive dampers in case of a power outage. They are also globally stable since they can only dissipate energy, but cannot inject energy into the system. The power requirements of an MR damper are also much lower than that of an active force actuator. A commercial MR damper from Lord Corporation is the RD-1005-3 which works with 12 VDC and its maximum input current is 2A. Therefore, the maximum power it requires is 24 W. A typical force actuator used in active 6 DOF parallel

platforms is a linear voice-coil actuator. A linear voice-coil actuator suitable for the dimensions and the mass of the parallel platform mechanism used within this work is the LA25-42-000A model from BEI Technologies. Its power requirement at peak force is 375 W. This is more than 15 times than the power requirement of the MR damper at its peak force. Considering that a parallel platform mechanism requires six actuators or dampers, the power requirement of the active system is $6 \times (375 - 24) \approx 2100$ W more than that of the semi-active system.

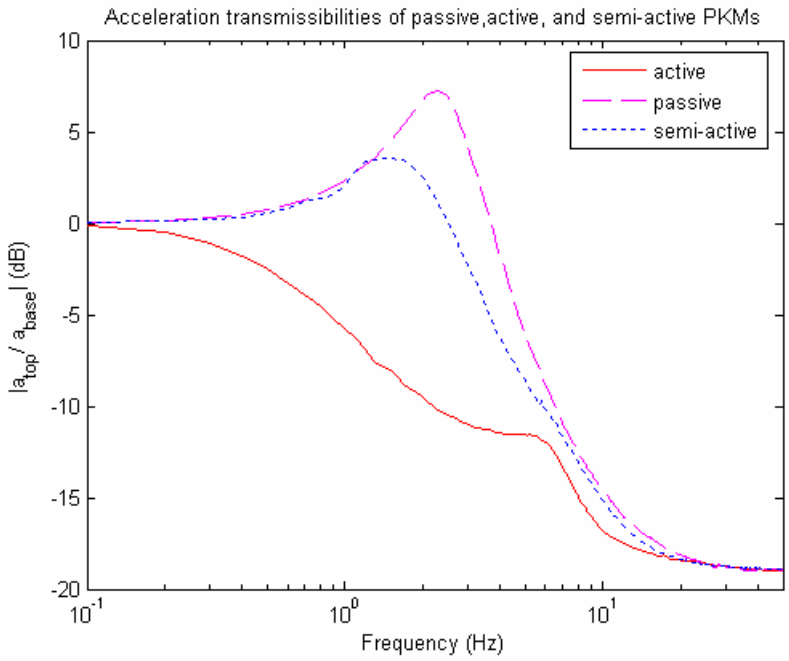

Figure 7-26. Comparison of the acceleration transmissibility between the top and bottom platforms of the passive, active, and semi-active two-stage connector legs

7.3 6 DOF Vibration Isolation of the Semi-active PKM

The previous simulations had the parallel platform mechanisms subjected to a sinusoidal disturbance in the z-axis. In this section, disturbances in other directions will be applied to the bottom platform of the semi-active two-stage parallel platform mechanism and the transmissibility between the top and bottom platforms will be

calculated in the relevant degrees-of-freedom. These disturbances include sinusoidal force inputs in the x- and y-axes along with torques around all three axes. In this chapter, only results which show considerable vibrations in the relevant degrees-of-freedom due to the input disturbance are shown. Additional results are given in Appendix D.

7.3.1 Linear Disturbance in the X-axis

For the previous simulations, the linear sinusoidal disturbance was in the z-axis. Now the performance of the semi-active parallel platform mechanism will be quantified when the disturbance is in the x- and y-axes.

The acceleration transmissibility in the x-axis between the top and bottom platforms is shown in Figure 7-27 for a sinusoidal input force to the bottom platform in the x-axis. It is seen that there is only a slight decrease in the transmissibility in the x-axis when the MR damper input current is increased.

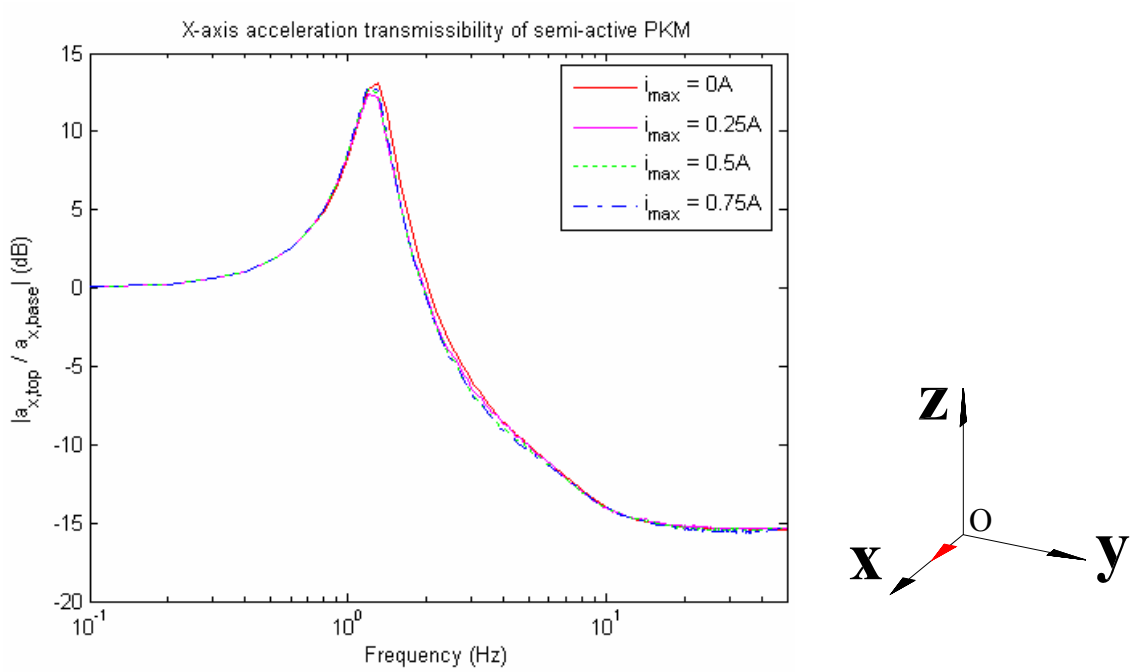

Figure 7-27. X-axis RMS acceleration transmissibility between the top and bottom platforms for an input sinusoidal force in the x-axis

7.3.2 Linear Disturbance in the Y-axis

The acceleration transmissibility in the y-axis between the top and bottom platforms is shown in Figure 7-28 for a sinusoidal input force to the bottom platform in the y-axis. Figure 7-28 is very similar to Figure 7-27 due to the symmetrical character of the parallel platform about the x- and y-axes. It is seen that there is only a slight decrease in the transmissibility in the y-axis when the MR damper input current is increased.

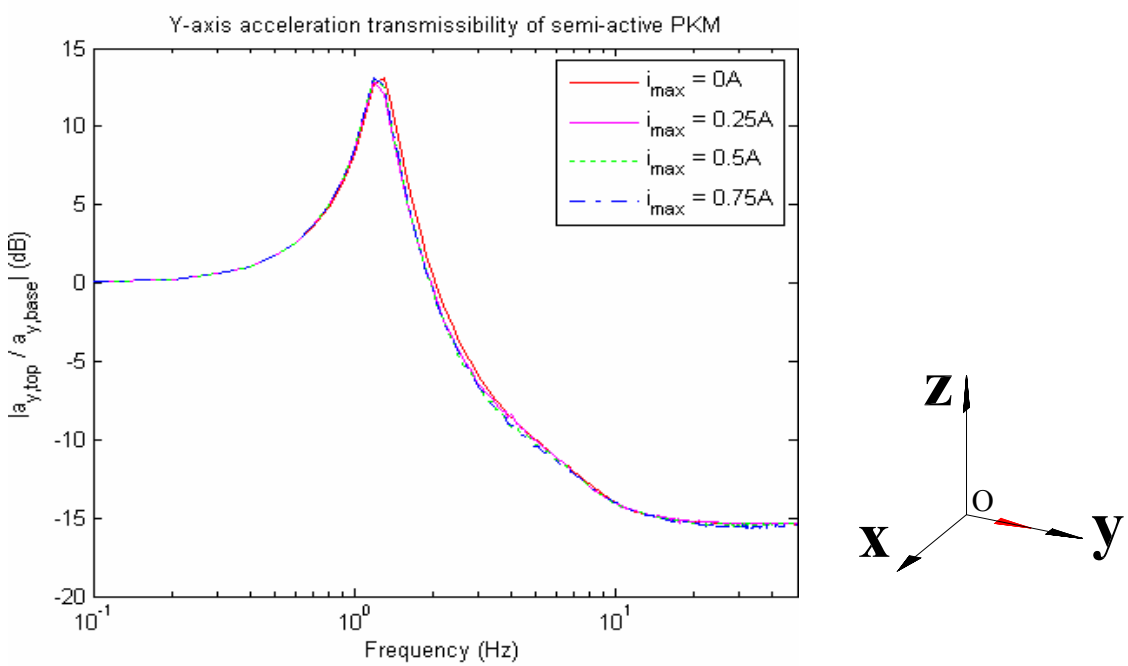

Figure 7-28. Y-axis RMS acceleration transmissibility between the top and bottom platforms for an input sinusoidal force in the y-axis

7.3.3 Angular Disturbance around the Z-axis

Aside from linear disturbances in all three axes, sinusoidal angular disturbances at the center of mass of the bottom platform are applied around all three axes and the transmissibility between the top and the bottom platforms is calculated in all relevant degrees-of-freedom.

The angular acceleration transmissibility around the z-axis between the top and the bottom platforms is shown in Figure 7-29 for a sinusoidal input torque to the bottom

platform around the z-axis. It is seen that a slight increase in the MR damper input current lowers the resonant peak, but increasing the current further does not have any significant decrease in the transmissibility.

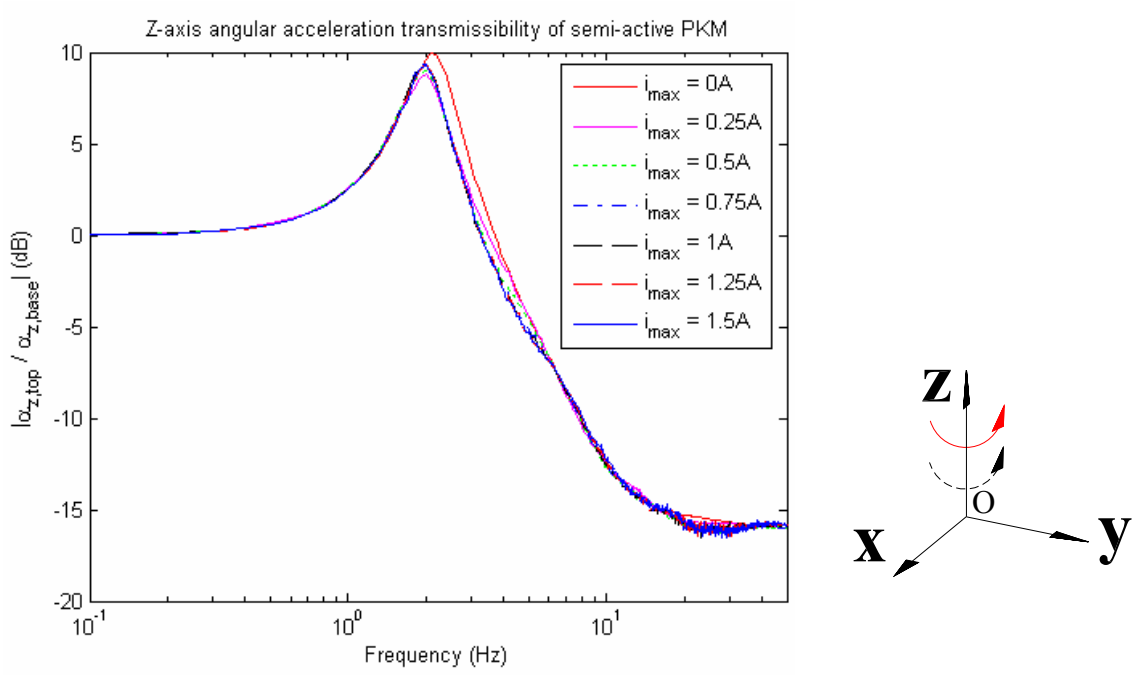

Figure 7-29. Z-axis RMS angular acceleration transmissibility between the top and bottom platforms for an input sinusoidal torque around the z-axis

7.3.4 Angular Disturbance around the X-axis

The angular acceleration transmissibility around the x-axis between the top and bottom platforms is shown in Figure 7-30 for a sinusoidal input torque to the bottom platform around the x-axis. Increasing the maximum input current to the MR damper lowers the resonant peak significantly.

7.3.5 Angular Disturbance around the Y-axis

The angular acceleration transmissibility around the y-axis between the top and the bottom platforms is shown in Figure 7-31 for a sinusoidal input torque to the bottom platform around the y-axis. Increasing the maximum input current to the MR damper lowers the resonant peak significantly.

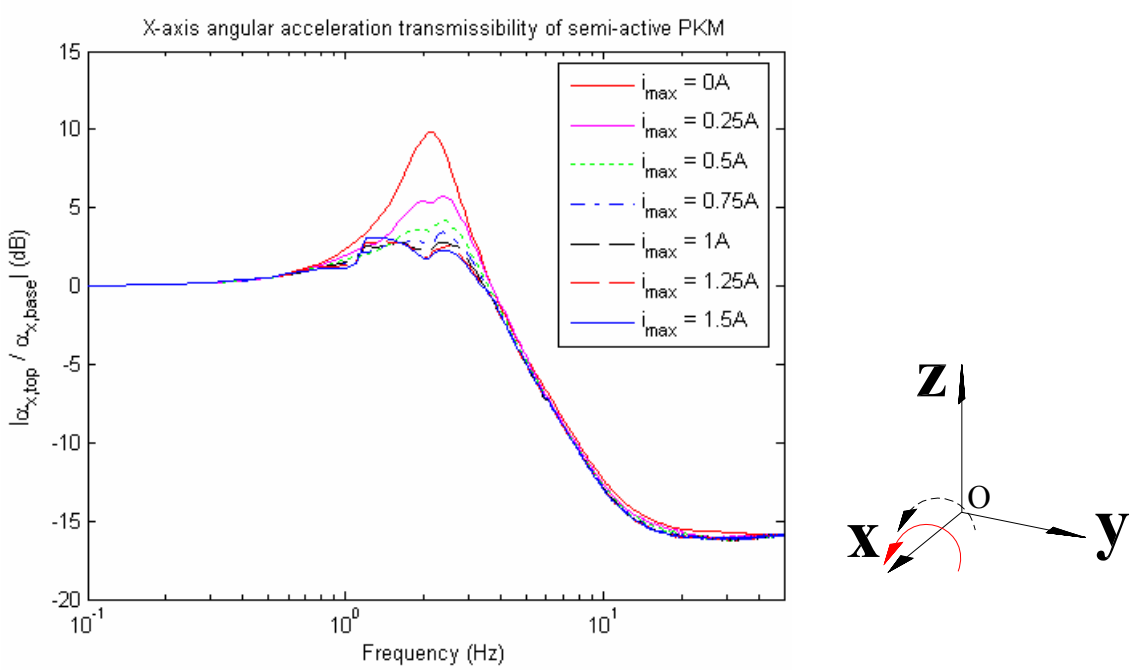

Figure 7-30. X-axis RMS angular acceleration transmissibility between the top and bottom platforms for an input sinusoidal torque around the x-axis

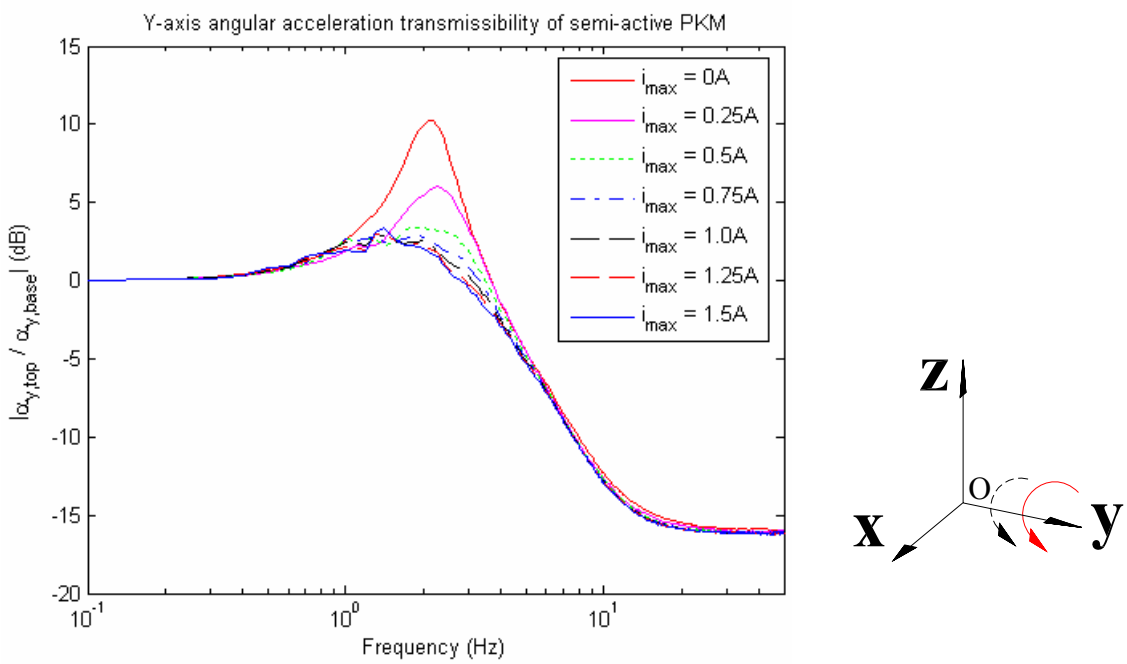

Figure 7-31. Y-axis RMS angular acceleration transmissibility between the top and bottom platforms for an input sinusoidal torque around the y-axis

7.4 6 DOF Positioning

In this section, 6 DOF positioning control is carried out by the active force actuators incorporated in series with the MR damper in the connector legs of the parallel platform mechanism. This displays the capability of the mechanism to provide positioning as well vibration isolation. A position control block shown in Figure 7-32 is incorporated into the semi-active platform with the two-stage connector legs. The 6 DOF model is displayed in Figure 7-33. A sinusoidal desired rotation around the x, y, and z axes and a desired trajectory in the x, y, and z axes are generated. By using a block subsystem already available in SimMechanics demos which performs the inverse kinematics of a Stewart platform, the corresponding leg lengths which would enable the desired trajectory are calculated.

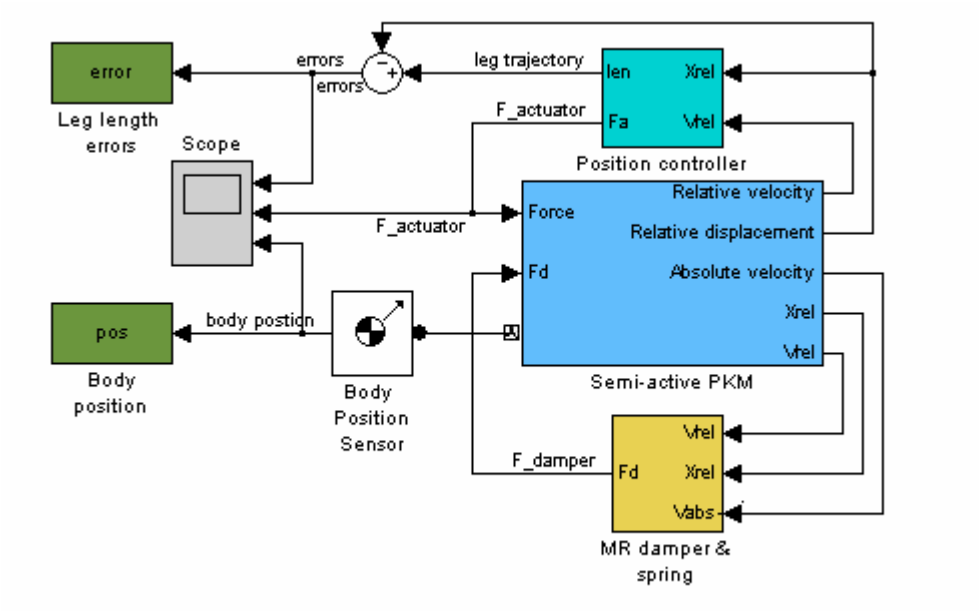

Figure 7-32. SimMechanics block diagram for positioning control of the semi-active parallel platform mechanism

As a starting point, the parallel platform is not subjected to any disturbances. The top platform is made to follow a sinusoidal trajectory. More precisely, the desired trajectory of the top platform center of mass is

$$\begin{aligned} x &= 5\sin 3t \ \text{ cm} & \theta_x &= -0.3\sin 3t \ \text{ rad} \\ y &= 7.5\sin 3t \ \text{ cm} & \theta_y &= 0.3\sin 3t \ \text{ rad} \\ z &= 35.75 + 5\sin 3t \ \text{ cm} & \theta_z &= 0.3\sin 3t \ \text{ rad} \end{aligned} \tag{7-3}$$

The initial height of the top platform is 35.75 cm. The position of the top platform in the x, y, and z-axes as it follows the desired trajectory is shown in Figure 7-34.

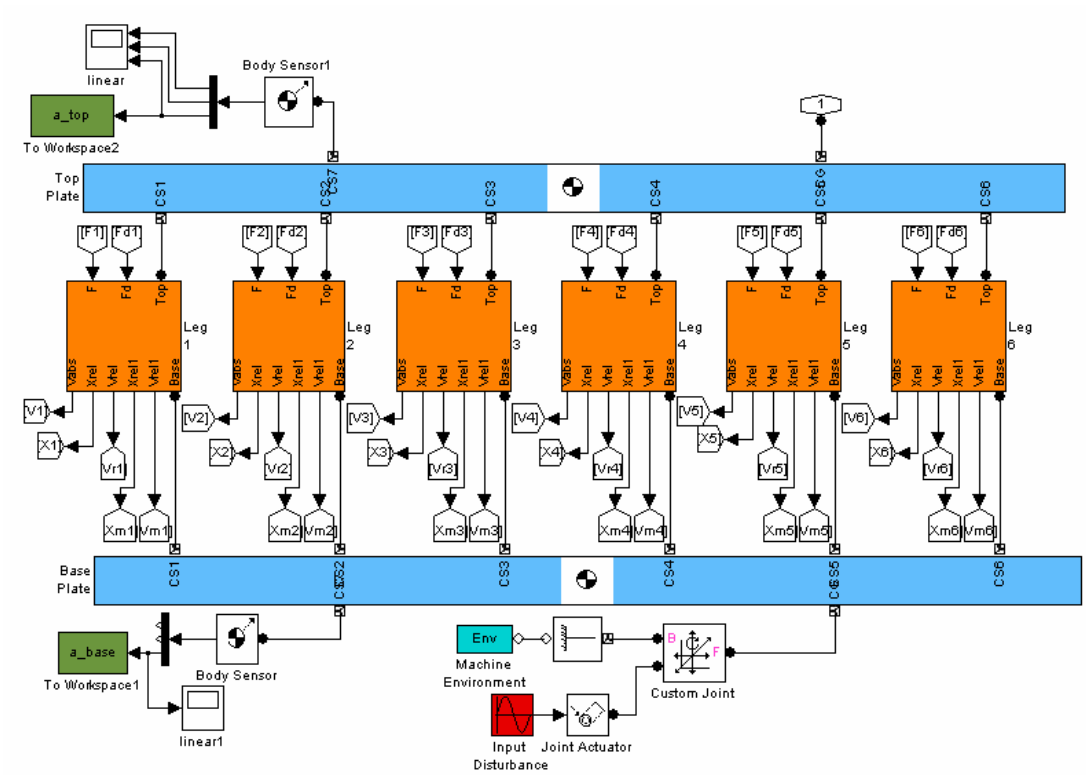

Figure 7-33. Semi-active parallel platform mechanism used in positioning control

The position errors in the x, y, and z-axes are given in Figure 7-35. The force that needs to be applied by each actuator in order to follow the desired trajectory is shown in Figure 7-36.

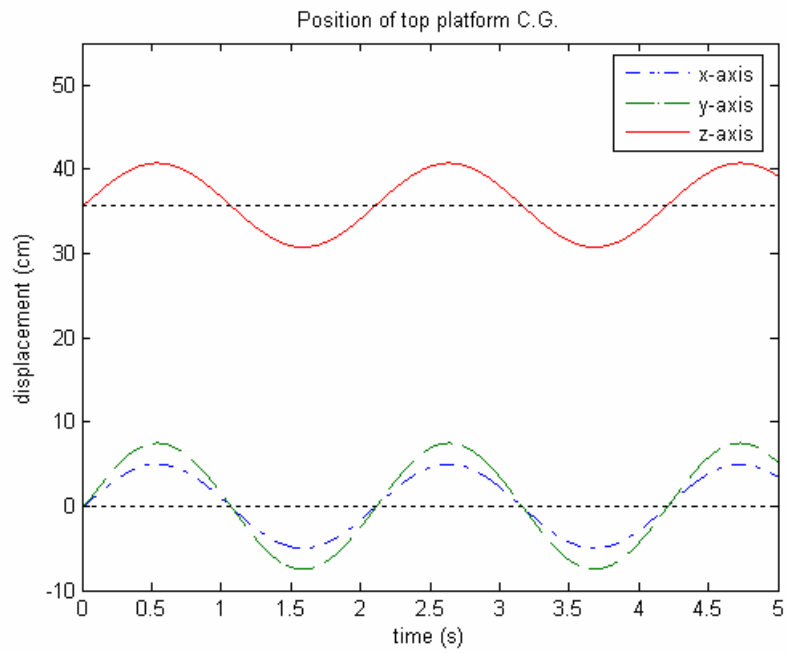

Figure 7-34. Position of the top platform center of mass

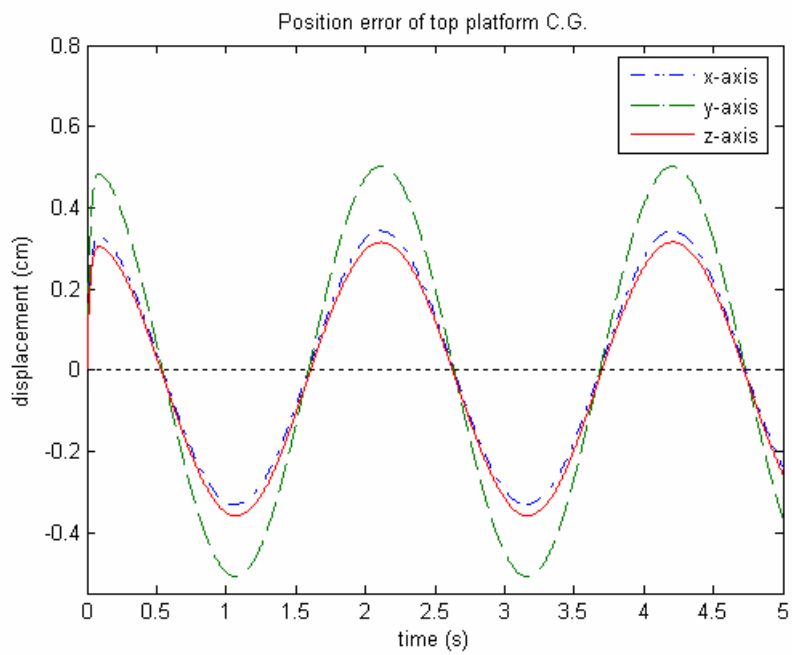

Figure 7-35. Position errors in all three axes

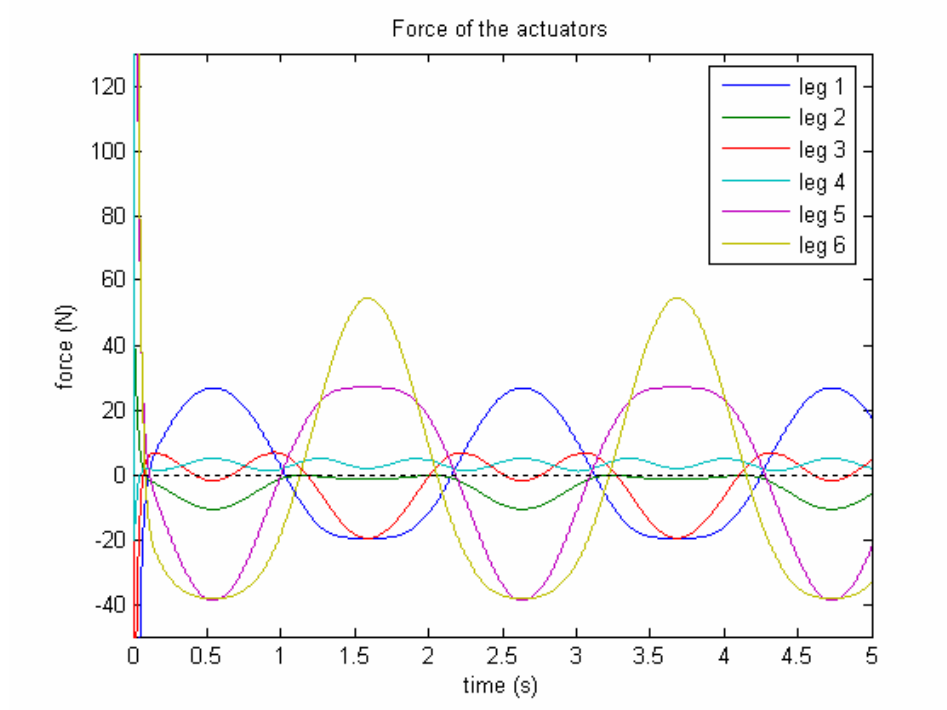

Figure 7-36. Force applied by the actuators

7.4.1 Positioning with Linear Disturbance in the Z-axis

A linear sinusoidal disturbance in the z-axis is applied to the base platform center of mass while the top platform center of mass is made to follow a sinusoidal trajectory in the z-axis. The input disturbance force is $F_{in} = 30\sin(11.43t + \pi/2)$ N. The frequency of this force is chosen to be the resonant frequency found from Figure 7-25. The initial height of the top platform is 35.75 cm and the desired trajectory is $z = 35.75 + 5\sin 3t$ cm. Figure 7-37 compares the position of the top platform center of mass of the semi-active platform mechanism with the two-stage legs for the following three cases:

- The platform is not exposed to any disturbances.
- The platform is exposed to the sinusoidal disturbance described above in the z-axis and no vibration control is used to compensate for the disturbance.
- The platform is exposed to the sinusoidal disturbance described above in the z-axis and vibration control is used to isolate the top platform from the disturbance.

It is seen from Figure 7-37 that the vibration control system gets rid of the oscillations in the trajectory due to the disturbance, but the amplitude of the actual motion remains smaller than that of the desired motion. This may also be seen in Figure 7-38 which shows a comparison of the position errors in the z-axis for the three cases.

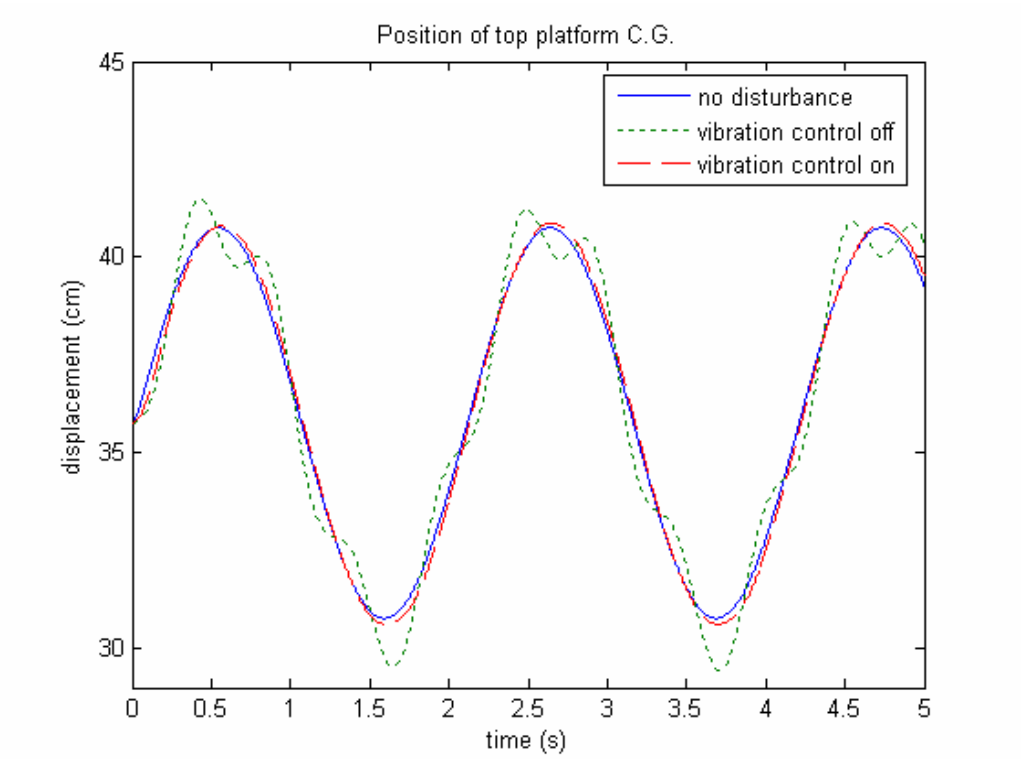

Figure 7-37. Position of the top platform center of mass in the z-axis with and without vibration control for a sinusoidal disturbance in the z-axis and with no disturbance

Besides getting rid of the oscillations in the motion, the vibration control system also significantly reduces the amount of force exerted by the actuators to follow the desired trajectory as seen in Figure 7-39.

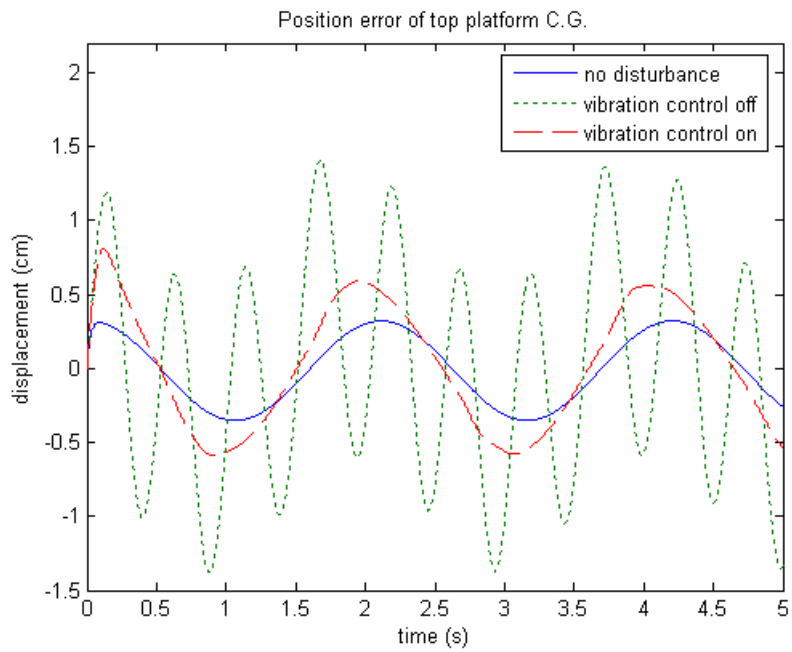

Figure 7-38. Position error of the top platform center of mass in the z-axis with and without vibration control for a sinusoidal disturbance in the z-axis and with no disturbance

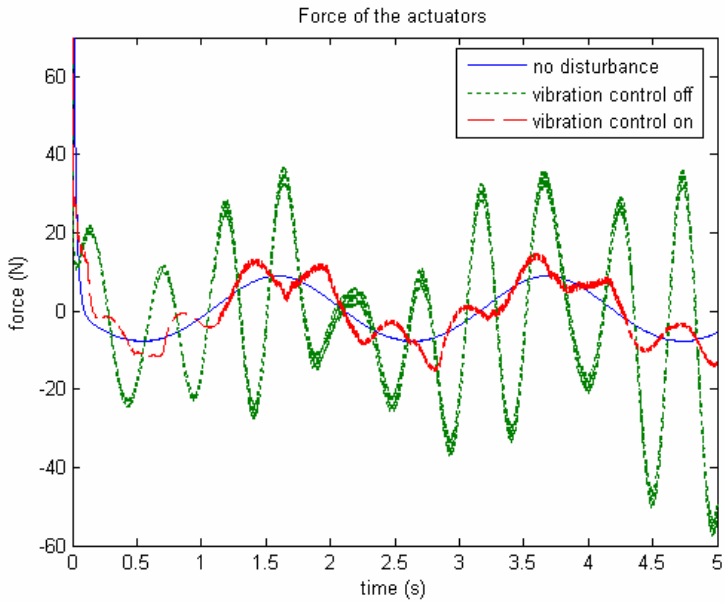

Figure 7-39. Force applied by a single actuator with and without vibration control for a sinusoidal disturbance in the z-axis and with no disturbance

7.4.2 Positioning with Linear Disturbance in the Y-axis

A linear sinusoidal disturbance in the y-axis is applied to the base platform center of mass while the top platform center of mass is made to follow a sinusoidal trajectory in the y-axis. The input disturbance force is $F_{in} = 30\sin(7.91t + \pi/2)$ N. The frequency of this force is chosen to be the resonant frequency found from Figure 7-28. Since the platform mechanism is symmetrical around the x- and y-axes, the results in this section also represent the case where positioning in the x-axis is realized under a disturbance in the x-axis. The desired trajectory in the y-axis is $y = 5\sin 3t$ cm. Figure 7-40 compares the position of the top platform center of mass of the semi-active platform mechanism with the two-stage legs for the three cases. Besides getting rid of the oscillations in the motion as shown in Figure 7-40 and Figure 7-41, the vibration control system also significantly reduces the amount of force exerted by the actuators to follow the desired trajectory as seen in Figure 7-42.

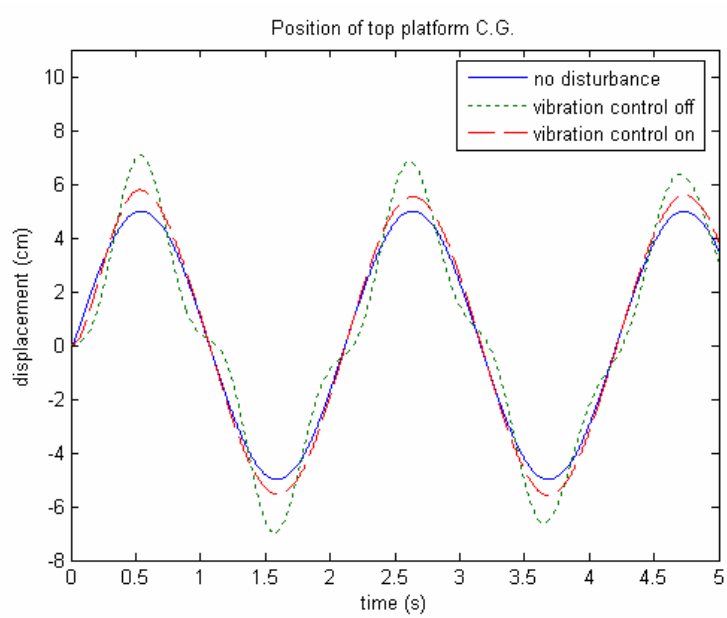

Figure 7-40. Position of the top platform center of mass in the y-axis with and without vibration control for a sinusoidal disturbance in the y-axis and with no disturbance

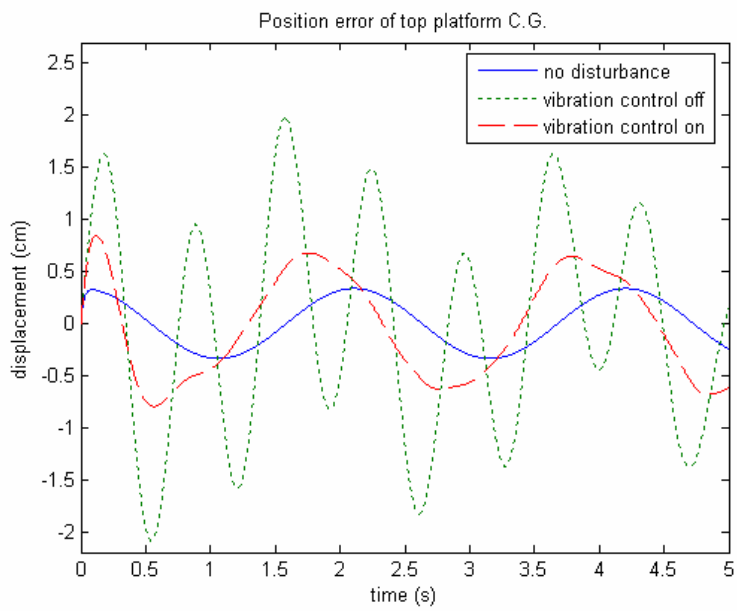

Figure 7-41. Position error of the top platform center of mass in the y-axis with and without vibration control for a sinusoidal disturbance in the y-axis and with no disturbance

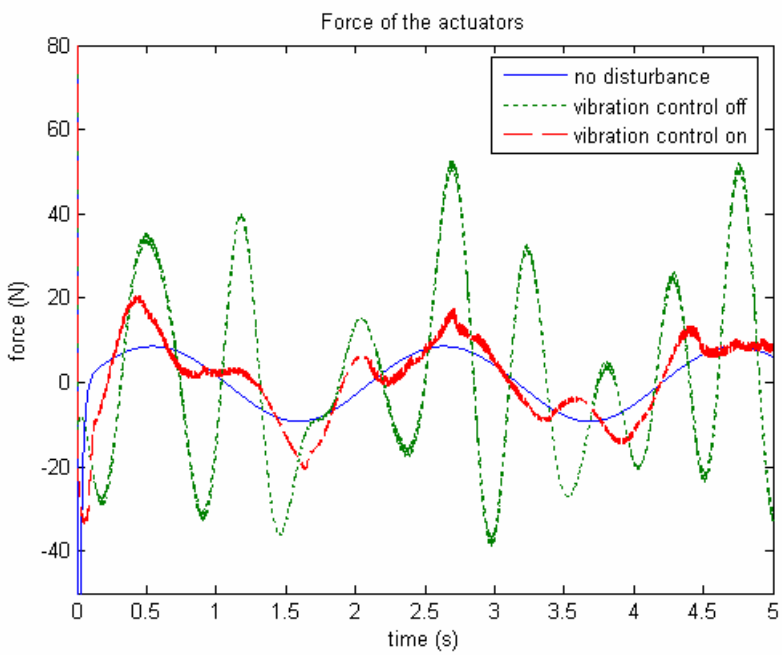

Figure 7-42. Force applied by a single actuator with and without vibration control for a sinusoidal disturbance in the y-axis and with no disturbance

7.4.3 Positioning with Angular Disturbance around the Z-axis

An angular sinusoidal disturbance around the z-axis is applied to the base platform center of mass while the top platform center of mass is made to follow a sinusoidal trajectory around the z-axis. The input disturbance torque is $\tau_{in} = 10\sin(12.56t + \pi/2)$ Nm. The frequency of this torque is chosen to be the resonant frequency found from Figure 7-29. The desired trajectory around the z-axis is $\theta_z = 5\sin 3t$ rad. Figure 7-43 compares the position of the top platform center of mass of the semi-active platform mechanism with the two-stage legs for the three cases. Besides getting rid of the oscillations in the motion as shown in Figure 7-43 and Figure 7-44, the vibration control system also significantly reduces the amount of force exerted by the actuators to follow the desired trajectory as seen in Figure 7-45.

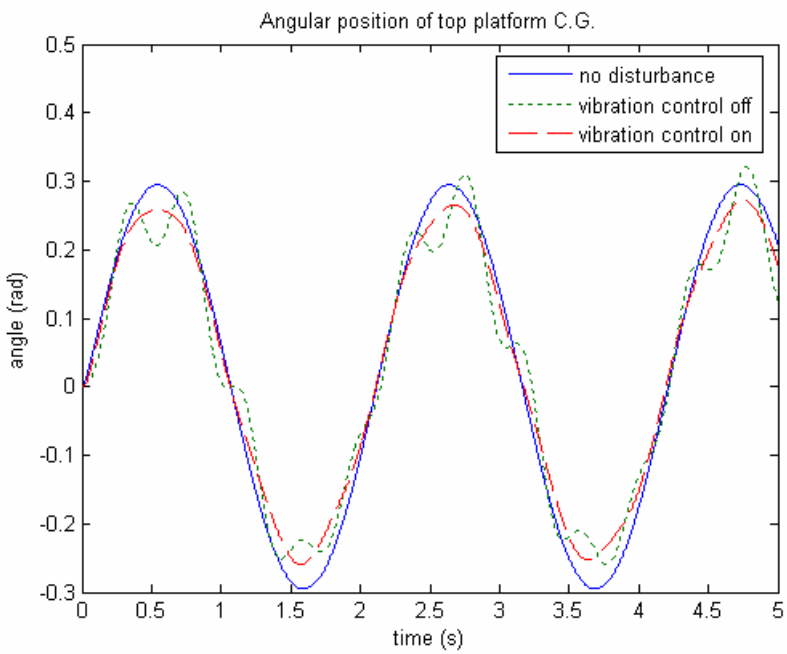

Figure 7-43. Position of the top platform center of mass around the z-axis with and without vibration control for a sinusoidal disturbance around the z-axis and with no disturbance

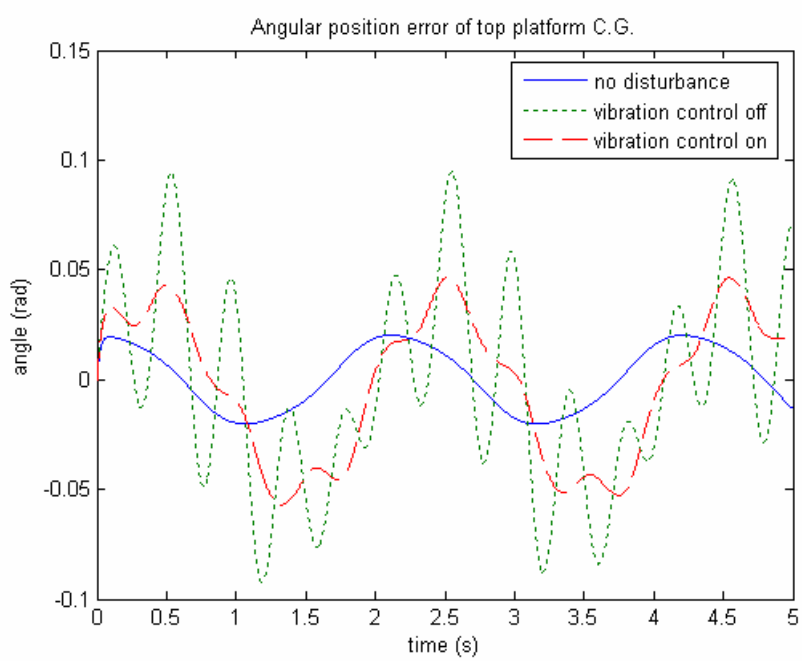

Figure 7-44. Position error of the top platform center of mass around the z-axis with and without vibration control for a sinusoidal disturbance around the z-axis and with no disturbance

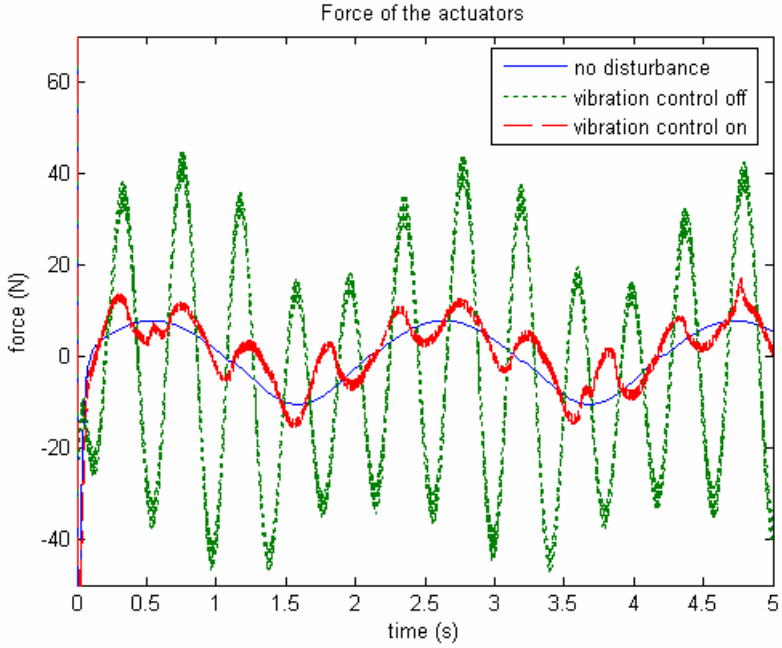

Figure 7-45. Force applied by a single actuator with and without vibration control for a sinusoidal disturbance around the z-axis and with no disturbance

7.4.4 Positioning with Angular Disturbance around the Y-axis

An angular sinusoidal disturbance around the y-axis is applied to the base platform center of mass while the top platform center of mass is made to follow a sinusoidal trajectory around the y-axis. The input disturbance torque is $\tau_{in} = 10\sin(12.56t + \pi/2)$ Nm. The frequency of this torque is chosen to be the resonant frequency found from Figure 7-31. Since the platform mechanism is symmetrical around the x- and y-axes, the results in this section also represent the case where positioning in the x-axis is realized under a disturbance in the x-axis. The desired trajectory around the y-axis is $\theta_y = 5\sin 3t$ rad. Figure 7-46 compares the position of the top platform center of mass of the semi-active platform mechanism with the two-stage legs for the three cases. Besides getting rid of the oscillations in the motion as shown in Figure 7-46 and Figure 7-47, the vibration control system also significantly reduces the amount of force exerted by the actuators to follow the desired trajectory as seen in Figure 7-48.

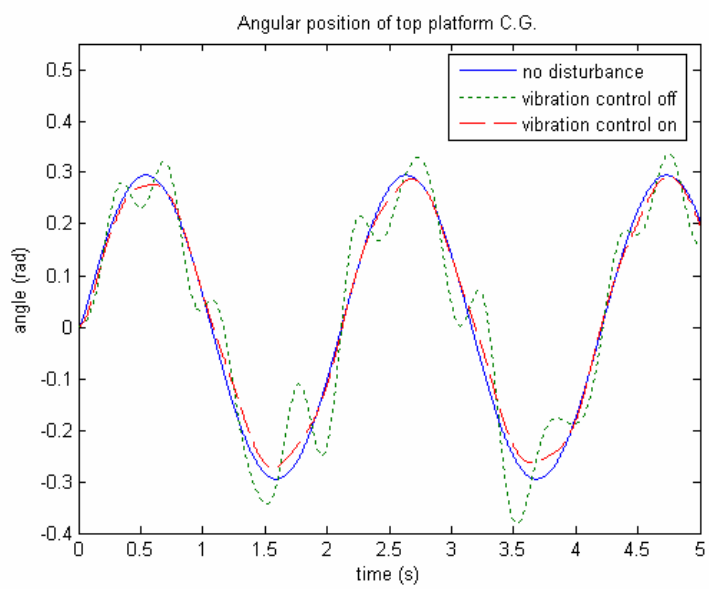

Figure 7-46. Position of the top platform center of mass around the y-axis with and without vibration control for a sinusoidal disturbance around the y-axis and with no disturbance

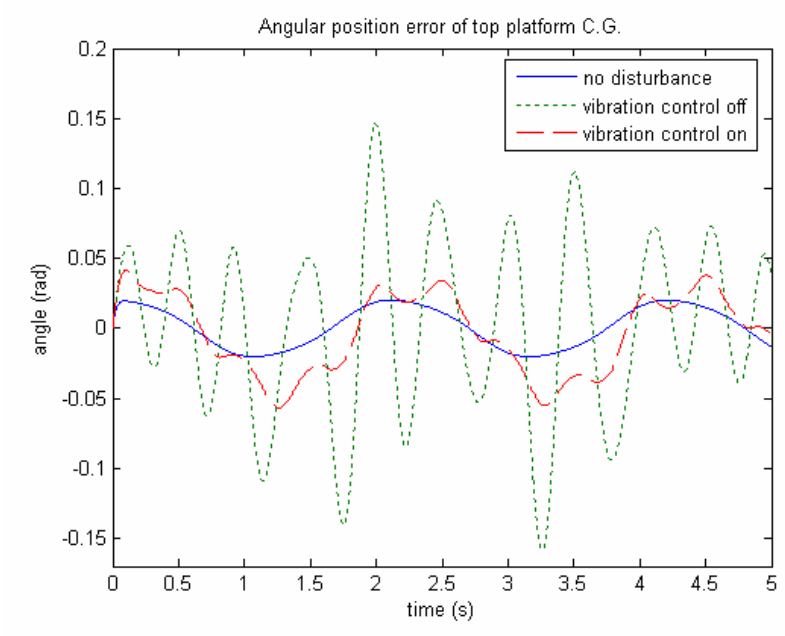

Figure 7-47. Position error of the top platform center of mass around the y-axis with and without vibration control for a sinusoidal disturbance around the y-axis and with no disturbance

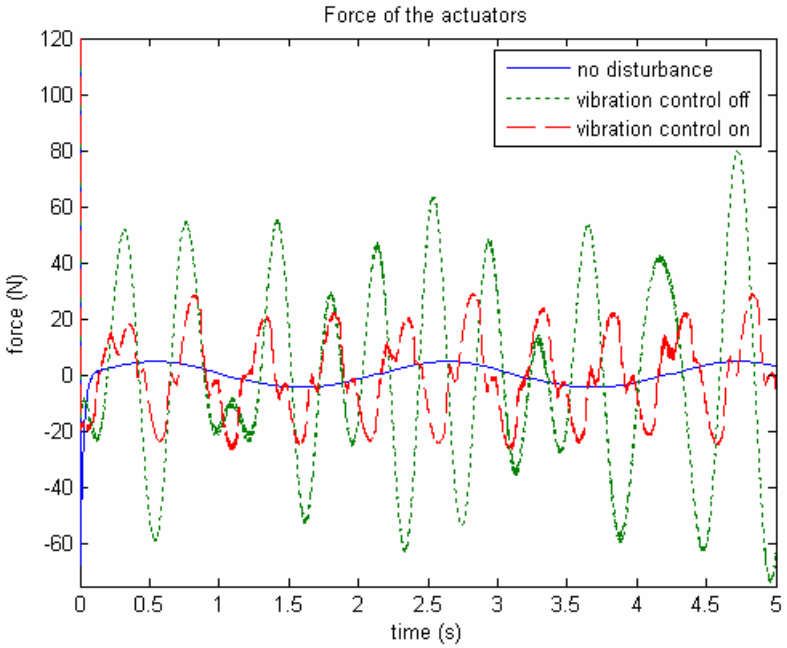

Figure 7-48. Force applied by a single actuator with and without vibration control for a sinusoidal disturbance around the y-axis and with no disturbance

CHAPTER 8
CONCLUSIONS

8.1 Summary and Conclusions

In this dissertation, the model of a 6 DOF vibration isolation system utilizing semi-active control was created. Magnetorheological (MR) dampers with adjustable damping are incorporated in series with passive dampers in the connector legs of the mechanism to attenuate the effects of vibrations. The 6 DOF system is a parallel platform mechanism which is also ideal for precision positioning. Active actuators were used in the model for positioning the payload.

In the literature, there are examples of parallel platform mechanisms which perform active vibration control and positioning, but this is the first known work where a 6-6 parallel platform mechanism which combines semi-active damping with MR dampers and active positioning is investigated. Skyhook damper control was used to avoid the resonant peak at the natural frequency without the penalty of reduced isolation at higher frequencies. The active skyhook damper control which employs an active force actuator to apply a force proportional to the absolute velocity of the clean body was adapted to be used with the MR damper. The control strategy was modified in a way which takes into account the lower and upper limits of the damping force which the MR damper can generate. Also, the fact that the MR damper is a dissipative device and cannot inject energy into the system was taken into account. When the absolute velocity of the clean body and its relative velocity to the base have different signs, the damper cannot deliver a force in the desired direction. The best it can do is to apply no force at all. Therefore, the

MR damper model in the simulations was made to apply its minimum damping force in this case and dissipate the minimum possible energy from the system when the skyhook damper control system requires it to actually inject energy into the system.

Before the MR damper was chosen as a means of incorporating semi-active damping into the parallel platform mechanism, other smart materials used in semi-active damping, including piezoelectric materials, shape memory alloys, ionic gels, electroactive polymers, and electrorheological (ER) fluids, were reviewed and it was seen that MR dampers stand out from the rest of the smart material dampers. The reasons which led to this conclusion were MR dampers' minimal voltage requirement, high force capability, global stability, ability to function as passive dampers in case of a power outage and insensitivity to temperature variations.

The criteria for designing MR dampers were investigated before the first MR damper prototype was built. The force delivered by the MR damper consists of two parts: the uncontrollable force and the controllable force. The goal was to keep the uncontrollable force minimum while having a controllable force as high as possible to have a damper with the widest dynamic range possible. This was a relatively difficult task. The first difficulty arises from the friction in the system which makes up a considerable portion of the uncontrollable force. In order to prevent the leakage of the MR fluid, seals which do not deteriorate through continuous contact with the fluid have to be used. Increasing the contact surface between the seal and the moving shaft reduces the leakage of the fluid, but also the inherent friction of the system. Several aspects of building an MR damper require very high machining tolerances. There is an optimal size of the gap through which the MR fluid flows from one chamber to the other as the shaft is

moving. Reducing the size of this gap increases the effect of the magnetic field on the MR fluid, but it also increases the plastic viscous force which in turn increases the uncontrollable force. The inside diameter and the outside diameter of the metal parts between which the fluid flows have to be machined with a very tight tolerance to attain to desired gap size. Another important aspect of the design process is to make sure the moving shaft is properly aligned. The misalignment of the shaft causes contact between the shaft and other metal surfaces in addition to eliminating the symmetry of the magnetic field around the circumference of the gap. Finally, where to place the electromagnetic coil is another important design consideration. Placing it inside the housing introduces problems such as the sealing of the coil and the electric wires, inserting the wires into the housing, and the heating up of the fluid. Having the coil outside the housing makes for a less compact design.

During the course of this work, four MR damper prototypes were built. All four prototypes were double-shafted to avoid using an accumulator to compensate for the volume change inside the housing as the shaft is going into and out of the housing. The first design had the electromagnetic coil inside an aluminum housing. The MR damper had to flow through a gap between the body housing the coil and an intermediate cylindrical part. A Teflon seal was used outside the cylindrical part to limit the flow of the MR fluid only to the gap. This seal introduced a lot of extra friction to the system. In the second prototype, the Teflon seal was removed and instead the gap was located directly between the magnetic housing and the outer housing which was made of low carbon steel. The electromagnetic coil was also divided into two parts to increase the effective surface area of the magnetic field. Both of these prototypes suffered from the

fact that the coil was located inside the housing. It made troubleshooting very difficult as the coil had to be removed from inside the hosing filled with MR fluid. It was also difficult to isolate the coil from the MR fluid and there were occasional breaks in the electric wiring. For this reason, in the final two designs, the coil was moved to outside the housing. Several tests were conducted with the prototypes including shaker tests, and compression and tensile tests. The dynamic range was found to be low in all the prototypes and the inherent friction and the misalignment problems described earlier were encountered.

Before the system including the connector legs and the whole platform was modeled, it was necessary to determine the dimensions of the platform. For this purpose, the quality index of the parallel platform mechanism was calculated. The quality index was used to determine the relative sizes of the base and the top platform and the initial height of the top platform. Not only were designs which would lead to low or zero quality indexes avoided, but also the geometry of the 6-6 parallel platform was determined by setting dimensions which gave the highest quality index possible at the nominal home position and orientation. The forward and reverse static analyses of the parallel platform mechanism as well as its stiffness mapping at the unloaded central configuration were also given.

The six identical connector legs which are incorporated into the parallel platform model were modeled in three different ways starting with the basic connector leg model, to which first a coupling stage, then a decoupling stage and lastly semi-active MR dampers were incorporated. The state-space formulations were given for each model and the frequency responses were calculated in MATLAB®. For verification purposes, these

were compared to the frequency responses of the identical models created in Simulink®. It was seen that the results obtained from the state-space models in MATLAB were the same as the results of the Simulink block diagrams. Once the validity of the models was verified, the performances of the basic connector, the two-stage connector, and the connector with the decoupling stage were compared. It was seen that the performance of the two-stage connector leg model was superior to that of the basic connector leg model. The decoupling stage which was originally added to two-stage connector did not have any significant influence on the frequency response of the leg. Semi-active dampers with adjustable damping were implemented in the coupling and decoupling stages of this model and four modes of operations were considered. Since none of the four modes of the connector model with the decoupling stage had a superior performance over the two-stage connector model which would make it worthwhile to incorporate the decoupling stage to the connector leg model, the two-stage connector model was chosen as the model to be incorporated into the 6 DOF model due to its simplicity in design and its performance which is superior and comparable to the performance of the basic connector model and the connector model with the decoupling stage, respectively.

In order to determine which model to use in the simulations for the semi-active MR damper, first the experimental results of the MR prototypes were examined. Using curve-fitting on the force-velocity curves of the double-shafted damper with the steel housing, the damper model was obtained. The damping force exerted by the prototype MR damper was determined to be too high for the size of the parallel platform mechanism considered. Therefore, another MR damper model with a lower damping force range was considered for the simulations of the parallel platform mechanism and a

semi-active skyhook damper control was created for this model. This controller calculated the desired force which was proportional to the absolute velocity of the clean mass and applied an input current to the MR damper so that the damping force would be equal to this desired force. However, since the semi-active damper can only dissipate energy from the system, when the desired force required energy to be injected into the system, the damper was made to apply its minimum damping force. The controller also made sure that the desired force lay within the operating range of the MR damper.

After the connector leg model and the MR damper model were determined, the 6 DOF parallel platform model was created. The 6 DOF parallel platform model was first built using the simpler basic connector legs before going on to modeling the more complex parallel platform with the two-stage connector legs.

The simulations were carried out, starting with the simplest one DOF model and eventually simulating the 6 DOF semi-active model in all degrees-of-freedom. Each leg model was simulated first in Simulink. Since the blocks in Simulink represent mathematical operations, the equations of motion had to be known for each model. The results of the Simulink block models were used to verify the SimMechanics models. To further confirm the validity of the leg models, the natural frequencies of the basic connector leg and the two-stage connector leg were calculated and it was shown that the natural frequency peaks are present in the transmissibility plots.

Each leg model and the 6 DOF platform model based on the specific leg model were simulated using passive, active, and semi-active control. The single DOF passive, active, and semi-active model results agreed with the theoretical single DOF model results which are commonly present in the literature. The results showed that the passive

isolator design involved a trade-off between the resonance peak attenuation and reduction in the high frequency transmissibility reduction. The active control eliminates this trade-off and a reduction in both the resonance peak and the high frequency isolation is achieved. The semi-active control similarly eliminates this trade-off with a slightly reduced performance. In the 6 DOF transmissibility results, the performances of passive, active, and semi-active systems were comparable at frequencies above 30 Hz. The semi-active system was able to provide more reduction of the transmissibility at lower frequencies compared to the passive system. Overall, the active system had the best performance in reducing the resonance peak. The choice between an active and a semi-active system requires a careful evaluation of the application. While the vibration isolation of the active system is better, there are several reasons why the semi-active system may be preferred:

1. The displacement of the active actuators is very limited. Typical active actuators used in hexapods for vibration isolation system are voice coil, magnetostrictive, piezoceramic, and electromagnetic actuators. A literature search was carried out and the largest stroke of an active force actuator incorporated in a hexapod used for vibration control was found to be 5 mm. The actuator was a voice coil actuator used in the hexapod by Hood Technology and University of Washington (Thayer *et al.*, 2002). This characteristic of the active actuators limits the use of the vibration isolation system to precision positioning applications which involve very small displacements.

2. The power requirement of a semi-active MR damper is much lower than an active force actuator. The power requirement of a typical commercial MR damper is around 24 W at peak force (12 VDC, 2A). A linear voice coil actuator which could be

incorporated into the connector legs of the parallel platform mechanism in this work is the LA25-42-000A model from BEI Technologies and it requires 375 W at its peak force.

3. Active actuators may cause instability because they inject energy into the system while semi-active dampers have guaranteed stability as they only dissipate energy from the system.

4. The failure of the active control system or a power outage result in no vibration isolation at all where as in a similar situation the semi-active dampers behave as passive dampers.

5. The active actuators cost more than MR dampers. The LA25-42-000A model from BEI Technologies costs $850. The price of a typical commercial MR damper (RD-1005-3 from Lord Corporation) is $210.

All the simulations described previously involved an input disturbance in the z-axis and the acceleration transmissibilities of the top and base platforms were calculated in the z-axis. The performance of the semi-active parallel platform with the two-stage connector was quantified in other degrees-of-freedom as well. Since the platform mechanism is symmetrical about the x-axis and the y-axis, the same results were obtained as expected when these two axes were involved. It was seen that increased damping in the legs did not result in better vibration isolation in the x- and y-axes when a linear disturbance was applied to the base platform in these axes. Slightly more reduction was obtained at the resonant frequency around the z-axis when a torque around this axis was applied to the base platform. The vibration isolation performance was much better around the x- and y-axes when torques around the x and y-axis were applied to the base platform, respectively.

In the final part of this work, a positioning controller was added to the semi-active parallel platform mechanism. The top platform was made to follow a linear trajectory in the x- , y- , and z-axes, respectively as a linear disturbance was applied to the base platform in the x-, y, and z, axes, respectively. In the second part of the simulations, the top platform was made to follow an angular trajectory around the x- , y- ,and z-axes, respectively as an angular disturbance was applied to the base platform around the x-, y, and z-axes, respectively. The vibration control eliminated the small oscillations in the positioning due to the sinusoidal disturbance and enabled the top platform to follow the desired trajectory more closely than when the vibration control was off. When there was no vibration control present, the active actuator tried to oppose the disturbances in the process of tracking the desired trajectory. This resulted in higher actuator forces. The vibration control reduced the amount of force applied by each actuator.

8.2 Future Work

Within this research, the vibration isolation of the parallel platform mechanism was quantified in all degrees of freedom when a sinusoidal input force or torque was applied in or around a single axis. Also, the performance of the position controller was observed to see how it was affected by the presence of the vibration control. There are several more test cases which may be looked at to further evaluate the performance of the parallel platform mechanism. The vibration isolation performance may be observed when

a) the redundancy of the parallel platform mechanism is lost when one or more of the MR dampers fail to operate.

b) there is an uneven weight distribution on the top platform. This would put more load on some MR dampers than others. Since the vibration control of each leg is

independent from the other legs, theoretically an uneven weight distribution should not affect the performance.

c) the base platform is exposed to input disturbances in more than one axis and the transmissibility in all six axes is calculated and combined to have a metric which shows the 6 DOF transmissibility of the platform.

There is a growing interest in smart dampers as an alternative to passive and active systems in vibration control applications. In order to make the MR dampers more attractive, there are several characteristics of these dampers that need to be improved. First of all, the MR damper is highly nonlinear in nature. The vibration isolation performance of the platform may potentially be improved by using a more accurate MR damper model and a more sophisticated nonlinear semi-active control system. Reducing the size of MR dampers would also make them more attractive since the trend in hexapods is to build smaller and lighter platforms.

Finally, the construction of a parallel platform mechanism with six MR dampers and comparing the simulation results to the experimental results is a logical next step to this research.

APPENDIX A
MATLAB CODE

A.1 Basic Connector Leg Model

```
% Created 04/18/06
% Basic connector model
% 2 masses connected by a spring & damper pair
% The bottom mass is excited
% Frequency response between input force and top mass displacement is found
% and compared with the identical Simulink model for verification purposes
%%%%%%%%%%%%%%%%%%%%%%%%%%%%%%%%%%%%%%%%%%%%%%%%%%%%%%%%%%%%%%%%%%%%%%%%%%%%

clear all
close all

% initialize magdb matrix
magDB_b=[];

% mass and stiffness
M0=38 ; M1=16; k=5000 ;

Bf = [1 ; 0] ;
M = [M0 0 ; 0 M1];
K = [k -k ; -k k];

% frequency bandwidth
w = linspace(0.1, 2*pi*50, 10000);

% natural frequencies
wn = sqrt(eig(K,M))  %rad/sec
f = wn/(2*pi)  %Hz

% vary damping%%%%%%%%%%%%%%%%%%%%%%%%%%%%%%%%%%%%%%%%%

for m = 1:6
    b = 50 + 150*(m-1)

damp = [b -b ; -b b];

% state-space
A = [zeros(2,2) , eye(2) ; -inv(M)*K , -inv(M)*damp];
B = [zeros(2,1) ; inv(M)*Bf];
C = [1 0 0 0 ; 0 1 0 0 ];
D = zeros(size(C,1), size(B,2));

sys = ss(A,B,C,D)
[mag,phase] = bode(sys(2,1),w);
magdb = 20*log10(mag);
magDB_b(m,:) = magdb(1,1,:);

% transfer function
[n,d] = ss2tf(A,B,C,D);
tf1 = tf(n(1,:),d);
tf2 = tf(n(2,:),d);

% bode plot
figure(1)
bode(sys(2,1),w), hold on

end

% frequency response
figure(2)
semilogx(w/(2*pi),magDB_b(1,:),'r-', w/(2*pi),magDB_b(2,:),'m--',
w/(2*pi),magDB_b(3,:),'g:',...
    w/(2*pi),magDB_b(4,:),'b-.', w/(2*pi),magDB_b(5,:),'k--', w/(2*pi),magDB_b(6,:),'b-')
title('Frequency response function of passive basic connector leg')
xlabel('Frequency (Hz)'); ylabel('|X_1 / F| (dB)');
```

```
legend('b_1 = 50 Ns/m','b_1 = 200 Ns/m','b_1 = 350 Ns/m','b_1 = 500 Ns/m','b_1 = 650
Ns/m','b_1 = 800 Ns/m');
AXIS([0.1 50 -180 -20])

save basic_leg_model


wn =

    0.0000
   21.0732


f =

    0.0000
    3.3539


b =

    50


a =
            x1      x2      x3      x4
   x1        0       0       1       0
   x2        0       0       0       1
   x3   -131.6   131.6  -1.316   1.316
   x4    312.5  -312.5   3.125  -3.125


b =
            u1
   x1        0
   x2        0
   x3  0.02632
   x4        0


c =
        x1  x2  x3  x4
   y1    1   0   0   0
   y2    0   1   0   0


d =
        u1
   y1    0
   y2    0

Continuous-time model.

b =

   200


a =
            x1      x2      x3      x4
   x1        0       0       1       0
   x2        0       0       0       1
   x3   -131.6   131.6  -5.263   5.263
   x4    312.5  -312.5    12.5   -12.5


b =
            u1
   x1        0
   x2        0
   x3  0.02632
   x4        0


c =
        x1  x2  x3  x4
   y1    1   0   0   0
   y2    0   1   0   0
```

```
d =
       u1
   y1   0
   y2   0

Continuous-time model.

b =

   350


a =
            x1       x2       x3       x4
   x1        0        0        1        0
   x2        0        0        0        1
   x3   -131.6    131.6   -9.211    9.211
   x4    312.5   -312.5    21.88   -21.88


b =
             u1
   x1         0
   x2         0
   x3   0.02632
   x4         0


c =
       x1  x2  x3  x4
   y1   1   0   0   0
   y2   0   1   0   0


d =
       u1
   y1   0
   y2   0

Continuous-time model.

b =

   500


a =
            x1       x2       x3       x4
   x1        0        0        1        0
   x2        0        0        0        1
   x3   -131.6    131.6   -13.16    13.16
   x4    312.5   -312.5    31.25   -31.25


b =
             u1
   x1         0
   x2         0
   x3   0.02632
   x4         0


c =
       x1  x2  x3  x4
   y1   1   0   0   0
   y2   0   1   0   0


d =
       u1
   y1   0
   y2   0

Continuous-time model.

b =

   650


a =
```

```
            x1       x2       x3       x4
   x1        0        0        1        0
   x2        0        0        0        1
   x3   -131.6    131.6   -17.11    17.11
   x4    312.5   -312.5    40.63   -40.63


b =
             u1
   x1         0
   x2         0
   x3   0.02632
   x4         0


c =
        x1  x2  x3  x4
   y1    1   0   0   0
   y2    0   1   0   0


d =
        u1
   y1    0
   y2    0

Continuous-time model.

b =

   800


a =
            x1       x2       x3       x4
   x1        0        0        1        0
   x2        0        0        0        1
   x3   -131.6    131.6   -21.05    21.05
   x4    312.5   -312.5       50      -50


b =
             u1
   x1         0
   x2         0
   x3   0.02632
   x4         0


c =
        x1  x2  x3  x4
   y1    1   0   0   0
   y2    0   1   0   0


d =
        u1
   y1    0
   y2    0

Continuous-time model.
```

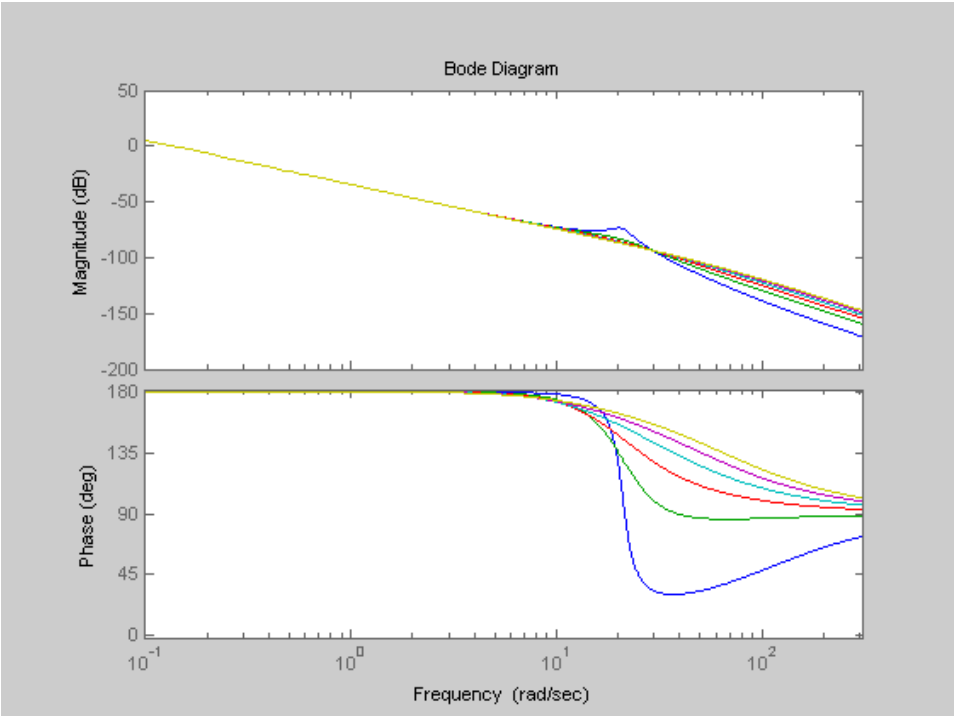

Figure A-1. Magnitude and phase frequency response plots of passive basic connector leg with varying damping

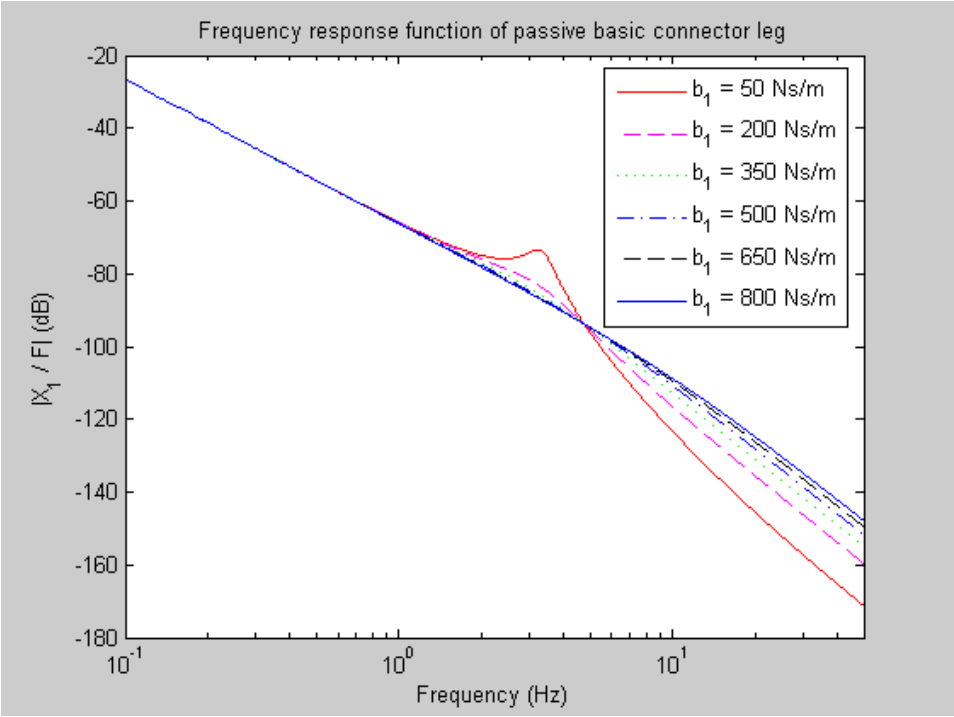

Figure A-2. Magnitude of the frequency response for the passive basic connector leg with varying damping

A.2 Two-stage Connector Leg Model

```
% Created 04/18/06
% Two-stage connector model with coupling stage
% 3 masses connected by 2 spring & damper pairs
% The bottom mass is excited
% Frequency response between input force and top mass displacement is found
% and compared with the identical Simulink model for verification purposes
%%%%%%%%%%%%%%%%%%%%%%%%%%%%%%%%%%%%%%%%%%%%%%%%%%%%%%%%%%%%%%%%%%%%%%%%%%

clear all

% initialize magdb matrix
magDB_c=[];

% 3 masses separated by 2 spring-damper pairs

M0=23 ; M1=15; M2=16;
k1=10000 ; k2=5000;
b1= 100;

Bf = [1 0 ; 0 0 ; 0 0];
M = [M0 0 0 ; 0 M1 0 ; 0 0 M2];
K = [k1 -k1 0 ; -k1 (k1+k2) -k2 ; 0 -k2 k2];

% frequency bandwidth
w = linspace(0.1, 2*pi*50, 10000);

% natural frequencies
wn = sqrt(eig(K,M))  %rad/sec
f = wn/(2*pi)  %Hz

% vary damping%%%%%%%%%%%%%%%%%%%%%%%%%%%%%%%%%%%%%%%%%

for m = 1:6
    b2 = 50 + 150*(m-1)

damp = [b1 -b1 0 ;  -b1 (b1+b2) -b2 ; 0 -b2 b2];

% state-space
A = [zeros(3,3) , eye(3) ; -inv(M)*K , -inv(M)*damp];
B = [zeros(3,2) ; inv(M)*Bf];
C = [eye(3) , zeros(3,3)];
D = zeros(size(C,1), size(B,2));

sys = ss(A,B,C,D)

% transfer function
[n,d] = ss2tf(A,B,C,D,1);
tf1 = tf(n(1,:),d);
tf2 = tf(n(2,:),d);
tf3 = tf(n(3,:),d)

[mag,phase] = bode(sys(3,1),w);
magdb = 20*log10(mag);
magDB_c(m,:) = magdb(1,1,:);

% bode plot
figure(2)
bode(sys(3,1),w), hold on

end

% frequency response
figure(3)
semilogx(w/(2*pi),magDB_c(1,:), w/(2*pi),magDB_c(2,:), w/(2*pi),magDB_c(3,:),
w/(2*pi),magDB_c(4,:)...
    , w/(2*pi),magDB_c(5,:), w/(2*pi),magDB_c(6,:))
title('Frequency response function of passive two-stage connector leg')
xlabel('Frequency (Hz)'); ylabel('|X_2 / F| (dB)');
legend('b_2 = 50 Ns/m','b_2 = 200 Ns/m',' b_2 = 350 Ns/m',' b_2 = 500 Ns/m',' b_2 =
650 Ns/m',' b_2 = 800 Ns/m');
AXIS([0.1 50 -200 -20])

save coupled_leg_model
```

```
wn =
```

```
        0 + 0.0000i
  18.7104
  37.3792


f =

        0 + 0.0000i
   2.9778
   5.9491


b2 =

    50


a =
            x1      x2      x3      x4      x5      x6
   x1        0       0       0       1       0       0
   x2        0       0       0       0       1       0
   x3        0       0       0       0       0       1
   x4   -434.8   434.8       0  -4.348   4.348       0
   x5    666.7   -1000   333.3   6.667     -10   3.333
   x6        0   312.5  -312.5       0   3.125  -3.125


b =
            u1       u2
   x1        0        0
   x2        0        0
   x3        0        0
   x4  0.04348        0
   x5        0        0
   x6        0        0


c =
        x1  x2  x3  x4  x5  x6
   y1    1   0   0   0   0   0
   y2    0   1   0   0   0   0
   y3    0   0   1   0   0   0


d =
        u1  u2
   y1    0   0
   y2    0   0
   y3    0   0

Continuous-time model.

Transfer function:
 -3.197e-014 s^5 - 1.137e-012 s^4 - 2.365e-011 s^3 + 0.9058 s^2 + 181.2 s + 9058
--------------------------------------------------------------------------------
s^6 + 17.47 s^5 + 1796 s^4 + 9783 s^3 + 4.891e005 s^2 - 2.749e-009 s - 1.826e-008


b2 =

   200


a =
            x1      x2      x3      x4      x5      x6
   x1        0       0       0       1       0       0
   x2        0       0       0       0       1       0
   x3        0       0       0       0       0       1
   x4   -434.8   434.8       0  -4.348   4.348       0
   x5    666.7   -1000   333.3   6.667     -20   13.33
   x6        0   312.5  -312.5       0    12.5   -12.5


b =
            u1       u2
   x1        0        0
   x2        0        0
   x3        0        0
   x4  0.04348        0
   x5        0        0
   x6        0        0
```

```
c =
       x1  x2  x3  x4  x5  x6
   y1   1   0   0   0   0   0
   y2   0   1   0   0   0   0
   y3   0   0   1   0   0   0


d =
       u1  u2
   y1   0   0
   y2   0   0
   y3   0   0

Continuous-time model.

Transfer function:
    3.553e-014 s^5 + 4.547e-013 s^4 + 2.183e-011 s^3 + 3.623 s^2 + 452.9 s + 9058
-------------------------------------------------------------------------------------
s^6 + 36.85 s^5 + 1943 s^4 + 2.446e004 s^3 + 4.891e005 s^2 + 1.971e-009 s + 7.479e-008


b2 =

   350


a =
           x1      x2      x3      x4      x5      x6
   x1       0       0       0       1       0       0
   x2       0       0       0       0       1       0
   x3       0       0       0       0       0       1
   x4  -434.8   434.8       0  -4.348   4.348       0
   x5   666.7   -1000   333.3   6.667     -30   23.33
   x6       0   312.5  -312.5       0   21.88  -21.88


b =
           u1       u2
   x1       0        0
   x2       0        0
   x3       0        0
   x4 0.04348        0
   x5       0        0
   x6       0        0


c =
       x1  x2  x3  x4  x5  x6
   y1   1   0   0   0   0   0
   y2   0   1   0   0   0   0
   y3   0   0   1   0   0   0


d =
       u1  u2
   y1   0   0
   y2   0   0
   y3   0   0

Continuous-time model.

Transfer function:
     1.35e-013 s^5 + 2.274e-012 s^4 + 5.093e-011 s^3 + 6.341 s^2 + 724.6 s + 9058
-------------------------------------------------------------------------------------
s^6 + 56.22 s^5 + 2090 s^4 + 3.913e004 s^3 + 4.891e005 s^2 + 1.739e-009 s + 5.834e-008


b2 =

   500


a =
           x1      x2      x3      x4      x5      x6
   x1       0       0       0       1       0       0
   x2       0       0       0       0       1       0
   x3       0       0       0       0       0       1
   x4  -434.8   434.8       0  -4.348   4.348       0
   x5   666.7   -1000   333.3   6.667     -40   33.33
```

```
   x6       0   312.5  -312.5       0   31.25  -31.25


b =
             u1       u2
   x1        0        0
   x2        0        0
   x3        0        0
   x4  0.04348        0
   x5        0        0
   x6        0        0


c =
       x1  x2  x3  x4  x5  x6
   y1   1   0   0   0   0   0
   y2   0   1   0   0   0   0
   y3   0   0   1   0   0   0


d =
       u1  u2
   y1   0   0
   y2   0   0
   y3   0   0

Continuous-time model.

Transfer function:
   -1.421e-014 s^5 - 4.547e-013 s^4 - 4.366e-011 s^3 + 9.058 s^2 + 996.4 s + 9058
-------------------------------------------------------------------------------
s^6 + 75.6 s^5 + 2236 s^4 + 5.38e004 s^3 + 4.891e005 s^2 - 2.244e-009 s + 3.188e-025


b2 =

   650


a =
            x1      x2      x3      x4      x5      x6
   x1        0       0       0       1       0       0
   x2        0       0       0       0       1       0
   x3        0       0       0       0       0       1
   x4   -434.8   434.8       0  -4.348   4.348       0
   x5    666.7   -1000   333.3   6.667     -50   43.33
   x6        0   312.5  -312.5       0   40.63  -40.63


b =
             u1       u2
   x1        0        0
   x2        0        0
   x3        0        0
   x4  0.04348        0
   x5        0        0
   x6        0        0


c =
       x1  x2  x3  x4  x5  x6
   y1   1   0   0   0   0   0
   y2   0   1   0   0   0   0
   y3   0   0   1   0   0   0


d =
       u1  u2
   y1   0   0
   y2   0   0
   y3   0   0

Continuous-time model.

Transfer function:
     5.684e-014 s^5 - 1.819e-012 s^4 - 7.276e-011 s^3 + 11.78 s^2 + 1268 s + 9058
-------------------------------------------------------------------------------
s^6 + 94.97 s^5 + 2383 s^4 + 6.848e004 s^3 + 4.891e005 s^2 + 2.643e-009 s + 2.447e-008


b2 =
```

```
   800

a =
            x1      x2      x3      x4      x5      x6
   x1        0       0       0       1       0       0
   x2        0       0       0       0       1       0
   x3        0       0       0       0       0       1
   x4   -434.8   434.8       0  -4.348   4.348       0
   x5    666.7   -1000   333.3   6.667     -60   53.33
   x6        0   312.5  -312.5       0      50     -50

b =
             u1       u2
   x1         0        0
   x2         0        0
   x3         0        0
   x4   0.04348        0
   x5         0        0
   x6         0        0

c =
        x1  x2  x3  x4  x5  x6
   y1    1   0   0   0   0   0
   y2    0   1   0   0   0   0
   y3    0   0   1   0   0   0

d =
        u1  u2
   y1    0   0
   y2    0   0
   y3    0   0

Continuous-time model.

Transfer function:
     5.684e-014 s^5 + 5.912e-012 s^4 + 2.91e-010 s^3 + 14.49 s^2 + 1540 s + 9058
--------------------------------------------------------------------------------
s^6 + 114.3 s^5 + 2530 s^4 + 8.315e004 s^3 + 4.891e005 s^2 + 3.717e-009 s + 3.411e-008
```

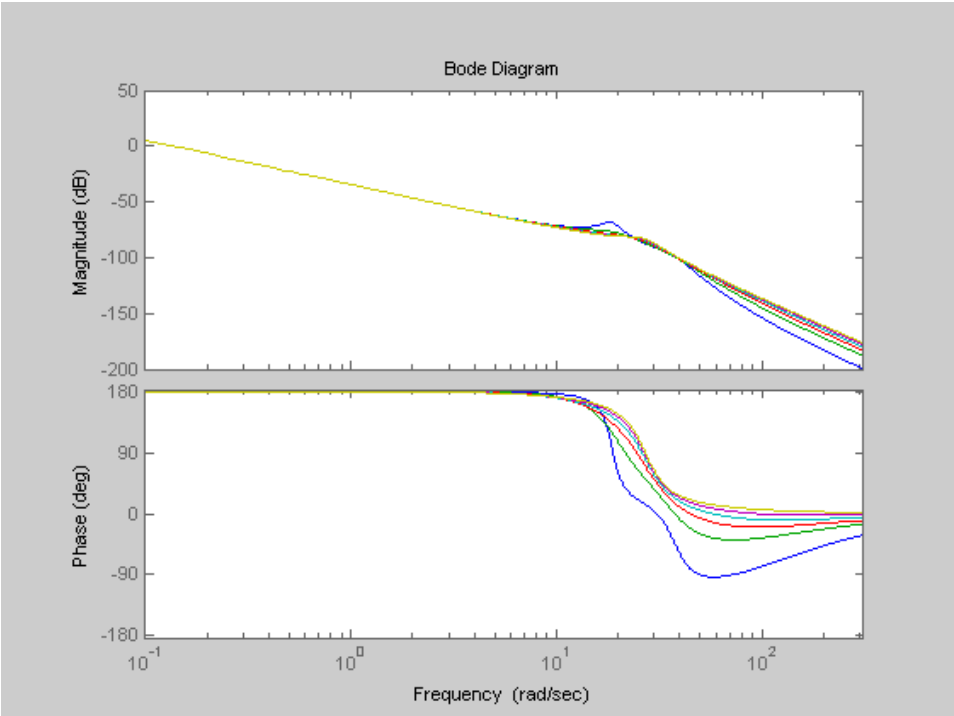

Figure A-3. Magnitude and phase frequency response plots for the passive two-stage connector leg with varying damping

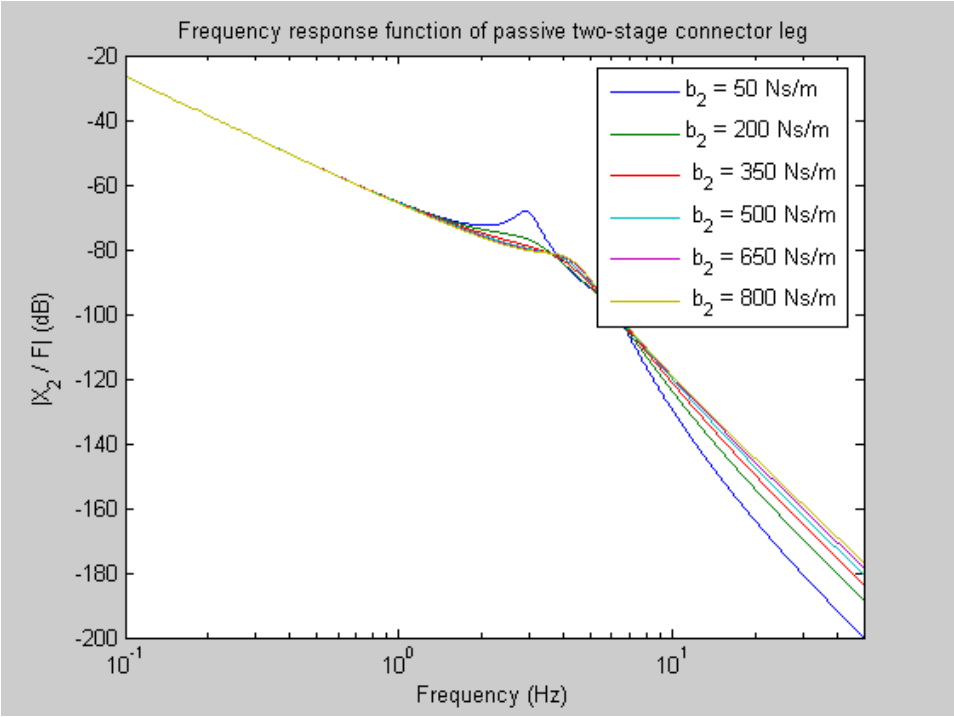

Figure A-4. Magnitude of the frequency response for the passive two-stage connector leg with varying damping

A.3 Connector Leg Model with Decoupling Stage

```
% Created 04/18/06
% Connector model with decoupling stage
% 3 masses connected by 2 spring & damper pairs in parallel with the
% decoupled stage which has a 4th mass incorporated
% The bottom mass is excited
% The decoupling stage is lowly damped and the coupling stage damping is
% varied
% Frequency response between input force and top mass displacement is found
% and compared with the identical Simulink model for verification purposes
%%%%%%%%%%%%%%%%%%%%%%%%%%%%%%%%%%%%%%%%%%%%%%%%%%%%%%%%%%%%%%%%%%%%%%%%%%%%%

clear all
close all

% initialize magdb matrix
magDB_d=[];

% 3 masses separated by 2 spring-damper pairs
% + decoupling stage mass, spring, damper (M3, k3, b3)

M0=23 ; M1=15; M2=16; M3=10;
k1=10000 ; k2=5000; k3=10000;
b1=100; b3=100; % Low damping in the decoupling stage

Bf = [1 ; 0 ; 0 ; 0];
M = [M0 0 0 0 ; 0 M1 0 0 ; 0 0 M2 0 ; 0 0 0 M3];
K = [(k1+k3) -k1 0 -k3 ; -k1 (k1+k2) -k2 0  ; 0 -k2 k2 0  ; -k3 0 0 k3 ];

% frequency bandwidth
w = linspace(0.1, 2*pi*50, 10000);

% natural frequencies
wn = sqrt(eig(K,M))  %rad/sec
f = wn/(2*pi)  %Hz

% vary damping%%%%%%%%%%%%%%%%%%%%%%%%%%%%%%%%%%%%%%%%%%%%

for m = 1:6
    b2 = 50 + 150*(m-1)

damp = [b1 -b1 0 0 ; -b1 (b1+b2) -b2 0  ; 0 -b2 (b2+b3) -b3 ; 0 0 -b3 b3 ];

% state-space
A = [zeros(4,4) , eye(4) ; -inv(M)*K , -inv(M)*damp];
B = [zeros(4,1) ; inv(M)*Bf];
C = [eye(4) , zeros(4,4)];
D = zeros(size(C,1), size(B,2));

inputs = {'F1'};
outputs = {'X1' 'X2' 'X3' 'X4'};

sys = ss(A,B,C,D,'inputname',inputs,'outputname',outputs);

% transfer function
[n,d] = ss2tf(A,B,C,D,1);
tf1 = tf(n(1,:),d);
tf2 = tf(n(2,:),d);
tf3 = tf(n(3,:),d)
tf4 = tf(n(4,:),d);

[mag,phase] = bode(sys(3,1),w);
magdb = 20*log10(mag);
magDB_d(m,:) = magdb(1,1,:);

% bode plot
figure(1)
bode(sys(3,1),w)
hold on
  end
hold off

% frequency response
figure(2)
semilogx(w/(2*pi),magDB_d(1,:),'r-', w/(2*pi),magDB_d(2,:),'m--',
w/(2*pi),magDB_d(3,:),'g:',...
    w/(2*pi),magDB_d(4,:),'b-', w/(2*pi),magDB_d(5,:),'k--',
w/(2*pi),magDB_d(6,:),'b-.')
```

```
title('Frequency response of connector leg with decoupling stage')
xlabel('Frequency (Hz)'); ylabel('|X_2 / F| (dB)');
legend('b_2 = 50 Ns/m','b_2 = 200 Ns/m',' b_2 = 350 Ns/m',' b_2 = 500 Ns/m',' b_2 =
650 Ns/m',' b_2 = 800 Ns/m');
AXIS([0.1 50 -200 -20])

save decoupled_leg_model
```

```
wn =

        0 + 0.0000i
  17.2460
  32.8653
  42.4796


f =

        0 + 0.0000i
   2.7448
   5.2307
   6.7608


b2 =

    50


Transfer function:

 -7.105e-015 s^7 + 1.364e-012 s^6 + 2.91e-011 s^5 + 0.9058 s^4 + 462 s^3 + 1.449e004 s^2
                                                                  + 5.435e005 s + 9.058e006
-----------------------------------------------------------------------------------------
-
s^8 + 33.72 s^7 + 3495 s^6 + 7.33e004 s^5 + 3.155e006 s^4 + 3.478e007 s^3 + 5.797e008 s^2
                                                              - 5.774e-006 s - 6.166e-005


b2 =

   200


Transfer function:

-7.105e-015 s^7 + 4.547e-013 s^6 + 1.455e-011 s^5 + 3.623 s^4 + 760.9 s^3 + 2.264e004 s^2
                                                                + 8.152e005 s + 9.058e006
-----------------------------------------------------------------------------------------
-
s^8 + 53.1 s^7 + 3898 s^6 + 1.175e005 s^5 + 3.677e006 s^4 + 5.217e007 s^3 + 5.797e008 s^2
                                                              + 6.414e-006 s + 6.465e-005


b2 =

   350


Transfer function:

 -4.547e-012 s^6 - 2.91e-010 s^5 + 6.341 s^4 + 1060 s^3 + 3.08e004 s^2 + 1.087e006 s
                                                                              + 9.058e006
-----------------------------------------------------------------------------------------
--
s^8 + 72.47 s^7 + 4301 s^6 + 1.617e005 s^5 + 4.198e006 s^4 + 6.957e007 s^3 + 5.797e008
s^2
                                                              - 2.145e-007 s - 7.986e-006
```

```
b2 =

   500

Transfer function:

-1.421e-014 s^7 - 3.638e-012 s^6 - 2.619e-010 s^5 + 9.058 s^4 + 1359 s^3 + 3.895e004 s^2
                                                                  + 1.359e006 s + 9.058e006
-----------------------------------------------------------------------------------------
-
s^8 + 91.85 s^7 + 4704 s^6 + 2.059e005 s^5 + 4.72e006 s^4 + 8.696e007 s^3 + 5.797e008 s^2
                                                                + 5.629e-006 s + 2.564e-005


b2 =

   650

Transfer function:

 1.421e-014 s^7 + 7.276e-012 s^6 + 3.201e-010 s^5 + 11.78 s^4 + 1658 s^3 + 4.71e004 s^2
                                                                   + 1.63e006 s + 9.058e006
-----------------------------------------------------------------------------------------
--
s^8 + 111.2 s^7 + 5107 s^6 + 2.501e005 s^5 + 5.242e006 s^4 + 1.043e008 s^3 + 5.797e008
s^2
                                                                + 7.323e-006 s + 4.036e-005


b2 =

   800

Transfer function:

 1.137e-013 s^7 + 8.185e-012 s^6 + 5.821e-010 s^5 + 14.49 s^4 + 1957 s^3 + 5.525e004 s^2
                                                                  + 1.902e006 s + 9.058e006
-----------------------------------------------------------------------------------------
--
s^8 + 130.6 s^7 + 5510 s^6 + 2.944e005 s^5 + 5.764e006 s^4 + 1.217e008 s^3 + 5.797e008
s^2
                                                                - 2.133e-005 s - 7.596e-005
```

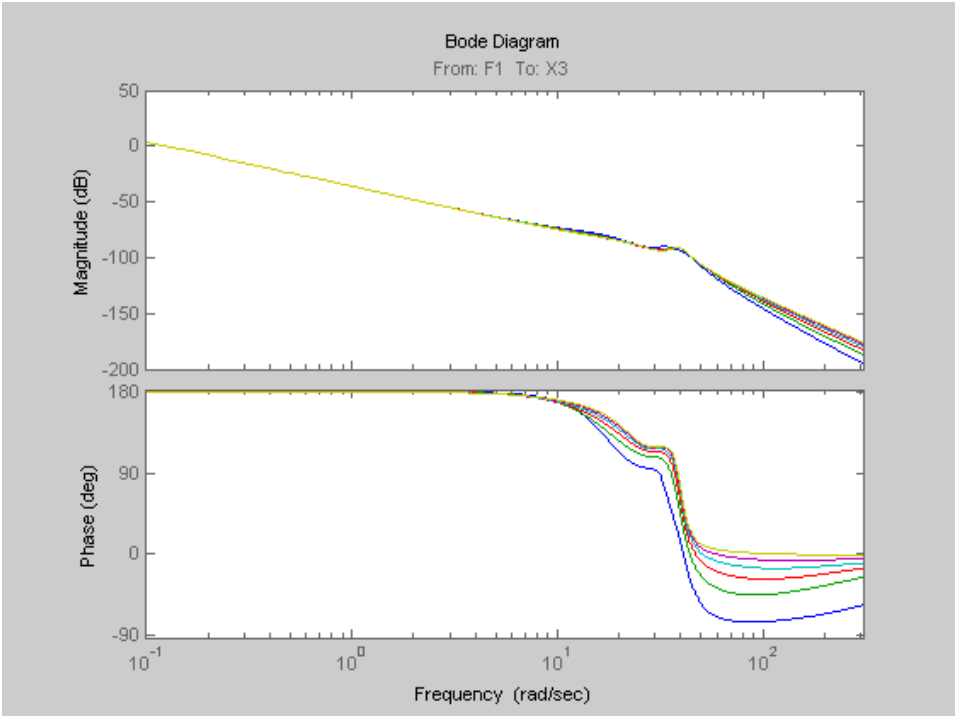

Figure A-5. Magnitude and phase frequency response plots for the passive two-stage connector leg with varying damping

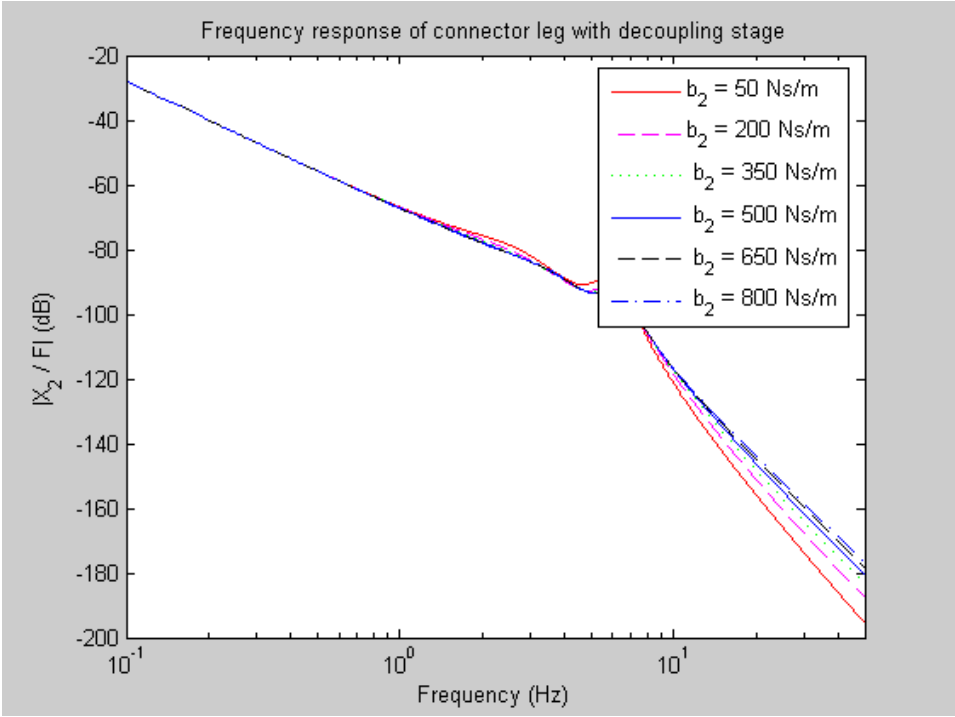

Figure A-6. Magnitude of the frequency response for the passive two-stage connector leg with varying damping

A.4 Two-Stage Connector Leg Natural Frequencies

```
% Created 04/18/06
% Two-stage connector model
% The bottom mass is excited
% Natural frequencies are calculated for verification
%%%%%%%%%%%%%%%%%%%%%%%%%%%%%%%%%%%%%%%%%%%%%%%%%%%%%%%%%%%%%%%%%%%%%%%%%%

clear all
close all

% initialize magdb matrix
magDB_b=[];

% mass and stiffness
M1=15 ; M2=16; k1=10000 ; k2=5000 ;
b1=100; b2=200;

Bf = [1 ; 0] ;
M = [M2 0 ; 0 M1];
K = [k2 -k2 ; -k2 k1+k2];
damp = [b2 -b2 ; -b2 b1+b2];

% frequency bandwidth
w = linspace(0.1, 2*pi*50, 10000);

% natural frequencies
wn = sqrt(eig(K,M))  %rad/sec
f = wn/(2*pi)  %Hz

% % state-space
% A = [zeros(2,2) , eye(2) ; -inv(M)*K , -inv(M)*damp];
% B = [zeros(2,1) ; inv(M)*Bf];
% C = [1 0 0 0 ; 0 1 0 0 ];
% D = zeros(size(C,1), size(B,2));
%
% sys = ss(A,B,C,D)
% [mag,phase] = bode(sys(2,1),w);
% magdb = 20*log10(mag);
%
% % transfer function
% [n,d] = ss2tf(A,B,C,D);
% tf1 = tf(n(1,:),d);
% tf2 = tf(n(2,:),d);
%
% % bode plot
% figure(1)
% bode(sys(2,1),w)
%
% % frequency response
% figure(2)
% semilogx(w/(2*pi),magdb(1,:))
% title('Frequency response function of passive two-stage connector leg')
% xlabel('Frequency (Hz)'); ylabel('|X_1 / F| (dB)');
% legend('b_2 = 200 Ns/m');
% %AXIS([0.1 50 -180 -20])
```

```
wn =

   13.5916
   33.5823


f =

    2.1632
    5.3448
```

APPENDIX B
SIMULINK MODELS OF CONNECTOR LEGS

B.1 Basic Connector Leg Model

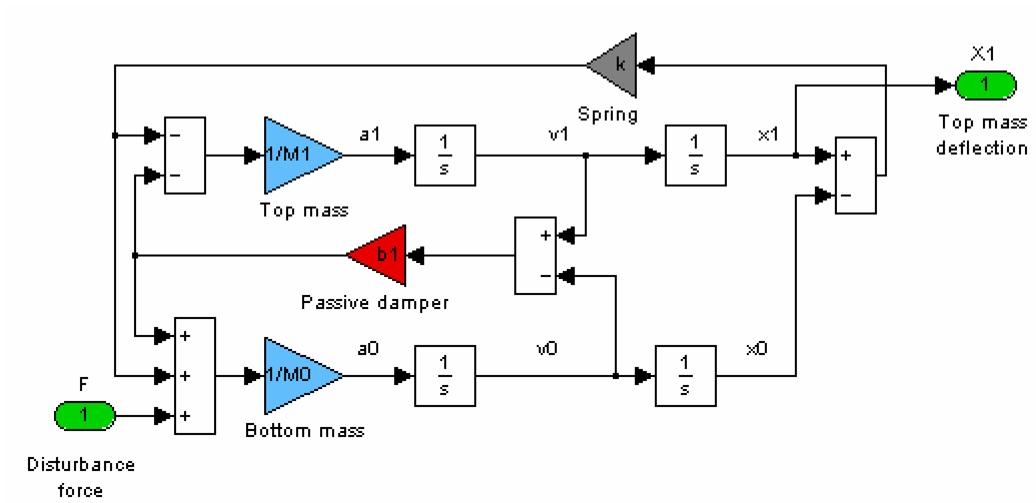

Figure B-1. Simulink block diagram of the passive basic connector leg

```
% Created 04/6/06
% Basic connector leg
% Linearize the simulink model and find the frequency response
%%%%%%%%%%%%%%%%%%%%%%%%%%%%%%%%%%%%%%%%%%%%%%%%%%%%%%%%%%%%%%%

clear all

% mass and stiffness
k=5000; M0=38; M1=16;

% vary damping%%%%%%%%%%%%%%%%%
for m = 1:6
    b1 = 50 + 150*(m-1)

% linearize Simulink model and get transfer function between input force
% and output displacemt

[A,B,C,D]=linmod('FRF_basic')
[num,den]=ss2tf(A,B,C,D);
sys = tf(num,den)

% frequency response
f=linspace(0.1,50,3000);
w=2*pi*f;

figure(1)
bode(sys,w)
title('Frequency response')
hold on

end

hold off
```

```
b1 =

    50

Warning: Using a default value of 0.2 for maximum step size. The simulation step size
will be limited to be less than this value.

A =

         0    1.0000         0         0
 -312.5000   -3.1250    3.1250  312.5000
  131.5789    1.3158   -1.3158 -131.5789
         0         0    1.0000         0


B =

         0
         0
    0.0263
         0


C =

    1.0000         0         0         0


D =

     0


Transfer function:
  3.553e-015 s^3 - 2.274e-013 s^2 + 0.08224 s + 8.224
-------------------------------------------------------
s^4 + 4.441 s^3 + 444.1 s^2 - 1.456e-012 s + 1.161e-011


b1 =

   200

Warning: Using a default value of 0.2 for maximum step size. The simulation step size
will be limited to be less than this value.

A =

         0    1.0000         0         0
 -312.5000  -12.5000   12.5000  312.5000
  131.5789    5.2632   -5.2632 -131.5789
         0         0    1.0000         0


B =

         0
         0
    0.0263
         0


C =

    1.0000         0         0         0


D =

     0


Transfer function:
  1.066e-014 s^3 - 1.705e-013 s^2 + 0.3289 s + 8.224
-------------------------------------------------------
s^4 + 17.76 s^3 + 444.1 s^2 - 1.568e-013 s + 1.161e-011


b1 =

   350
```

```
Warning: Using a default value of 0.2 for maximum step size. The simulation step size
will be limited to be less than this value.

A =

         0    1.0000         0         0
 -312.5000  -21.8750   21.8750  312.5000
  131.5789    9.2105   -9.2105 -131.5789
         0         0    1.0000         0


B =

         0
         0
    0.0263
         0


C =

    1.0000         0         0         0


D =

     0


Transfer function:
  3.197e-014 s^3 + 5.684e-014 s^2 + 0.5757 s + 8.224
-----------------------------------------------------
s^4 + 31.09 s^3 + 444.1 s^2 + 1.217e-012 s + 1.161e-011


b1 =

   500

Warning: Using a default value of 0.2 for maximum step size. The simulation step size
will be limited to be less than this value.

A =

         0    1.0000         0         0
 -312.5000  -31.2500   31.2500  312.5000
  131.5789   13.1579  -13.1579 -131.5789
         0         0    1.0000         0


B =

         0
         0
    0.0263
         0


C =

    1.0000         0         0         0


D =

     0


Transfer function:
 4.263e-014 s^3 + 7.958e-013 s^2 + 0.8224 s + 8.224
----------------------------------------------------
s^4 + 44.41 s^3 + 444.1 s^2 + 2.7e-012 s + 1.161e-011


b1 =

   650

Warning: Using a default value of 0.2 for maximum step size. The simulation step size
will be limited to be less than this value.
```

```
A =

         0    1.0000         0         0
 -312.5000  -40.6250   40.6250  312.5000
  131.5789   17.1053  -17.1053 -131.5789
         0         0    1.0000         0


B =

         0
         0
    0.0263
         0


C =

    1.0000         0         0         0


D =

     0


Transfer function:
   5.684e-014 s^3 + 7.39e-013 s^2 + 1.069 s + 8.224
-----------------------------------------------------
s^4 + 57.73 s^3 + 444.1 s^2 - 9.969e-014 s + 1.161e-011


b1 =

   800

Warning: Using a default value of 0.2 for maximum step size. The simulation step size
will be limited to be less than this value.

A =

         0    1.0000         0         0
 -312.5000  -50.0000   50.0000  312.5000
  131.5789   21.0526  -21.0526 -131.5789
         0         0    1.0000         0


B =

         0
         0
    0.0263
         0


C =

    1.0000         0         0         0


D =

     0


Transfer function:
   2.842e-014 s^3 + 9.095e-013 s^2 + 1.316 s + 8.224
-----------------------------------------------------
s^4 + 71.05 s^3 + 444.1 s^2 + 1.422e-013 s + 1.161e-011
```

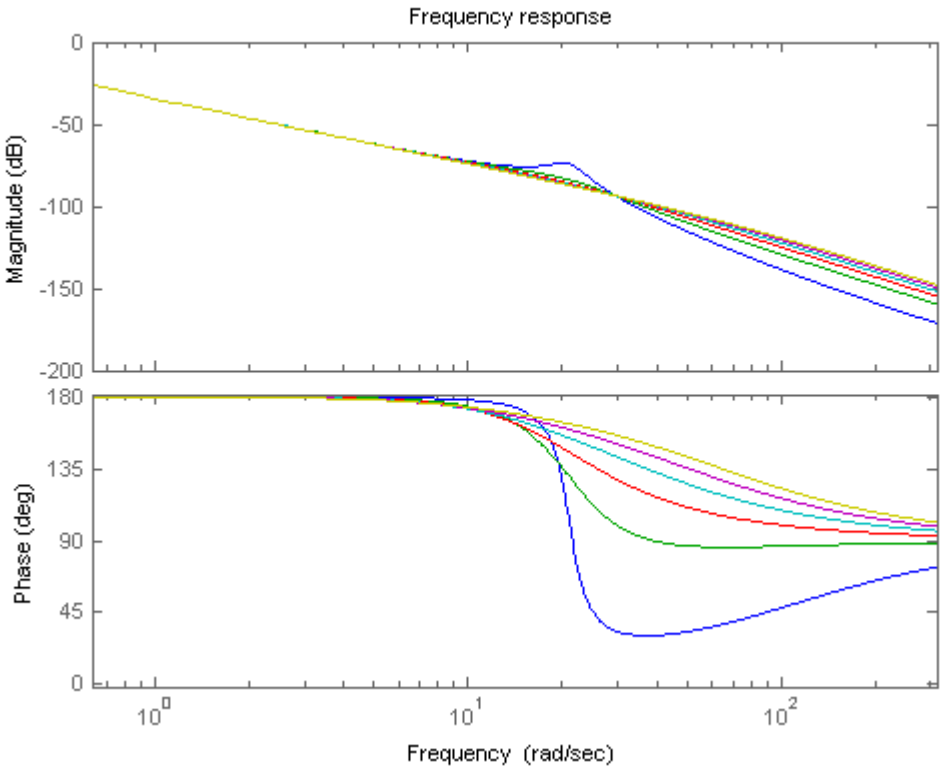

Figure B-2. Magnitude and phase frequency response plots of the passive basic connector leg

B.2 Two-Stage Connector Leg Model

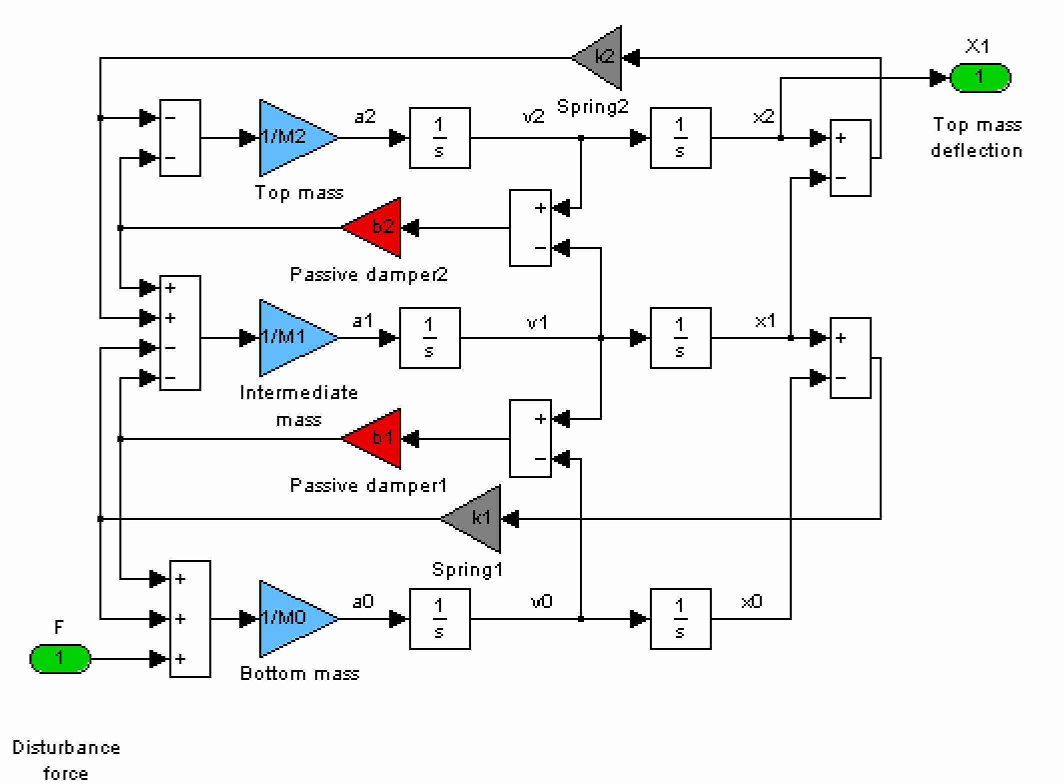

Figure B-3. Simulink block diagram of the passive two-stage connector leg

```
% Created 04/6/06
% Two-stage connector leg
% Linearize the simulink model and find the frequency response
%%%%%%%%%%%%%%%%%%%%%%%%%%%%%%%%%%%%%%%%%%%%%%%%%%%%%%%%%%%%%%

clear all

% 3 masses separated by 2 spring-damper pairs
M0=23 ; M1=15; M2=16;
k1=10000 ; k2=5000;
b1= 100;

% frequency response
f=linspace(0.1,50,3000);
w=2*pi*f;

% vary damping%%%%%%%%%%%%%%%%%%%%
for m = 1:6
    b2 = 50 + 150*(m-1)

% linearize Simulink model and get transfer function between input force
% and output displacement
[A,B,C,D]=linmod('FRF_coupling')
[num,den]=ss2tf(A,B,C,D);
sys = tf(num,den)

% frequency response
figure(1)
bode(sys,w)
title('Frequency response')
hold on

end

hold off
```

```
save frf_coupling


b2 =

    50

Warning: Using a default value of 0.2 for maximum step size. The simulation step size
will be limited to be less than this value.

A =

  1.0e+003 *

         0         0         0         0         0    0.0010
    0.3333   -0.0100    0.0067   -1.0000    0.6667    0.0033
         0    0.0043   -0.0043    0.4348   -0.4348         0
         0    0.0010         0         0         0         0
         0         0    0.0010         0         0         0
   -0.3125    0.0031         0    0.3125         0   -0.0031


B =

         0
         0
    0.0435
         0
         0
         0


C =

    1.0000         0         0         0         0         0


D =

     0


Transfer function:
 1.421e-014 s^5 - 1.592e-012 s^4 + 2.001e-011 s^3 + 0.9058 s^2 + 181.2 s + 9058
-------------------------------------------------------------------------------
s^6 + 17.47 s^5 + 1796 s^4 + 9783 s^3 + 4.891e005 s^2 - 2.021e-010 s + 3.833e-008


b2 =

   200

Warning: Using a default value of 0.2 for maximum step size. The simulation step size
will be limited to be less than this value.

A =

  1.0e+003 *

         0         0         0         0         0    0.0010
    0.3333   -0.0200    0.0067   -1.0000    0.6667    0.0133
         0    0.0043   -0.0043    0.4348   -0.4348         0
         0    0.0010         0         0         0         0
         0         0    0.0010         0         0         0
   -0.3125    0.0125         0    0.3125         0   -0.0125


B =

         0
         0
    0.0435
         0
         0
         0


C =

    1.0000         0         0         0         0         0
```

```
D =

     0


Transfer function:
    -4.263e-014 s^5 + 2.274e-013 s^4 - 2.183e-011 s^3 + 3.623 s^2 + 452.9 s + 9058
-------------------------------------------------------------------------------------
s^6 + 36.85 s^5 + 1943 s^4 + 2.446e004 s^3 + 4.891e005 s^2 + 2.137e-009 s + 5.242e-008


b2 =

   350

Warning: Using a default value of 0.2 for maximum step size. The simulation step size
will be limited to be less than this value.

A =

  1.0e+003 *

         0         0         0         0         0    0.0010
    0.3333   -0.0300    0.0067   -1.0000    0.6667    0.0233
         0    0.0043   -0.0043    0.4348   -0.4348         0
         0    0.0010         0         0         0         0
         0         0    0.0010         0         0         0
   -0.3125    0.0219         0    0.3125         0   -0.0219


B =

         0
         0
    0.0435
         0
         0
         0


C =

    1.0000         0         0         0         0         0


D =

     0


Transfer function:
    1.279e-013 s^5 + 4.547e-012 s^4 + 1.528e-010 s^3 + 6.341 s^2 + 724.6 s + 9058
-------------------------------------------------------------------------------------
s^6 + 56.22 s^5 + 2090 s^4 + 3.913e004 s^3 + 4.891e005 s^2 - 9.299e-009 s + 7.312e-009


b2 =

   500

Warning: Using a default value of 0.2 for maximum step size. The simulation step size
will be limited to be less than this value.

A =

  1.0e+003 *

         0         0         0         0         0    0.0010
    0.3333   -0.0400    0.0067   -1.0000    0.6667    0.0333
         0    0.0043   -0.0043    0.4348   -0.4348         0
         0    0.0010         0         0         0         0
         0         0    0.0010         0         0         0
   -0.3125    0.0312         0    0.3125         0   -0.0312


B =

         0
         0
```

```
    0.0435
         0
         0
         0


C =

    1.0000         0         0         0         0         0


D =

     0


Transfer function:
  -1.563e-013 s^5 - 5.457e-012 s^4 - 1.601e-010 s^3 + 9.058 s^2 + 996.4 s + 9058
--------------------------------------------------------------------------------
s^6 + 75.6 s^5 + 2236 s^4 + 5.38e004 s^3 + 4.891e005 s^2 + 6.03e-010 s + 4.033e-009


b2 =

   650

Warning: Using a default value of 0.2 for maximum step size. The simulation step size
will be limited to be less than this value.

A =

  1.0e+003 *

         0         0         0         0         0    0.0010
    0.3333   -0.0500    0.0067   -1.0000    0.6667    0.0433
         0    0.0043   -0.0043    0.4348   -0.4348         0
         0    0.0010         0         0         0         0
         0         0    0.0010         0         0         0
   -0.3125    0.0406         0    0.3125         0   -0.0406


B =

         0
         0
    0.0435
         0
         0
         0


C =

    1.0000         0         0         0         0         0


D =

     0


Transfer function:
     1.563e-013 s^5 + 9.095e-013 s^4 - 5.821e-011 s^3 + 11.78 s^2 + 1268 s + 9058
--------------------------------------------------------------------------------
s^6 + 94.97 s^5 + 2383 s^4 + 6.848e004 s^3 + 4.891e005 s^2 - 1.006e-009 s + 4.033e-009


b2 =

   800

Warning: Using a default value of 0.2 for maximum step size. The simulation step size
will be limited to be less than this value.

A =

  1.0e+003 *

         0         0         0         0         0    0.0010
    0.3333   -0.0600    0.0067   -1.0000    0.6667    0.0533
         0    0.0043   -0.0043    0.4348   -0.4348         0
```

```
         0    0.0010         0         0         0         0
         0         0    0.0010         0         0         0
   -0.3125    0.0500         0    0.3125         0   -0.0500

B =

         0
         0
    0.0435
         0
         0
         0

C =

    1.0000         0         0         0         0         0

D =

     0

Transfer function:
     1.421e-014 s^5 - 4.547e-013 s^4 - 4.366e-011 s^3 + 14.49 s^2 + 1540 s + 9058
--------------------------------------------------------------------------------
s^6 + 114.3 s^5 + 2530 s^4 + 8.315e004 s^3 + 4.891e005 s^2 - 5.076e-009 s - 2.264e-008
```

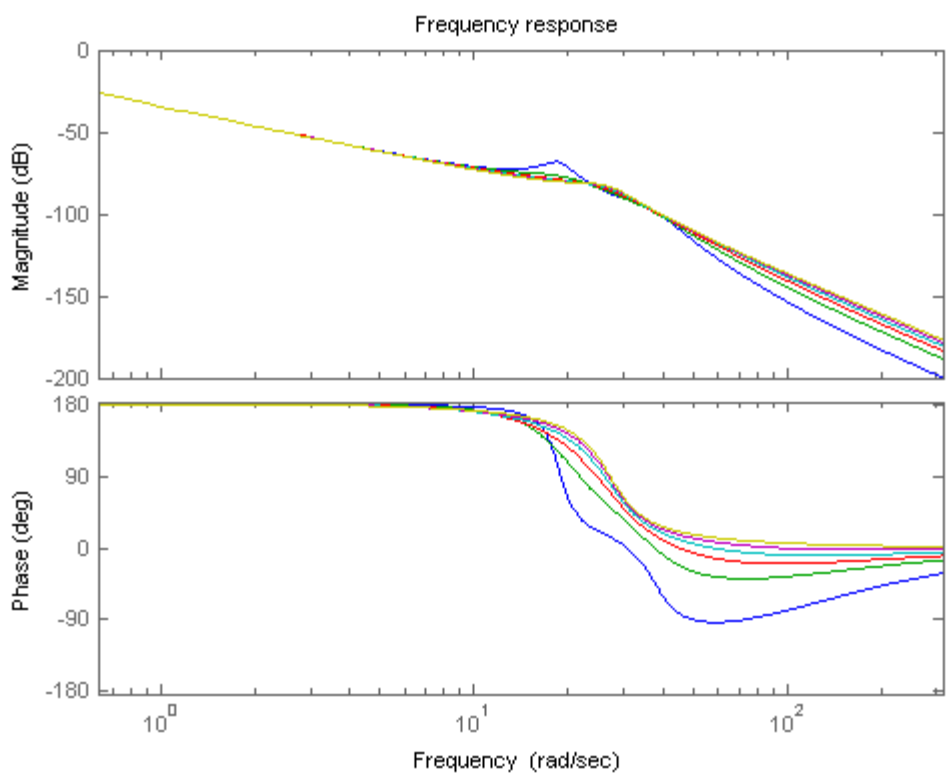

Figure B-4. Magnitude and phase frequency response plots of the passive two-stage connector leg

B.3 Connector Leg Model with Decoupling Stage

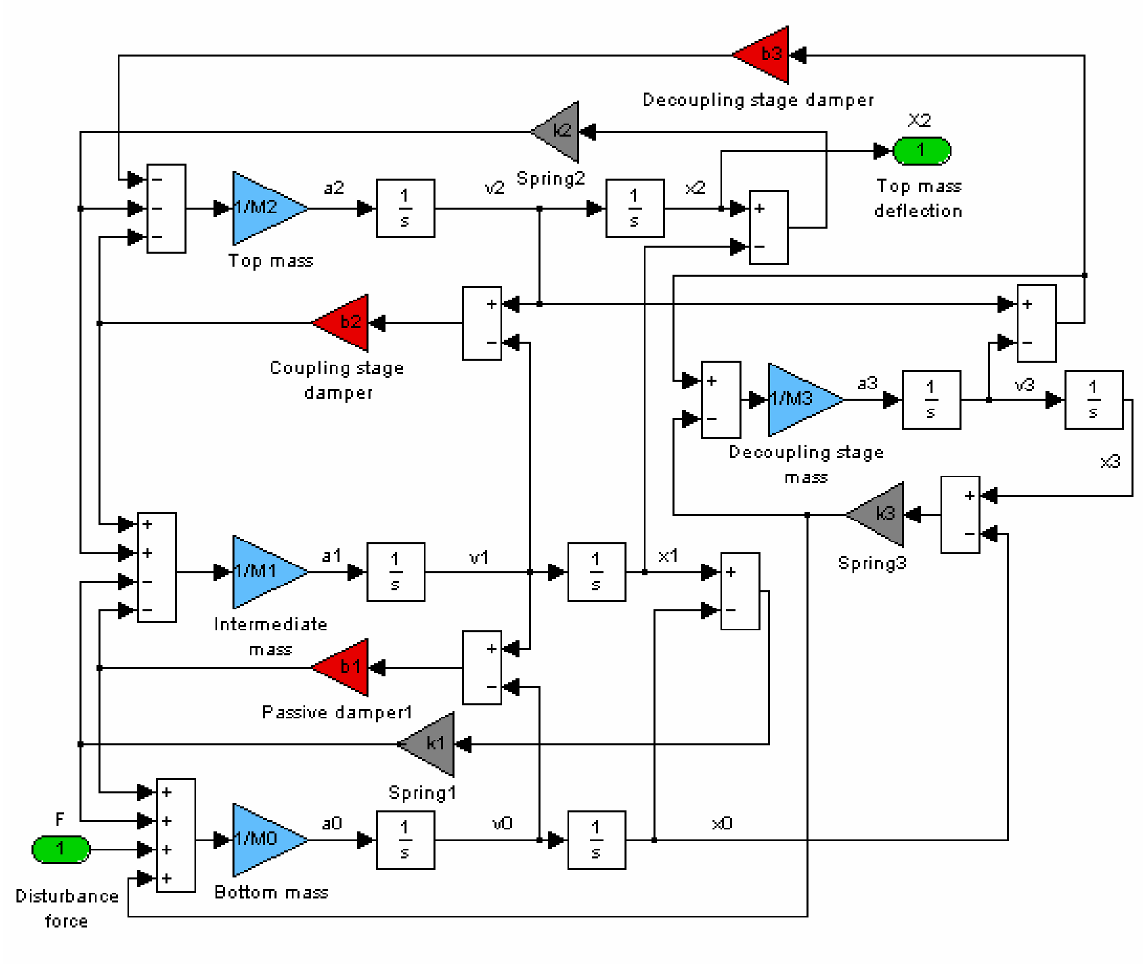

Figure B-5. Simulink block diagram of the passive connector leg with decoupling stage

```
% Created 04/6/06
% Connector leg with decoupling stage
% Linearize the simulink model and find the frequency response
%%%%%%%%%%%%%%%%%%%%%%%%%%%%%%%%%%%%%%%%%%%%%%%%%%%%%%%%%%%%%%

clear all

% 3 masses separated by 2 spring-damper pairs
% + decoupling stage mass, spring, damper (M3, k3, b3)

M0=23 ; M1=15; M2=16; M3=10;
k1=10000 ; k2=5000; k3=10000;
b1=100; b3=100;

f=linspace(0.1,50,3000);
w=2*pi*f;

% vary damping%%%%%%%%%%%%%%%%%%%%%
for m = 1:6
    b2 = 50 + 150*(m-1)

[A,B,C,D]=linmod('FRF_decoupling')
[num,den]=ss2tf(A,B,C,D);
```

```
sys = tf(num,den)

% frequency response
figure(1)
bode(sys,w)
title('Frequency response function of passive connector leg with decoupled stage')
hold on

end

hold off

save frf_decoupling
```

```
b2 =

    50

Warning: Using a default value of 0.2 for maximum step size. The simulation step size
will be limited to be less than this value.

A =

  1.0e+003 *

         0         0         0         0         0         0    0.0010         0
    0.3333   -0.0100    0.0067   -1.0000    0.6667         0    0.0033         0
         0    0.0043   -0.0043    0.4348   -0.8696    0.4348         0         0
         0    0.0010         0         0         0         0         0         0
         0         0    0.0010         0         0         0         0         0
         0         0         0         0         0         0         0    0.0010
   -0.3125    0.0031         0    0.3125         0         0   -0.0094    0.0062
         0         0         0         0    1.0000   -1.0000    0.0001   -0.0001


B =

         0
         0
    0.0435
         0
         0
         0
         0
         0


C =

    1.0000         0         0         0         0         0         0         0


D =

     0


Transfer function:

 3.638e-012 s^6 + 7.276e-012 s^5 + 0.9058 s^4 + 453 s^3 + 1.27e004 s^2 + 4.538e005 s
                                                                                + 9.058e006
-----------------------------------------------------------------------------------------
--
s^8 + 23.82 s^7 + 3322 s^6 + 5.121e004 s^5 + 3.002e006 s^4 + 2.429e007 s^3 + 5.797e008
s^2
                                                                - 3.756e-006 s - 6.485e-005


b2 =

   200

Warning: Using a default value of 0.2 for maximum step size. The simulation step size
will be limited to be less than this value.
```

```
A =

  1.0e+003 *

         0         0         0         0         0         0    0.0010         0
    0.3333   -0.0200    0.0067   -1.0000    0.6667         0    0.0133         0
         0    0.0043   -0.0043    0.4348   -0.8696    0.4348         0         0
         0    0.0010         0         0         0         0         0         0
         0         0    0.0010         0         0         0         0         0
         0         0         0         0         0         0         0    0.0010
   -0.3125    0.0125         0    0.3125         0         0   -0.0187    0.0062
         0         0         0         0    1.0000   -1.0000    0.0001   -0.0001


B =

         0
         0
    0.0435
         0
         0
         0
         0
         0


C =

    1.0000         0         0         0         0         0         0         0


D =

     0


Transfer function:

 -7.105e-015 s^7 + 5.457e-012 s^6 + 8.731e-011 s^5 + 3.623 s^4 + 725 s^3 + 1.816e004 s^2
                                                                  + 7.255e005 s + 9.058e006
-----------------------------------------------------------------------------------------
-
s^8 + 43.2 s^7 + 3534 s^6 + 9.397e004 s^5 + 3.295e006 s^4 + 4.168e007 s^3 + 5.797e008 s^2
                                                             + 1.031e-005 s + 9.043e-005


b2 =

   350

Warning: Using a default value of 0.2 for maximum step size. The simulation step size
will be limited to be less than this value.

A =

  1.0e+003 *

         0         0         0         0         0         0    0.0010         0
    0.3333   -0.0300    0.0067   -1.0000    0.6667         0    0.0233         0
         0    0.0043   -0.0043    0.4348   -0.8696    0.4348         0         0
         0    0.0010         0         0         0         0         0         0
         0         0    0.0010         0         0         0         0         0
         0         0         0         0         0         0         0    0.0010
   -0.3125    0.0219         0    0.3125         0         0   -0.0281    0.0062
         0         0         0         0    1.0000   -1.0000    0.0001   -0.0001


B =

         0
         0
    0.0435
         0
         0
         0
         0
         0
```

```
C =

    1.0000         0         0         0         0         0         0         0


D =

     0


Transfer function:

 6.395e-014 s^7 + 5.002e-012 s^6 + 3.783e-010 s^5 + 6.341 s^4 + 997 s^3 + 2.362e004 s^2
                                                                    + 9.973e005 s + 9.058e006
-----------------------------------------------------------------------------------------
--
s^8 + 62.57 s^7 + 3745 s^6 + 1.367e005 s^5 + 3.588e006 s^4 + 5.907e007 s^3 + 5.797e008
s^2
                                                                - 2.093e-006 s - 6.074e-006


b2 =

   500

Warning: Using a default value of 0.2 for maximum step size. The simulation step size
will be limited to be less than this value.

A =

  1.0e+003 *

         0         0         0         0         0         0    0.0010         0
    0.3333   -0.0400    0.0067   -1.0000    0.6667         0    0.0333         0
         0    0.0043   -0.0043    0.4348   -0.8696    0.4348         0         0
         0    0.0010         0         0         0         0         0         0
         0         0    0.0010         0         0         0         0         0
         0         0         0         0         0         0         0    0.0010
   -0.3125    0.0312         0    0.3125         0         0   -0.0375    0.0062
         0         0         0         0    1.0000   -1.0000    0.0001   -0.0001


B =

         0
         0
    0.0435
         0
         0
         0
         0
         0


C =

    1.0000         0         0         0         0         0         0         0


D =

     0


Transfer function:

 -4.263e-014 s^7 - 1.046e-011 s^6 - 6.985e-010 s^5 + 9.058 s^4 + 1269 s^3 + 2.909e004 s^2
                                                                    + 1.269e006 s + 9.058e006
-----------------------------------------------------------------------------------------
--
s^8 + 81.95 s^7 + 3956 s^6 + 1.795e005 s^5 + 3.881e006 s^4 + 7.646e007 s^3 + 5.797e008
s^2
```

```
                                                                    + 2.349e-006 s - 3.326e-005


b2 =

   650

Warning: Using a default value of 0.2 for maximum step size. The simulation step size
will be limited to be less than this value.

A =

  1.0e+003 *

         0         0         0         0         0         0    0.0010         0
    0.3333   -0.0500    0.0067   -1.0000    0.6667         0    0.0433         0
         0    0.0043   -0.0043    0.4348   -0.8696    0.4348         0         0
         0    0.0010         0         0         0         0         0         0
         0         0    0.0010         0         0         0         0         0
         0         0         0         0         0         0         0    0.0010
   -0.3125    0.0406         0    0.3125         0         0   -0.0469    0.0062
         0         0         0         0    1.0000   -1.0000    0.0001   -0.0001


B =

         0
         0
    0.0435
         0
         0
         0
         0
         0


C =

    1.0000         0         0         0         0         0         0         0


D =

     0


Transfer function:

 -5.684e-014 s^7 - 2.728e-012 s^6 - 2.91e-010 s^5 + 11.78 s^4 + 1541 s^3 + 3.455e004 s^2

                                                                    + 1.541e006 s + 9.058e006

-----------------------------------------------------------------------------------------
--
s^8 + 101.3 s^7 + 4167 s^6 + 2.222e005 s^5 + 4.174e006 s^4 + 9.386e007 s^3 + 5.797e008
s^2

                                                                    + 6.949e-006 s + 4.251e-005


b2 =

   800

Warning: Using a default value of 0.2 for maximum step size. The simulation step size
will be limited to be less than this value.

A =

  1.0e+003 *

         0         0         0         0         0         0    0.0010         0
    0.3333   -0.0600    0.0067   -1.0000    0.6667         0    0.0533         0
         0    0.0043   -0.0043    0.4348   -0.8696    0.4348         0         0
         0    0.0010         0         0         0         0         0         0
         0         0    0.0010         0         0         0         0         0
         0         0         0         0         0         0         0    0.0010
   -0.3125    0.0500         0    0.3125         0         0   -0.0562    0.0062
         0         0         0         0    1.0000   -1.0000    0.0001   -0.0001
```

```
B =

         0
         0
    0.0435
         0
         0
         0
         0
         0
         0

C =

    1.0000         0         0         0         0         0         0         0

D =

     0

Transfer function:
 3.979e-013 s^7 + 7.276e-012 s^6 + 8.731e-010 s^5 + 14.49 s^4 + 1813 s^3 + 4.001e004 s^2
                                                                  + 1.813e006 s + 9.058e006
-----------------------------------------------------------------------------------------
-
s^8 + 120.7 s^7 + 4378 s^6 + 2.65e005 s^5 + 4.467e006 s^4 + 1.112e008 s^3 + 5.797e008 s^2
                                                                - 1.425e-005 s - 6.582e-005
```

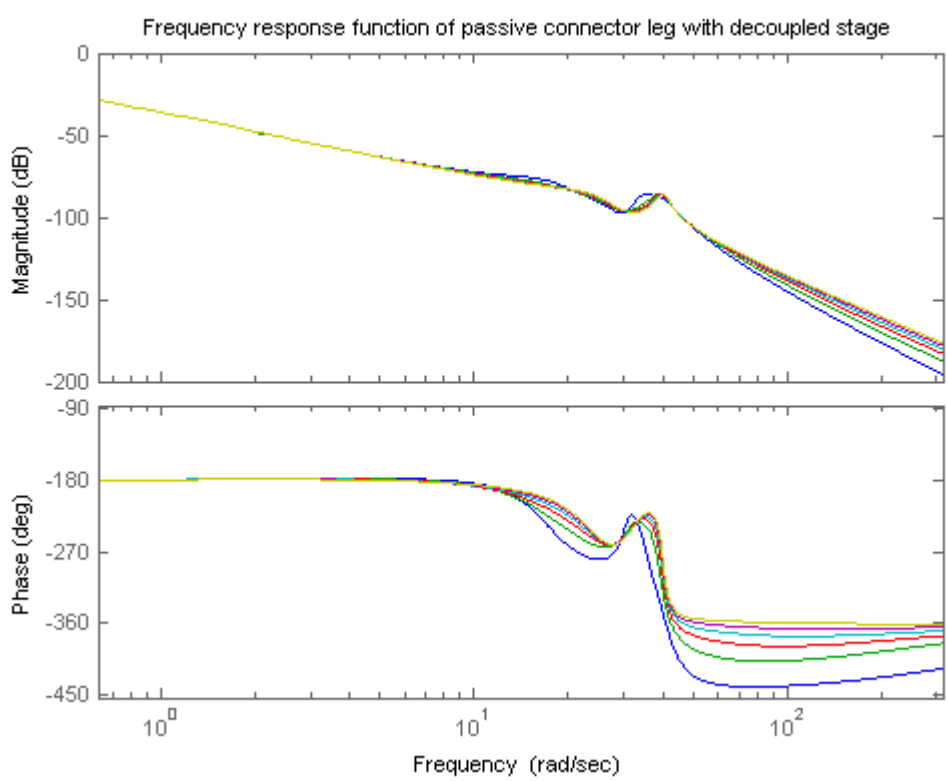

Figure B-6. Magnitude and phase frequency response plots of the passive connector leg with decoupling stage

APPENDIX C
PROTOTYPE DRAWINGS

C.1 Prototype 1: Double-Shafted Damper with Aluminum Housing

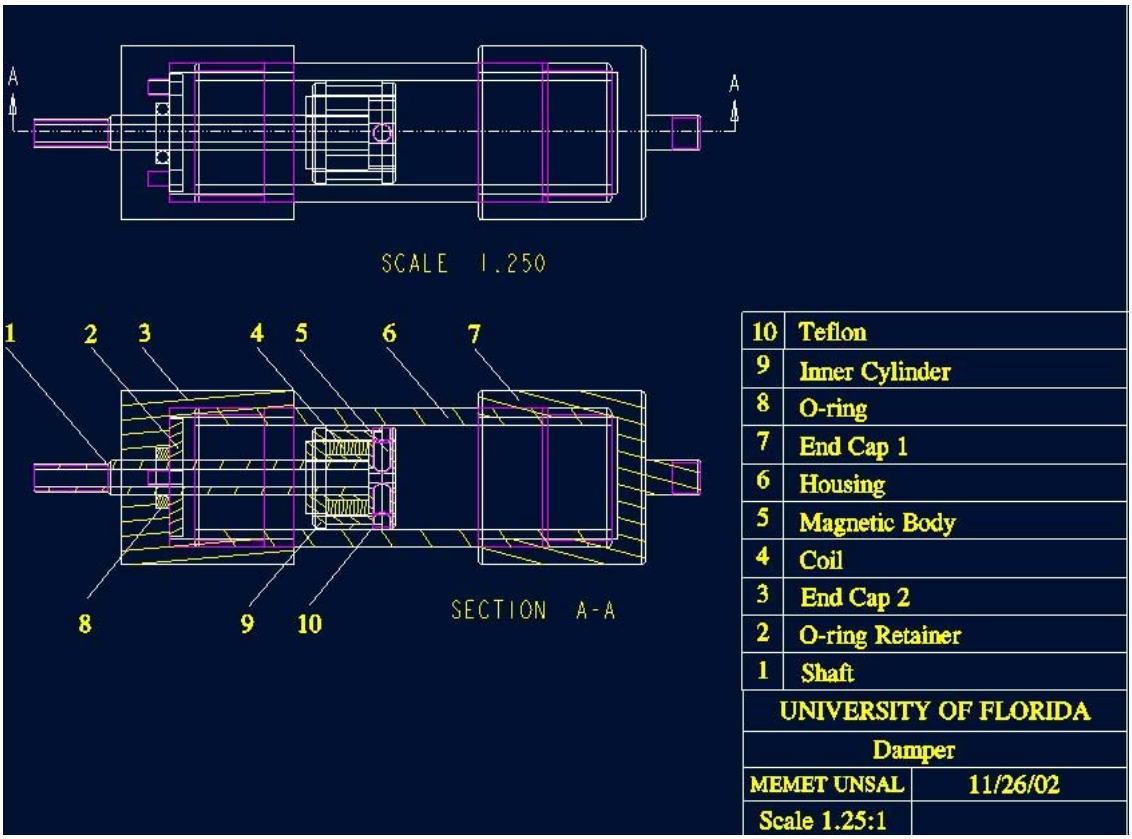

Figure C-1. Technical drawing of double-shafted damper with aluminum housing

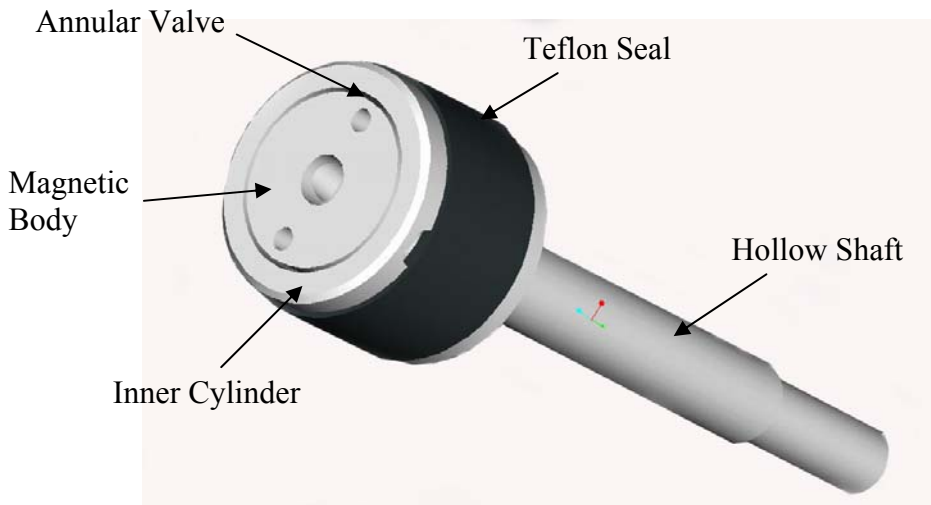

Figure C-2. Inside view of damper showing Teflon seal

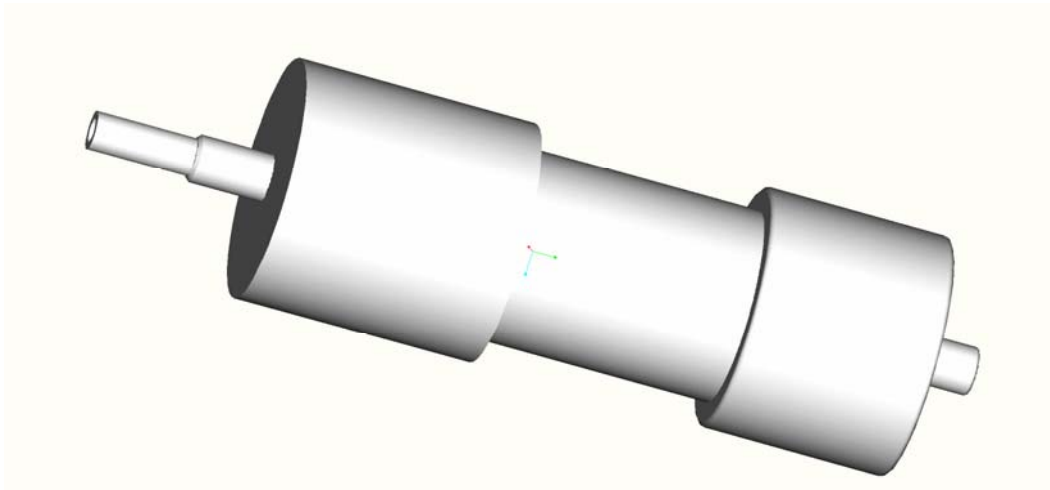

Figure C-3. Outside view of double-shafted damper with aluminum housing

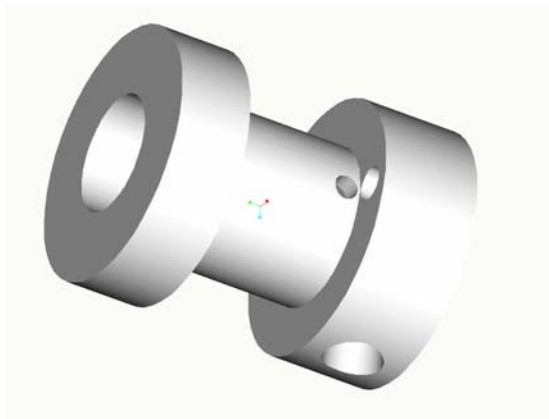

Figure C-4. Magnetic body around which the magnet wire is wrapped

C.2 Prototype 2: Double-Shafted Damper with Steel Housing

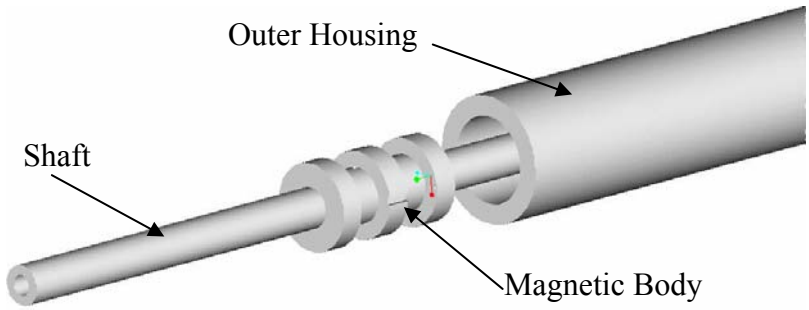

Figure C-5. Schematic of the double-shafted damper with steel housing

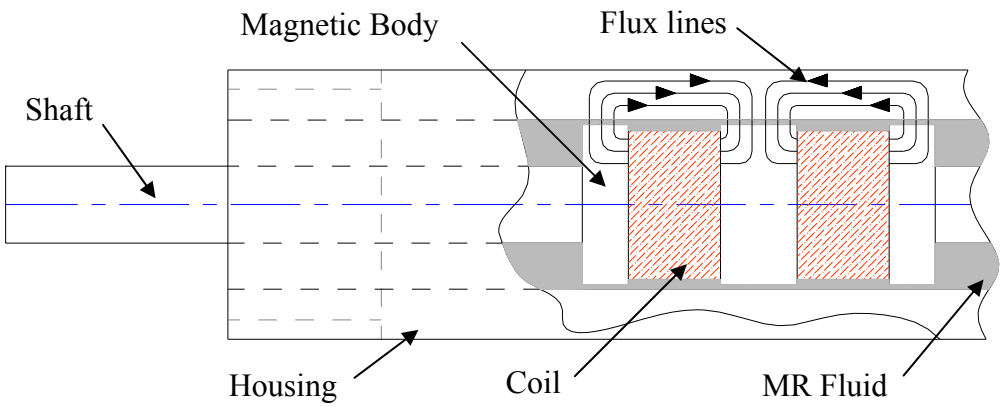

Figure C-6. Schematic of the damper showing the path of the flux lines

Figure C-7. Low-carbon steel housing of the double-shafted damper

Figure C-8. Double-shafted MR damper with steel housing

C.3 Prototype 3: Syringe-Type Damper with Parallel Rod

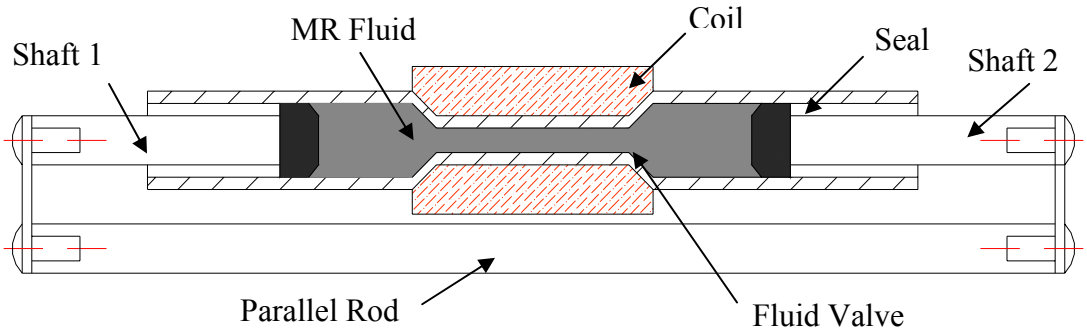

Figure C-9. Syringe type damper with parallel rod

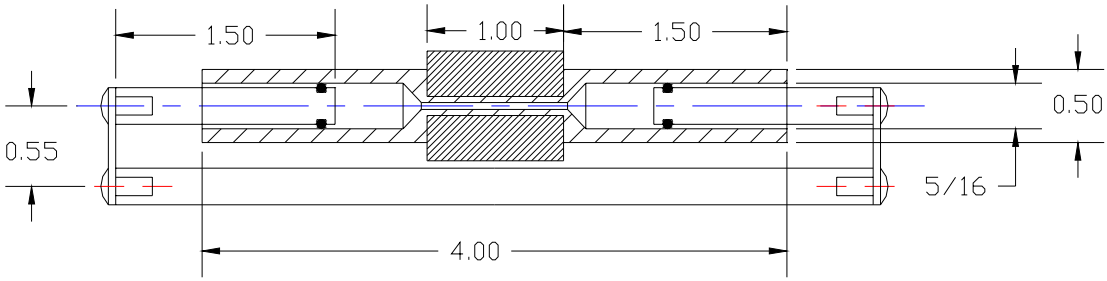

Figure C-10. Technical drawing of syringe type damper with parallel rod

C.4 Prototype 4: Syringe Type Damper with Cylindrical Outer Housing

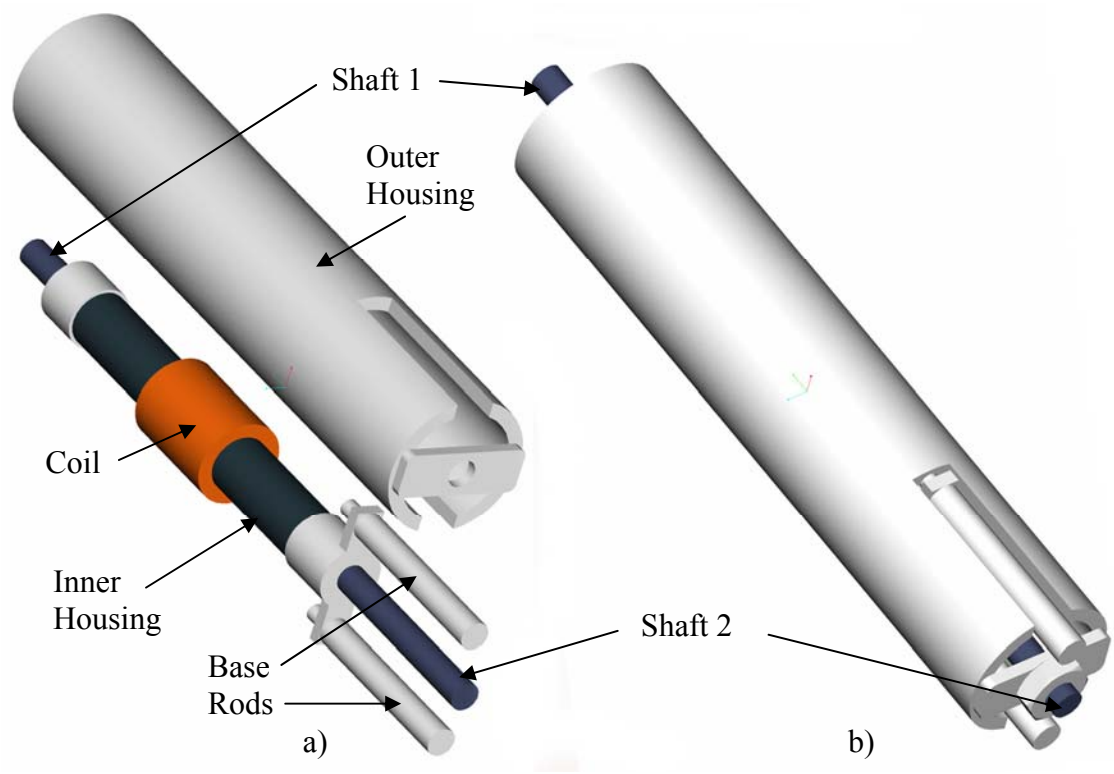

Figure C-11. Syringe type damper with cylindrical outer housing with a) exploded view showing the inner housing and the coil; b) view of the fully assembled damper

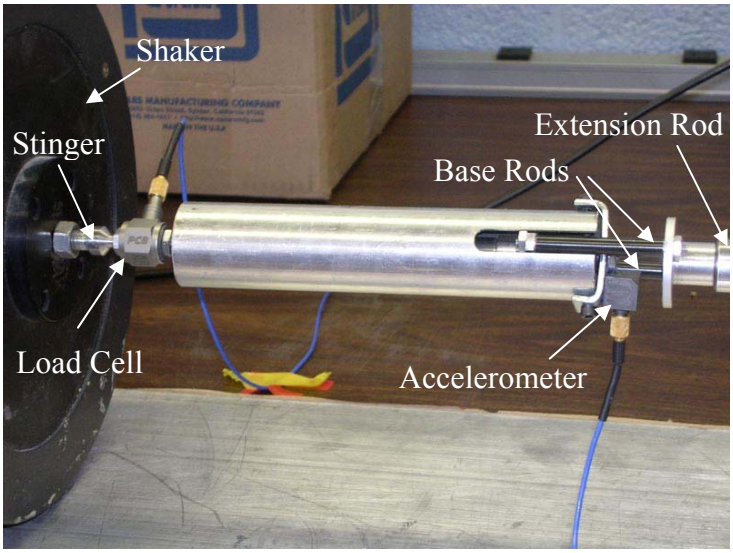

Figure C-12. Syringe type damper on the experimental setup

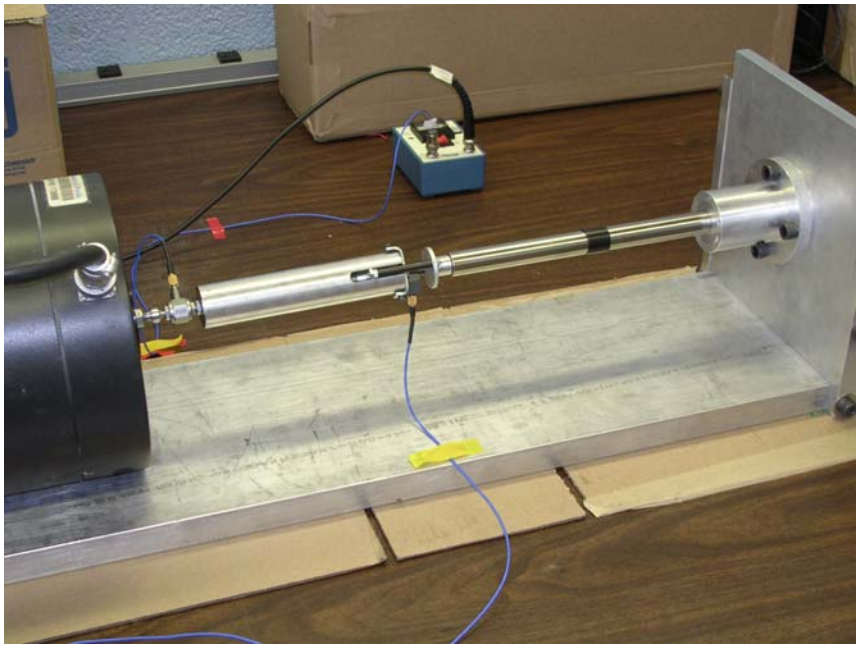

Figure C-13. Syringe type damper on the experimental setup connected to the shaker

APPENDIX D
6 DOF VIBRATION ISOLATION ADDITIONAL RESULTS

Additional results are provided in this appendix for linear and angular sinusoidal disturbances in the x- and y-axis.

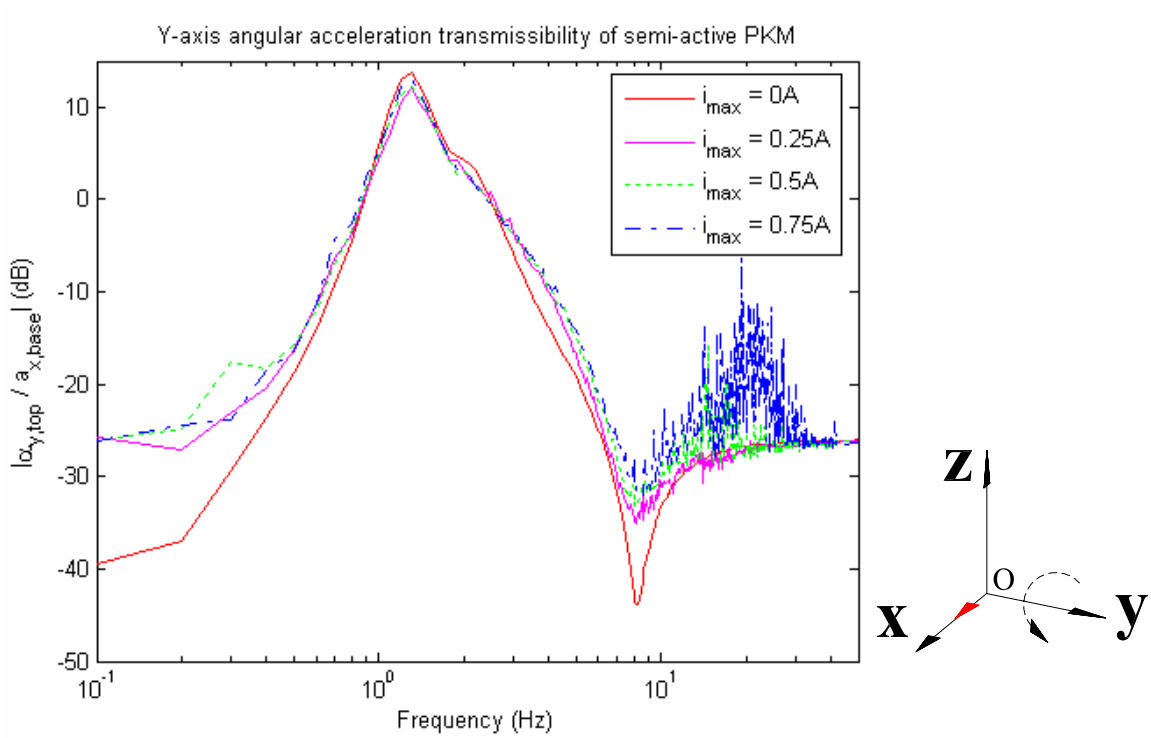

Figure D-1. RMS transmissibility between the top platform angular acceleration around the y-axis and the bottom platform linear acceleration around the x-axis for an input sinusoidal force in the x-axis

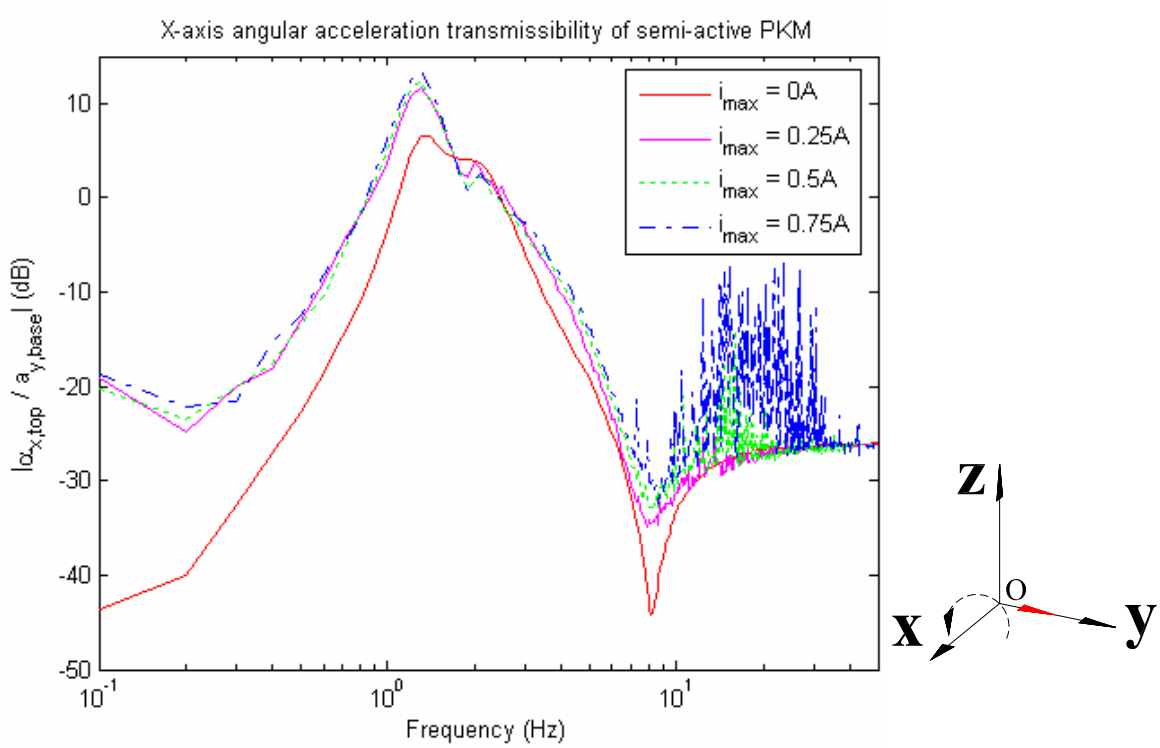

Figure D-2. RMS transmissibility between the top platform angular acceleration around the x-axis and the bottom platform linear acceleration in the y-axis for an input sinusoidal force in the y-axis

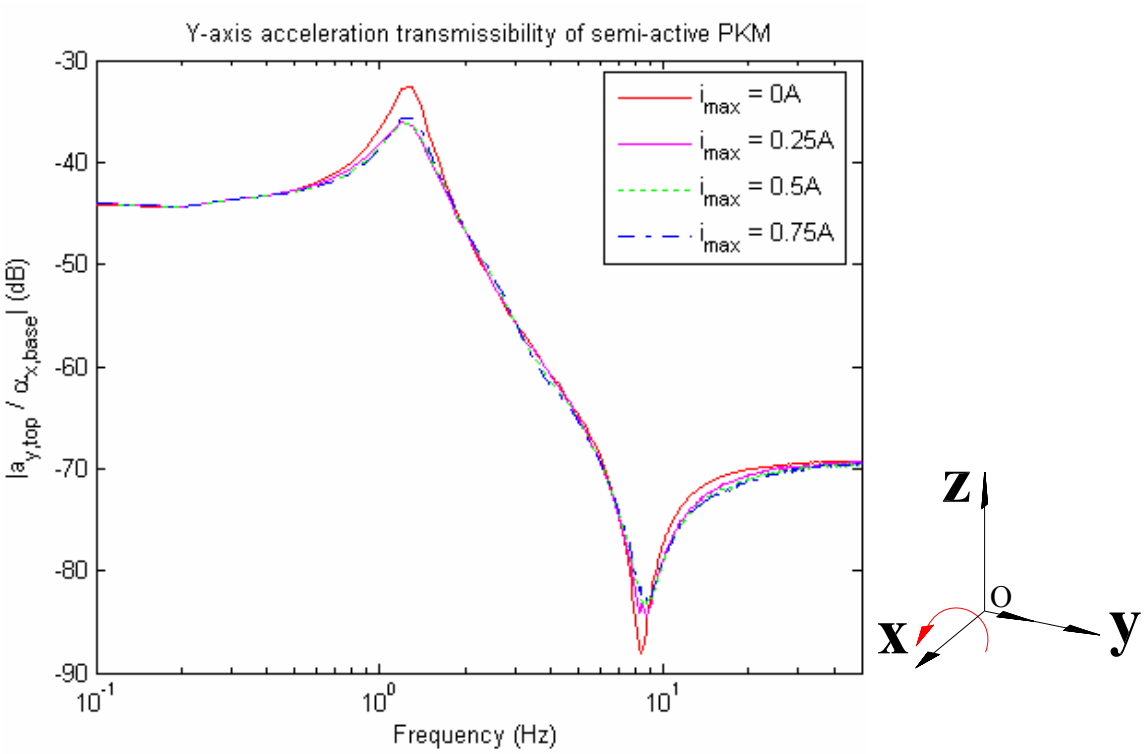

Figure D-3. RMS transmissibility between the top platform linear acceleration in the y-axis and the bottom platform angular acceleration around the x-axis for an input sinusoidal torque around the x-axis

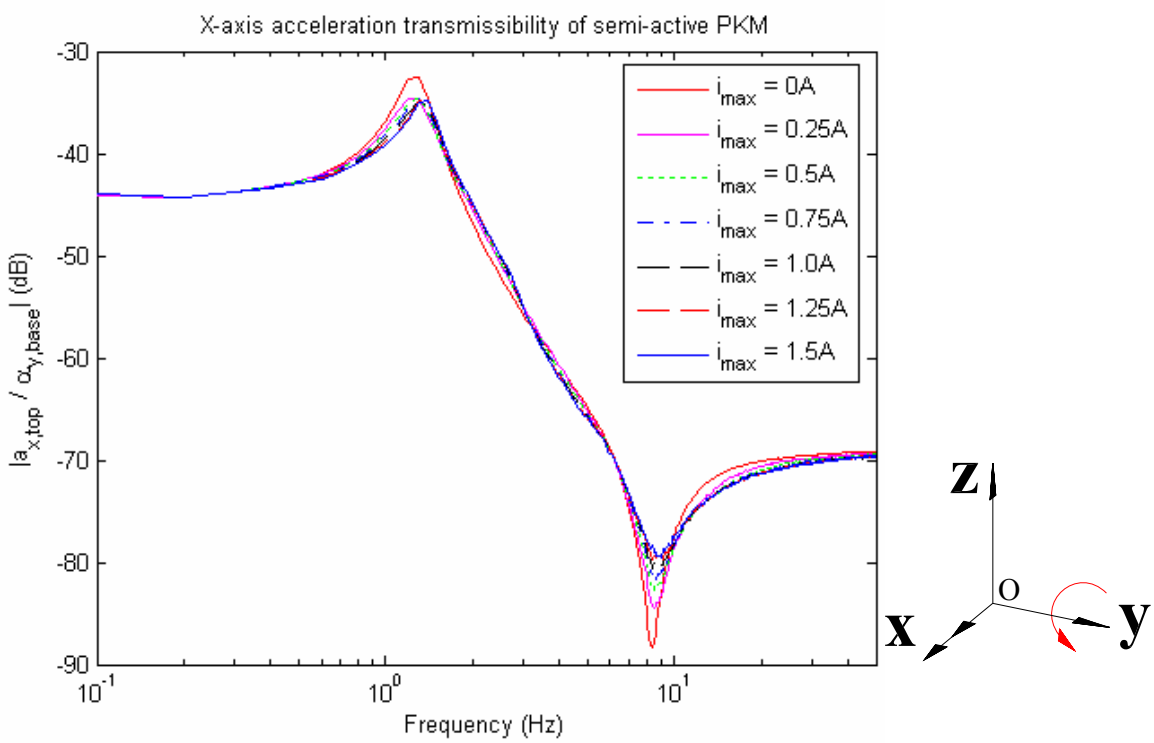

Figure D-4. RMS transmissibility between the top platform linear acceleration in the x-axis and the bottom platform angular acceleration around the y-axis for an input sinusoidal torque around the y-axis

LIST OF REFERENCES

Abu Hanieh, A., *Active isolation and damping of vibrations via stewart platform*, Ph.D. Dissertation, Universite Libre de Bruxelles, Department of Mechanical Engineering and Robotics, Brussels, Belgium, 2003.

Anderson, E. H., Cash, M. F., Hall, J. L., and Pettit, G. W., "Hexapods for precision motion and vibration control," *American Society for Precision Engineering, Control of Precision Systems*, April 2004, 2004.

Anderson, E. H., Fumo, J. P., and Erwin, R. S., "Satellite ultraquiet isolation technology experiment (suite),"*IEEE Aerospace Conference Proceedings*, v 4 2000, p 299-313, 2000.

Anderson, E. H., Leo, D. J., and Holcomb, M. D., "Ultraquiet platform for active vibration isolation," *Proceedings of SPIE—The International Society for Optical Engineering*, v 2717 1996, p 436-451, 1996.

Baiges-Valentin, I., *Dynamic modeling of parallel manipulators*, Ph.D. dissertation, University of Florida, Mechanical Engineering Department, Gainesville, Florida, 1996.

Bamford, R., Kuo, C. P., Glaser, R., and Wada, B. K., "Long stroke precision pzt actuator," *AIAA/ASME/ASCE/AHS Structures, Structural Dynamics & Materials Conferenc Collection of Technical Papers*, v 5 1995. AIAA, New York, NY, USA, p 3278-3284, 1995.

Brennan, M. J., Day, M. J., and Randall, R. J., "Experimental investigation into the semi-active and active control of longitudinal vibrations in a large tie-rod structure," *Journal of Vibration and Acoustics, Transactions of the ASME*, v 120 n 1 Jan 1998, p 1-12, 1998.

Carlson, J. D. and Spencer Jr., B. F., "Magneto-rheological fluid dampers for semi-active seismic control," *Proceedings of 3rd International Conference on Motion and Vibration Control*, v 3, Chiba, Japan, p 35–40, 1996.

Cobb, R. G., Sullivan, J. M., Das, A., Porter Davis, L., Tupper Hyde, T., Davis, T., Rahman, Z. H., and Spanos, J. T., "Vibration isolation and suppression system for precision payloads in space," *Smart Materials and Structures*, v 8 n 6 Dec 1999, p 798-812, 1999.

Crane, C. D., Rico, J. M., and Duffy J., “Screw theory and its application to spatial robot manipulators,” p. 79-95, Cambridge University Press, 2006.

Crosby, M. J., and Karnopp, D. C., "The Active Damper," *The Shock and Vibration Bulletin* v 43, Naval Research Laboratory, Washington, D.C., 1973.

Denoyer, K. K. and Johnson, C., “Recent achievements in vibration isolation systems for space launch and on-orbit applications,” *Proceedings of the 52nd International Astronautical Congress*, Toulouse, France, October 1-5, 2001.

Dogrouz, M. B., Wang, E. L., Gordaninejad, F., and Stipanovic, A. J., “Augmenting heat transfer from fail-safe magneto-rheological fluid dampers using fins,” *Journal of Intelligent Material Systems and Structures*, v 14 n 2 February 2003, p 79-86, 2003.

Dyke, S. J., Spencer, B. F., Sain, M. K., and Carlson, J. D., “Modeling and control of magnetorheological dampers for seismic response reduction,” *Smart Materials and Structures*, v 5 n 5 October 1996, p 565-575, 1996.

Fichter, E. F., “A Stewart-Platform based manipulator: general theory and practical construction,” *International Journal of Robotics Research*, v 5 n. 2 July 1986, p 157-182, 1986.

Flint, E. and Anderson, E., “Multi-degree of freedom parallel actuation system architectures for motion control,” *AIAA Space 2001 Conference*, Albuquerque, NM, Aug. 2001, AIAA Paper 2001-4750, 2001.

Fujita, T., Tagawa, Y., Kajiwara, K., Yoshioka, H., Takeshita, A., and Yasuda, M., “Active 6-dof microvibration control system using piezoelectric actuators,” *Proceedings of SPIE - The International Society for Optical Engineering*, v 2040 1993, p 514-528, 1993.

Garrett, G. T., Chen, G., Cheng, F. Y., and Huebner, W., “Experimental characterization of piezoelectric friction dampers,” *Proceedings of SPIE - The International Society for Optical Engineering*, v 4330 2001 p 405-415, 2001.

Geng, Z. J. and Haynes, L. S., “Six degree-of-freedom active vibration control using the stewart platforms,” IEEE Transactions on Control Systems Technology, v 2 n 1 Mar 1994, p 45-53, 1994.

Geng, Z. J., Pan, G. G., Haynes, L. S., Wada, B. K., and Garba, J. A., “Intelligent control system for multiple degree-of-freedom vibration isolation,” *Journal of Intelligent Material Systems and Structures*, v 6 n 6 Nov 1995, p 787-800, 1995.

Grant, D. and Hayward, V., “Design of shape memory alloy actuator with high strain and variable structure control,” *Proceedings of IEEE International Conference on Robotics and Automation*, v 3 1995, IEEE, Piscataway, NJ, USA, p 2305-2312, 1995.

Griffis, M., *Kinestatic control: a novel theory for simultaneously regulating force and displacement,* Ph.D. Dissertation, University of Florida, Department of Mechanical Engineering, Gainesville, Florida, 1991.

Guangqiang, Y., "Large-scale magnetorheological fluid damper for vibration mitigation: Modeling, testing and control," *Ph.D. Dissertation, University of Notre Dame, Department of Civil Engineering and Geological Sciences, Notre Dame, Indiana*, 2001.

Guntur, R.R. and Sankar, S., "Fail-Safe Vibration Control Using Active Force Generators," *ASME Journal of Vibration, Acoustics, Stress, and Reliability in Design*, v 105, n 3, p. 361-368, 1983.

Hac, A. and Youn, I., "Optimal semi-active suspension with preview based on a quarter car model," *Journal of Vibration, Acoustics, Stress, and Reliability in Design*, v 114 n 1 Jan 1992, p 84-92, 1992.

Hagood, N. W. and Von Flotow, A., "Damping of structural vibrations with piezoelectric materials and passive electrical networks," *Journal of Sound and Vibration*, v 146 n 2 Apr 22 1991, p 243-268, 1991

Hall, J. L., Pettit, G. W., Lindler, J. E., Anderson, E. H., Flint, E. M., "Compact lightweight six-axis point-and-hold positioning system," *Smart Structures and Materials 2003: Industrial and Commercial Applications of Smart Structures Technologies*, p 287-300, v 5054, 2003.

Hauge, G. S. and Campbell, M. E., "Sensors and control of a space-based six-axis vibration isolation system," *Journal of Sound and Vibration*, v 269 n 3-5 Jan 22 2004, p 913-931, 2004.

Jean, P., Ohayona, R., and Le Bihan, D., "Semi-active control using magneto-rheological dampers for payload launch vibration isolation," *SPIE Symposium on Smart Structures and Materials* 2006, San Diego, California, USA, February 2006.

Johnson, C. D., Wilke, P. S., and Darling, K. R., "Multi-axis whole-spacecraft vibration isolation for small launch vehicles," *Proceedings of SPIE - The International Society for Optical Engineering*, v 4331 2001, p 153-161, 2001.

Jolly, M. R., Bender, J. W., and Carlson, J. D., "Properties and applications of commercial magnetorheological fluids," *Proceedings of SPIE - The International Society for Optical Engineering*, v 3327 1998, p 262-275, 1998.

Kornbluh, R., Pelrine, R., Prahlad, H., Stanford, S., Rosenthal, M., and von Guggenberg, P., "Rubber to rigid, clamped to undamped: Toward composite materials with wide-range controllable stiffness and damping," *Smart Structures and Materials 2004: Industrial and Commercial Applications of Smart Structures Technologies, v 5388*, 2004.

Lane, J. S. and Ferri, A. A., "Control of a flexible structure using combined active and semi-active elements," *AIAA/ASME/ASCE/AHS Structures, Structural Dynamics & Materials Conference - Collection of Technical Papers*, AIAA, NY, USA, v 2 1995, p 719-728, 1995.

Lee, J., *Investigations of Quality Indices of In-Parallel Platform Manipulators and Development of Web Based Analysis Tool,* University of Florida, Department of Mechanical Engineering, Gainesville, Florida, 2000.

Lee, J. K. and Clark, W. W., "Semi-active control of flexural vibrations with an mr fluid actuator," *Proceedings of SPIE - The International Society for Optical Engineering*, v 3672 1999, p 167-174, 1999.

Lee, J., and Duffy, J., "The Optimum Quality Index for Some Spatial In-Parallel Devices," *1999 Florida Conference on Recent Advances in Robotics*, Gainesville, FL, April 1999.

Lee, J., Duffy, J., and Keler, M., "The Optimum Quality Index for the Stability of In-Parallel Planar Platform Devices," *Proceedings of the ASME 24th Biennial Mechanisms Conference*, 96-DETC/MECH-1135, Irvine, Ca., 1996.

Lee-Glauser, G. J., Ahmadi, G., and Layton, J. B., "Satellite active and passive vibration control during liftoff," *Journal of Spacecraft and Rockets*, v 33 n 3 May-Jun 1996, p 428-432, 1996.

The Mathworks, Inc., Documentation, SimMechanics © 2006, What is SimMechanics?, http://www.mathworks.com/access/helpdesk/help/toolbox/physmod/mech/, April 2006.

Merlet J-P., "Redundant parallel manipulators," *Journal of Laboratory Robotic and Automation*, v 8 n 1, p 17-24, 1996.

NASA, Electroactive Polymers Technology Promotion © 2004, NASA LaRC TCPO and TeCCenter, Electroactive polymers, http://www.teccenter.org/electroactive_polymers, March 2006.

Ni, Y. Q., Liu, H. J., and Ko, J. M., "Experimental investigation on seismic response control of adjacent buildings using semi-active MR dampers," *Smart Structures and Materials 2002: Smart Systems for Bridges, Structures, and Highways*, 2002.

Park, S.-E. and Shrout, T. R., "Ultrahigh strain and piezoelectric behavior in relaxor based ferroelectric single crystals," *Journal of Applied Physics*, v 82 n 4 Aug 15 1997, p 1804-1811, 1997.

Preumont, A., "Vibration Control of Active Structures: An Introduction", p 116-119, Kluwer Academic Publishing, Boston, 2002.

Rabinow, J., "The magnetic fluid clutch," *AIEE Transactions,* v 6, p 1308–1315, 1948.

Red Team Too, Darpa Grand Challenge 2005 Team Technical Papers, © 2005, http://www.darpa.mil/grandchallenge05/TechPapers/RedTeamToo.pdf, May 2006.

Scruggs, J. and Lindner, D., "Active energy control in civil structures," *Proceedings of SPIE - The International Society for Optical Engineering*, v 3671 1999, p 194-205, 1999.

Sims, N. D., Stanway, R., and Johnson, A. R., "Vibration control using smart fluids: a state-of-the-art review," *Shock and Vibration Digest*, v 31 n 3 1999, p 195-205, 1999.

SMA/MEMS Research Group and University of Alberta, Shape memory alloys, © 2001, http://www.cs.ualberta.ca/~database/mems/sma_mems/sma.html, December 2004.

Snyder, R. A., Kamath, G. M., and Wereley, N. M., "Characterization and analysis of magnetorheological damper behavior due to sinusoidal loading," *Proceedings of SPIE - The International Society for Optical Engineering*, v 3989 2000, p 213-229, 2000.

Snyder, R. A. and Wereley, N. M., "Characterization of a magnetorheological fluid damper using a quasi-steady model," *Proceedings of SPIE - The International Society for Optical Engineering*, v 3668 n I 1999, p 507-519, 1999.

Sodeyama, H., Sunakoda, K., Fujitani, H., Soda, S., Iwata, N., and Hata, K., "Dynamic tests and simulation of magneto-rheological dampers," *Computer-Aided Civil and Infrastructure Engineering*, v 18 n 1 January 2003, p 45-57, 2003.

Spencer Jr., B. F., Sain, M. K., and Carlson, J. D., "Phenomenological model of a magnetorheological damper," *Journal of Engineering Mechanics, v 183, n 3, p 230-238*, 1997.

Stanway, R., Sproston, J. L., and Stevens, N. G., "Non-linear modelling of an electro-rheological vibration damper," *Journal of Electrostatics*, v 20 n 2, p 167-184, 1987.

Sunakoda, K., Sodeyama, H., Iwata, N., Fujitani, H., and Soda, S., "Dynamic characteristics of magneto-rheological fluid damper," *Proceedings of SPIE - The International Society for Optical Engineering*, v 3989 2000, p 194-203, 2000.

Symans, M. D. and Constantinou, M. C., "Experimental testing and analytical modeling of semi-active fluid dampers for seismic protection," *Journal of Intelligent Material Systems and Structures*, v 8 n 8 Aug 1997, p 644-657, 1997.

Taniwangsa, W. and Kelly, J. M., "Experimental testing of a semi-active control scheme for vibration suppression," *Proceedings of SPIE - The International Society for Optical Engineering*, v 3045 1997, p 130-139, 1997.

Tarics, A. G., Way, D. and Kelly, J.M., *The implementation of base isolation for the foothill communities law & justice center*, Technical Report, RTA, San Francisco, 1984.

Thayer, D., Campbell, M., Vagners, J., and Von Flotow, A., "Six-axis vibration isolation system using soft actuators and multiple sensors," *Journal of Spacecraft and Rockets*, v 39 n 2 March/April 2002, p 206-212, 2002.

Thomson, W. T., *Theory of vibration with applications*, Prentice Hall, 3rd Edition, N.J., 1988.

Tsai, L., "Robot analysis: The mechanics of serial and parallel manipulators", *John Wiley & Sons*, New York, 1999.

Unsal, M., Niezrecki, C., and Crane III, C., "A new semi-active piezoelectric-based friction damper," *Proceedings of SPIE - The International Society for Optical Engineering*, v 5052 2003, p 413-420, 2003.

Vaillon, L., Petitjean, B., Frapard, B., and Lebihan, D., "Active isolation in space truss structures: From concept to implementation," *Smart Materials and Structures*, v 8 n 6 Dec 1999, p 781-790, 1999.

Wereley, N. M., Pang, L., and Kamath, G., "Idealized hysteresis modeling of electrorheological and magnetorheological dampers," *Journal of Intelligent Material Systems and Structures*, v 9 n 8 1999, p 642-649, 1999.

Williams, K., Chiu, G., and Bernhard, R., "Adaptive-passive absorbers using shape-memory alloys," *Journal of Sound and Vibration*, v 249 n 5 Jan 31 2003, p 835-848, 2002.

Winthrop, M. F. and Cobb, R. G., "Survey of state-of-the-art vibration isolation research and technology for space applications," *Proceedings of SPIE—The International Society for Optical Engineering*, v 5052 2003, p 13-26, 2003.

Yalcintas, M., "Magnetorheological fluid based torque transmission clutches," *Proceedings of the International Offshore and Polar Engineering Conference*, v 4 1999, p 563-569, 1999.

Yang, G., Carlson, J. D., Sain, M. K., and Spencer, Jr., "Large-scale mr fluid dampers: Modeling and dynamic performance considerations," *Engineering Structures*, v 24 n 3 March 2002, p 309-323, 2002.

BIOGRAPHICAL SKETCH

The author was born in 1977 in Ankara, Turkey. After much traveling around the country, when it was time to go to high school, he decided to leave his family in the quiet, Aegean town of Izmir and move to Istanbul which happens to be the most chaotic and beautiful city on the planet (according to the author). He graduated with a Bachelor of Science in mechanical engineering in May 2000 from Istanbul Technical University. Making up his mind that he probably needed to live in a quieter place for a while, he took the first plane to sunny Florida, to the not-so-chaotic town of Gainesville where he obtained a Master of Science degree in mechanical engineering in August 2002. When his advisor presented him the opportunity to work with "smart" fluids and robots, he decided he rather enjoyed the life of a graduate student (especially if it would involve working with "smart" fluids and robots) and stayed in Gainesville for a few more years to earn his Ph.D. in mechanical and aerospace engineering in August 2006 from the University of Florida.